Characterization and Improvement of Copper / Glass Adhesion

by

Baofeng He

A Doctoral Thesis submitted in partial fulfilment of the
requirements for the award of Doctor of Philosophy
of Loughborough University

April 2012

CERTIFICATE OF ORIGINALITY

This is to certify that I am responsible for the work submitted in this thesis, that the original work is my own except as specified in acknowledgments or in footnotes, and that neither the thesis nor the original work contained therein has been submitted to this or any other institution for a degree.

…… (Signed)

…… (Date)

ABSTRACT

The development of glass substrates for use as an alternative to printed circuit boards (PCBs) attracts significant industrial attention, because of the potential for low cost but high performance interconnects and optical connection. Electroless plating is currently used to deposit conductive tracks on glass substrates and the quality of copper / glass adhesion is a key functional issue. Without adequate adhesive strength the copper plating will prematurely fail. Existing studies have covered the relationship between surface roughness and adhesion performance, but few of them have considered the detail of surface topography in any depth. This research is specifically considering the mechanical contribution of the glass surface texture to the copper / glass adhesive bond, and attempting to isolate new ISO 25178 areal surface texture parameters that can describe these surfaces.

Excimer laser machining has been developed and used to create a range of micro pattern structured surfaces on CMG glass substrates. Excimer mask dimensions and laser operation parameters have been varied and optimized according to surface topography and adhesion performance of the samples. Non-contact surface measurement equipment (Zygo NewView 5000 coherence scanning interferometry) has been utilized to measure and parameterize (ISO 25178) the surface texture of the glass substrates before electroless copper metallization. Copper adhesion quality has been tested using quantitative scratch testing techniques, providing an identification of the critical load of failure for different plated substrates. This research is establishing the statistical quality of correlation between the critical load values and the associated areal parameters.

In this thesis, the optimal laser processing parameter settings for CMG glass substrate machining and the topographic images of structured surfaces for achieving strong copper / glass plating adhesion are identified. The experimental relationships between critical load and areal surface parameters, as well as the discussions of a theoretical approach are presented. It is more significant to consider *Sq*, *Sdq*, *Sdr*, *Sxp*, *Vv*, *Vmc* and *Vvc* to describe glass substrate surface topography and the recommended data value ranges for each parameter have been identified to predict copper / plating adhesion performance.

Keywords: Glass, surface texture, areal parameters, adhesion, laser machining

ACKNOWLEDGMENTS

My deepest gratitude goes first and foremost to Dr Jon Petzing, my first supervisor, for his encouragement and guidance during the course of my study. Secondly, I would like to express my sincere gratitude to Dr Patrick Webb and Professor Richard Leach for their help and supervision.

I would like to thank the technicians Mr. Peter Wileman, Mr. Andy Sandaver and Mr. Jagpal Singh for their advice and assistance. My thanks also go to the following academic and technical staff in Loughborough University: Mr. Trevor Atkinson, Dr Keith Yendall and Dr Alun Owen. I would also like to thank Prof. Mark Gee and Dr John Nunn at UK National Physical Laboratory for their help in scratch testing. The gratitude also goes to Mr Andy Gray of Qioptiq Ltd for the supply of CMG glass.

I also appreciate the funding of this research provided by UK National Physical Laboratory 2008 – 2011 Length Programme and the EPSRC 3D-Mintegration Grand Challenge project.

Finally, I want to dedicate this thesis to my beloved husband Yi Zhang for his loving consideration and great support in me all through these years.

PUBLICATIONS

The following publications have been generated from this work:

- B. He, J. N. Petzing, D. P. Webb and P. P. Conway. Using areal parameters to improve electroless copper plating bond strength on glass substrates. *13th International Conference on Metrology and Properties of Engineering Surfaces*, Twickenham, London, 12-14 April 2011.

- B. He, D. P. Webb, J. Petzing and R. Leach. Improving Plated Copper Adhesion for Metallization of Glass PCBs. *ICEPT-HDP*, Shanghai, China, 8-11 August 2011.

- B. He, J. N. Petzing, D. P. Webb and P. P. Conway and R. Leach. The assessment of areal surface texture parameters for characterizing the adhesive bond strength of copper plated micro-machined glass. *Euspen 12th International Conference*, Stockholm, Sweden, June 2012, Oral presentation.

- B. He, J. N. Petzing, D. P. Webb, P. P. Conway and R. Leach. The use of areal surface texture parameters to characterize the mechanical bond strength of copper on glass plating applications. *NPL report ENG 34, Queen's Printer and Controller of HMSO*, 25 pages, January 2012, ISSN:1754-2987.

- B. He, J. N. Petzing, D. P. Webb and R. K. Leach. Laser micro-patterning of structures on glass to improve copper plating bonding characteristics. Manuscript in writing, to be submitted to the Journal of Laser Micro/Nano-Engineering, 2012.

CONTENT

Chapter 1 Introduction

1.1 Introduction

This thesis considers the role that surface topography may have on influencing the adhesive bond strength of electroless copper plating on glass substrates. Chapter 1 identifies the need for good quality copper bonding on glass substrates, and sets out the aims and objectives of the research reported in this thesis. The chapter then provides an overview of three dimensional surface texture parameters development, and an analysis of existing research that has considered the role of surface texture in adhesion. The chapter introduces issues of surface wettability, before finishing with a brief summary on the proposed experimental methodology used throughout the work.

1.2 Research background

High performance electronic packaging requires that circuit boards and substrate materials ideally have a combination of optimized properties, including low mass, high thermal stability, high thermal conductivity, low coefficient of thermal expansion (CTE), high glass transition temperature (Tg), high mechanical strength, low dielectric constant, low moisture absorption, good chemical resistance and low cost [1].

The drive towards increasing densities of components and integrated circuit inputs / outputs (i/o's) in electronics is pushing the capabilities of conventional printed circuit board (PCB) manufacture to its limits. While sub-100 μm metal features can be produced, the dimensional instability of organic material based boards (such as polyimide materials) in response to changes in temperature or humidity means such features cannot be reliably aligned. Inorganic materials (such as alumina substrates) have drawbacks including high cost and poor CTE which induces shear stresses causing failure. Fibre reinforced composite series 4 (FR4) is the most currently used composite material because of its good mechanical and physical properties. However, thermal mismatch and dimensional instability restrict its application especially at higher temperature and frequencies [2].

Glass is attractive as an alternative substrate material for use in electronic packaging because it is relatively low cost, environmentally friendly and highly thermally stable with CTE values similar to that of silicon. It is also transparent which could simplify assembly and inspection of components with area array or hidden interconnects, and facilitate developments in optoelectronic circuitry. These appealing advantages attract researchers and the concept of using glass for high density interconnect has been explored by several groups. Previous work using glass for high density interconnect has examined the generation of laser micro-machined channels [3], the development of laser machined microvias [4-6], and the formulation of effective interface chemistry to allow better electroless copper plating [4, 7].

Electroless plating has been applied to deposit conductive tracks on the insulating glass substrate surface, which is important for the manufacture of electronic components, because many devices are becoming miniaturised and more complex but must still cost less. However, it is difficult for metallization on the smooth glass surface due to physical, chemical and mechanical mismatch between the metal coating and glass substrate. Therefore improving the plated layer adhesion is one of the most important considerations for development of the technology, as without adequate adhesion the coating tends to peel off and not perform the task for which it is intended.

Increasing the roughness of glass surface by surface treatments such as plasma roughening, mechanical abrasion, chemical modification, bead blasting and excimer laser machining can improve plating adhesion. One of the most significant issues is the quality of bonding of copper plating (circuit layup) to the glass substrate, with adhesive bond strength being a function of electrochemical and surface topography components. Whilst significant work has previously examined the electrochemical components of glass / copper adhesion, little attention has been paid to the role that surface topography may play. This is partly due to the inadequacy of two dimensional surface texture parameters for describing three-dimensional effects, but also due to the difficulty of generating and controlling the glass surface topography.

A key hypothesis in this work has been to consider the potential of characterizing glass surface texture using non-contact areal surface topography measurement, coupled with the new areal surface texture parameters in the ISO 25178 suite of standards specifically ISO / FDIS 25178: 2 [8]. The areal parameters in principle capture much more of the complexity of

surfaces than traditional profile parameters such as *Ra*. It is anticipated that these areal parameters should provide much better understanding of surface morphology, allowing greater comprehension of the mechanical adhesion characteristics of glass substrates for copper bonding.

Furthermore, the overall aims of this research were to:

- Correlate quantified adhesion strength measurements using scratch testing techniques with areal parameters.

- Identify eligible parameters that can characterize adhesive bonding performance and therefore reduce the design / testing cycle of glass surface preparation / acceptance for film deposition.

- Refine and optimise the surface texture preparation for improving mechanical copper plating adhesion on glass, thus potentially improving electronic functionality and life cycle.

1.3 Research objectives and novelty

Plating adhesion is a relatively new and developing field of application of three dimensional (3D) analysis where surface topography is of importance. This project concentrates on applying areal surface texture parameters for functional characterisation of surfaces with respect to adhesion. It should then be possible to proactively design surface features that enhance adhesion quality.

The objectives and perceived novelty of this work presented here is identified as follows:

1. Glass as the study material is a promising substitute material for use in the PCB manufacturing industry. Different methods for roughening the glass surface are to be investigated and compared for improving copper plating adhesion on glass substrate.

2. Investigate manufacturing processes for producing (controlled) random surfaces on

glass substrates. Potential methods of texturing include bead blasting, micro-sand blasting, plasma treatment and chemical etching.

3. A variety of novel and bespoke micrometric scale features at different depths are to be investigated on glass by laser machining. The laser is a potentially effective tool for the generation of micro pattern array structures on glass, using a dragging process. Optimal surface topography for strong adhesive bonding of electroless copper plating is to be identified. This section of work is expected to have novelty.

4. Apply and / or develop contact / non-contact metrology techniques to routinely measure surface topography on glass substrates and generate areal surface texture parameters for different surface textures. This section of work will recognize and use existing intellectual knowledge.

5. Assimilate and develop copper plating chemistry for the metallization of textured glass surfaces. Plating parameters such as operation temperature, chemical concentration and dipping time in solution is to be optimised for consistency and thickness of coating. This section of work will recognize existing intellectual knowledge, but, is expected to have novelty with respect to the glass used.

6. Apply a quantifiable testing technique for assessing copper / glass adhesive bond strength (critical load). This section of work will be completed in collaboration with the UK National Physical Laboratory.

7. Investigation of the application of a range of ISO 25178 areal surface texture parameters for correlation with copper plating adhesion. Produce statistics that demonstrate the quality of correlation between critical load values (adhesive bond strength) and a range of ISO 25178 areal parameters, and provide understanding for the trends and observed behaviour. This section of work is expected to have novelty.

8. Identify key ISO 25178 areal parameters that provide routinely robust characterisation of glass textured surface suitability for copper bonding and predicting adhesion quality with the potential for use in an industrial manufacturing environment. This section of work is expected to have novelty.

1.4 Progress in areal surface topography characterisation

1.4.1 Advantages of areal surface texture parameters

In recent years the significance of surface topographic features has been emphasized by researchers and industrialists in many fields. As shown in Figure 1.1, surface texture measurement and control assists both designers and engineers [9]. Surface metrology has two roles in industry: one to help control manufacture, including controlling processing and machine tools, and the other is to help optimize the function of manufactured objects. These two roles can have a profound impact on quality. Controlling the manufacture helps repeatability and hence quality of conformance. Functional optimization helps the designer and thereby assists in the quality of design. Surface texture parameters quantify surface texture and so play an important role in product design and manufacture.

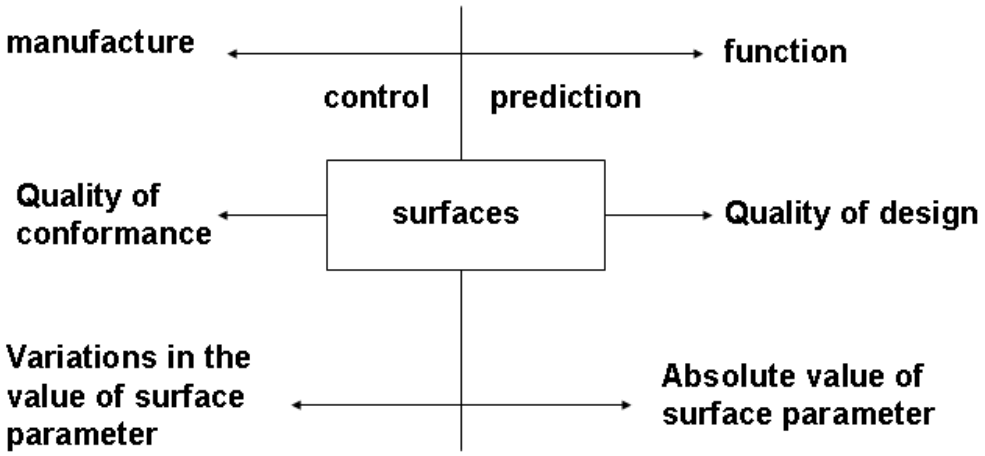

Figure 1.1 Roles of surface metrology [9]

Two dimensional (2D) profile surface roughness parameters such as *Ra* and *Rq* are the most commonly used in most industrial applications [10]. The analyses traditionally performed, computed on profile data, are very poor from a statistical point of view because the values obtained are very sensitive to the sampled region and direction of profile. The surfaces produced and measured in this study are randomly rough or micro pattern structured, which are three dimensional and anisotropic in nature. However, only when the surface is isotropic and homogeneous, can a single 2D profile be representative of the surface [11].

Since 2D profiles do not provide sufficient topographic information in the direction perpendicular to that profile, the functional information that can be provided by 2D parameters is not comprehensive. In comparison, a 3D approach to surface analysis can provide more information to assess surface topography, which is not available from the conventional analysis by 2D techniques and largely overcomes these limitations of 2D surface analysis.

Additionally 3D surface texture parameters can assess areal properties of roughness which may relate better to the manufacturing route and the surface functionality (hence the description-areal parameters). The amplitude and spatial characteristics of areal surface topography dominates the functional performance in applications like wear, friction, lubrication, fatigue, sealing, jointing, reflectance, painting and so on. Further, the performance and reliability of engineering components such as bearings, gears, and engine bores can potentially be increased by selecting and controlling the appropriate 3D topographic characteristics. Different industries use different surface texture parameters for their specific applications. The possibility of using specific areal parameters to describe textural properties is another advantage.

Areal surface topography greatly influences not only the mechanical and physical properties of contacting parts, but also the optical and coating properties of some non-contacting components. Areal techniques are expected to gain increasingly widespread use not only in the areas where mainly areal surface texture parameters could produce meaningful results, such as biology and chemistry, but also in the areas where traditional profile measurements have been conventionally applied, such as optical and mechanical engineering.

Notwithstanding areal surface topography may play an important role in determining the satisfactory performance of the workpiece in many industrial fields, few researchers and industrialists use areal techniques to describe surface texture for specific application. For example, there is a lot of experience with profile parameters to characterize lubricating surfaces, but very little with areal parameters. Functional characterisation is seen as the most important aspect of data processing from an industrial view point, so it is timely to study the application of areal parameters for particular technological applications.

1.4.2 Historical development of the areal approach

The first steps in 3D surface topography probably date back to the 1970's when Grieve *et al*. developed simple operating systems to record parallel profiles and produce contour maps [12]. The advent of the new generation of PC computers, which arrived in the late 1980's, made areal analysis more practicable and accelerated the development.

During the 1990s, the European Community supported important programmes in the field of surface characterisation, specifically the Development of Methods for the Characterisation of Roughness in Three Dimensions under the leadership of Birmingham University (UK) [8]. In 1993, a proposal was made for an areal surface texture numerical parameter set called the "Birmingham 14 parameters", since a large part of the work had been undertaken at Birmingham University. This parameter set, though widely accepted, was considered to be somewhat theoretical with insufficient practical evidence for its applicability. Other areal surface texture parameters were later suggested by a variety of workers and institutions.

From 1998 to 2001, the AUTOSURF project led by Rover / Brunel University (UK) and the SURFSTAND project led by Huddersfield University (UK) were two important programmes. These two projects reported to ISO / TC 213 in 2002. The AUTOSURF project proposed that further parameters were added to the Birmingham 14 parameters [8].

In 2003, the "Green book" was published [13] containing the detailed results from the SURFSTAND project. Following this feat, areal parameter study has been pursued by many researchers and in recent years progress has been rapid, thanks to the development of microcomputer capability in hardware and software and advanced measurement and analysis techniques. This has allowed collection of texture data over areas instead of only along lines. Furthermore, the basic work for standardization of the measurement and analysis methods has been carried out, due to pressure from industrial companies interested in surface topography. In the currently published version of the proposed ISO standard (ISO 25178:2), the parameter list has grown to encompass over 30 parameters. Other published elements of ISO 25178 also deal with areal texture measurement instruments and calibration.

It is recognized that 3D surface topography of engineered surfaces is complex and cannot be described completely by a single or a few parameters. Each parameter can only describe one

aspect of the topography. Thus in ISO 25178:2, two classes of surface texture parameters "Field" and "Feature" parameters are identified. Field parameters apply statistics to the continuous surface from each portion of the scale-limited surface and include a number of parameters which cover amplitude, spatial, hybrid (combining amplitude and spatial) and some functional aspects. Some of these parameters are naturally extended from their 2D counterparts; others are uniquely defined for 3D surface topography features such as texture type (isotropy or anisotropy), texture direction, material volume, void volume, pits or troughs which are invisible from 2D profiles. Feature parameters apply statistics from a sub-set of pre-defined topographic features. Feature parameters are defined using a toolbox of pattern recognition techniques that can be used to characterize specified features on a scale-limited surface.

1.4.3 Review of areal surface texture parameters application

The recent advancements achieved in 3D analysis of surface texture have raised great interest amongst researchers and industrial users for the possibilities of the new techniques, in spite of parameter complexity. The theoretical and applied research literature on the analysis and applications of areal surface topography is spread across a diverse range of subjects over the last twenty years, including; manufacturing, materials, tribology, chemistry and biology. Examples of industrial applications of areal surface analysis related to the functional features are illustrated in Table 1.1 [14-39].

Table 1.1 Example publications concerning the general application of areal surface parameters

Researchers	Year	Application area	Parameters used	Ref.
Stout and Sullivan	1991	Sheet surfaces through rolling	*Sa Sq Ssk Sku*	14
Wennerberg *et al.*	1995	Engineering and biomaterial surfaces	*Sa Sq Sz Ssk Sku Sk Spk Svk Sr1 Sr2*	15
Dong and Stout	1995	Surface wear	*Sq Sz Ssk Sku Sal Str Sds SΔq Ssc Sdr Svi Sbi*	16
Blunt and Ebdon	1996	Grinding wheel topography	*Sds Sq Sz Ssk Sku Str Sal Std SΔq Ssc Sdr Sbi Sci Svi*	17
Xie *et al.*	1999	Cold-rolled steel sheet	*Sq Sds*	18

Table 1.1 (continued)

Researchers	Year	Application area	Parameters used	Ref.
Jiang, Blunt and Stout	1999	Bio-engineering	*Sq Sz Ssk Sku Sds Str Sal Std SΔq Ssc Sdr Sbi Sci Svi*	19
Ramasawmy and Blunt	2001 2005	Electrochemical polishing surfaces and white layer thickness in EDM	*Sq Sz Sds Sm Sc Sv Sa* *S5z*	20, 21
Butler *et al*.	2002	Grinding wheels	*Sds Ssc Sq*	22
Al-Nawas *et al.*	2003	Dental implants	*Sa Sdr*	23
Suh *et al.*	2003	Wear conditions of discs and steel pins	*Sa Sq Sz Ssk Sku Sds Str Std SΔq Ssc Sdr Sbi Sci Svi*	24
Benard *et al*.	2005	Adhesion of composites	*Sa*	25
Kundrak *et al*.	2006	Hard turned bore holes	*Sa Sq Sz Ssk Sku Sds Str Std Sal SΔq Ssc Sdr Sbi Sci Svi*	26
Krzyzak and Pawlus.	2006	Piston skirts surface wear	*Sq Ssk Str S Δq St±3σ Sku, Sds, SSc*	27
Senin *et al.*	2006	Segmentation through clustering	*Sa Sq Sz Ssk Sku Sds Str Std SΔq Ssc Sdr Sbi Sci Svi*	28
Sul *et al.*	2007	Titanium implants in bone	*Sa Sdr Sds*	29
Le Guéhennec *et al.*	2007	Titanium dental implants for rapid osseointegration	*Sa*	30
Ávila *et al.*	2008	The crater wear in coated hard metal tools	*Sa Sq Sk Svk Spk Ssk Sku*	31
Michalski	2008	The cylindrical gear tooth flanks	*SPa SPq Spt SPsc SPku SpΔa SPmr SPsk*	32
Waikar and Guo	2008	Turned and ground surfaces	*Sa Sq Sp Sv St Sz Ssk Sku Sds Str Sal Std SΔq Ssc Sdr STp Smmr Smvr*	33
Nguyen and Butler	2008	Grinding wheel topography	*Sds Ssc Sq Sal*	34
Aris and Cheng	2008	Precision machined engineering surfaces	*Sz Sq Ssk Sku Ssc SΔ, Ssc Sal Sdr*	35
Scardino *et al.*	2009	Antifouling technology	*Sa Ssk Str*	36
Czifra and Horváth	2011	Sliding friction of steel-ferodo material pair	*Sq Sku SΔq*	37
Wang *et al*.	2011	Biomedical titanium surface texture	*Sds Ssc Spd Spc Svd Svc S10z S5p S5v*	38
Tian *et al*.	2011	Cartilage surfaces for osteoarthritis diagnosis	*Sa Sq Ssk Sku Sz Str Sdr Smc Sxp Sk Vmp Vmc Vvv Vvc Spc S10z S5p S5v Sda Sha*	39

This table reviews the general range of application for three dimensional surface analyses, with special reference to industrial applications. It is noticed that some older parameters

summarized in this table are no longer specified in the new ISO / FDIS 25178:2 suite. The emergence of commercial 3D measurement systems such as Coherent Scanning Interferometry have emphasised the importance of 3D surface topography in science and engineering applications, and an advent of measurement and characterisation of surface topography in three dimensions. From the literature survey and publications identified in Table 1.1, the main development and application fields of areal surface texture parameters are listed as follows:

1.4.3.1 Manufacturing

One of the first examples of using areal parameters to characterize surface topography is Stout and Sullivan [14]. They firstly used 3D analysis techniques to characterize sheet surfaces formed through rolling. Afterwards a primary set of areal surface texture parameters were selected to qualify various types of engineered surfaces processed by turning, grinding, finishing, hobbing and chiselling, plain milling and end milling. Although traditional 2D (profile) measurements have been conventionally applied and dominated in manufacturing engineering, it was demonstrated that the use of individual profile or areal parameters was insufficient to characterize a surface topography. The 3D surface topography maps revealed the anisotropic and repeatable nature of a turned surface which was in contrast with the random and anisotropic nature of a ground surface.

1.4.3.2 Materials

Scardino *et al*. [36] provided *Sa*, *Ssk* and *Str* as quantified key surface parameters to guide the development of new materials with surface properties that confer fouling resistance and release. There were some case studies about characterisation of grinding wheel topography using areal surface texture parameters *Sds*, *Ssc* and *Sq*. A detailed knowledge of the nature of the topography of the grinding wheel would provide further insight into the surface interaction of the grinding wheel as well as enabling improved control of the grinding process in general. Nguyen and Butler [34] tried to correlate grinding wheel topography with its performance through the employment of areal surface characterisation parameters.

1.4.3.3 Tribology and lubrication

Dong and Stout [16] introduced a new method for qualitative and quantitative characterisation of surface wear. It was found that different parameters had different sensitivities to different types of surface wear. Some parameters have monotonic changes as surfaces wear, whilst others have non-monotonic changes as the surface topography is restructured. Moreover, functional parameters can be used to detect surface topography change from one functional zone to another.

There is a lot of experience with 2D surface texture parameters to characterize lubricating surfaces, but very little with areal parameters. Suh *et al*. [24] conducted controlled tribological scuffing experiments on typical engineering surfaces under starved lubrication conditions to simulate the contact conditions in an automotive air conditioning compressor. The functional roughness parameters were found to capture most accurately certain prominent characteristics in the worn topography of the disc surfaces and could be used to correlate the topographical changes to the meaningful physical changes occurring during progressive wear leading to scuffing. Although some functional parameters can characterize bearing property and fluid retention capability, other parameters such us *Sq*, *Ssk*, *Str Sku* and *Sds* were also found useful and recommended for worn surface description.

1.4.3.4 Biology

Surface topography is of significant importance for the bio-engineering field in areas such as joint prosthesis surfaces, replacement heart valve seal quality, contact lens quality and osseointegration of titanium implants. Jiang *et al*. [19] gave a comprehensive study of the surface topography using areal parameters. They presented an applicable tool for better understanding and characterizing of the three dimensional surface topography of orthopaedic joint prostheses. All the main areal parameters were employed for quantitative evaluation of roughness features. The functional properties, such as bearing area, material volume and void volume which are significantly affected by large peaks, pits and scratches were studied and the location of isolated peaks, pits and scratches in the different scales was also clearly characterized.

1.4.3.5 Chemistry

Ramasawmy and Blunt [20, 21] used the 14 primary areal surface parameters as a basis in order to assess the effect of different electrolytes in an electrochemical polishing process (ECP) on the surface topography of electro discharge machining (EDM) surfaces. The surface parameters which showed a greater sensitivity to the process parameters had been investigated individually. It was observed that areal surface texture parameters *Sq*, *Sm*, *Sc* and *Sv* (namely material volume of the surface *Sm* and core void volume of the surface *Sc*, now non-standard parameters) were more sensitive to the main EDM process variables. Moreover, a linear relationship between current and *Sq*, and a parabolic or quadratic relationship between pulse duration and *Sq* were also found.

1.4.3.6 Adhesion

From 2005 to 2009, Bénard *et al*. [25] published a series of papers using the areal surface texture parameter *Sa* to characterize the average roughness of adhesion of composite surfaces, showing the correlation between the surface characteristics of composite materials and adhesion performances of corresponding surface assemblies. However, only *Sa* was selected among the whole areal surface texture parameters list family, and apparently one parameter is inadequate to characterize the complex adhesive performance, but also difficult to understand the influence of areal parameter upon the whole surface properties towards adhesion.

1.5 Development of the characterisation of surface texture for adhesion

1.5.1 Theories of adhesion

Several theories attempt to describe the phenomena of adhesion. However, no single theory explains adhesion in a general, comprehensive way. Some theories are more applicable for certain substrates and applications; other theories are more appropriate for different circumstances. The most common theories of adhesion are based on:

1.5.1.1 Adsorption theory

The mechanical strength of any solid material originates from the various forces of attraction between the ultimate particles which may include ionic and covalent bonds, hydrogen bonds, dipole interactions and secondary or van der Waals' forces. Which of these forces are significant in any particular material depends upon the chemistry involved. These interactions have been mainly considered from the point of view of the cohesion which they provide within a single material. The only requirement is that the two materials being joined are in sufficiently close and intimate contact [40-45].

1.5.1.2 Diffusion theory

The fundamental concept of the diffusion theory is that adhesion arises through the inter-diffusion of molecules from one material to another across the interface. As a result of diffusive bonding, there is no longer a true interface, but rather an interphase in which the properties of the two materials change gradually into each other. There are some examples in which this concept has been put to use. Hildebrand and Scott [46] developed the theory of simple solution. Lyengar and Erickson [47] carried out a series of simple experiments in which a range of adhesives were used to make peel specimens between sheets of Polyethylene terephthalate (PET). The diffusion theory is primarily applicable when both the adhesive and adherend are polymeric, having compatible long-chain molecules capable of movement. This theory is not useful in considering adhesion between smooth and rigid materials where the molecules are essentially fixed and not mobile [40-45].

1.5.1.3 Electrostatic interactions theory

The electrostatic theory proposes that adhesion takes place due to electrostatic effects between the adhesive and the adherend. This theory gains support from the fact that electrical discharges have been noticed when an adhesive is peeled from a substrate. Electrostatics can play a role in bond-making and can control the strength of an adhesive bond, but only when substantial differences in electronegativity exist between the materials brought into contact. It is believed that for conventional adhesive bonds, the electrostatic contribution to the total work of adhesion is quite small in comparison to van der Waals' forces [40-45].

1.5.1.4 Mechanical interlocking theory

The idea that adhesion depends on the mechanical interlocking of the adhesive with surface roughness is frequently advanced and is believed on a wide scale. According to this theory, adhesion occurs by the penetration of adhesives into pores, cavities, and other surface irregularities on the surface of the substrate. As shown in Figure 1.2. If the adhesive can displace the air in the pockets on the surface, the two materials are in intimate contact along a complex path. If a wedge is driven into the edge of this bond, we can see no abrupt plane of stress transfer. Rather, for the crack to propagate across the bond, the lines of force have to take detours. Some of the detours go into the adhesive. In most cases, the adhesive can deform more than the adherend. If either the adhesive (or the adherend) plastically deforms during the debonding, energy is consumed and the strength of the adhesive bond appears to be higher.

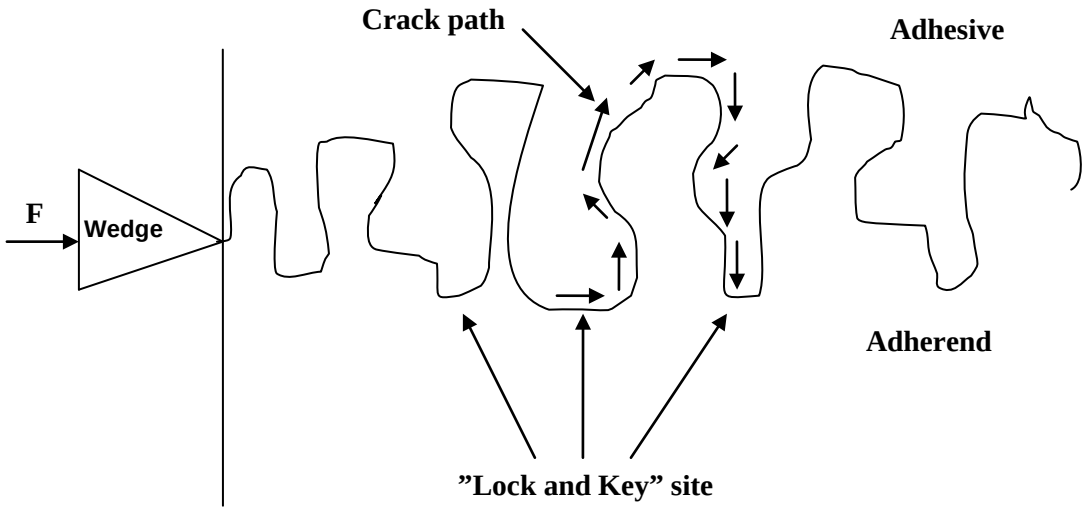

Figure 1.2 Complex interface between two adhering materials [43]

It is concluded that an adhesive penetrating into the surface roughness of an adherend can bond them and the adhesive bond strength results from the mechanical locking of the adhesive and the adherends. In Figure 1.2, arrows indicate a segment of the surface. In this segment, the adhesive has completely filled a pore on the surface. At this pore, the exit of the adhesive is partially blocked by part of the adherend. This place in the interphase will exhibit the so-called “lock and key” effect. A key, when turned into the tumblers of a lock, cannot be removed from the lock because of the physical impediment provided by the tumblers. In the same way, a solid adhesive in a pore cannot move past the “overhang” of the pore without

plastically deforming. Plastic deformation acts as an energy absorbing mechanism and the strength of the adhesive bond appears to increase.

Another reason surface roughness improves adhesion is purely a matter of physical area of contact. From Figure 1.2, it can be seen that the surface area is increased substantially. If the interfacial interactions are the basis for adhesion, then the sum of those interactions will scale as the area of contact. If the actual area of contact is increased by a large amount, the total energy of surface interaction increases by an amount proportional to the surface area [40-45].

1.5.1.5 Chemical bonding theory

In certain applications the formation of covalent, ionic or hydrogen bonds occurs across the interface. Chemical bonding requires that there be mutually reactive chemical groups tightly bound on the substrate and in the adhesive. These strong and durable bonds are generally the result of the close contact or adsorption of the adhesive on the surface followed by a chemical reaction. Perhaps the most widely employed example of the chemical bonding theory is with adhesion promoters or coupling agents. These multifunctional chemicals provide a "molecular bridge" between the substrate and the adhesive [40-45].

1.5.1.6 Weak boundary layers theory

If a region of low cohesive strength exists at the interface between a substrate and a hardened adhesive, failure will occur at a low stress level. The region is termed a 'weak boundary layer'. Polyethylene and metal oxides are examples of two materials that may inherently contain weak boundary layers. Some contaminants such as rust and oils or greases can form weak boundary layers [40-45].

Unfortunately, there is no unifying theory relating actual adhesion phenomena. The study reported in this thesis is about generating various surface roughness topography on glass substrates to improve copper / glass adhesion strength, therefore chemical and diffusion related theories are not considered. Based on the review of applicability of these adhesion theories, mechanical interlocking and adsorption may be of most relevance to explain this performance.

1.5.2 Characterisation of surface texture for adhesion

The complex relationship between roughness and adhesion has interested scientists and engineers for more than 50 years. Examples of research output are identified in Table 1.2, where authors identify that varying degrees and types of roughness appear to have beneficial effect on adhesion [48-62].

Table 1.2 Development of characterisation of surface texture for adhesion

People	Year	Material	Methods	Parameter used	Ref.
Takadoum and Bennani	1997	TiN deposited on steel substrate	Scratch test	*Ra*	48
Hallab *et al*.	2001	Metallic and polymeric biomaterial	Shear test	*Ra*	49
Shahid *et al*.	2002	Cleavage joint strength	Tensile destructive test	*Ra*	50
Chong *et al*.	2003	Plated platinum to poly(ethylene terephthalate) films	Tape test	*Rq*	51
Garbacz *et al*.	2005	Concrete	Pull-off test	*Ra*	52
Bénard *et al.*	2006	Gass/epoxy and carbon/epoxy composites	Shear test	*Sa*	53
Minaki *et al.*	2005 2007	Plating of martensitic stainless steel	Scratch test	*Ra*	54 55
Menezes *et al.*	2006	Ground EN8 steel flats	Scratch test	*Ra*	56
Jiang *et al.*	2007	Silica glass / polyarylacetylene resin composites	Shear test	*Ra*	57
Zappone *et al.*	2007	Polymer	Peel test	*Rq*	58
Novak *et al.*	2008	Poly(imide-siloxane) (PIS) block copolymers	Peel test and shear test	Surface energy E	59
Indolfi *et al.*	2009	Coating onto 316L steel stent	Pull-off test	*Ra* *Rq*	60
Ayrilmis and Winandy	2009	Adhesive bonding strength between MDF surface and veneer sheet	Delamination test	*Ra*	61
Audry *et al.*	2009	adhesion force of a sapphire particle onto alumina substrates	AFM with the colloidal probe technique	*Rq*	62

Although the impact of surface topography on adhesion has attracted researchers' attention as a potential tool for quantifying issues of adhesion bonding, only a few surface texture parameters have been used for surface texture characterisation. Furthermore only 2D surface texture parameters have been used by the majority of researchers even though they can give only a limited visualization of manufactured surfaces.

Benard *et al*. [53] first used the areal surface roughness parameter *Sa* to characterize the roughness of adhesion between glass / epoxy and carbon / epoxy composites. The aim was to show the correlation between the surface characteristics of composite materials and adhesion performances of corresponding surface assemblies. The interest of surface treatment to increase surface roughness was discussed in terms of wettability. However, *Sa* in this paper was only used as a tool to compare general roughness. Apparently one areal parameter is not only inadequate to characterize the complex surface texture but it is also difficult to understand the influence of areal parameter upon the whole surface properties towards adhesive performance.

Minaki *et al*. investigated the relationships between adhesive strength, surface texture and wettability for plating martensitic stainless steel for adhesion using only the 2D surface texture parameter *Ra*. They concluded that wettability was improved and adhesive strength increased when surface roughness *Ra* increased [54, 55]. In this report, contact angle was measured on the surface of the workpiece after blasting in order to examine the adhesion between composite materials and the workpiece, and it evaluated that blasting conditions had an effect on the wettability of the work surface. These papers demonstrate that the effect of surface roughness on plating had already attracted people's attention in recent years. However, surface topography lacked adequate description because most typically only the 2D parameter *Ra* was adopted for characterisation.

1.6 Theoretical and Experimental Study of Wetting Phenomena

The study of adhesion should be considered in parallel with the study of wettability and contact angle phenomena. It has been recognized for some time that there is a relationship between the contact angles which liquids make with surfaces and the strength of adhesive bonds to the surfaces. The wettability of the adherend is of significant importance in getting a strong and durable bond as it allows more intimate molecular contact at the interface. The

relationship between wettability and surface energy relates to adhesion strength, consequently good adhesion typically occurs with high wettability.

1.6.1 Development of Theories of Wetting Phenomena

In 1805, Young proposed the famous Young's Equation (Figure 1.3 and Equation 1-1) [63]. However, it applies only to one dimensional spreading and the substrate must be smooth, flat, homogenous, inert, insoluble, non-reactive, non-porous and non-deformable. Wetting in reality turns out to be much more complex, because the non-ideality of substrates means that they are usually rough and chemically heterogeneous.

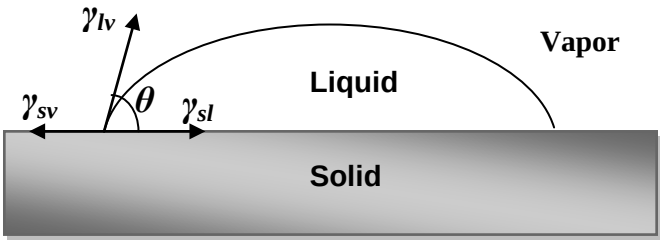

Figure 1.3 Schematic showing the condition for Young's equation

$$\cos\theta = \frac{\gamma_{sv} - \gamma_{sl}}{\gamma_{lv}} \qquad 1\text{-}1$$

Where θ is the Young's contact angle, γ are the interfacial tensions: solid – vapour tension (γ_{sv}), solid – liquid tension (γ_{sl}) and liquid – vapour tension (γ_{lv}).

Further work by Wenzel resulted in Wenzel's equation (Equation 1-2) for rough surfaces as shown in Figure 1.4 [64].

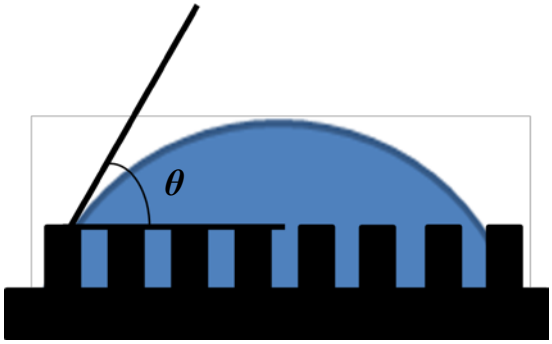

Figure 1.4 Schematic showing the condition for Wenzel's equation

$$\gamma_{lv}\cos\theta = r(\gamma_{sv} - \gamma_{sl}) \qquad 1\text{-}2$$

Where *r* is the ratio of the actual area of a rough surface to the geometric projected area, this factor is always larger than unity.

In the case of a flat, chemically heterogeneous surface, the wetting is typically described by applying the Cassie equation as shown in Figure 1.5 [65]. For a two-component system with an ideally flat surface, the wetting is described by Equation 1-3.

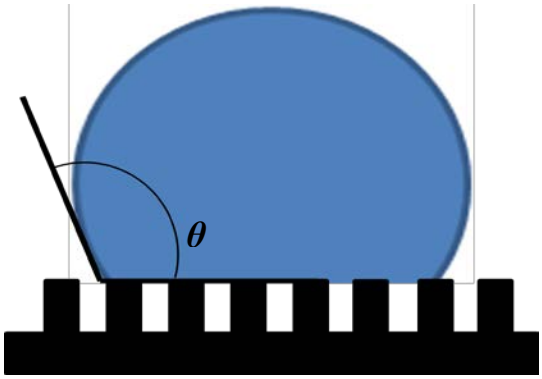

Figure 1.5 Schematic showing the condition for Cassie's equation

$$\cos\theta' = f\cos\theta + (1-f)\cos 180° = f\cos\theta + f - 1 \qquad 1\text{-}3$$

Where θ' is the apparent contact angle that the droplet sits on a composite surface of air and solid. f is the solid surface fraction of the area of the top of the asperities with respect to the projected area.

Despite the fact that theoretical contact angle values derived from either the Cassie or the Wenzel equation are often in good agreement with experimentally determined contact angles, this is not always the case. Further models considering thermodynamic and geometrical aspects have been established to give a better explanation of wetting phenomenon, for example, Johnson and Dettre [66], De Coninck *et al*. [67], Zhou and Hosson [68] and Chen *et al*. [69]. These models indicate the effect of the factors of wetting on rough surfaces.

Swain and Lipowsky proposed a generalized Young's equation for the contact angle which is valid for a substrate both chemically and geometrically inhomogeneous and under the influence of gravity [70]. Palasantzas and De Hosson established a model to associate the apparent contact angle with the surface roughness, but not including the system of liquids and solid substrates [71]. Zhang *et al.* established the Z-Y-H model to rebuild the relationship of surface roughness, material characteristic and contact angle [72]. Then Nosonovsky proposed a modified Wenzel's and Cassie's equation for non-uniform roughness and heterogenous surfaces [73].

Fox and Zisman obtained an estimate of the surface free energy of a solid by the linear relationship (Equation 1-4) between the contact angle and the critical surface tension of wetting [74].

$$\cos\theta = 1 + b(\gamma_{lv} - \gamma_c) \qquad 1\text{-}4$$

Where γ_c is defined as the critical surface tension of wetting for the solid and b is a constant.

Further steps have been made to extend the early work identified above including Good and Girifalco [75], Fowkes [76], Kaelble and Uy [77] together with Owens and Wendt [78].

Fowkes suggested that the surface tension of a solid or liquid (γ) could be described as the sum of components which arise from different intermolecular force, dispersion (γ^d), polar (γ^p) and hydrogen bonding (γ^h), as described in Equation 1-5.

$$\gamma = \gamma^d + \gamma^p + \gamma^h \qquad 1\text{-}5$$

Fowkes further proposed that the interfacial tension for dispersion force interactions along the interfacial free energy could be expressed as:

$$\gamma_{sl} = \gamma_s + \gamma_l - 2(\gamma_s{}^d \gamma_l{}^d)^{1/2} \qquad 1\text{-}6$$

Where γ_s is the surface tension of solid, γ_l is the surface tension of liquid, γ_s^d is the surface dispersion force of solid and γ_l^d is the surface dispersion force of liquid.

Kaelble and Uy together with Owens and Wendt suggested that all polar interactions including hydrogen bonding interactions could be considered as one term (Equation 1-7).

$$\gamma_{lv}(1+\cos\theta) = 2(\gamma_S{}^d \gamma_L{}^d)^{1/2} + 2(\gamma_S{}^P \gamma_L{}^p)^{1/2} \qquad 1\text{-}7$$

Where γ_s^p is the surface polar force of solid and γ_l^p is the surface polar force of liquid.

1.6.2 Development of Experimental Approaches to Wetting Phenomena

Tamai and Aratani [79] verified Wenzel's relation experimentally and concluded that the contact angle should be decided in terms of surface energy of the solid, the liquid, and the rough solid-liquid interface. An experimental study by Oliver *et al*. was made of the influence of surface roughness on the equilibrium spreading of liquids on solids [80].

Garoff *et al*. used X-ray reflectivity to show that the roughness of the underlying solid affects the roughness of the liquid-vapour interface of the thin film [81]. Whilst Wolansky and Marmur proposed a modification to Young's equation for rough surfaces by including the effects of line tension that is directly proportional to the geodesic curvature of the underlying surface and the directional derivative of the line tension [82].

Progress has recently been made towards resolving engineering surface problems of the superhydrophobic properties because of their potential application in antifogging and self-cleaning. Miller *et al.* [83], Shibuichi *et al.* [84], Onda *et al.* [85], Bico *et al.* [86], Lau *et al.* [87], Jopp *et al.* [88], Fan *et al.* [89], Meiron *et al.* [90] and Abdelsalam *et al.* [91] have fabricated patterned / rough surfaces by means of photolithography, templation, plasma etching, plasma deposition, chemical deposition, colloidal assembly, sol-gel chemistry, phase separation, or crystal growth to study the applicability of the Wenzel and Cassie theories. Conflicting results have been obtained depending on the system studied.

The results of a series of experiments made by Extrand [92], Gao and McCarthy [93] and Bhushan *et al*. [94] for uniform and non-uniform rough and chemically heterogeneous surfaces are in agreement with the theoretical contact angle from the generalized Wenzel-Cassie Equation.

Marmur proposed the Gibbs energy curve for a real surface with multiple local minima. In a situation where the roughness features are comparable to the size of the drop, a drop can have multiple contact angle values along the contact line, and the Wenzel equation does not always predict the correct apparent contact angle [95]. Butt proposed a method to calculate the capillary pressure on rough surfaces. He calculated the height distribution function of a rough surface based on the data generated from X-ray photoelectron spectroscopy (XPS) or atomic force microscopy (AFM) scans and in turn multiplied this function with the area and Laplace pressure term to obtain the capillary pressure [96].

A vast literature has evolved as research attempts to understand and characterize the wettability of solid surfaces. Contact angle measurements are used extensively in surface characterisation and this method often can be used as a non-destructive tool to analyze roughness and estimate the interfacial energy and wettability of substrate. However, the relationship between the structure and chemistry of a surface and its wettability by a fluid of interest can be very complex, and much effort is still directed towards understanding the wetting process. Although wetting of solid substrates by liquids is a fundamental phenomenon related to coating application, the wettability and contact angle measurement were not explored further in the study reported in this thesis since advanced metrology techniques for surface topography measurement were developed afterwards.

1.7 Basic experimental methodology

1.7.1 Experimental methodology

The basic methodology and techniques to be used in this study to correlate surface topography with adhesion performance are illustrated in Figure 1.6.

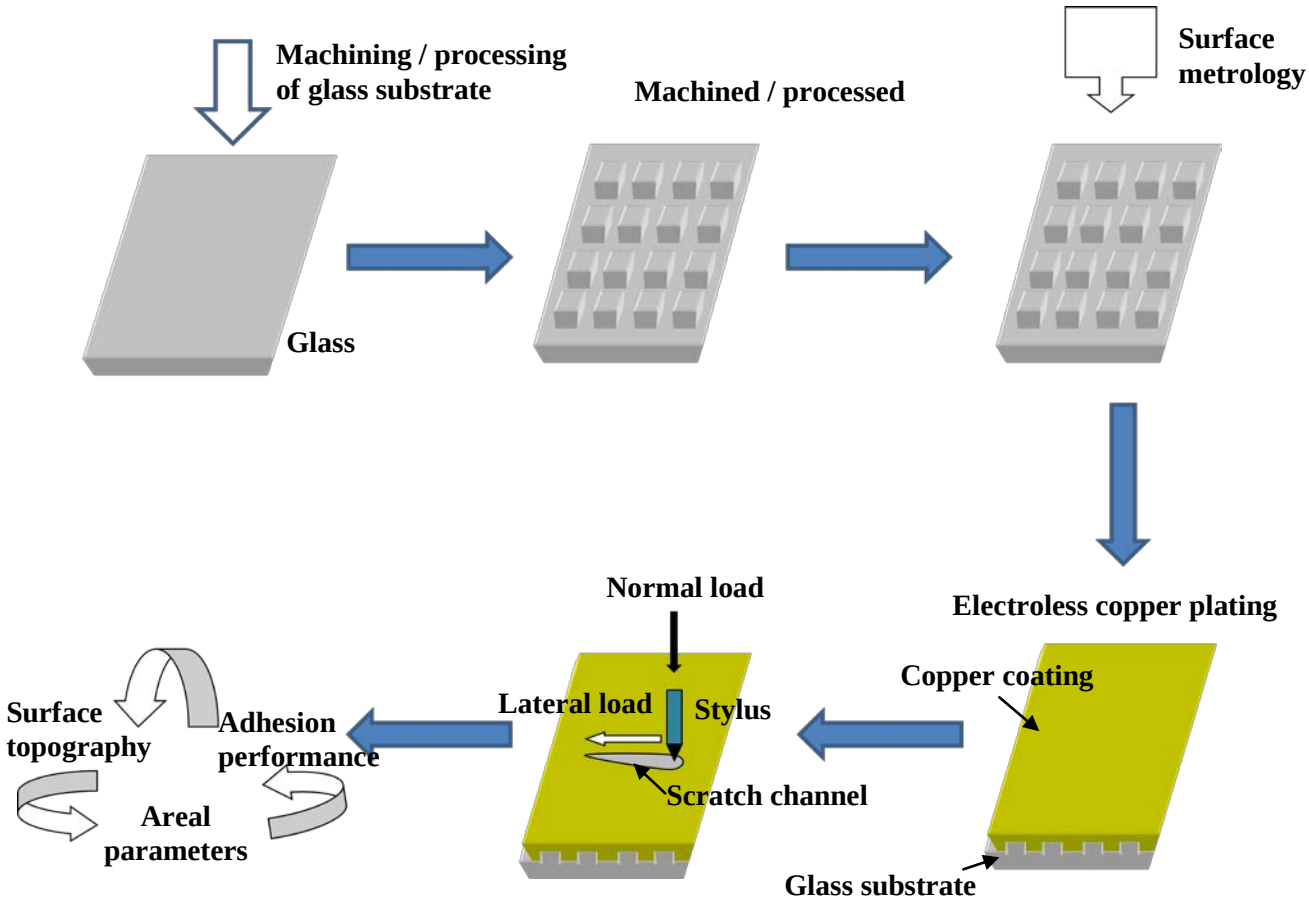

Figure 1.6 Experimental methodology and techniques

Stout and Blunt [97] developed the idea of surface classifications. Structured surfaces refer to surfaces with a deterministic pattern of usually high aspect ratio geometric features designed to give a specific function. Random surfaces refer to surfaces produced by random and psuedo-random processes often with the specific intention of removing systematic features. In the study reported in this thesis, the performance of structured surfaces is to be compared against random surfaces acting as an experimental control. Bead blasting was eventually chosen to generate the random surfaces on glass and excimer laser machining was eventually employed to create different structured surfaces. Contact / non-contact surface measurement equipment such as a Coherent Scanning Interferometer was utilized to characterize the machined surfaces via the new ISO 25178 areal surface texture parameters prior to coating.

Electroless copper plating with a study of the control of plating variables was employed to deposit conductive tracks on the insulating substrate. Following electroless copper metallization, scratch testing (identification of critical load of failure) was used to give a

quantitative assessment of adhesion strength. Indications of correlations were then sought between individual areal parameters and the adhesion strengths. More samples were created and more adhesion testing carried out to allow statistical hypothesis testing of the candidate correlations.

1.7.2 Materials

Glass comes in a variety of specifications. However, two types of glass were used for experimentation. Firstly, glass microscope slides (Fisher Scientific Ltd, product number FB58620) were chosen as robust substrates for mechanical / chemical processing. Secondly, commercially available CMG glass supplied by Qioptiq Ltd was chosen as a substrate material due to its attractive thermal expansion coefficient and susceptibility to machining by ultraviolet (UV) laser radiation. The glass sheets were supplied as square samples with dimensions 40 mm × 40 mm with thicknesses of 100 μm and 500 μm. CMG glass is a borosilicate type glass with a nominal cerium dioxide content and highly absorbing to light with a wavelength shorter than approximately 320 nm [98]. Its physical properties are listed as shown in Table 1.3.

Table 1.3 Physical properties of CMG glass [98]

	Density (g/cm^3)	**Thermal Expansion Coefficient CTE (10^{-6}/K)**	**Young's Modulus (GPa)**	**Poisson's Ratio**	**Refractive Index (nd)**
CMG glass	2.554 ± 0.010	5.6 ± 0.4	78.7 ± 1.0	0.175 ± 0.10	1.516 ± 0.003

The data demonstrates that CMG glass has the potential to meet the requirements of high reliablility and functionality for electronic packaging:

- Low thermal expansion coefficient that is similar to silicon (3×10^{-6}/K). A CTE mismatch can lead to stresses in two adjacent materials.
- High dimensional stability and high glass transition temperature.
- Transparency allows for better visual references for machining and multiple layer alignment for interconnects.

- Thermal stability that is suitable for higher melting point lead free solders.
- Low cost and environmentally benign.

Previous studies [6, 7] had used an alternative glass variant (CMZ) from Qioptiq Ltd (for similar reasons of electronic compatibility) but this glass variant had been discontinued at the point that this research started. CMG glass has similar physical properties compared to CMZ glass.

1.8 Summary

In this chapter, the background and the objectives of this research have been introduced. The characteristics and the feasibility of the use of areal parameters in a variety of applications and the development of the characterisation of surface texture for adhesion have been reviewed. The theories of adhesion and the relationship between wettablility and adhesion were also discussed in this chapter.

These application examples of areal parameters demonstrate a breadth of surface texture parameter identification. In a series of applications, three-dimensional surface roughness analysis has been found to be a powerful and versatile concept, compared to two-dimensional profilometry used in connection with visual inspection. However, it is noted that some of the reports do not link understanding of the influence of each parameter to the surface properties or functionality, or necessarily provide explanations for the original choices of parameter. First, most workers have typically only considered surface topography in a superficial manner and made no real use of the areal surface texture parameters, because few of them presented a comprehensive study of areal surface texture parameters, and most of the research literature lacks full understanding of the influence of each parameter upon the surface properties and explanations of the reason why they chose that parameter. Second, few researchers used areal surface texture parameters for describing surfaces for adhesive bond quality. So adhesion is a promising application for using areal surface texture parameters.

Although 2D surface parameters may potentially be restrictive and misleading, very few adhesion researchers have considered areal surface texture parameters to characterize surface roughness over the last twenty years. Even though an example of the use of the *Sa* parameter can be cited in the context of adhesion [53], little attempt has been made to consider the

breadth of parameters (and consequently surface description) available especially for publications concerning bespoke texturing of glass for electroless copper plating.

The lack of a significant body of knowledge concerning the use of areal parameters for adhesion, and specifically electroless copper coating of glass, is both a hindrance (i.e. a lack of published research direction) but also an opportunity for this current research to demonstrate unique and novel findings.

The rest of the thesis structure is identified as follows:

- Chapter 2 briefly discusses surface topography measurement and introduces the ISO / FDIS 25178:2 areal parameters.

- Chapter 3 details methods of producing textured surfaces on glass, both random and structured in nature.

- Chapter 4 identifies the electroless chemistry required to deposit copper onto the CMG glass substrates, and the variables involved.

- Chapter 5 introduces the quantitative scratch testing required to assess critical failure loads (adhesive bond strength) of copper coated glass - data required for correlation with areal parameters.

- Chapter 6 examines the statistical relationship between the areal parameterization of textured glass and critical load measurement of the copper coatings.

- Chapter 7 identifies the key conclusions from the research and discusses issues of further work.

Chapter 2 Surface topography measurement and areal surface texture parameters

2.1 Introduction

Surface topography measurement and characterisation are important elements and functionality indicators in the context of this study. Chapter 2 highlights contact and non-contact options for topography measurement before introducing the coherence scanning interferometer as a key measurement tool. Areal parameters are described in detail with reference to ISO / FDIS 25178:2, before consideration is given to the sensitivity of parameters to filter selection for structured glass and random glass samples.

2.2 Areal surface topography measurement equipment

2.2.1 Introduction to surface topography measurement equipment

The development of areal surface topography measurement owes much to the recent technological improvements of the instruments used which allows collection of texture data over areas instead of only along profile lines. There has been significant development of digital data processing techniques along with the dramatic increase of computing power and speed. Moreover, new and reliable measurement techniques have been introduced offering interesting prospects. These advantages meet the growing needs of industry to potentially achieve better control of production and of the functional properties of surfaces.

Areal surface topography measurements are undertaken by either contact or non-contact measurement instruments. The most common contact type of equipment is stylus-based surface texture instrumentation. The basic principle of non-contact range measurement systems is to project an optical source onto an object and process the reflected signal to determine its vertical range [99]. Table 2.1 summarizes the comparison between optical and stylus methods.

Table 2.1 Summary of optical and stylus methods [9]

Stylus	**Optical**
Possible damage	No damage
Measures geometry	Measures optical path
Tip dimension and angle independent	Spot resolution and angle dependent
Stylus can break	Probe cannot be broken
Insensitive to tilt of workpiece	Limited tilt only allowed
Relatively slow speed	Can be very fast scan
Removes unwanted debris and coolant	Measures everything good and bad
Can be used to measure physical parameters as well as geometry	Only optical path
Roughness calibration accepted at all scales	Difficult to calibrate by standards
Temporal and spatial influence / dynamic effects	Spatial influence / geometric effects
Existing ISO standards for 2D (e.g. ISO 4287 / 4288) ISO standards published for 3D (ISO 25178)	ISO standard in development (ISO 25178)

Although stylus-based surface texture equipment has been a reliable and traceable method, the main drawback is the physical size of the stylus that prevents it from penetrating sharp surface valleys, and convolution effects occur where sharp steps on a specimen surface tend to be smoothed. Another problem is that the stylus can damage or scratch the surface (depending on material hardness) and therefore the stylus technique may potentially be a destructive test. Non-contact measurement is of significant interest because it avoids deformation of the products and mechanical errors in the contact measurement. However, it is recognized that optical techniques contain optical sources of error. Optical methods are more suitable for generating areal surface texture parameters due to fast scan speeds and small resolution [100, 101]. Advanced measurements of areal surface topography in this study were carried out using a Zygo NewView 5000 coherence scanning interferometer (CSI). The NewView system uses scanning white light interferometry to image and measure the micro structure and topography of surfaces in three dimensions without contacting the surface.

2.2.2 Measuring principles of coherence scanning interferometer

Generally, the coherent scanning interferometry technique utilizes the superposition property of the light waves. The amplitudes of two light waves with the same frequency will add up or cancel depending on whether these two waves are in phase or out of phase by 180º which results in a set of dark and light bands known as interference fringes that indicate the surface structure of the part being tested. Quantitative measurement of specimen surface height is carried out by detecting the phase of a number of interference patterns produced by the two reflecting wavefronts from the reference surface and the specimen surface and implementing appropriate algorithms. This characterizes how well a wave can interfere with itself at a different time by measuring interference patterns each associated with a different axial position of the reference or specimen surface [102, 103].

The detector measures the intensity of the light as the interferometric objective is actuated in the vertical direction and detects the maximum interference. Each pixel of the image sensor measures the intensity of the light and the fringe envelope obtained can be used to calculate the position of the surface. When the objective lens is moved downwards, there is a change of intensity due to interference that will be observed for each pixel when the distance from the test surface to the beam splitter is the same as the distance from the reference plane to the beam splitter and the highest points on the surface will cause interference first. Figure 2.1 demonstrates how to build up an interferogram on a surface. A series of interferograms are generated as the objective is scanned perpendicular to the illuminated surface, while recording the detector data. The data acquired in this way consists of an array of interferograms, representing the variation in intensity as a function of scan position. The interferograms stored in the computer are individually processed and generate a complete three dimensional image constructed from the height data and corresponding image plane coordinates [102, 103].

The behaviour of the two plane wavefronts and their interaction can be mathematically described [103]. The amplitude of a plane wave at a position (x, y, z) and time, t, may be expressed as:

$$E(x, y, z, t) = \alpha\cos(\omega t - kz) \qquad 2\text{-}1$$

where α is the amplitude of the wave, $\omega = 2\pi\upsilon$ is the circular frequency (υ being the frequency of the light) and $k = 2\pi / \lambda$ is the wave number (λ being the wavelength of the light).

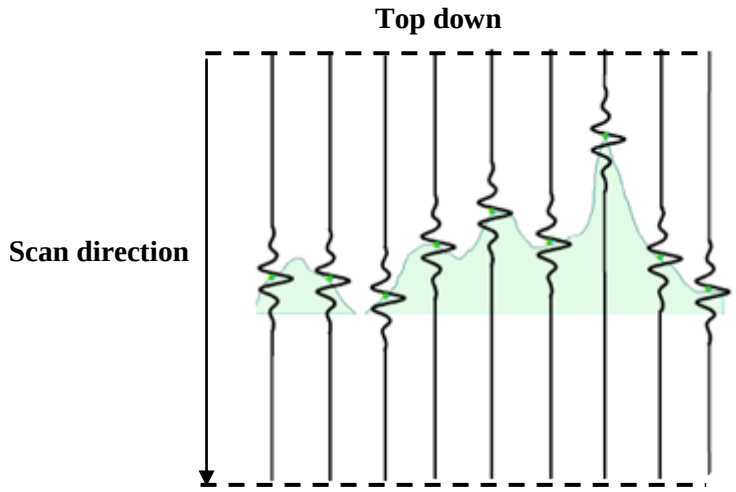

Figure 2.1 Mechanism of interferogram development on a surface [102]

2.2.3 Zygo NewView 5000 CSI

The Zygo NewView 5000 is a commercial coherence scanning interferometer from Zygo corporation (now superseded by the 6000 / 7000 models) and this instrument can be broken down into two basic subsystems: the microscope and the computer. The microscope measures the sample surface topography and generates the raw data needed for analysis and includes: the microscope itself, objectives, stage, video monitor, electronics, and a vibration isolation system. Automated systems also include a motorized stage and related electronics. The computer controls the measurement process, performs calculations, and displays measurement results on a color monitor. The instrument includes optics for imaging an object surface and a reference surface with both images brought together onto a solid-state imaging array, resulting in an interference intensity pattern that is read electronically into the computer.

The optical system is shown in Figure 2.2. A beam from a white light source is passed through an interferometric objective (typically a Mirau objective for 10 × → 100 × objectives, Michelson objective for 1.0 × → 5 × objectives) and is split into a reference beam and a test beam. The reference beam reflects from an internal reference surface in the objective and the test beam reflects from the object surface. These two illumination components are combined

to create interference. Both beams are directed onto a solid-state camera and the intensities are converted into images for three dimensional measurements by the Zygo Corp. MetroPro software. The test part is scanned by vertically moving the objective with a piezoelectric transducer (PZT). As the objective scans, a video system captures intensities at each camera pixel. Lateral measurements, in the plane of the surface, are performed by calculating the pixel size from the field of view of the objective in use. The Scan Length control determines the actual length of the scan. The longer the scan, the more time required for acquiring data.

The Zygo NewView 5000 CSI used in this study has a manual image zoom with a range from 0.4 × to 2.0 × and objective lens from 2.5 × to 50 ×. The camera model has an image array size of 640 × 480 pixels. Depths up to 100 micrometers and resolution of 0.1 nanometre are imaged independent of objective magnification. The MetroPro capability for profile and areal parameterisation is very limited, so surface roughness measurement has been processed and analysed using the TalyMap Platinum v5.1 (DigitalSurf Mountains) surface texture processing software that is compliant to ISO / FDIS 25178:2. It provides graphic images and high resolution numerical analyses to characterize the surface structure of test parts.

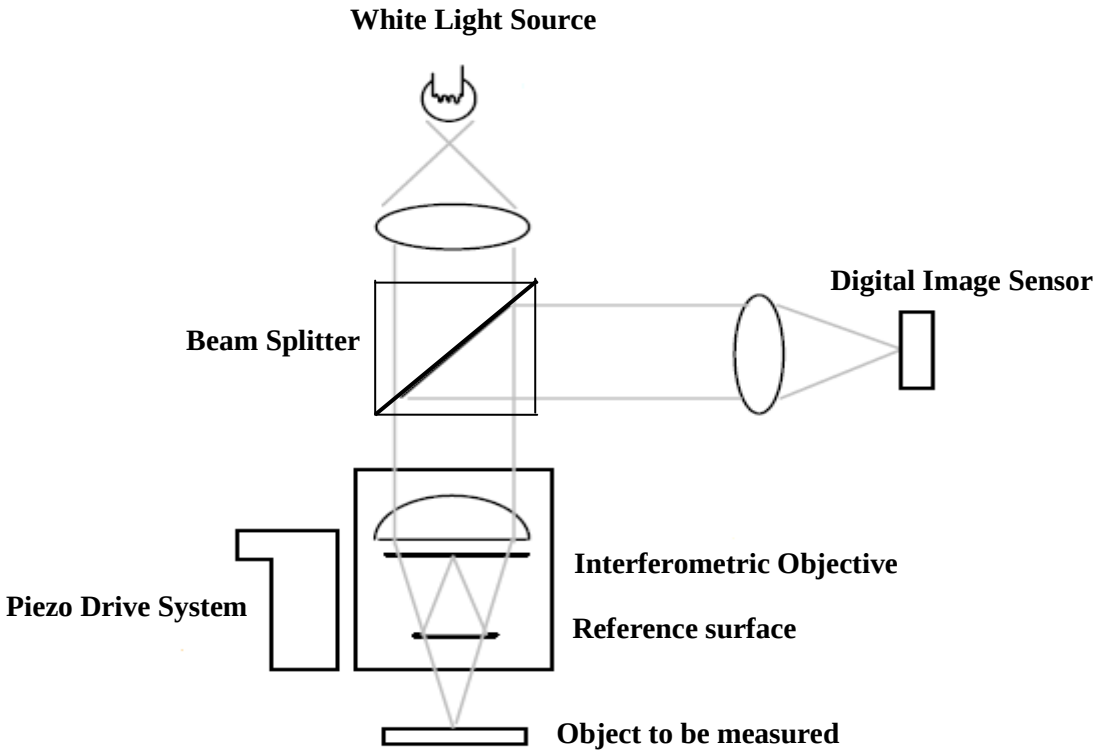

Figure 2.2 Schematic diagram of Zygo optical system [104]

2.3 Areal surface texture parameters

Areal surface topography of engineered surfaces is complex and cannot be described completely by a single or a few parameters. Each parameter can only describe one aspect of the topography. Published primary parameter sets include a number of parameters which cover amplitude, spatial, hybrid (combining amplitude and spatial), feature and some functional aspects. Some of these parameters are naturally extended from their profile counterparts (ISO 4287 [10]). Others are uniquely defined for areal surface topography features such as texture type (isotropy or anisotropy), texture direction, material volume, void volume, pits or troughs, which are typically not quantified with profile parameters. However, any parameter set cannot include all quantification which can describe surface topography completely. Only some major topographic properties related to geometry, statistics and function can be and are necessary to be described [8, 105-111].

In the latest draft of ISO / FDIS 25178:2, the parameter list has grown to encompass over 30 parameters and a primary parameter set was defined in order to have a comprehensive characterisation of areal surface topography. In this section, some areal surface texture parameters that are based on sound mathematical and / or statistical principles are selected to characterize surface topography for copper plating adhesion and introduced along with their definitions taken from ISO / FDIS 25178:2 [8, 111]. Parameters such as *Sv*, *Sp*, S_{10z} were not chosen in this study because they are not representative of the whole surface information.

2.3.1 Height parameters

Height parameters defined in this category give information regarding the areal height deviation of the surface topography, and are naturally an extension of their profile counterparts. However, they cannot be directly compared due to different mathematical techniques. All the areal surface texture parameters use areal filters whereas profile surface texture parameters use profile filters. The definitions of height parameters which were chosen in this study are listed in Table 2.2.

Table 2.2 Height parameters (with *A* being the definition area, z(*x*,*y*) height of the scale limited surface at position *x*,*y*) [8, 111]

Parameter	**Units**	**Definition**	**Mathematical formula**
Sq	µm	Root mean square height of the scale limited surface	$Sq = \sqrt{\frac{1}{A}\iint_A z^2(x,y)dxdy}$
Ssk	unitless	Skewness of the scale limited surface	$Ssk = \frac{1}{Sq^3}[\frac{1}{A}\iint_A z^3(x,y)dxdy]$
Sku	unitless	Kurtosis of the scale limited surface	$Sku = \frac{1}{Sq^4}[\frac{1}{A}\iint_A z^4(x,y)dxdy]$
Sa	µm	Arithmetical mean height	$Sa = \frac{1}{A}\int_A \lvert z(x,y)\rvert dxdy$

Sq is a widely used parameter which measures the dispersion of the distribution of the heights and indicates surface roughness in a well-known statistical form. *Sa* is arithmetic mean of the absolute of the height within a definition area. Similar to the profile parameter *Rq* and *Ra*, these two parameters are sensitive to the size of the sampling area.

Ssk is the quotient of the mean cube value of the ordinate values and the cube of *Sq* within a definition area. Skewness is a measurement of the symmetry of the surface deviations about the mean reference plane. It can effectively be used to describe certain aspects of the shape of a topographic height distribution. For a surface with a symmetric height distribution, such as a Gaussian surface, the skewness is zero. For an asymmetric distribution of topography heights, the skewness may be negative if the distribution has a longer tail in the downward direction of the mean plane or positive if the distribution has a longer tail in the upward direction of the mean plane. From a surface function point of view, this parameter can give some indication of the existence of spiky features. However, this parameter cannot distinguish if the profile spikes are evenly distributed above or below the mean plane and is strongly influenced by isolated peaks or isolated valleys.

Sku is the quotient of the mean quartic value of the ordinate values and the fourth power of *Sq* within a definition area. *Sku* is usually presented in conjunction with the skewness to measure the peakedness or sharpness of the surface height distribution. This parameter can not only

characterize the spread of the height distribution but also provides a measure of the sharpness of the area. A spiky surface will have a high kurtosis value while a bumpy surface will have a low kurtosis value. A kurtosis of a Gaussian surface characterized by normally distributed heights about the mean plane has a value of 3. A centrally distributed topography height distribution has a kurtosis value of larger than 3 where as the kurtosis of a well spread height distribution is less than 3. Some literature has reported that this parameter is useful in predicting component performance with respect to wear and lubrication retention. [16, 24] However *Sku* cannot differentiate between a peak and a valley. With the combination of the skewness and kurtosis it may be possible to identify deep valleys and flat tops in surfaces.

2.3.2 Spatial parameters

Spatial parameters refer to the spacing of certain topographic features. They are primarily dependent on the information in the scanning and tracing directions. Generally speaking, the spatial properties are difficult to describe by parameters, owing to their general wavelength randomness combined with multi-wavelength variations of surfaces. It is impossible to define parameters to cover all aspects of the spatial property, and not all aspects can be effectively characterized by existing techniques.

In order to characterize the spatial property of surfaces effectively, it is first necessary to define the autocorrelation function (ACF) as the correlation between a surface and the same surface translated by (*tx*, *ty*), given by

$$ACF(tx,ty) = \frac{\iint_A z(x,y)z(x-tx,y-ty)dxdy}{\iint_A z(x,y)z(x,y)dxdy} \qquad 2\text{-}2$$

With A being the definition area, *tx*, *ty* refer to the ACF at the position (*x*, *y*).

The ACF describes the general dependence of the values of the data at one position on the values at another position. It is recognized that the ACF is a very useful tool for processing random signals. It provides basic information about the spatial relation and dependence of the data. The ACF decays rapidly along the cross lay direction, which suggests less correlation of the data in the corresponding direction. However the ACF decays slowly along the surface

lay direction, which suggests high correlation of the data in the corresponding direction. Obviously, this property of the ACF offers a good way to distinguish isotropy and anisotropy of surfaces. The periodicity of irregularities and the texture are very important aspects of the surface characterisation. The definitions of spatial parameters which were chosen in this study are listed in Table 2.3.

Table 2.3 Spatial parameters [8, 111]

Parameter	**Units**	**Definition**	**Mathematical formula**
Sal	μm	Auto-correlation length	$Sal = \min\sqrt{tx^2 + ty^2}$
Str	unitless	Texture aspect ratio	$Str = \dfrac{\min\sqrt{tx^2 + ty^2}}{\max\sqrt{tx^2 + ty^2}}$

Sal is a parameter in length dimension used to describe the autocorrelation character of the ACF. It is defined as the shortest horizontal distance that has the fastest decay to a threshold *s*, with $0 \leq s < 1$. In other words, this parameter is the shortest autocorrelation length during which the ACF decays to *s* in any possible direction. The defalt value of *s* is 0.2. A large value of *Sal* denotes that the surface is dominated by low spatial frequency (or long wavelength) components, while a small value for *Sal* denotes the opposite situation.

Str can be defined as the ratio of the fastest to slowest decay to correlation length *s* ($0 \leq s < 1$) of the surface ACF. By convention the value of *s* is 0.2. This parameter is used to identify texture pattern, isotropy or anisotropy. In principle, *Str* has a value between 0 and 1. Larger values, $Str > 0.5$, indicates uniform texture in all directions, whereas smaller values, $Str < 0.3$, indicates stronger anisotropy.

2.3.3 Hybrid parameters

A hybrid property is a combination of amplitude and spacing surface characteristics. Any changes that occur in either amplitude or spacing may have an effect on the hybrid property of the surface. Hybrid parameters have great sensitivity to scale and their values are dependent on the resolution of the data. The definitions of hybrid parameters which were chosen in this study are listed in Table 2.4.

Table 2.4 Hybrid parameters (with L_x and L_y being the lengths of the definition area)[8, 111]

Parameter	Units	Definition	Mathematical formula
Sdq	radians	Root mean square gradient of the scale limited surface	$Sdq = \sqrt{\frac{1}{A}\int_0^{Lx}\int_0^{Ly}(\frac{\partial z(x,y)}{\partial x})^2 + (\frac{\partial z(x,y)}{\partial y})^2 dydx}$
Sdr	unitless	Developed interfacial area ratio of the scale limited surface	$Sdr = \frac{1}{A}[\iint_A(\sqrt{[1+(\frac{\partial z(x,y)}{\partial x})^2 + (\frac{\partial z(x,y)}{\partial y})^2}] - 1)dxdy$

Sdq is the root-mean-square slope of a surface within the sampling area. This parameter is sensitive to the sampling interval. *Sdq*, from the theoretical point of view, is independent of the amplitude of roughness and describes the shape of the elements of microtopography. A higher value may signify a peaky surface whereas a low value may signify a smoother surface.

Sdr is the ratio of the increment of the interfacial area of the scale limited surface over the sampling area. A large value of *Sdr* indicates the significance of either the amplitude, or the spacing, or both. For rough surfaces manufactured by turning, shaping and boring, the values of the developed interfacial area ratio are usually larger than 1 %. For surfaces with high slope, the values of the developed interfacial area ratio may be larger than 10 %. However, for fine surfaces manufactured by honing, plateau honing and grinding, the values of the developed interfacial area ratio are usually smaller than 1 %. Functionally this parameter can reflect the transition of a tribological process in which a surface is from its origin to worn, and in adhesion applications, this parameter characterizes the real contact area between adherend and adhesive. This parameter is also sensitive to the sampling interval.

2.3.4 Functional and related parameters

The definitions of functional parameters are concentrated on some important and frequently applied aspects. In engineering applications, many surfaces are manufactured to have some specific functional properties such as bearing, sealing and lubricant retention capabilities. Depending on the functional requirements, these surfaces may be designed to possess specific topographic features that are beneficial to the intended applications. The above mentioned parameters give general descriptions of surface topography. However, it is sometimes more efficient and effective to use specifically defined functional parameters to describe the particular characteristics of a surface that are important for a specific functional application. The definitions of functional parameters are concentrated on some important and frequently applied aspects. So the parameters presented here are useful for characterizing surface bearing, fluid retention and relevant properties.

For functional parameters related with volume, the areal material ratio function of the scale limited surface is important, and is the function representing the areal material ratio of the scale limited surface as a function of height shown in Figure 2.3.

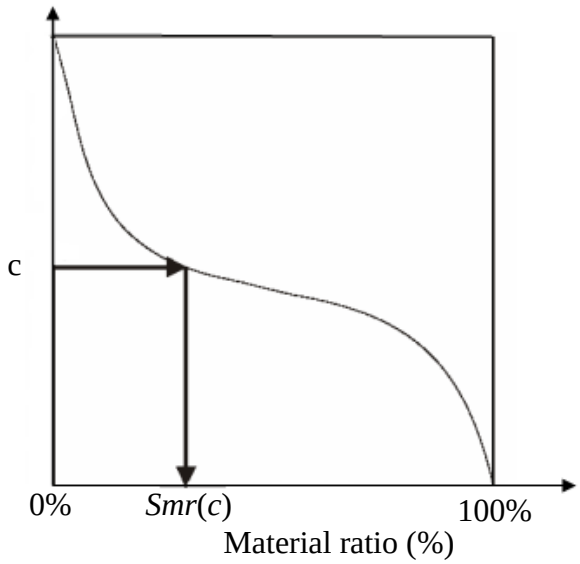

Figure 2.3 Areal material ratio [8]

This parameter is usually expressed as a percentage. *Sdc* (*mr*) and *Smr* (*c*) are directly derived from areal material ratio. *Sdc* (*mr*), inverse areal material ratio of the scale limited surface, is

the height *c* at which a given areal material ratio *mr* is satisfied. *Smr* (*c*), areal material ratio of the scale limited surface, is the ratio of the area of the material at a specified height c to the evaluation area. The definitions of functions and related parameters which were chosen in this study are listed in Table 2.5.

Table 2.5 Functions and related parameters [8, 111]

Parameter	**Units**	**Definition**	**Mathematical formula**
Vm	$\mu m^3/\mu m^2$	Material volume	$Vm(mr) = \frac{K}{100\%}\int_0^{mr} Sdc(q) - Sdc(mr)dq$
Vmp	$\mu m^3/\mu m^2$	Peak material volume of the scale limited surface	$Vmp = Vm\ (p)$ The default value of *p* is 10%.
Vmc	$\mu m^3/\mu m^2$	Core material volume of the scale limited surface	$Vmc = Vm\ (q) - Vm\ (p)$ The default value of *p* is 10% and *q* is 80%.
Vv	$\mu m^3/\mu m^2$	Void volume	$Vv(mr) = \frac{K}{100\%}\int_{mr}^{100\%} [Sdc(mr) - Sdc(q)]dq$
Vvc	$\mu m^3/\mu m^2$	Core void volume of the scale limited surface	$Vvc = Vv\ (p) - Vv\ (q)$ The default value of *p* is 10% and *q* is 80%.
Vvv	$\mu m^3/\mu m^2$	Dale void volume of the scale limited surface	$Vvv = Vv\ (p)$ The default value of *p* is 80%.
Sxp	µm	Peak extreme height	$Sxp = Smr\ (p\%) - Smr\ (q\%)$ The default value of *p* is 2.5% and *q* is 50%.

Sxp is the parameter related to the surface bearing property. This parameter is a measure of the difference in heights on the surface from the areal material ratio value between *p* % and *q* %. *Sxp* (*p* %, *q* %) indicates the depth of the remaining material to the lowest regions of the texture after it is worn or modified. Thus *Sxp* (*p* %, *q* %) may be used to determine the depth of material available after *q* % of the surface has either been removed or deformed to a plateau-like structure [112].

Vm (*mr*) is the volume of the material per unit area at a given material ratio calculated from the areal material ratio curve. *Vv* (*mr*) refers to the volume of the voids per unit area at a given material ratio calculated from the areal material ratio curve. Figure 2.4 shows the definition of volume parameters in the material ratio function.

Vmp is the material volume at *p*. A larger Peak material volume *Vmp* indicates a good bearing property. In a tribological process that a surface is from unworn to worn, this index increases correspondingly. Generally, this index is larger than zero.

Vmc is the difference in material volume between *p* and *q* material ratio. *Vvv* is the dale volume at *p* material ratio. A larger *Vvv* value indicates a good fluid retention capability in the valley zone. In a tribological process that a surface is from unworn to worn, this index usually keeps relatively stable.

Vvc is the difference in void volume between *p* and *q* material ratio. Good fluid retention occurs with larger value. A larger *Vvc* value indicates good fluid retention. In a tribological process that a surface is from unworn to worn, this index decreases correspondingly.

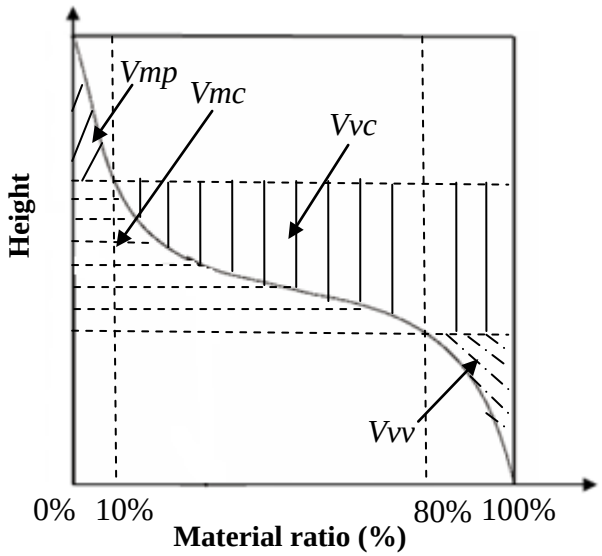

Figure 2.4 Volume parameters [8]

2.3.5 Feature parameters

Feature parameters are not specifically defined by an equation but instead have a toolbox of pattern recognition techniques that can be used to characterize specified features on a scale limited surface. The feature characterisation process is in five stages:

i. Selection of the type of texture feature
ii. Segmentation
iii. Determining significant features
iv. Selection of feature attributes
v. Quantification of feature attribute statistics

Based on the above five steps, the named feature parameters are listed in Table 2.6. Wolf pruning is an areal filter mechanism. Dale refers to regions around a pit such that all maximal downward paths end at the pit, hill refers to regions around a peak such that all maximal upward paths end at the peak, FC indicates that this is a feature characterisation, H indicates Hill, P indicates Peak and D indicates Dale.

Table 2.6 Feature parameters [8, 111]

Parameter	Units	Definition	Description
Spd	$1/\mu m^2$	Density of peaks	*Spd* = FC; H; Wolfprune: X%; All; Count; Density If not otherwise specified the default value of X% is 5%.
Spc	$1/\mu m$	Arithmetic mean peak curvature	*Spc* = FC; P; Wolfprune: X%; All; Curvature; Mean If not otherwise specified the default value of X% is 5%.
Sda	μm^2	Closed dale area	*Sda*(*c*) = FC; D; Wolfprune: X%; Open: c; Area; Mean If not otherwise specified the default value of X% is 5% and significant feature is closed.
Sha	μm^2	Closed hill area	*Sha*(*c*) = FC; H; Wolfprune: X%; Open: c; Area; Mean If not otherwise specified the default value of X% is 5% and significant feature is closed.

Spd and *Spc* reflect the basic geometric information of the micro-features. *Spd* is the number of peaks in a unit sampling area. This parameter has a significant functional sense in tribology and is greatly influenced by the sampling interval of the measurements. *Spc* is defined as an average of the principal curvatures of the peaks within the sampling area. This parameter can be calculated only after the summits have been found, and it is sensitive to the sampling interval as well. *Sda* (*c*) is the average area of dales connected to the edge at height *c*. *Sha* (*c*) is the average area of hills connected to the edge at height *c*.

2.4 Surface topography measurement

Different surface topography measurement operation parameters (reference plane, sampling area and filter) can lead to different characterisation results. Before measurement, these variables need to be specified and be consistently applied.

2.4.1 Reference plane

To provide a quantitative evaluation of the surface roughness, a reference or datum level is needed at first. The least squares mean plane derives from the least squares mean line which is adopted in current standards. It is defined as a plane such that the sum of the squares of the deviations from this plane is a minimum. Explicit mathematical algorithms are available to calculate it [102, 113], but the process is computationally intensive and ideally suited to computer processing.

2.4.2 Sampling area

The sampling area refers to the area portion used for defining the parameters characterising the scale limited surface. In this study, typically a 10 × objective lens and 1 × optical zoom were used to provide a lateral field of view of approximately 700 μm × 500 μm, which is predominately used as the sampling area in this research.

2.4.3 Filter

Filtration is important for surface metrology and it is the means by which the surface features of interest, such as roughness, waviness and form error, can be extracted from the measured data for further analysis. By applying different filtering, unwanted measurement noise or functionally irrelevant small or large scale features can be excluded from the final data set.

Filtering is used to isolate specific spatial frequency bands relevant to different component information of the surface by decomposing a signal occurring in the spatial frequency or scale domain. Areal measurement filter definitions currently being developed in ISO standards are based on digital Gaussian cut-off filters characterized by being phase correct and robust to single features such as scratches [102, 114].

A Gaussian filter is a good general purpose filter and it is the current standardized approach for the separation of the roughness and waviness components from a primary surface [115]. Both roughness and waviness surfaces can be acquired on a profile basis from a single filtering procedure with minimal phase distortion. Take the micro grid structured surface sample for example, which is machined by the excimer laser mentioned in Chapter 3, the effect of filtration to the 2D profile A-A´ is shown in Figure 2.5.

The L-filter is used to remove large scale lateral components from the primary surface. The S-filter is used to remove small scale lateral components from the surface resulting in the primary surface. Both roughness and waviness surfaces can be acquired from a single filtering procedure as shown in Figure 2.5. An 8 μm filter is used as the L-filter in Figure 2.5 (c) to separate roughness components by only allowing wavelengths below 8 μm to be assessed, with wavelengths above this value being removed. 8 μm is also used as an S-filter in Figure 2.5 (d) to determine the waviness of the residual surface. Filtration is necessary to isolate the interested roughness or waviness components from the unfiltered surface.

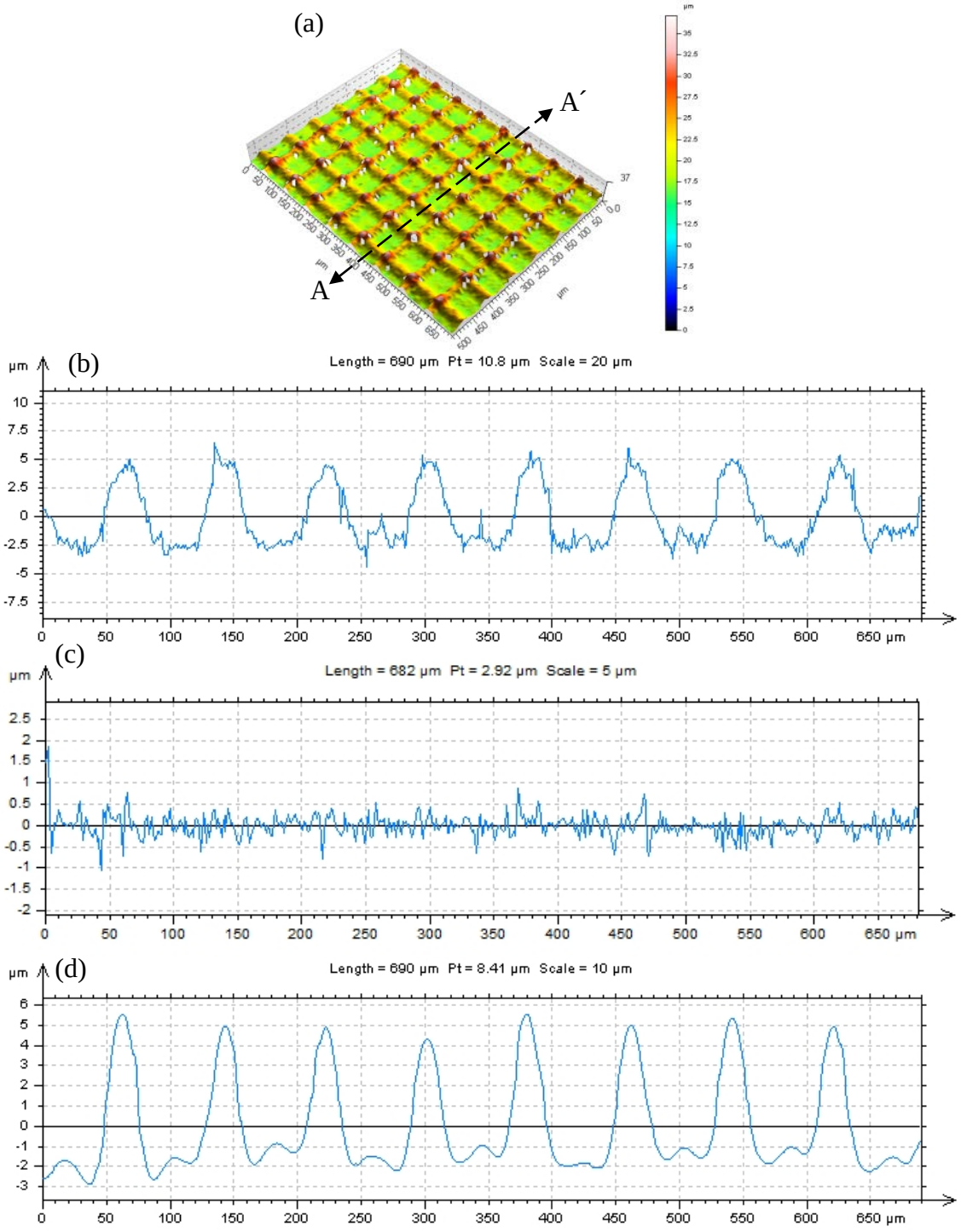

Figure 2.5 Effect of filter applied to the profile (A-A´) measurement

(a) Surface map (b) Raw profile (no filter) (c) Micro-roughness profile (8 µm L-filter) (d) Waviness profile (8 µm S-filter)

Since the filter is essential to the data results generation, the relationship between filter selection and areal surface texture parameters were investigated. The effects of filter applied to both structured surface (excimer laser) and random roughness surface (bead blasting) glass samples were processed and compared. Note that full details of these manufacturing methods are provided in Chapter 3. Figure 2.6 shows the surface topography of these two samples.

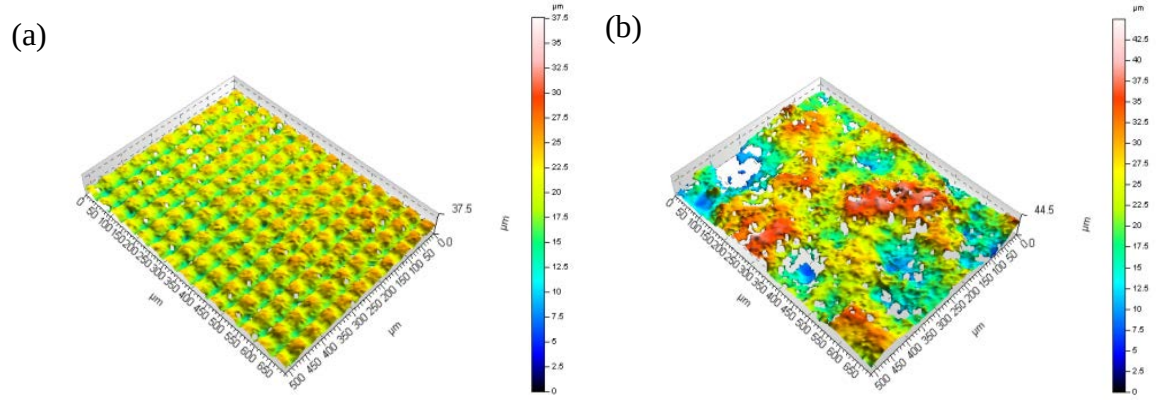

Figure 2.6 Surface topography of CMG glass samples
(a) Structured surface (b) Random surface

The data were processed using different filter setting applications and the diagram of the relationship between filter selection and area surface texture parameters were drawn individually. Details of the specific filter and parameters selection are listed in Table 2.7.

Table 2.7 Filter and areal parameters selection

Filter selection (μm)	**Areal parameters selection**			
20, 40, 60, 80 ,100, 120, 150, 250	Height parameters	Spatial and hybrid parameters	Functional parameters	Named feature parameters
	Sq, Ssk, Sku, Sa	*Sal, Str, Sdq, Sdr*	*Sxp, Vm, Vv, Vmp, Vmc, Vvc, Vvv*	*Spd, Spc, Sda, Sha*

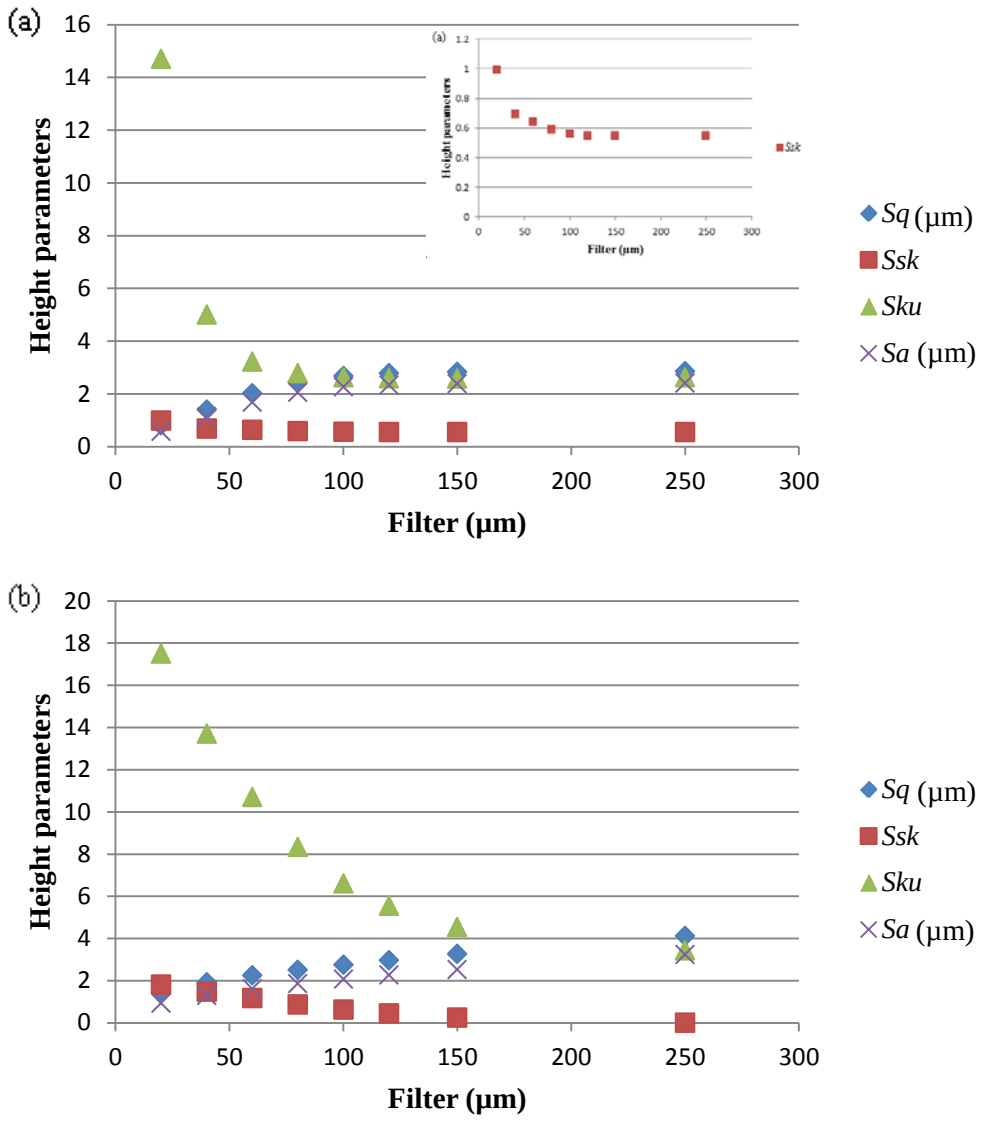

Figure 2.7 The relationship between filter selection and height parameters
(a) Structured surface (b) Random surface

Figure 2.7 shows the relationship between different filter selection and height parameters. The graphs show that: 1) *Sku* is sensitive to the filter selection for the structured glass surface. 2) *Sq* and *Sa* show the same trend in the sensitivity to the filter selection, which is to be expected from the definition. 3) *Ssk* is seen to be insensitive to the filter selection for the structured surface but sensitive for the random surface. 4) There is a threshold for parameters *Sq*, *Sa* and *Sku* in the structured surface. For example, the spacing of this micro pattern is 50 µm and when the filter is bigger than 80 µm, there is no obvious change for the values of these parameters, which gives a basis for later filter selections in Chapter 7.

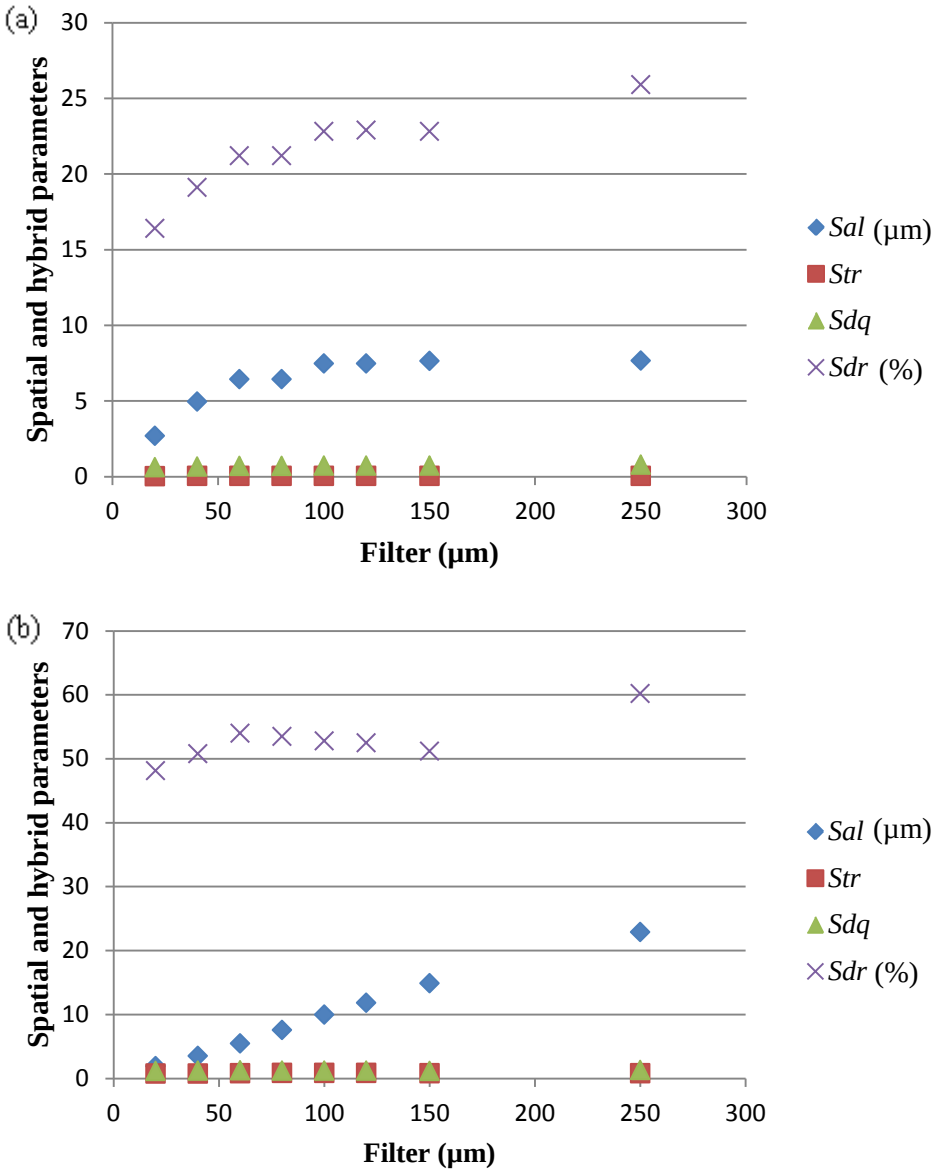

Figure 2.8 The relationship between filter selection and spatial / hybrid parameters (a) Structured surface (b) Random surface

Figure 2.8 shows the relationship between different filter selection, spatial and hybrid parameters. The graphs suggest that: 1) *Str* and *Sdq* are insensitive to the filter selection for both the structured glass surface and the random surface. 2) *Sal* and *Sdr* are insensitive to the filter selection for the structured surface when the filter value is above 80 μm. 3) *Sal* is sensitive to the filter selection for the random surface. The definitions of these parameters may provide the explanation. These spatial and hybrid parameters characterize surface feature components and texture pattern. For a specific structured surface, *Str*, *Sdq*, *Sal* and *Sdr* are insensitive when the filter value is above the feature spacing dimension.

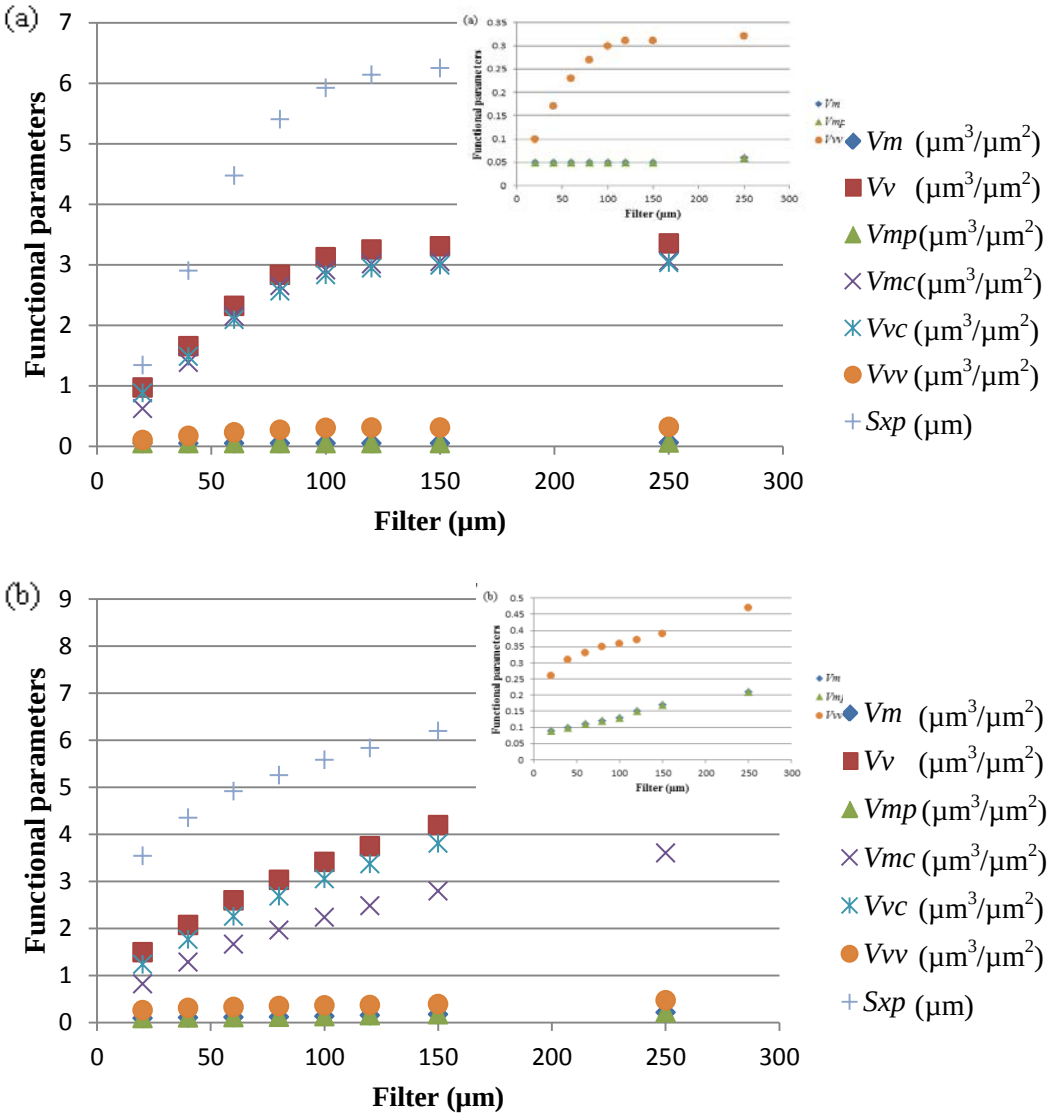

Figure 2.9 The relationship between filter selection and functional parameters
(a) Structured surface (b) Random surface

Figure 2.9 presents the relationship between different filter selection and functional parameters. The graphs show that: 1) *Vm*, *Vmp* and *Vvv* are insensitive to the filter selection whereas *Vv*, *Vmc*, *Vvc* and *Sxp* are sensitive to the filter selection for both the structured glass surface and the random surface. 2) *Vv*, *Vmc* and *Vvc* show the same trends to the filter selection. 3) Again there is a filter threshold of 80 μm for *Vv*, *Vmc*, *Vvc* and *Sxp* for the structured glass surface. The possible reason is that functional parameters are used for characterizing surface bearing and fluid retention properties, which may correlate with the feature component size of the surface.

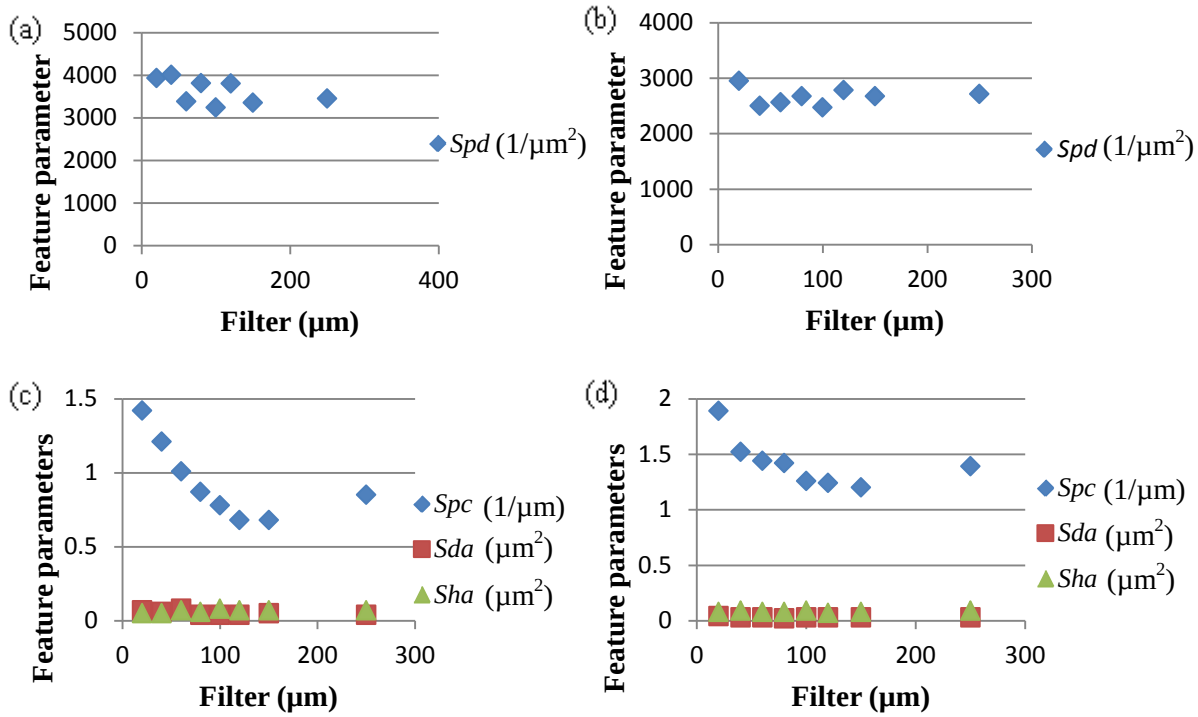

Figure 2.10 The relationship between filter selection and feature parameters
(a) and (c) Structured surface, (b) and (d) Random surface

Figure 2.10 presents the relationship between different filter selection and named feature parameters. The graphs show that 1) *Spc* is sensitive to the filter selection for both the structured glass surface and the random surface. 2) *Spd*, *Sda* and *Sha* are relatively insensitive to the filter selection for both the structured glass surface and the random surface.

Areal parameters show different sensitivities to filter selection as identified above. For the structured surface with a 50 µm pitch spacing, there is a threshold for the areal parameters which present sensitivity to filter selection. In this case, there is no obvious change for the values of these areal parameters when the filter value is above 80 µm. For the random surfaces, there is no threshold for the areal parameters values. As a result, the value of the filter is 250 µm which is typically more than ten times the scale of the coarsest structure of surface [111]. The summary of sensitivities of areal parameters to filter selection for structured surface and random surface is shown in Table 2.8.

Table 2.8 Sensitivities of areal parameters to filter selection (large sensitivity √√, medium sensitivity √, no sensitivity ×)

Areal parameters	**Structured surface sensitivity**	**Random surface sensitivity**	**Potential filter value for 50 µm pitch spacing**	**Potential filter value for random surface**
Sa	√	√	80 µm	250 µm
Ssk	×	√	-	250 µm
Sku	√√	√√	80 µm	250 µm
Sa	√	√	80 µm	250 µm
Sal	√√	√√	80 µm	250 µm
Str	×	×	-	-
Sdq	×	×	-	-
Sdr	√√	√	80 µm	250 µm
Vm	×	×	-	-
Vv	√√	√√	80 µm	250 µm
Vmp	×	×	-	-
Vmc	√√	√√	80 µm	250 µm
Vvc	√√	√√	80 µm	250 µm
Vvv	×	×	-	-
Sxp	√√	√√	80 µm	250 µm
Spd	×	×	-	-
Spc	√√	√√	80 µm	250 µm
Sda	×	×	-	-
Sha	×	×	-	-

2.4.4 Vacuum coating attempt

Sometimes it is difficult to access the measurement of a glass sample surface due to the transparency of the substrate. In such situations, coated sample replication can be made for measurement in order to get better signal feedback. In this study, a small number of glass samples were vacuum coated (copper and aluminium evaporation) before measurement. A Moorfields / Edwards E 306 Vacuum Coater was used for vacuum coating. Figure 2.11 and Figure 2.12 show the difference of CSI performance before and after vacuum coating of

CMG glass samples with line profiles taken through A-A´ and B-B´ respectively. However, it should be noted that Figure 2.11 is an extreme example of missing data for a non-coated sample. For most glass samples, better quality datasets are generated.

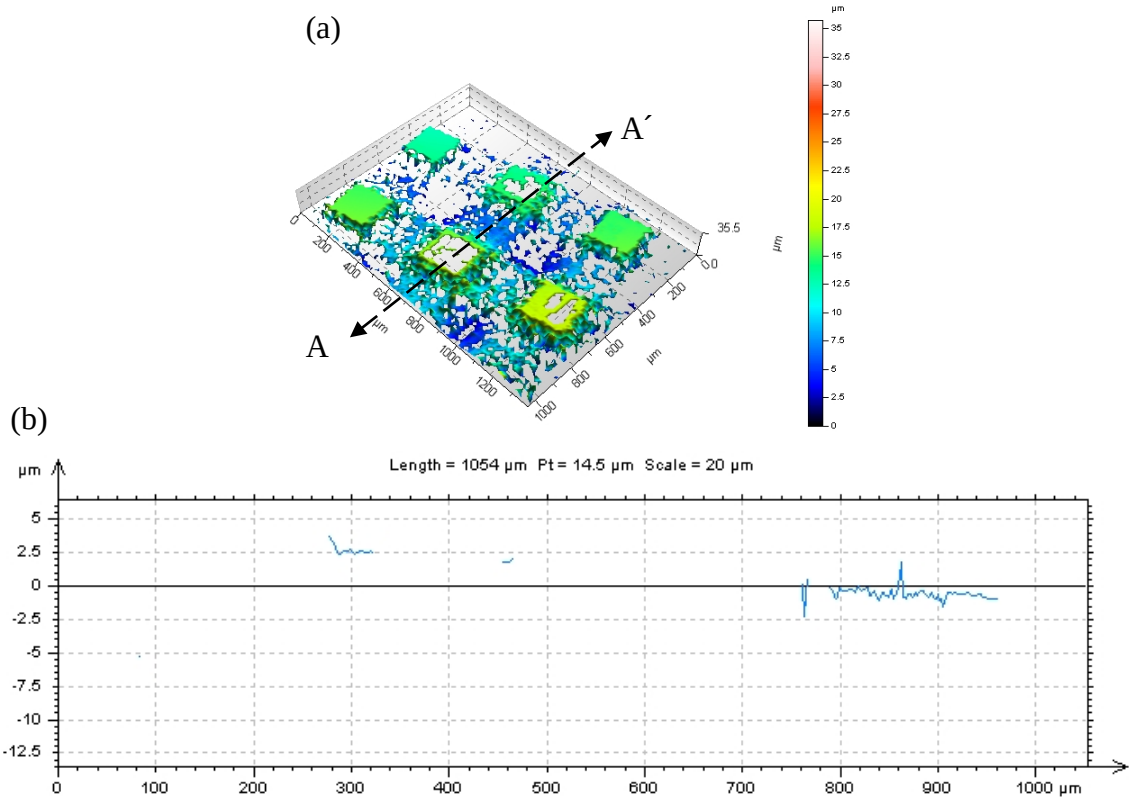

Figure 2.11 CMG glass with structured surface before vacuum coating

(a) Surface map (b) Profile A-A´

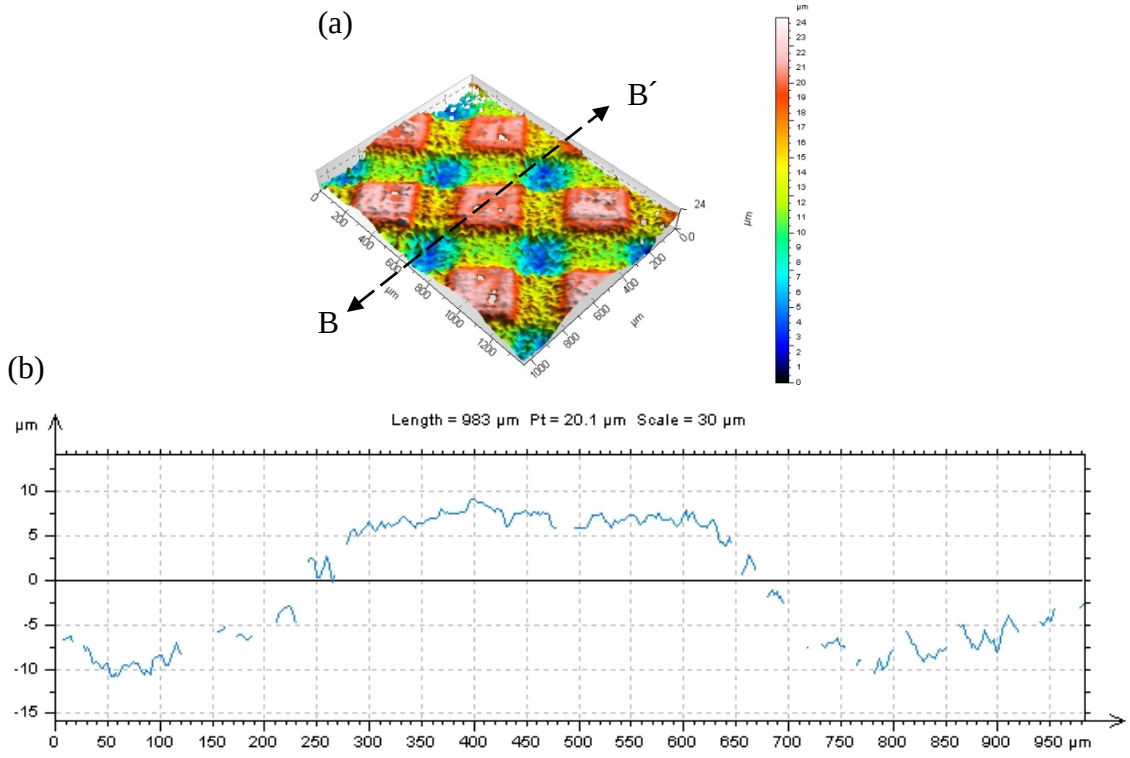

Figure 2.12 CMG glass with structured surface after vacuum coating

(a) Surface map (b) Profile B-B´

The CSI measurement result shows vacuum coating can sigificantly improve signal feedback quality from the surface. However, the pretreatment method of vacuum coating was not adopted in this study for two reasons. Firstly, it is difficult to produce two identical samples, especially for random surface samples because the manufacturing process is not repeatable. Sample pretreatments need to be consistent before measurements in order to make the results comparable. Secondly, even though this coating is only approximately a hundred nanometres thick, it modifies and smooths the real surface. As a result, a compromise needs to be considered which is dependent on measurement tolerance.

2.4.5 Areal surface texture parameters generation

Surface roughness measurement was processed and analysed using the TalyMap Platinum software as identified in Section 2.2.3. Areal parameters including field and feature parameters were generated according to ISO / FDIS 25178:2.

Sample levelling also affects the measurement outcome. Levelling of the sample with respect to the Zygo can be experimentally determined by minimizing the number of fringes patterns

visible on the computer screen during Zygo measurement, a process known as nulling. Further, levelling by the least squares mean method before data processing was further applied in Talymap.

Holes in the datasets (a function of CSI optics and surface signal [103]) result in the software not processing certain areal parameters including spatial and hybrid parameters. Height, functional and feature parameters can be generated no matter if there are data holes. Data filling may be used (with caution) when there is non-measurement of area. When the areal parameters failed to be generated, filling in of the non-measurement data points was undertaken by software interpolation, by replacing the non-measurement points with a smooth shape calculated from the neighbouring data. This process is illustrated and discussed by other authors [103]. In this study, there are two steps for areal parameters generation. Height, functional and feature parameters are firstly generated, then spatial and hybrid parameters are processed after data filling procedure.

2.5 Summary

In this chapter, areal surface topography measurement methods have been compared and the Zygo NewView 5000 coherent scanning interferometry (CSI) system was introduced for generating surface topography maps of glass substrates. A series of areal parameters taken from ISO / FDIS 25178:2 have been presented for characterizing the glass surface texture. The relationship between filter selection and areal parameters has also been discussed in this chapter. As a result of this initial work, the following key CSI variables were chosen for consistent measurement of glass samples:

- 10 × objective
- 1 × zoom multiplier
- 640 × 480 camera pixel resolution
- 700 μm × 500 μm sampling area
- Nulling of CSI fringe patterns before data acquisition
- Sample levelling prior to data generation
- Gaussian filter in TalyMap
- Filter specification based on surface structure feature (more details in Chapter 6)

Chapter 3 Producing textured surfaces on glass

3.1 Introduction

Modifying the surface of glass is a key issue in this research and a variety of methods are available to be explored. Chapter 3 explores plasma etching, chemical etching, mechanical abrasion, particle abrasion and laser machining, with the aim of identifying process that allow controlled surface modification.

3.2 Glass surface treatment background

Proper surface pretreatment is one of the decisive factors for achieving a high-quality adhesive joint [116]. Packham discussed the fundamental principles which are relevant to an understanding of the influence that interfacial roughness may have on adhesion [117]. Increasing roughness on glass surfaces is essential to improving copper / glass coating adhesion performance and surface topography correlates areal parameters with plating adhesion strength.

Different methods including; plasma treatment, chemical etching and mechanical abrasion were attempted in order to produce random surfaces on CMG glass substrates. It became clear that these methods are incapable of generating structured surfaces on glass, so excimer laser machining has been developed and used to create a range of micro pattern structured surfaces on CMG glass substrates. However, the background challenge is to identify an economic and feasible manufacturing method to achieve textured surface on glass for strong copper plating adhesion.

Previous researchers have reported that microcolumnar array (MCA) structures could enhance the adhesive bonding strength for metals and alloys. Starikov *et al*. fabricated MCA-structured surfaces by laser ablation on high-temperature stainless steels (Hastelloy 276™, alloy 321) and refractory metals (tungsten, tantalum, molybdenum, titanium) [118]. Baburaj *et al*. described modification of titanium surfaces by generating MCA structures and thereby increasing the adhesive bond strength between titanium plates [119]. The application of MCA for the bonding of silicon nitride and alloy steels for adhesive bonding was published by Zhang *et al*. [120]. They showed that the adhesive bond strength could be doubled by the

generation of MCA structures on ceramic and steel surfaces. Few researchers have reported creating MCA structures on glass surfaces and none have reported issues of improving adhesion performance, which is one part of the novelty of this study.

Before producing textured surfaces on glass, a virgin CMG glass sample was imaged using the Zygo CSI system, as shown in Figure 3.1. The result indicates that this virgin CMG glass is flat to a value of *Pt* = 33.6 nm. The *Sq* value is 7.27 nm. The topographic information of virgin glass provides a reference for comparison with the roughened surfaces produced by various manufacturing methods.

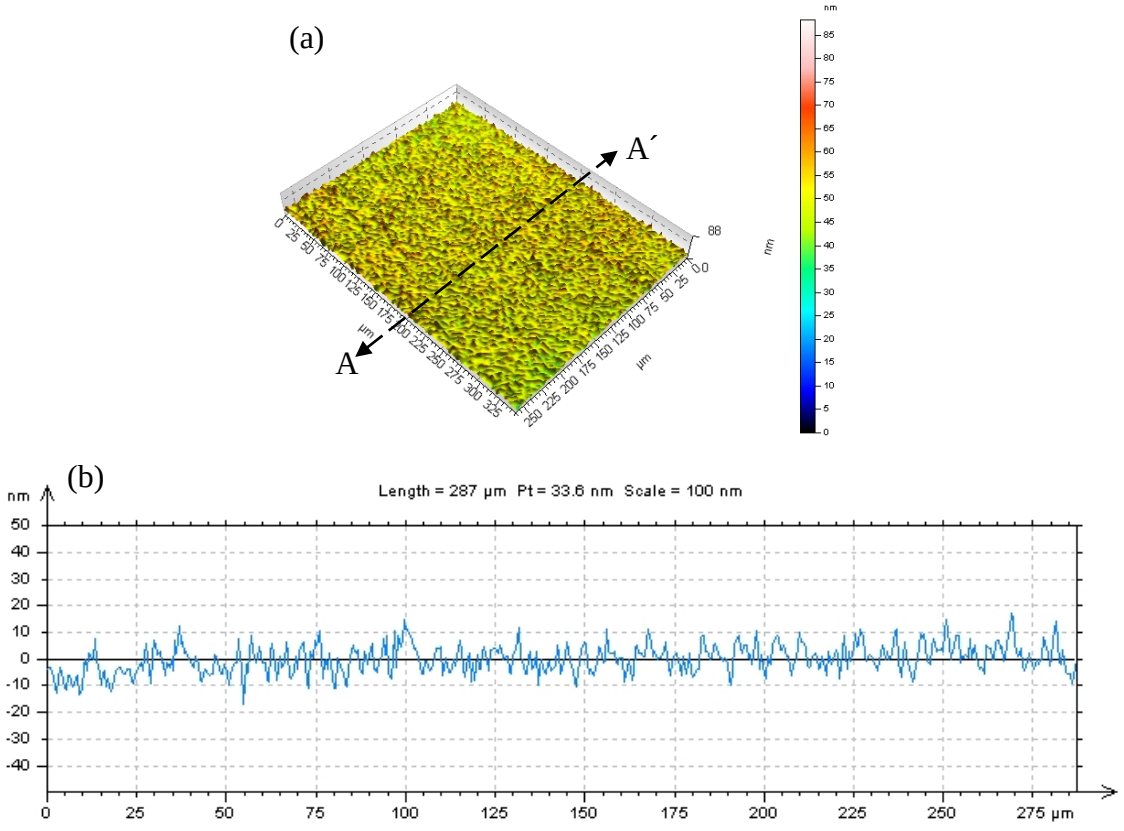

Figure 3.1 Virgin CMG glass (a) Surface map (b) Profile A-A´

3.3 Producing randomly rough surfaces on glass

3.3.1 Plasma treatment

Plasma etching involves a high-speed stream of glow discharge (plasma) of an appropriate gas mixture being accelerated in pulses at a sample. During the process, the plasma generates volatile etch products at room temperature from the chemical reactions between the elements of the material etched and the reactive species generated by the plasma. Eventually the atoms of the accelerated element embed themselves at or just below the surface of the target, thus modifying the physical properties of the target. Plasma surface treatment can improve wettability of the target material by raising its surface energy and improve adhesive characteristics by creating bonding sites [121].

The basic mechanisms of plasma etching are [122]:

- Sputtering in which ions mechanically eject substrate material at low pressure.
- Chemical gasification, where thermalized neutral radicals react with substrate material and form volatile products.
- Ion-enhanced energetic mechanisms in which there is little or no intrinsic surface reaction with neutral radicals, until energetic ions enhance the reactivity of a substrate or product layer allowing chemical reactions to gasify the material.
- Ion-enhanced inhibitor, or protected sidewall anisotropy where inhibitor species form a sidewall film which excludes the neutral etchant.

An existing gas composition for borosilicate glass reported in the literature [123-125] using Carbon Tetrafluoride (CF_4) gas and Oxygen (O_2) gas was chosen in the etching process. The base pressure of the system (Plasma Lab 80 equipment) was set to 5 mTorr and etch rate was 31 nm / min. Radio frequency forward power was set to 100 W. The plasma treatment was performed at a chamber pressure of 60 mTorr for 2 hours. Figure 3.2 shows a surface topographic map of the plasma treated CMG glass sample.

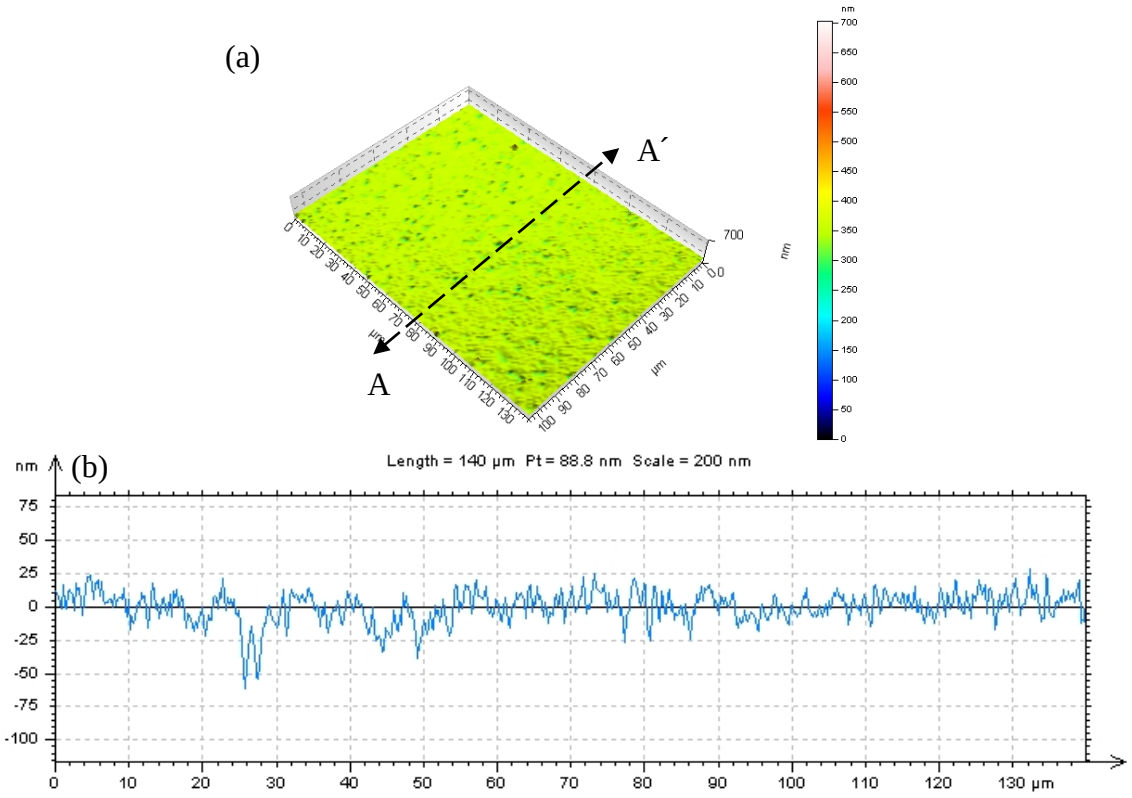

Figure 3.2 Plasma treatment CMG glass (a) Surface map (b) Profile A-A´

Comparing the result of the plasma treated sample with the virgin CMG glass, the surface roughness was increased to a limited extent by this recipe with the *Sq* value increasing to 11.7 nm. Although some researchers have reported the use of plasma etching to treat glass in order to increase surface roughness [123-125], the process is a relatively high-cost technique that can etch glass but is also time consuming. In addition, it is a time consuming process finding the most suitable recipe for new substrates.

3.3.2 Chemical etching

Hydrofluoric acid (HF) etching is a well known industrial process, but is hazardous due to its high corrosive nature and toxicity. This chemical must be handled with extreme care with protective equipment because hydrogen fluoride gas may immediately and permanently damage the lungs, the corneas of the eyes, and water solutions can cause tissue death if contacted [126]. The mechanism of glass etching by HF acid is the reaction between the fluoride anions and the silicon oxide which is the main ingredient in glass, to form silicon fluoride. In this study, CMG samples were dipped into 6 % HF solution for periods of 60 seconds, 90 seconds and 300 seconds at room temperature, and then rinsed and dried

thoroughly. The surface topography of the samples after chemical etching was investigated. Typical images are shown in Figure 3.3 to Figure 3.5.

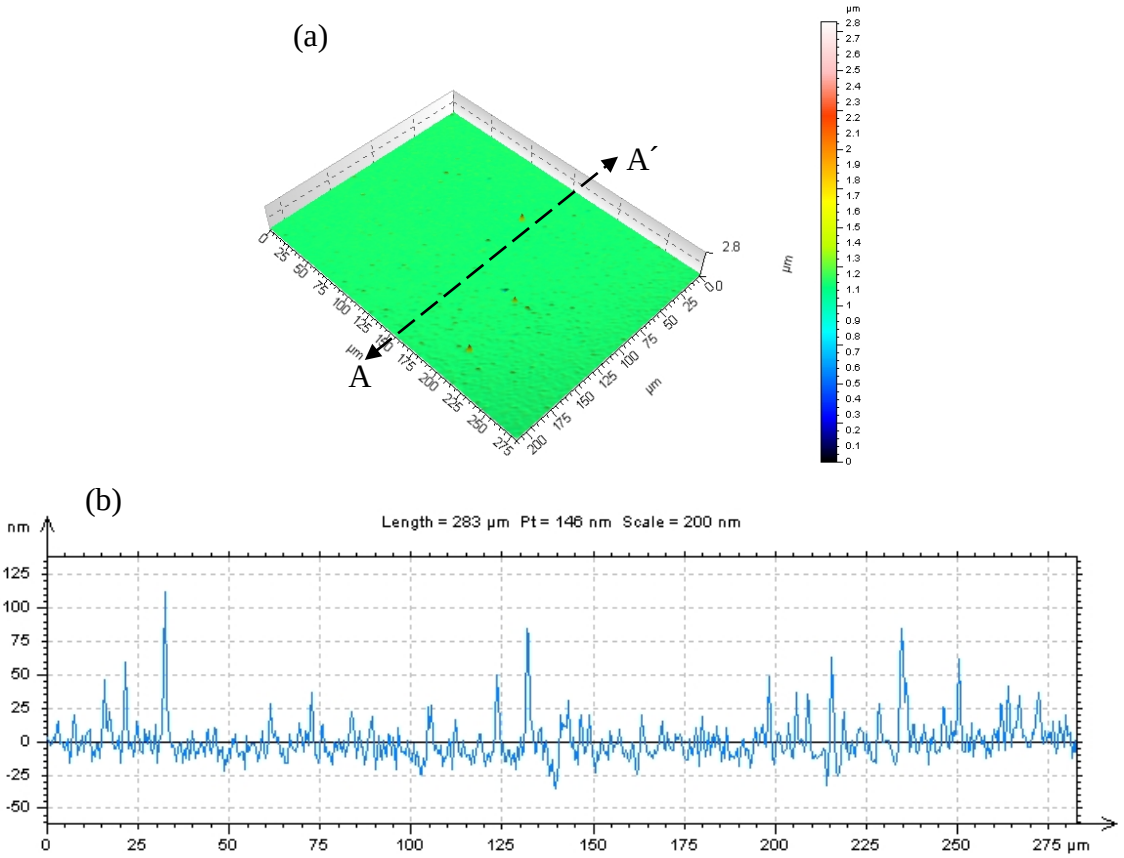

Figure 3.3 CMG glass sample dipped into 6 % HF solution for 60 s
(a) Surface map, (b) Profile A-A´

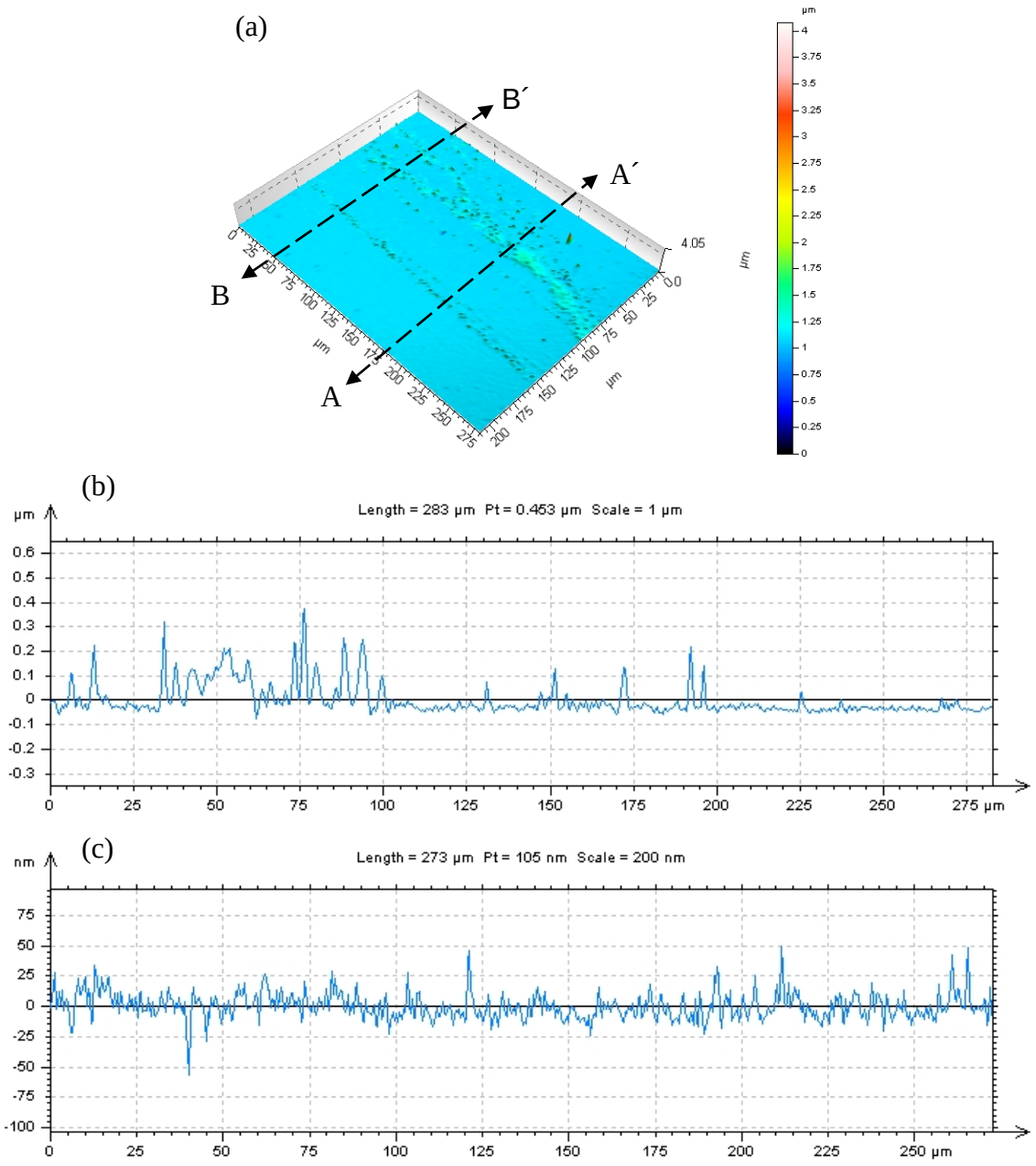

Figure 3.4 CMG glass sample dipped into 6 % HF solution for 90 s

(a) Surface map, (b) Profile A-A´, (c) Profile B-B´

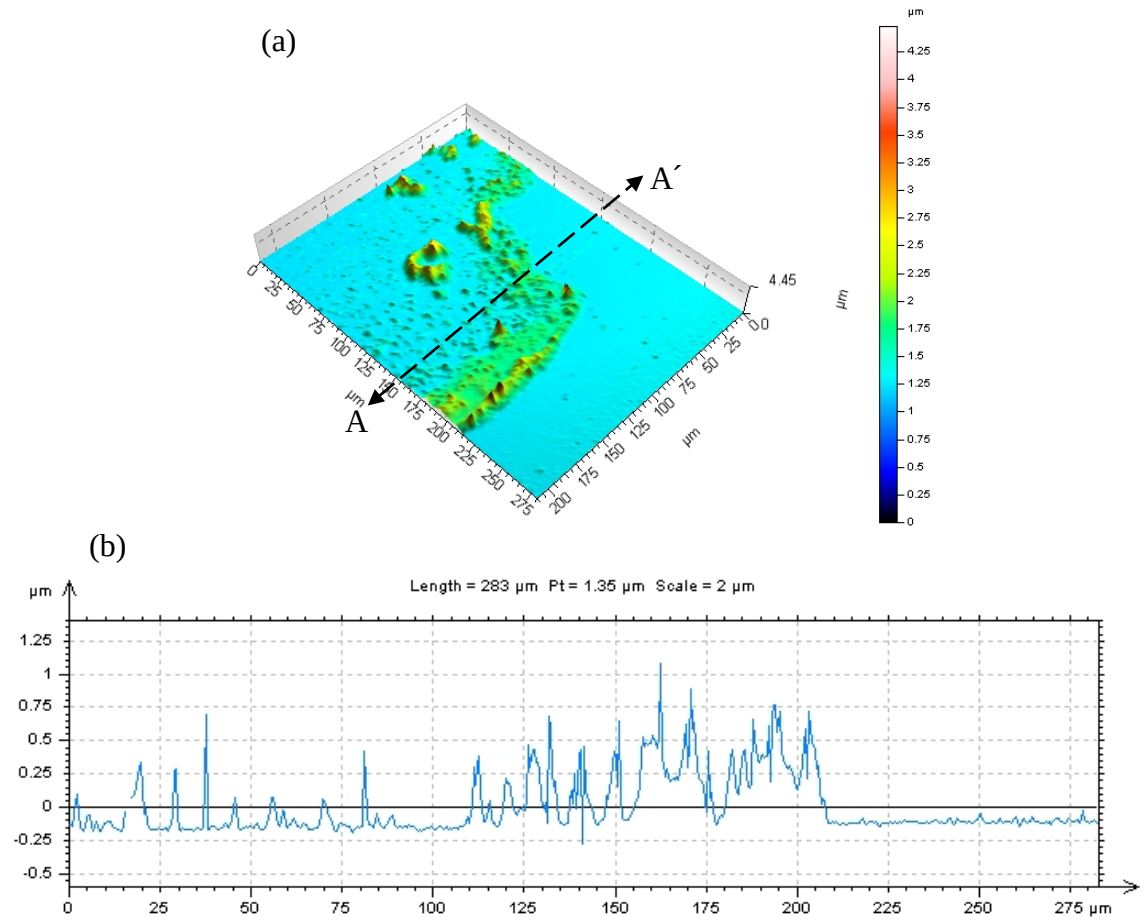

Figure 3.5 CMG glass sample dipped into 6 % HF solution for 300 s
(a) Surface map, (b) Profile A-A´

From the images it can be seen that the etched surface morphology changed dramatically with increasing dipping time with respect to the virgin glass in Figure 3.1. When the glass sample was etched for 60 seconds, there was no obvious change to the surface topography. With the dip time increased to 90 seconds, the etched area extended from independent shallow pits to a continuous deep valley. Once the etching time was increased to 300 seconds, there were visible rugged bumps and tracks on the glass surface.

The results identified that the HF acid did not etch the CMG glass samples uniformly. In some samples etching starts from a corner whereas in others there is an etched band in the middle. Even for the same sample, the etching effect was different from area to area. The possible reason for this is the variations in material surface properties. As shown in Figure 3.4 (b) and Figure 3.4 (c), two line profiles A-A´ and B-B´ were generated from the same 90 seconds dip time CMG glass sample, however, the profiles exhibited different etched surface

roughness characteristics. Line A-A´ showed surface roughness value of *Pt* = 453 nm, whereas line B-B´ showed significantly less variation (*Pt* = 105 nm). This is also a demonstration that profile based surface texture analysis cannot comprehensively represent the surface topography when the surface is anisotropic and inhomogeneous; therefore areal parameters are required to give more comprehensive and reliable surface information. Figure 3.6 shows the relationship between etching time for the glass samples and *Sq* value.

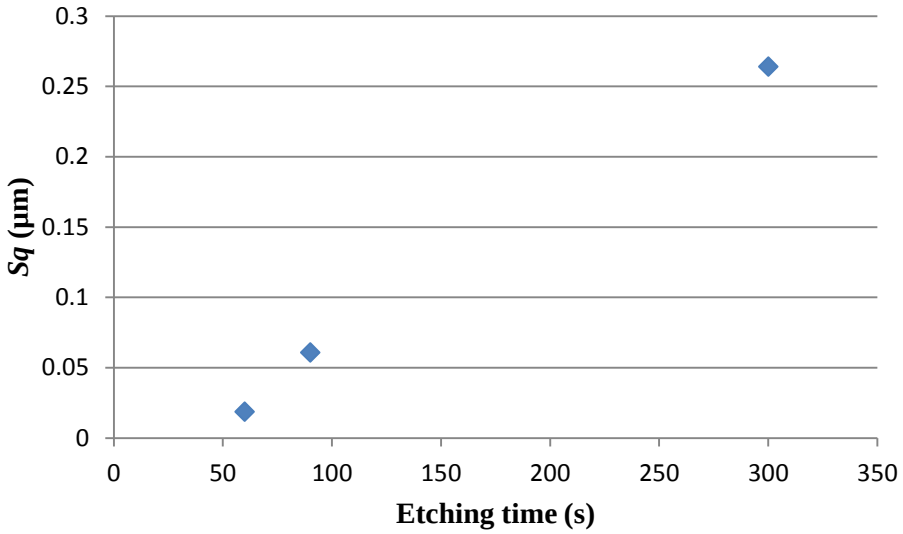

Figure 3.6 Relationship between sample etch time and *Sq* value

The plot demonstrated that the *Sq* value increases with dip time in the HF acid solution. In other words the surface roughness increases with etching time. In addition, it should be noticed that the *Sq* value is strongly dependent on the sampling area due to the inhomogeneous nature of the etching effect. In this case, the sampling area was randomly selected.

In conclusion, 6 % hydrofluoric acid etching is not a suitable pre-treatment method for CMG glass in the context of the research, because it does not give good control of surface topography, there is a high biological process risk factor, and the acid etching method has low repeatability and high process uncertainty.

3.3.3 Mechanical abrasion

Some mechanical abrasion methods such as grinding paper, scratching and grit-blasting were also investigated to assess the capability of rough surface generation on CMG glass. They present alternatives compared to the use of ecologically unfriendly chemicals.

3.3.3.1 Grinding paper scratching

P1200 grinding paper with an average particle diameter of 15.3 µm [127] was chosen to abrade the glass surface with an example shown in Figure 3.7.

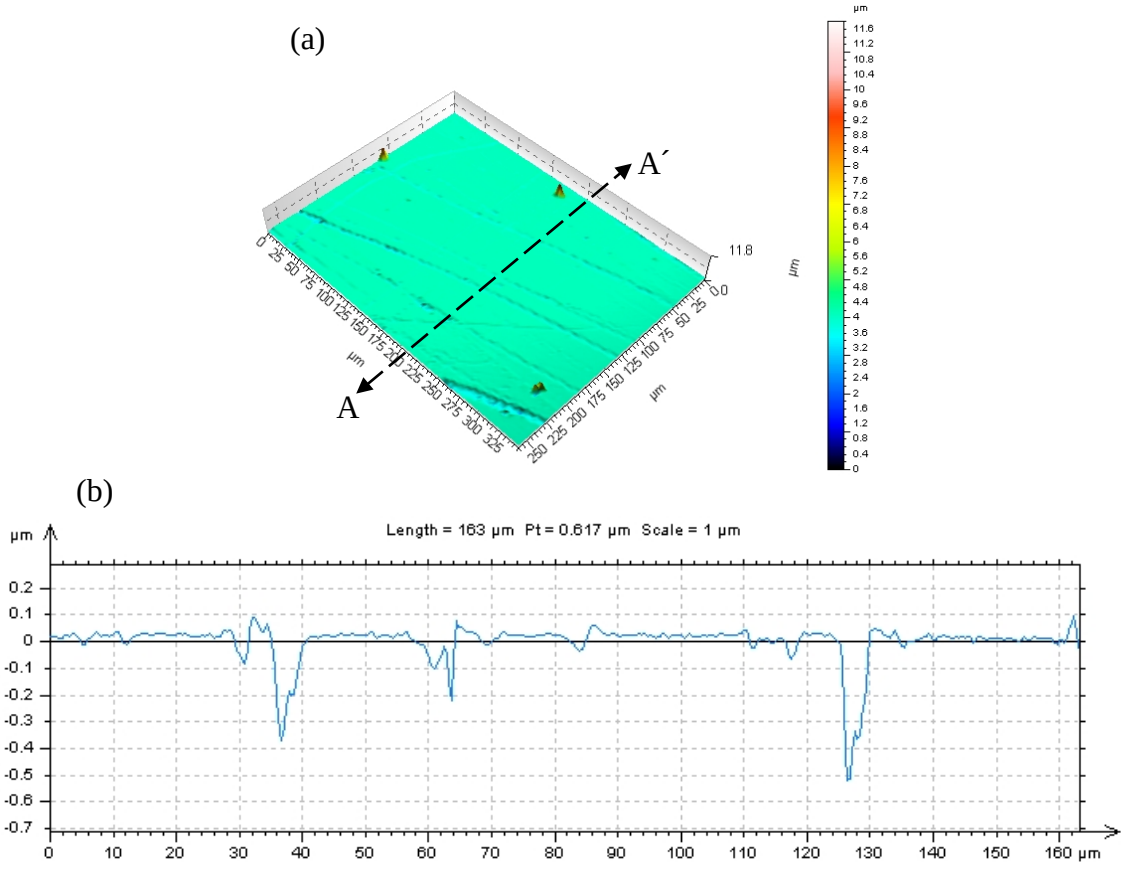

Figure 3.7 CMG glass scratched using P1200 grinding paper
(a) Surface map, (b) Profile A-A´

Abrasive scratch lines can be seen crossing the CMG glass sample. From the profile A-A´, it was noticed that scratch depth was random, ranging from 100 nm to 500 nm. The controllability of this method is small and the process uncertainty is significant.

3.3.3.2 Sand blasting

Sand blasted glass is widely used in interior design applications in both residential and commercial settings for providing privacy or for decoration purposes. This technique uses sand sprayed at high velocities over the surface of the glass to give a translucent surface. The depth and degree of the translucency of the sand blasted treatment varies with the force and type of sand used. By varying the sand size, pressure, angle of application to the glass and duration, various patterns can be impacted onto the surface layer of glass. Figure 3.8 shows surface topography maps of a sand blasted glass sample.

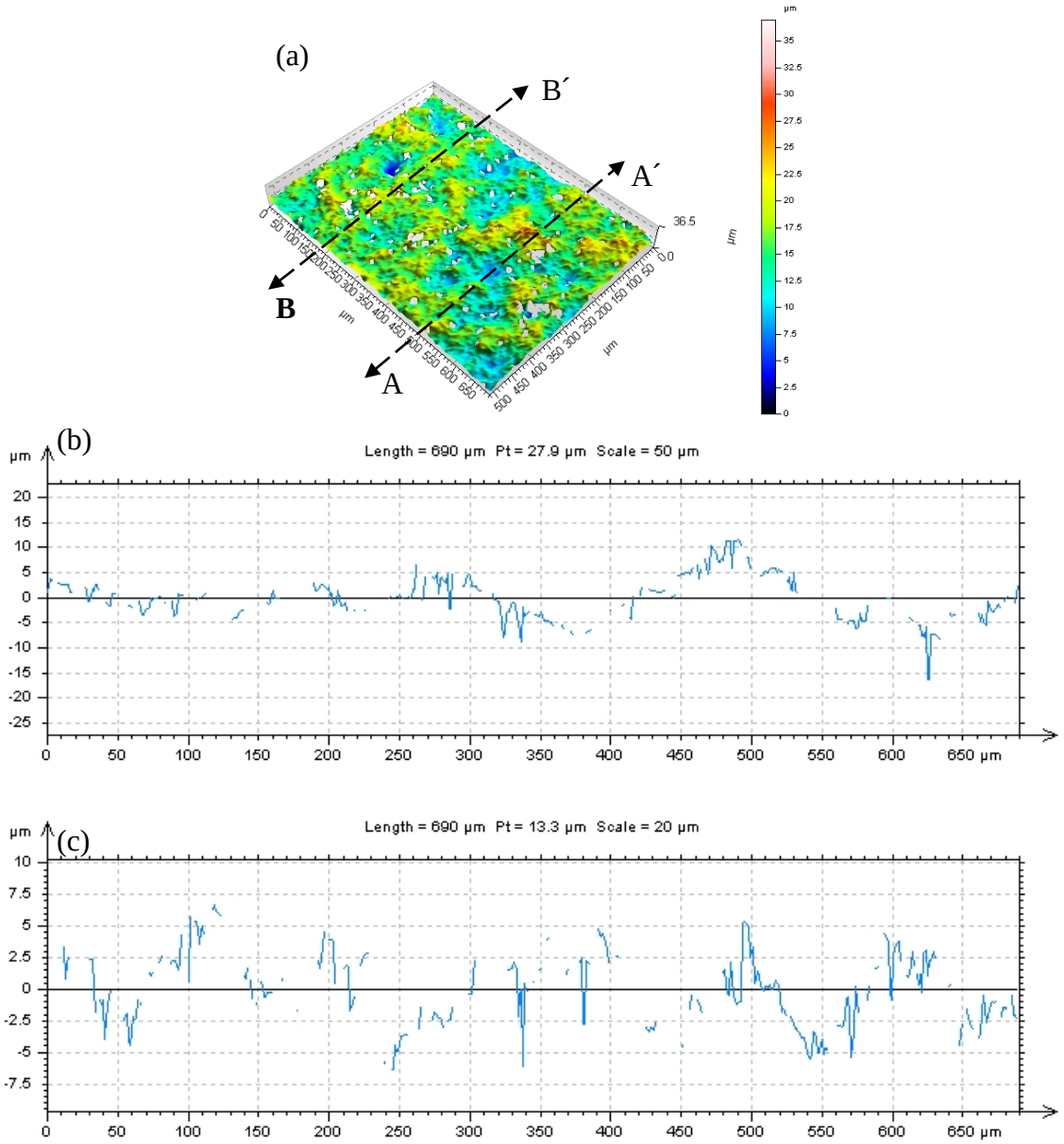

Figure 3.8 Sand blasted CMG glass sample

(a) Surface map, (b) Profile A-A´, (c) Profile B-B´

Two profiles (A-A´ and B-B´) were taken from the sampling area. From the results, it can be seen that there were large scale sinusoidal shaped wave-forms, as well as random microroughness, generated on the sand blasted glass surface. The profiles suggest the form feature diameter size varied from 100 µm (profile B-B´) to 200 µm (profile A-A´). *Sq* value was 3.51 µm, which indicates that sand blasting can significantly increase the surface roughness. Sand blasting is a feasible technique for producing random surface topography on glass, however, there is no experimental capability in Loughborough University. The measured sample was supplied by the Rutherford Appleton Laboratory (RAL), but the cost basis of the commercial process was beyond the scope of this project.

It should be noticed here that the line profiles in Figure 3.8 illustrate the issue of data voids in the surface map. These voids are a function of the local surface slope of the texture versus the numerical aperture of the CSI instrument [103]. This source of error is common in many surface texture measurements using optical instruments. Line profiles generated later in this thesis may also exhibit data voids as identified in section 2.4.5.

3.3.3.3 Bead blasting

Bead blasting is the process of removing surface materials by applying fine glass beads at a high pressure. In this study, GUYSON Formula F1400 equipment was used and Honite 14 (nominal size range of glass bead is 75 µm - 150 µm) was used to create random roughness on CMG glass surfaces. This was due to the availability of the existing experimental equipment. Guyson Honite is a premium quality soda-lime glass bead manufactured specifically for impact blast finishing applications. It is a chemically inert, iron-free product, available in a range of bead sizes and can be used for a wide variety of cleaning, finishing and peening operations [128].

Bead blasting is a low-cost and simple way to produce the random surface on glass. Surface roughness level can also be controlled by changing the diameter of the bead and blasting duration time. CMG glass samples were treated using Honite 14 glass bead for different blasting duration times of 1 second, 2 seconds and 3 seconds. Measurement results are shown in Figure 3.9 to Figure 3.11.

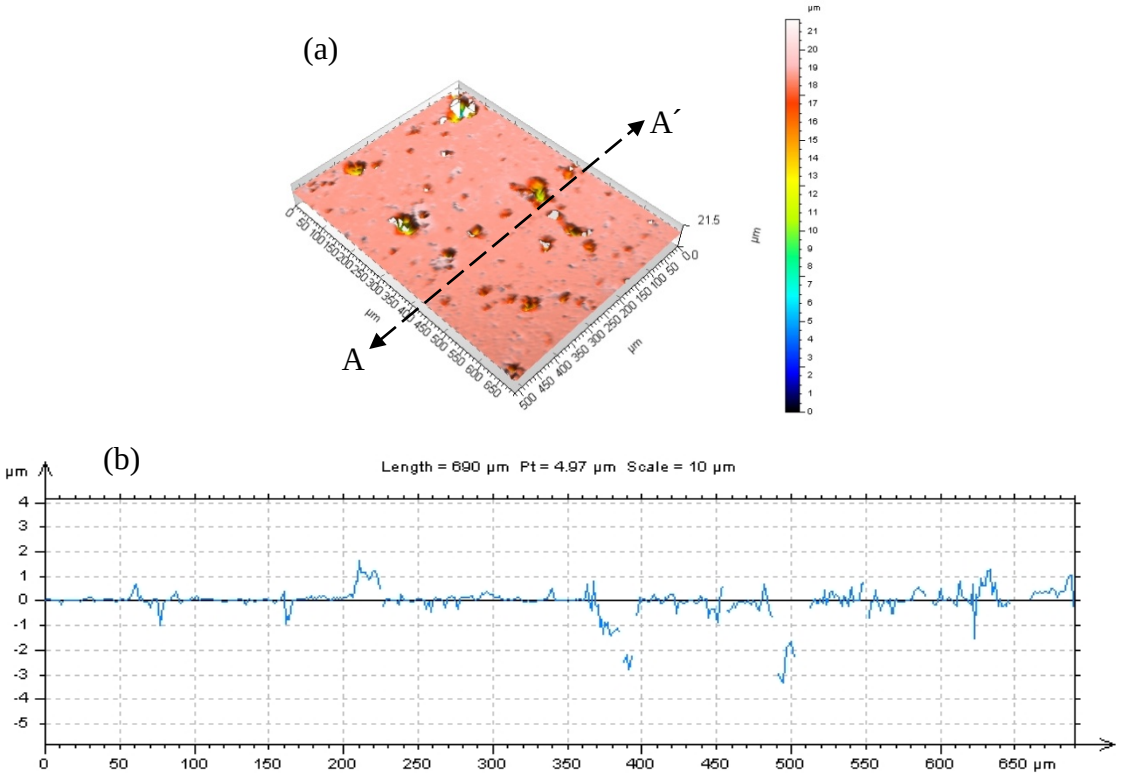

Figure 3.9 Bead blasted CMG glass sample (1 second treatment)

(a) Surface map, (b) Profile A-A´

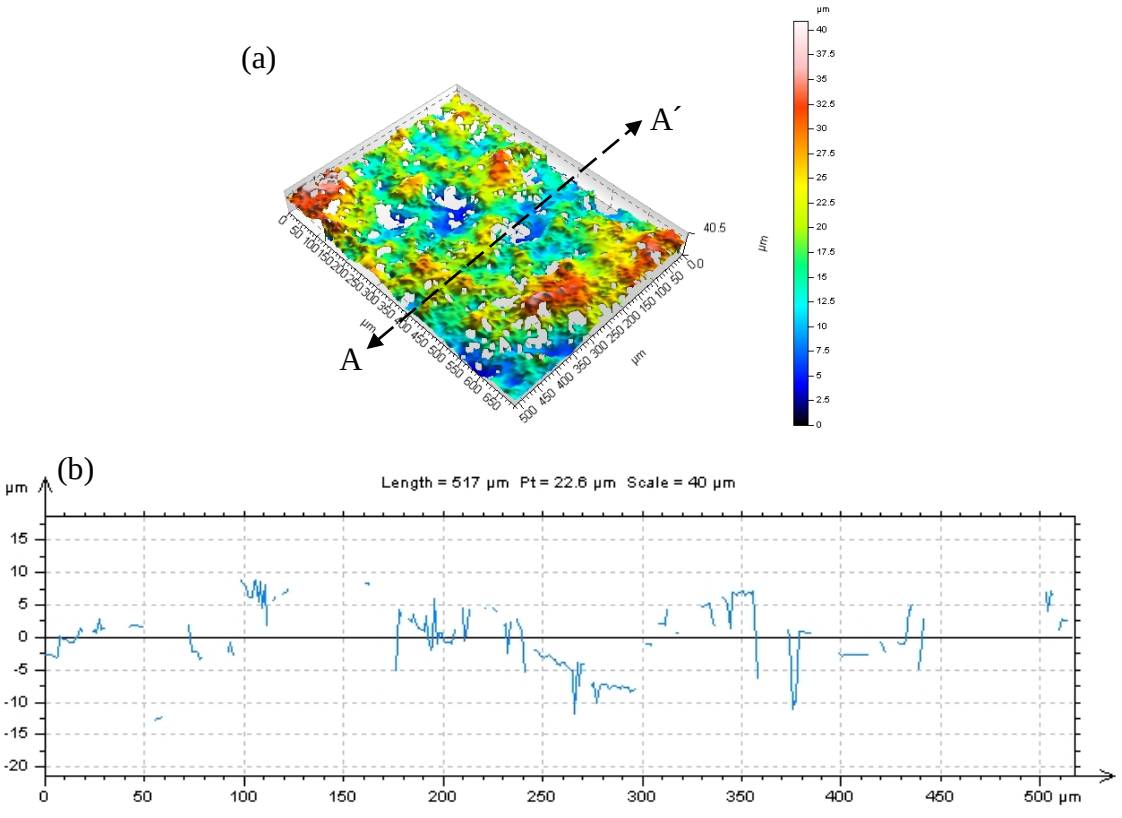

Figure 3.10 Bead blasted CMG glass sample (2 seconds treatment)

(a) Surface map, (b) Profile A-A´

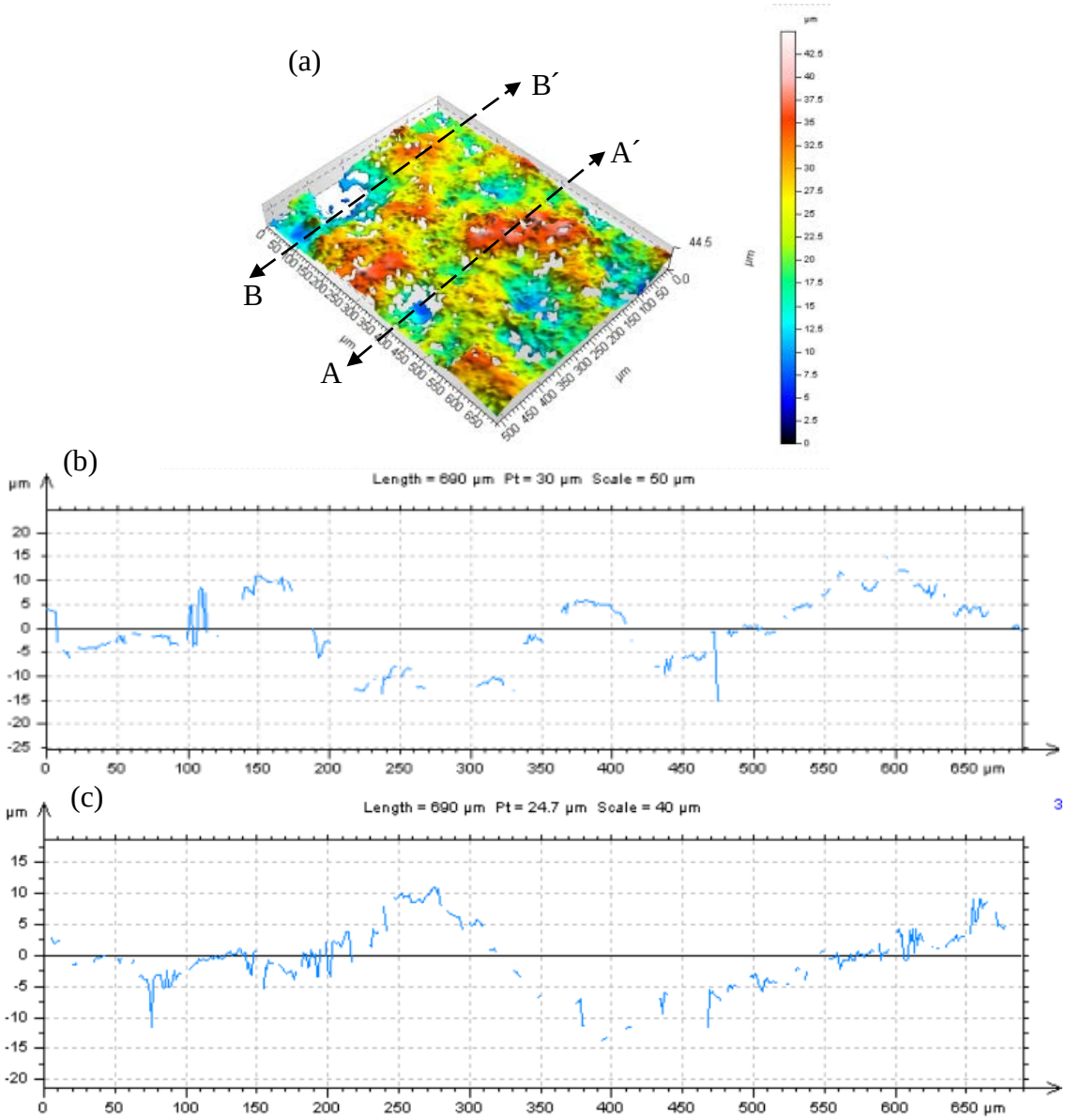

Figure 3.11 Bead blasted CMG glass sample (3 seconds treatment)
(a) Surface map, (b) Profile A-A´, (c) Profile B-B´

Comparing the results with the sand blasted samples, it is noticed that similar topography is exhibited. Large sinusoidal shape wave forms are apparent on the glass surface. The etched depth (amplitude of the wave in Figure 3.11 (b) and (c)) varied from 1 µm to 20 µm according to the blasting time duration. When the sample was exposed to glass bead fluid for 1 second, the typical feature diameter was only 30 µm, increasing to 100 µm when the blasting time was extended to 2 seconds. When this time reached 3 seconds, the feature diameter varied from 200 µm to 300 µm. Two line profiles (A-A´ and B-B´) were generated from the bead blasted glass sample with 3 seconds treatment as shown in Figure 3.11 (b) and Figure 3.11 (c).

Surface roughness increased with blasting time duration as well. When the blasting time durations were 1 second, 2 seconds and 3 seconds, the *Sq* values were 1.02 μm, 4.38 μm and 6.71 μm respectively. Comparing with the former methods, the results indicate that bead blasting treatment can significantly increase surface roughness within seconds. However, the controllability of roughness is very limited with this method.

3.4 Producing structured surfaces on glass

Excimer lasers are used in micromachining applications to remove material from substrates through the ablation mechanism. Zhang and Yung investigated the feasibility of the 248 nm excimer laser in the laser structuring of fine circuit lines on printed circuit boards [129]. These lasers are capable of making microstructures with feature size on the order of 1 μm - 100 μm and are applicable for glass-based materials [130]. The selection of a laser is closely associated to the absorption characteristics of the workpiece. CMG glass is highly absorbent to light with a wavelength (λ) shorter than approximately 320 nm, and it is noticed that for most glasses, laser radiation in the wavelength range from λ = 193 nm to λ = 308 nm is absorbed by more than 80 % [131]. As a result, a Krypton Fluoride (KrF) excimer laser (model EMG 203, Lambda Physik) operating at 248 nm was employed to machine structured surfaces on CMG glass.

3.4.1 Excimer laser characteristics

3.4.1.1 Excimer laser principles

“Excimer” is short for “excited dimer” and “dimer” refers to a diatomic molecule that contains two atoms of the same element. The term “excimer laser” refers to a class of rare gas halide molecules that emit pulses of light whose wavelengths are in the UV spectral region. In the early 1970s, it was found that inert gases (He, Ne, Ar, Kr, Xe) can form temporarily-bound molecules with halogens (Cl, F, Br, I) in an excited state. The rare gas halides are very unstable due to the chemical reactivity of atoms determined by the configuration of their outermost electrons, therefore they give up their excess energies by emission to the ground state, resulting in strongly-repulsive molecules in the ground state. Hence a population inversion is formed. Excited rare gas halide molecules are formed by the strong mutual attraction of positive and negative ions of rare gas and halogen atoms.

Figure 3.12 shows the binding energy diagram for the rare gas halide molecule KrF. The laser transition occurs from the B-stage (excited state) to the X-stage (ground state) by emitting the photon and the excited atomic levels of the rare gases are responsible for the formation of the B-state. During the B => X emission, the rare gas halide molecule KrF with a wavelength λ of 248 nm is used to produce laser action.

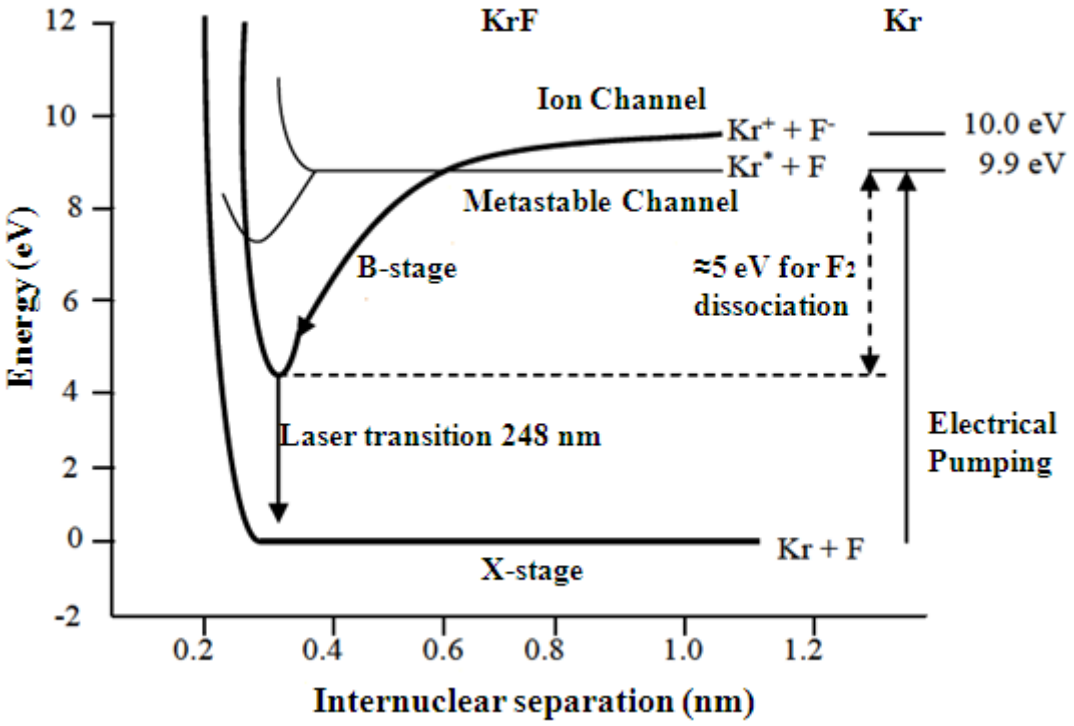

Figure 3.12 Binding energy versus internuclear separation for KrF [132]

Figure 3.13 shows the layout of an excimer laser machining system. The laser beam passes through a beam delivery system that folds the beam in the vertical direction and the horizontal direction. The beam delivery system mainly consists of several optical components for beam expansion, shaping, scanning and image projection. After this it is projected onto the mask plane where it can be passed through different size and shaped mask apertures which can tailor the shape and size of the beam at the work piece [6]. Finally, the beam passes through a projection lens which produces an approximate 1:10 reduced image of the mask on the work piece which is mounted on a computer numerically controlled (CNC) X-Y table. The attenuator (range of setting from 0.2-0.95) sits next to the beam shutter to help reduce the laser beam energy either by absorption or by reflection of part of the beam.

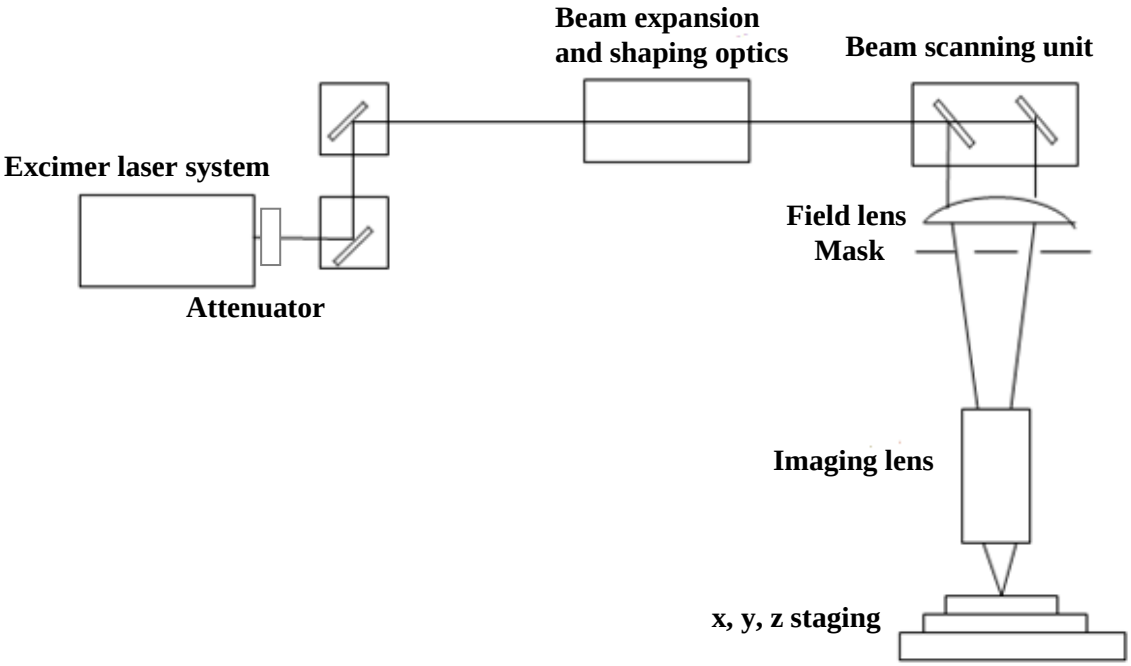

Figure 3.13 Layout of an excimer laser system [132]

3.4.1.2 The interaction of excimer laser radiation with glass

Excimer lasers can be more effectively used for machining micro structures on glass because of their high machining precision quality. Compared with Nd:YAG (λ = 1.06 μm) and CO_2 (λ = 10.6 μm) lasers, an excimer laser has a shorter wavelength which allows the laser beams to be focused to smaller spots and obtain higher energy intensities and a smaller heat-affected zone at the workpiece [132]. In comparison, longer wavelength lasers require more photon absorption to heat the workpiece hot enough to break apart chemical bonding during machining. Such high temperatures cause many heat problems such as combustion, melting, and boiling of the surrounding materials.

Since the ultimate resolution of an optical system is restricted by diffraction effects, which is proportional to the wavelength of the radiation involved, the excimer laser, normally with relatively short wavelengths (in UV range) and pulse time (20 ns), allows the high intensity energy to be absorbed in a very thin surface layer for the effective removal of material from a target area. The short wavelengths and short pulse duration allow the excimer laser to be

suitable for high resolution and high absorption in machining, which are important in making microscale structures with glass-based materials.

The mechanism to directly remove material from substrates is usually called laser ablation, by either photothermal or photochemical mechanisms, or by a combination of these two [133]. The photochemical mechanism is often referred to as a non-thermal process because the material removal is caused by direct chemical bond decomposition as energy is absorbed, whereas in the photothermal process, the absorbed laser energy is converted to lattice vibrational energy (thermal) causing melting and vaporization of the material [134].

Glass can be removed without generating a large amount of heat during ablation, which can damage or shatter the surrounding material, an issue which is especially important for brittle materials. The ablation mechanism of different glasses depends strongly on the composition of the glass. CMG glass is a borosilicate type glass which is highly absorbing to light with a wavelength shorter than approximately 320 nm. For a KrF excimer laser, photons with a wavelength of 248 nm have an energy of approximately 5 eV which is sufficient to break chemical bonds and causes a sudden pressure increase within the absorption region and ejects material in an explosive manner [135]. Since excimer laser pulse durations are short, the interaction with the material occurs very rapidly, and the opportunity for thermal damage to the surrounding material is minimized.

3.4.1.3 Excimer laser parameters

In this research, the KrF laser operating parameters could be preset and controlled by the CNC system and included:

- Energy density (workpiece fluence) – typically measured in J/cm^2. This parameter represents the energy input delivered into the workpiece per unit surface area.

- Attenuator position – as a function of energy density, from 0 to 1.0, where 1.0 is 100 % transmission.

- Pulse duration – in this work, the duration of each pulse was fixed at 20 ns.

- Pulse repetition rate – typically in the range of 5 Hz to 25 Hz.

- Focus position – determined by the lens system used in the optics.

- Beam length along groove length – refers to the length of the beam in the direction of travel and so it is dependent on the shape of the mask.

- Shots per area – the number of shots any exposed area receives during machining. The shots per area influences the speed at which the stages move for a given laser repetition rate.

- Feedrate – refers to the speed of work stage movement.

Feedrate (mm / minute) is determined by the size of the mask, the laser repetition rate and the shots per area. The relationship is expressed by the mathematical equation as follows [136]:

$$Feedrate = \frac{60LR}{N} \qquad 3\text{-}1$$

Where L (mm) is the laser beam length in the direction of the beam's movement;
R (Hz) is the laser pulse repetition rate;
N is the laser shots per area.

Before machining, the focus position must be adjusted according to the sample thickness at different elevation positions in order to guarantee laser machining quality. A focusing programme is shown in Appendix 2. During ablation, the work stage can move in both X and Y directions and rotate in the Z axis. The work stage is kept perpendicular to the laser beam during operation.

In order to systematically study the excimer laser, a series of experiments were designed and performed to find out the effect of each parameter and optimize the process to achieve the best adhesion. The effect of various excimer laser operating parameters such as

geometric shapes of the mask, energy density (fluence), and repetition rate were investigated separately.

3.4.2 Mask study

3.4.2.1 Single machined spot study

The systematic study started with a single machined spot using three different shapes of mask apertures; circular, square and equilateral triangular as shown in Figure 3.14 (all 1 mm masks). The masks were fixed on a mask holder and placed in the centre of the laser beam to obtain the optimal laser output quality. When the laser beam passes through a mask form, the mask pattern is projected onto a static workpiece and so the mask shape is ablated into the sample.

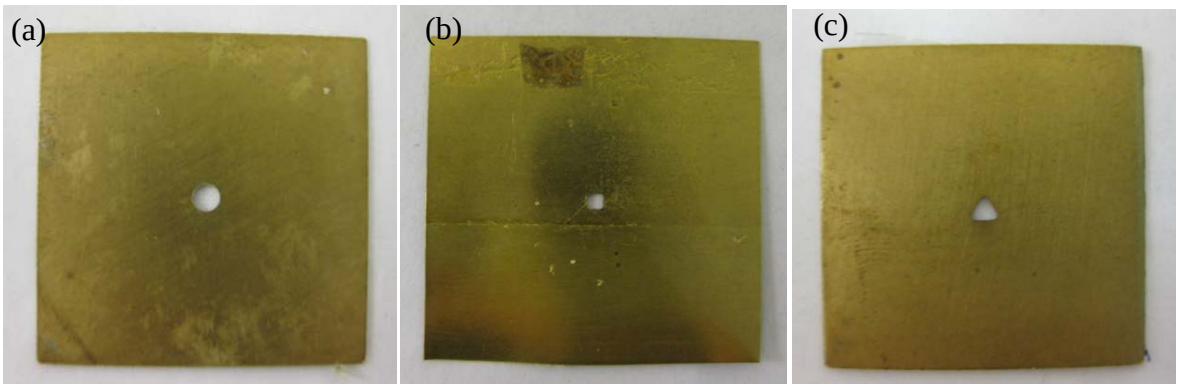

Figure 3.14 Photographs of masks
(a) Circular mask, (b) Square mask, (c) Equilateral triangular mask

The dimensions of the circular, square and equilateral triangular masks were; 1 mm diameter, 1 mm square and 1 mm side length respectively. Figures 3.15 to 3.17 show surface topography measurement results from the Zygo CSI system for each of the three mask shapes. All the machined spots were prepared using laser settings of energy density 2.0 J/cm^2 (output energy 220 mJ and attenuator position of 0.8), repetition rate 10 Hz and shots per area 50 (circular mask, shown in Figure 3.15), 50 (square mask, shown in Figure 3.16), and 200 (triangular mask, shown in Figure 3.17). It is noticeable that there are data holes on the wall sides of the profiles because the CSI system does not measure steep walls very well [103].

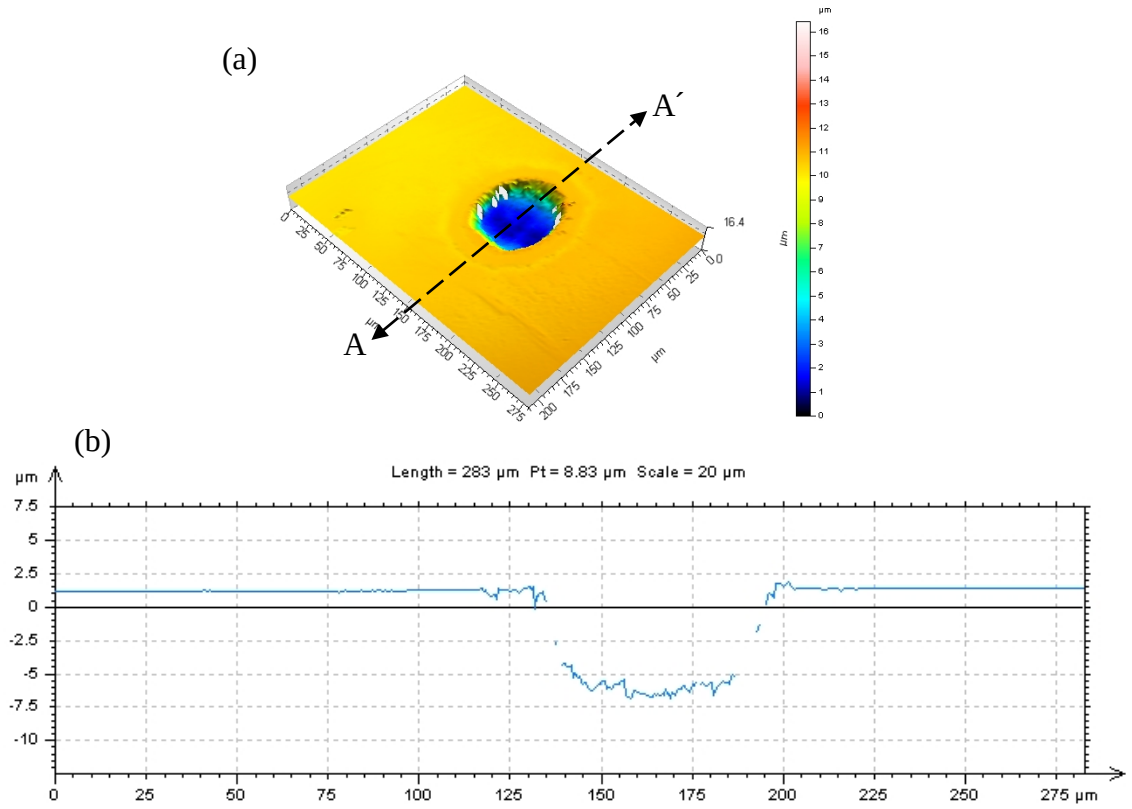

Figure 3.15 Machined feature with circular mask (a) Surface map, (b) Profile A-A´

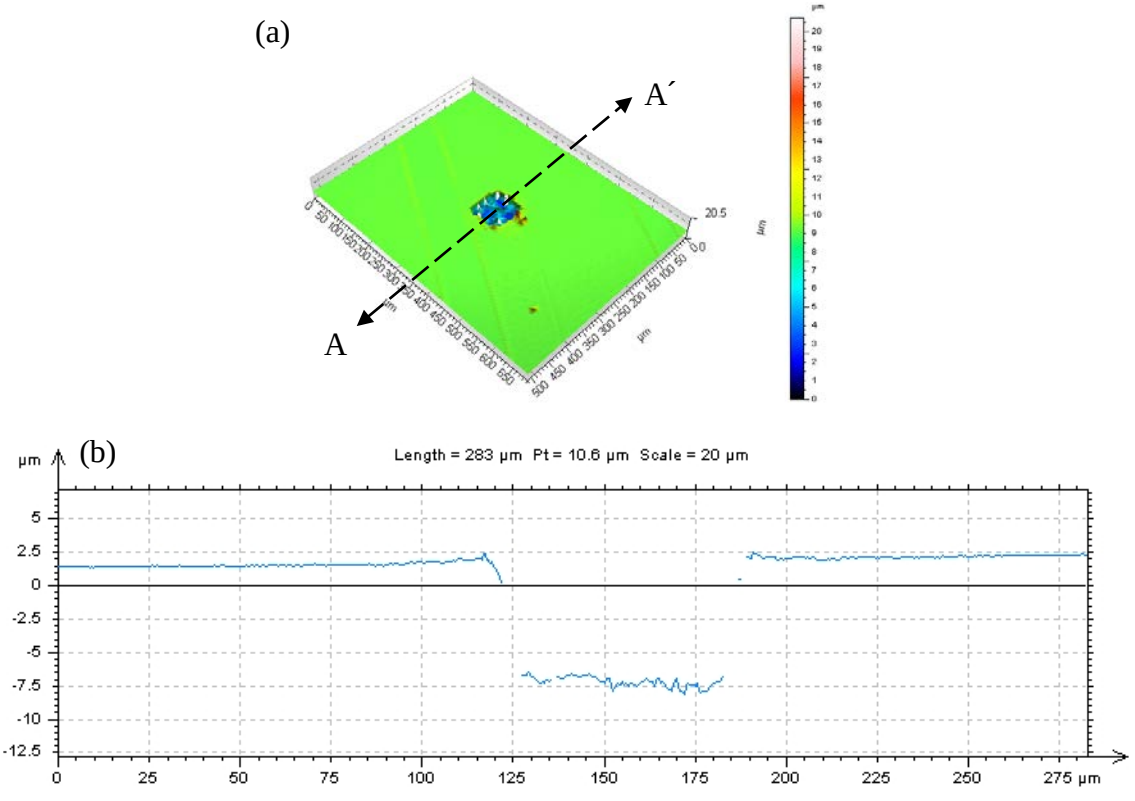

Figure 3.16 Machined feature with square mask (a) Surface map, (b) Profile A-A´

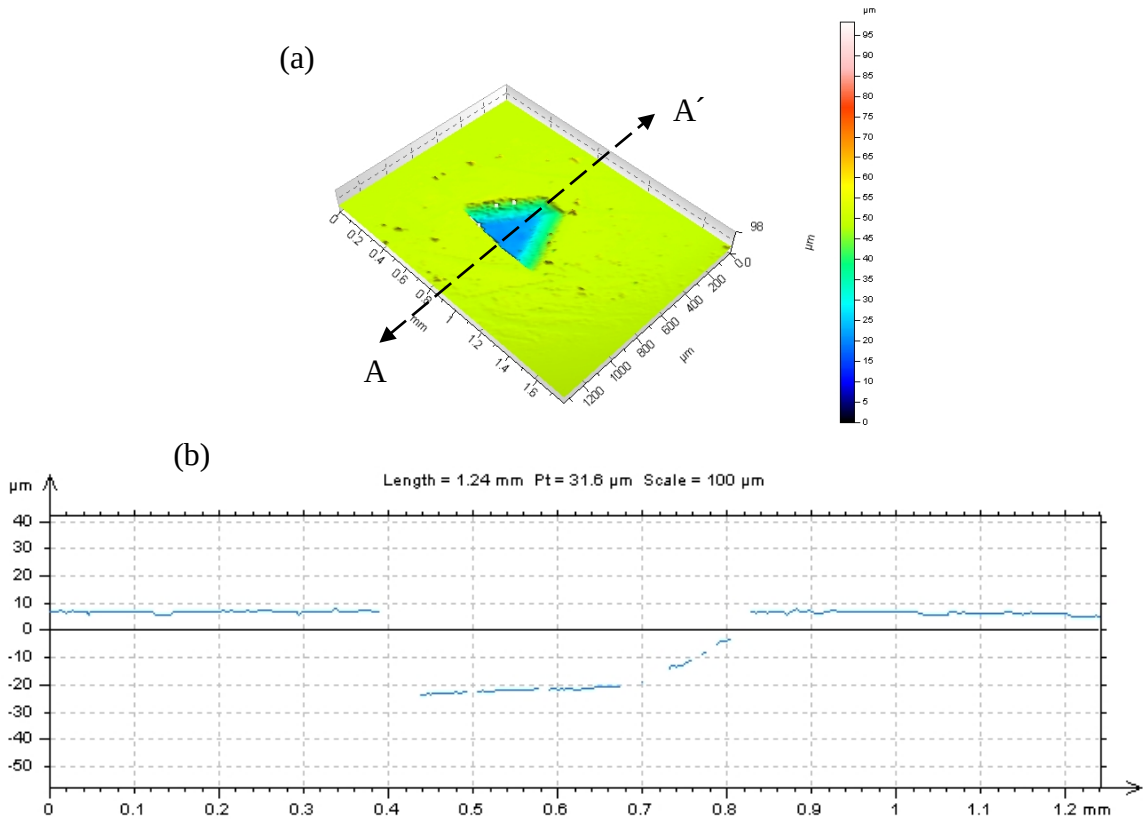

Figure 3.17 Machined feature with equilateral triangular mask

(a) Surface map, (b) Profile A-A´

From the three figures, it can be seen that:

1) The geometry of the masks is reproduced by their projection onto the surface of the workpiece and determines the feature of the machined area. The beam projected onto the sample is reduced proportionally due to the 1:10 reduction ratio of the projection lens. For example, the diameter of the circular mask is 1 mm +/- 0.2 mm, while the diameter of the machined feature is 0.1 mm +/- 0.02 mm.

2) Masks restrict the beam energy intensity projected onto the surface of the workpiece. When the larger size of mask was used, more beam energy of the excimer laser could be passed through and delivered to the surface of the sample.

As a result, structured surface feature design depends on sensible mask dimension choice.

3.4.2.2 Single machined groove study

Structures such as grooves can be produced when the mask is kept fixed in the mask holder and the workpiece is moved while the laser is firing, a process typically known as dragging. In a further experiment, single grooves were machined with the circular, square and equilateral triangular masks. CMG glass work pieces mounted on the work stage were dragged to form a single groove contour 10 mm along one direction. The dimensions of the circular, square and triangular masks were 1 mm, 1 mm and 5 mm respectively. All the machined grooves were machined using laser settings of energy density 2.0 J/cm^2 (output energy 220 mJ and attenuator position of 0.8) and 50 shots per area. Figures 3.18 to 3.20 show surface topography measurement results from the Zygo CSI system for each of the three mask shapes.

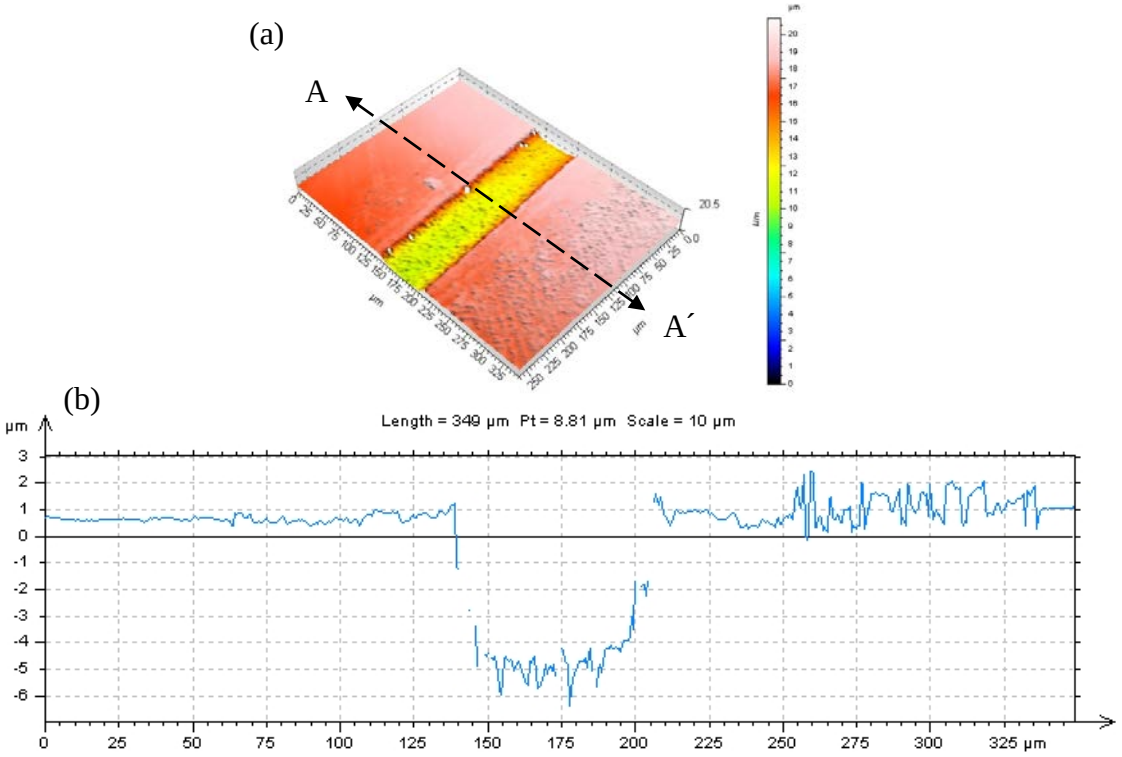

Figure 3.18 Machined groove with circular mask (a) Surface map, (b) Profile A-A´

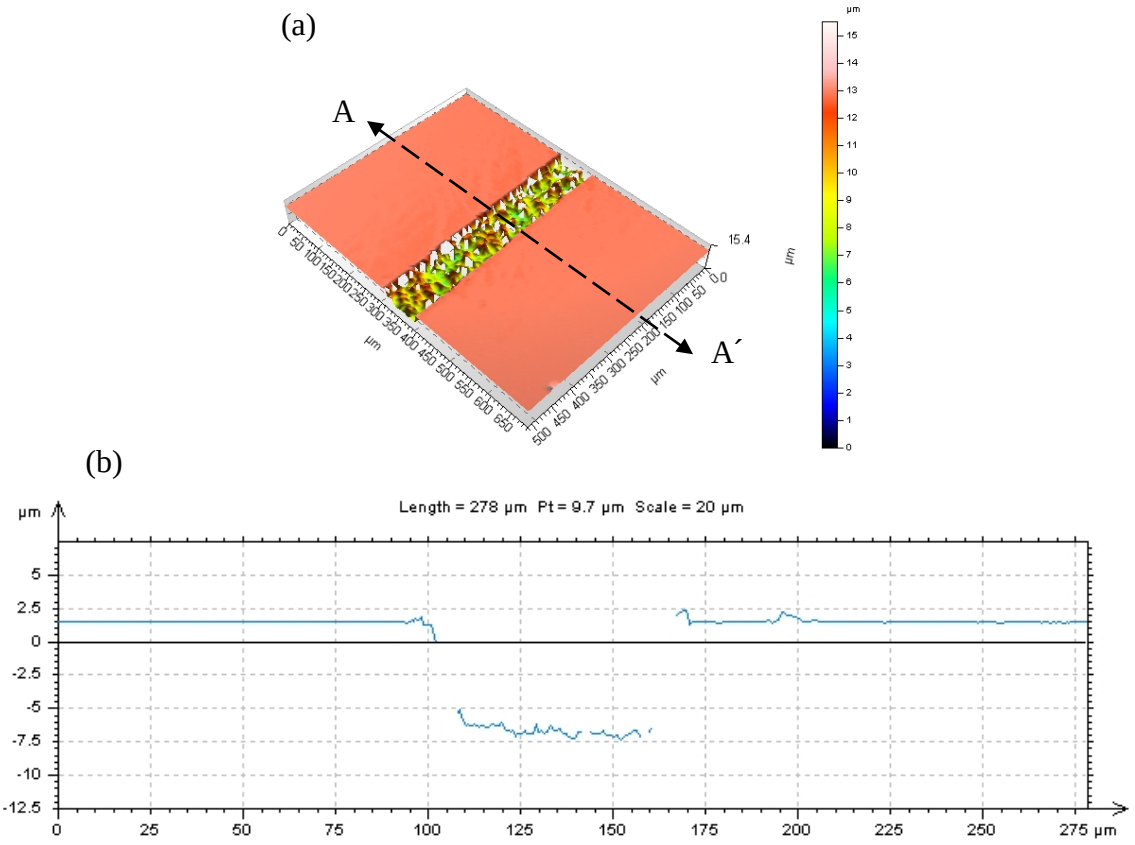

Figure 3.19 Machined groove with square mask (a) Surface map, (b) Profile A-A´

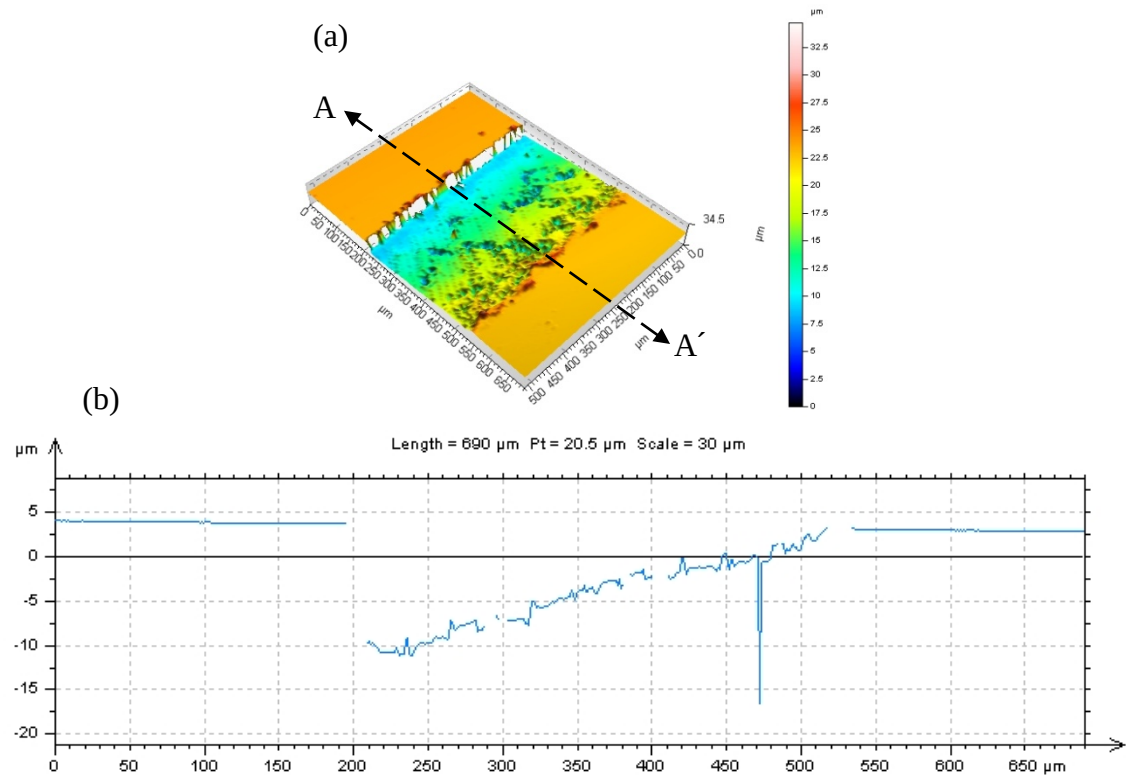

Figure 3.20 Machined groove with triangular mask (a) Surface map, (b) Profile A-A´

From the three figures, it can be seen that:

1) Material ablation is a function of integrated beam energy on the surface. Both the circular and square masks can produce similar depth groove ablation. However, when comparing with circular masks, there are much sharper (from an approximate 45° slope to a right angle) edges produced at the bottom of the machined groove using square masks (comparing Figure 3.18 (b) and Figure 3.19 (b)). This is because more material ablation occurs along the groove edge using the square mask compared to using the circular mask along the workpiece movement direction as shown in Figure 3.21.

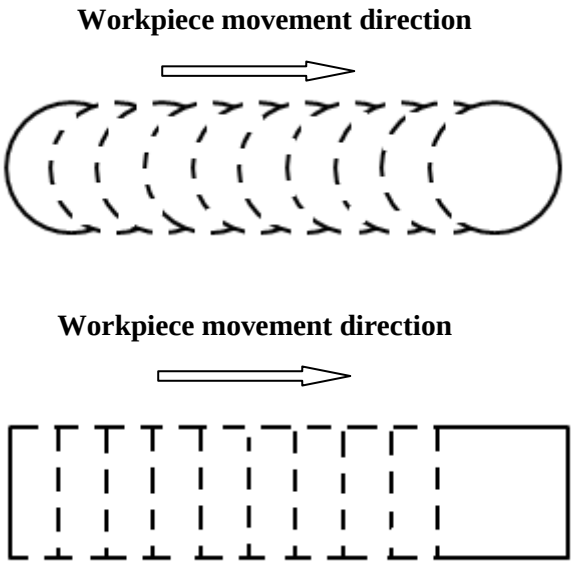

Figure 3.21 Material ablation during workpiece movement using circular and square masks

2) Triangular masks can produce a ramp structure on the surface by the dragging process. As shown in Figure 3.22, during the movement of the workpiece, the track overlapping part along the bottom edge of the mask is much bigger than the top point. This means more surface material ablation occurs along the bottom of the mask than the top. This demonstrates the potential to form complex topographies such as pyramidal surface structures on glass.

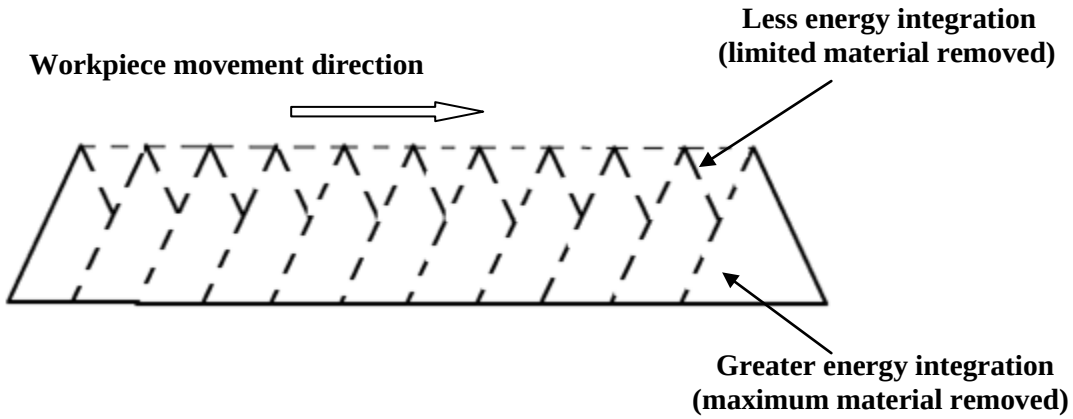

Figure 3.22 Material ablation during workpiece movement using a triangular mask

3) Grooves are the fundamental element of complex microstructure. These machined grooves provide the possibility of further producing various structured surfaces on glass by the dragging process, with parallel, perpendicular or angled grooves.

3.4.3 Laser system operation parameters study

3.4.3.1 Machining parameters matrix study

To determine the effects of energy density and shots per area, matrices with varying settings of attenuator position and number of shots at each machining position were machined into CMG glass samples. The movement of the samples and laser operation were controlled according to a G-Gode programme which is listed in Appendix 3. Different matrices using circular, square and triangular masks were achieved by conducting experiments over the total range of energy from 190 mJ to 250 mJ in increments of 10 mJ. In each matrix the number of pulses varied between 25 and 200 shots increasing in intervals of 25 shots, and the attenuator position varied from 0.2 to 0.9 with an interval of 0.1. The etch depth of each machined feature was investigated using the Zygo CSI system. Figure 3.23 illustrates an example of one of the matrices using a 1 mm diameter circular mask with pulse energy of 220 mJ and a repetition rate of 10 Hz.

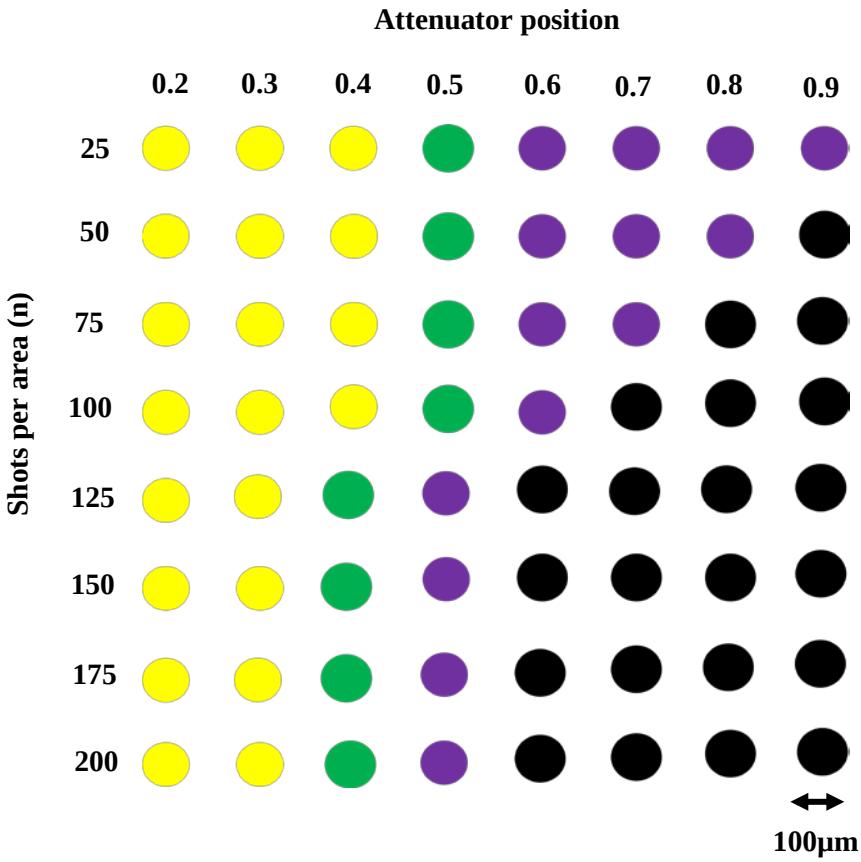

Figure 3.23 Schematic showing the area machining matrix of number of shots and attenuator position (Etch depth < 2 µm, Etch depth 2 µm - 5 µm, Etch depth 5 µm - 10 µm, Etch depth > 10 µm)

These matrices helped to illustrate the effect of energy density with specific laser operation setting versus the etch depth and the threshold ablation fluence of the CMG glass. By changing the laser shots per area and attenuator position, the excimer laser can ablate different depths according to the application. In the experiments, it was found that there was no obvious ablation effect on the surface of the samples when the excimer laser pulse energy was at 220 mJ and the attenuator position was on 0.2, 0.3. Therefore the ablation threshold for the CMG glass is the energy density at 220 mJ and attenuator position 0.4. This energy density value is approximately 1.4 J/cm^2 which was obtained by measuring using a COHERENT® Laser Power / Energy Meter.

Both the output pulse energy and attenuator position setting determine the energy density of the excimer laser, and therefore contribute to the etched depth and surface roughness of the machined dots. In order to investigate the effects of output pulse energy and attenuator

position to machined feature characteristics, a circular mask with 1 mm diameter, shots per area of 25, and repetition rate of 10 Hz was used. In this section, it was the bottom of the machined feature that was measured. The etch depth and surface roughness of each machined feature were measured using the Zygo CSI system, and *Sq* was used to characterize the surface roughness. The results are shown in Figure 3.24 to Figure 3.29.

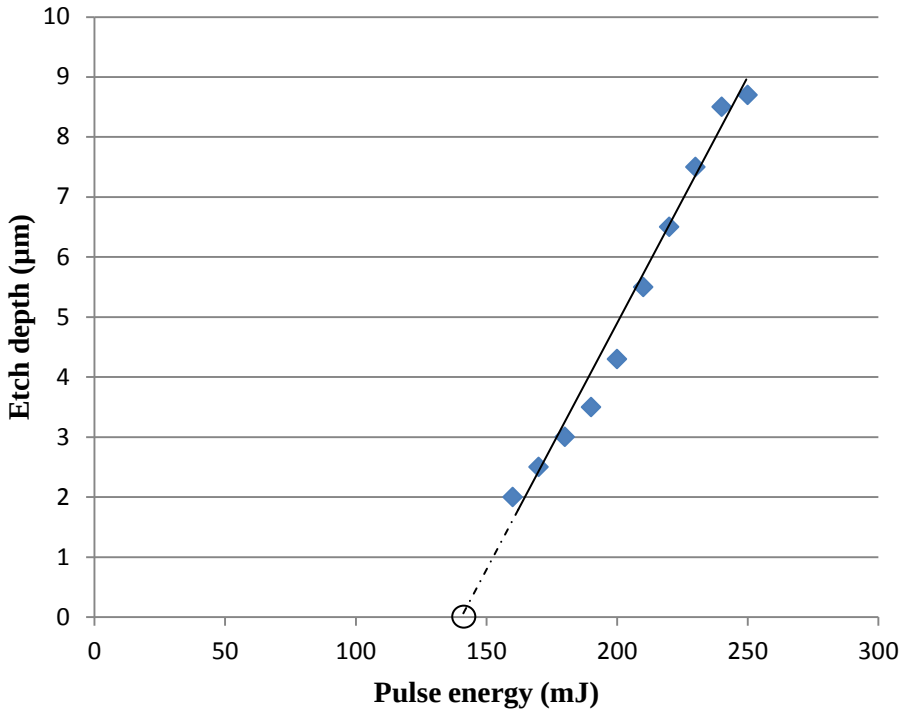

Figure 3.24 Relationship between pulse energy and etch depth on CMG glass matrix (attenuator position 0.9)

As shown in Figure 3.24, the etched depths of glass samples and the laser pulse energy exhibit an almost linear relationship. The more output pulse energy, the deeper the depth machined on the glass surface. The trend of the line indicates the threshold of pulse energy for laser etching is 140 mJ (when etch depth is zero as shown by the circle in Figure 3.24). As a result, the minimum pulse energy setting is 140 mJ for CMG glass ablation.

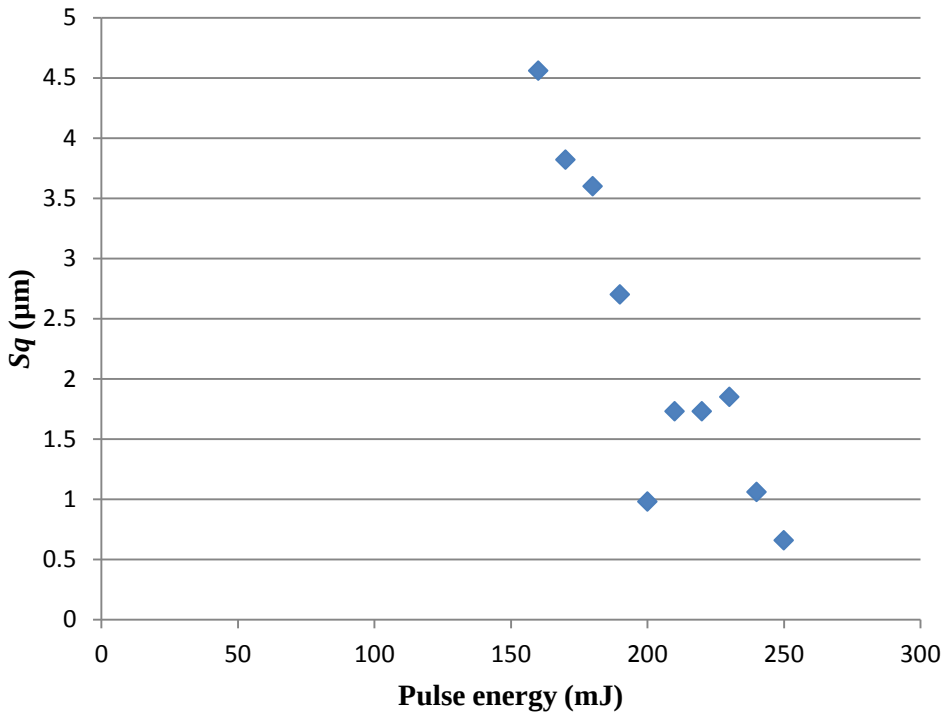

Figure 3.25 Relationship between pulse energy and *Sq* on CMG glass matrix (attenuator position 0.9)

Figure 3.25 shows that increasing pulse energy can decrease the surface roughness *Sq* value. The higher pulse energy results in a smoother surface. Figure 3.24 and Figure 3.25 indicate that the ablation depth and machined surface microroughness level depend on the total energy supplied to the workpiece surface. The possible reason is due to the intrinsic properties of the excimer laser beam and the CMG glass. An excimer laser beam is pulsed and typically inhomogeneous across the beam profile, and this unstable output laser energy results in inhomogeneous machining surface topography. When output pulse energy was increased, more energy was delivered onto the workpiece for removing the material, consequently decreasing surface roughness.

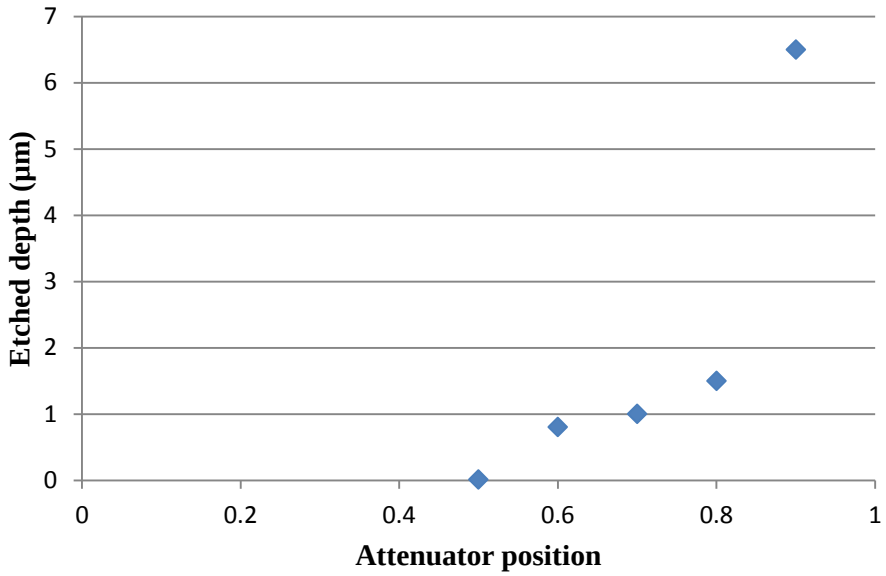

Figure 3.26 Relationship between attenuator position and etched depth on CMG glass matrix

Figure 3.26 shows the relationship between etched depth and attenuator position at 220 mJ with a 1 mm square mask. As mentioned in Figure 3.21, there is no obvious ablation effect for 25 shots per area with attenuator positions at 0.2, 0.3 and 0.4, so the data drawn in Figure 3.25 starts from attenuator positions at 0.5 to 0.9. The result suggests the ablation depth increases with attenuator position from 0.5 to 0.9, and the machining quality improves at the same time as shown in Figure 3.27. When the attenuator position is 0.5, the machined surface is rough and not uniform. However, an attenuator position of 0.9 provides better machining quality resulting in a smaller *Sq* value.

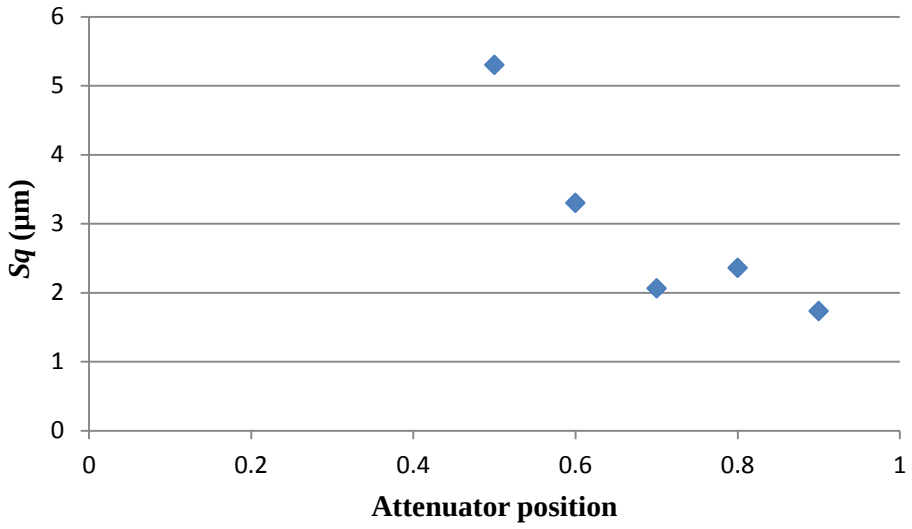

Figure 3.27 Relationship between attenuator position and *Sq* on CMG glass matrix

The function of the attenuator is to help reduce the output laser beam energy. Increasing the attenuator position allows more energy to pass through and project onto the samples. From the earlier pulse energy investigation, it is demonstrated that increasing output laser energy can increase etched depth and decrease surface roughness. The reason is the same as discussed earlier. Figure 3.26 and Figure 3.27 show the same trend with pulse energy as expected. A high attenuator position setting can increase the etched depth of the glass samples and improve machining homogeneity.

It was noticed that the square mask and the triangular mask presented the same trend as the circular mask, however, only the results of circular mask have been show here as an example. Although the results indicate the thresholds of pulse energy and attenuator position are 140 mJ and 0.5 respectively, pulse energy was set to 220 mJ (and sometimes larger) and the attenuator position was 0.8 or higher when machining structured glass surfaces later in the thesis in order to effectively utilize the energy of the excimer laser.

Energy density, shots per area and pulse repetition rate are the routinely used parameters in most literature. Thus these basic laser operation parameters were investigated systematically before the production of structured surfaces.

3.4.3.2 Changing energy density

Etch rate is a frequently used term in laser machining related literature. A mathematical correlation between the ablation depth and pulse number can be expressed as follows [135]:

$$\Delta d = d/N \qquad 3\text{-}2$$

Where d is the ablation depth (μm), N is the number of pulses or shots per area, and Δd is the ablation depth (μm) per pulse (or the ablation rate) which can be determined experimentally.

Section 3.4.3.1 demonstrates both output pulse energy and attenuator position contribute to energy density. In order to scale the relationship between ablation rate and energy density for CMG glass, energy densities of machined dots in a matrix (Figure 3.23) with varying output energy density were measured using the COHERENT® Laser Power / Energy Meter. The

ablation depth increases linearly with the pulse number. The results of energy density influence are shown in Figure 3.28 and Figure 3.29.

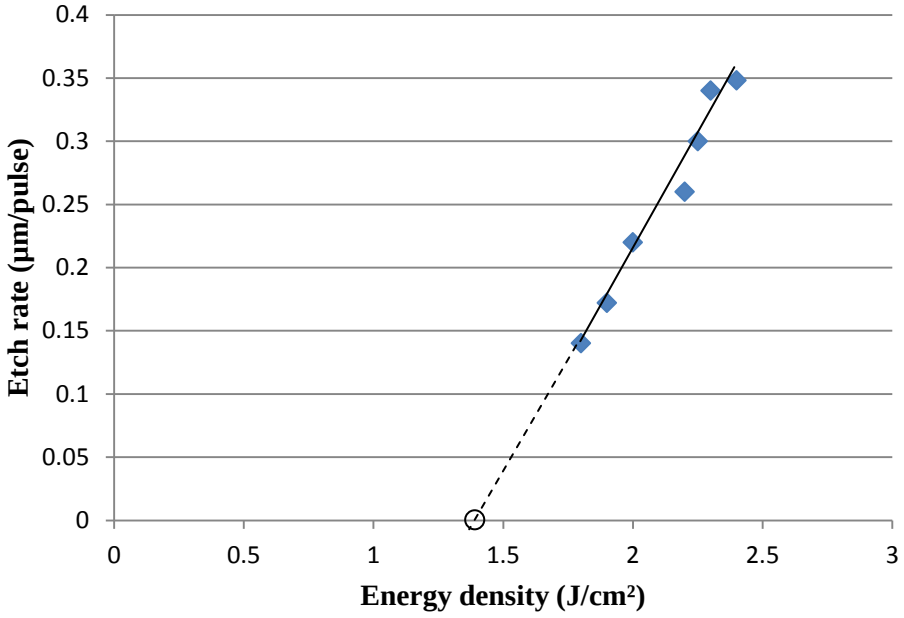

Figure 3.28 Relationship between energy density and etch rate on CMG glass

Figure 3.28 suggests the etch depth increased almost linearly with the energy density. The trend of the line also indicates the threshold of energy density for etching is 1.4 J/cm^2 (when etch rate is zero as shown by the circle in Figure 3.28). This is the minimum energy density for CMG glass ablation. Figure 3.29 shows the relationship between energy density and machined surface roughness which was characterized by *Sq*.

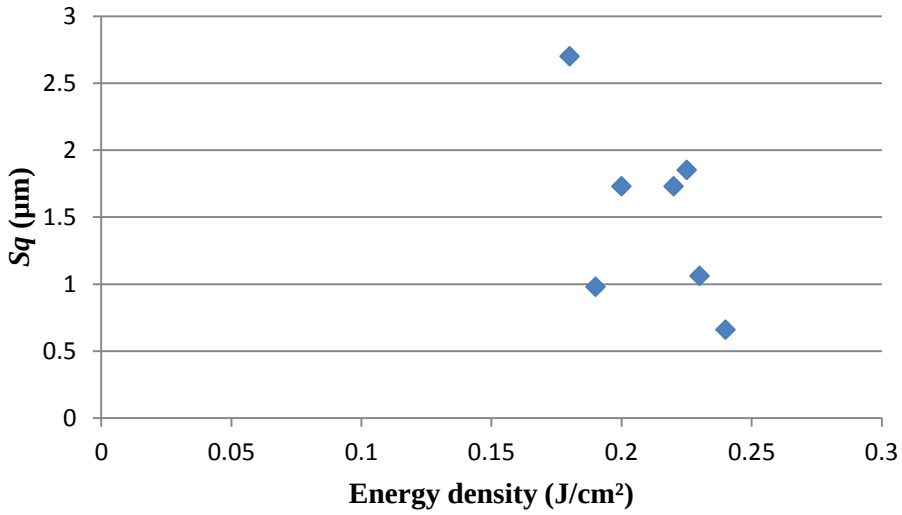

Figure 3.29 Relationship between energy density and *Sq* on CMG glass

As shown in Figure 3.28 and Figure 3.29, the graphs suggest the larger the energy density, the larger the etch rate and smoother the machined surface. These trends agree with the results of pulse energy and attenuator position experimentation. The possible reason is as discussed previously. From the measurements of the ablation rate, the controllability of the laser surface treatment can be optimized via the processing parameters; output pulse energy and attenator position.

3.4.3.3 Changing shots per area

In order to study the effect of shots per area on machined surfaces, machined dots in a matrix (Figure 3.23) with varying shots per area, a fixed attenuator position of 0.9 and pulse energy of 220 mJ were measured. The measurement results are shown in Figure 3.30 and Figure 3.31.

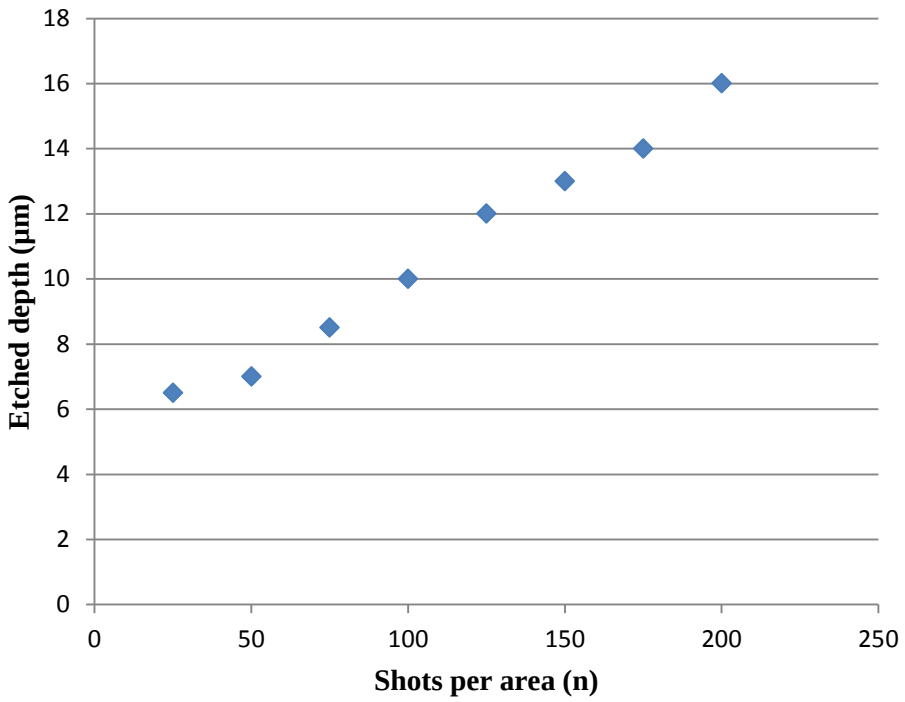

Figure 3.30 Relationship between shots per area and etched depth on CMG glass

From Figure 3.30, we can see the influence of the shots per area on the etched depth. Etch depth increases with increasing shots per area. This is consistent with the expectation of trend of pulse energy. With the increase in shots per area, more laser total energy is supplied to the material surface and causes greater material removal. Using this diagram, we can predict the structure depth. Figure 3.31 shows the effect of shots per area to surface machining quality which was characterized by *Sq*.

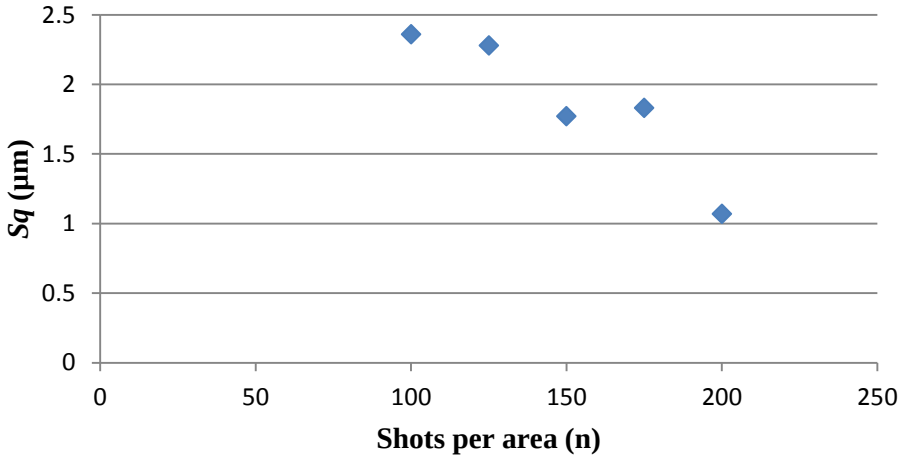

Figure 3.31 Relationship between shots per area and *Sq* on CMG glass

These measurement results suggest the more shots per area, the more uniform the machined surface. Shots per area provide another approach to improve machining quality. However, a decreasing shots per area can shorten the machining process significantly. A sensible choice of the number of shots per area is important when considering the compromise between machining quality and manufacturing processing time.

3.4.3.4 Changing repetition rate

In order to study the effect of repetition rate on the depths of laser structuring, experiments were carried out in which the repetition rate was changed and other parameters were fixed (energy density 2.2 J/cm^2, shots per area 25). G-code programme was used as listed in Appendix 4. The measurement results are shown in Figure 3.32 and Figure 3.33.

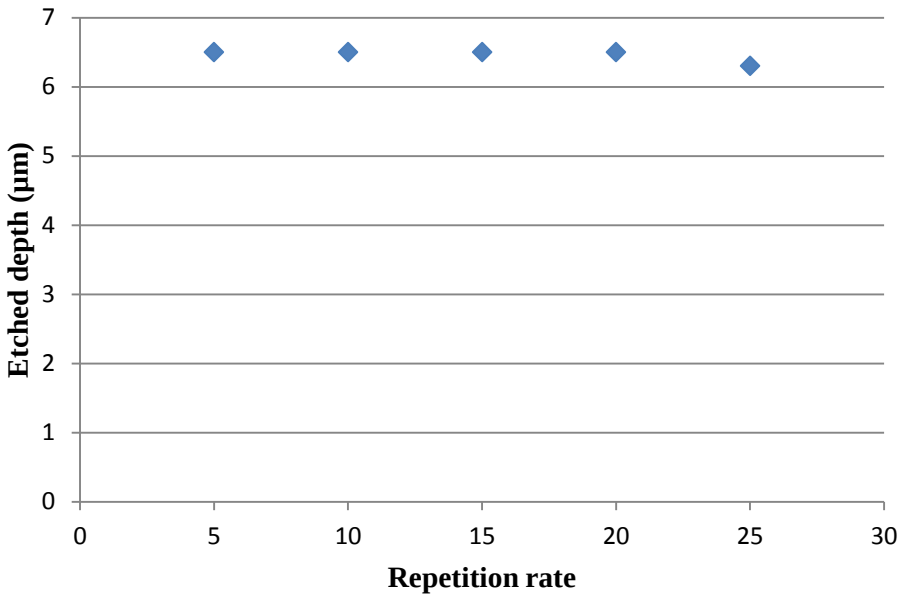

Figure 3.32 Relationship between repetition rate and etched depth on CMG glass

Figure 3.32 shows that repetition rate has very little effect on the etched depth because there is no change to the total energy delivered to the workpiece surface with varying repetition rate. However, repetition rate determines laser pulse frequency, which is related to machining speed. A higher repetition rate can accelerate the machining process and improve ablating efficiency. Figure 3.33 shows the relationship between repetition rate and machined surface roughness which was characterized by *Sq*.

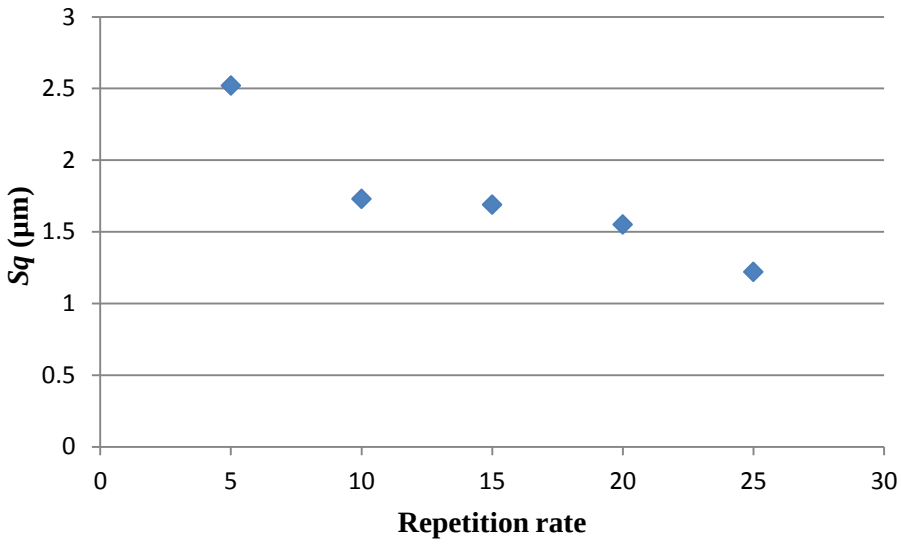

Figure 3.33 Relationship between repetition rate and *Sq* on CMG glass

The results indicate lower pulse repetition rate leads to rougher machined surface quality, while the higher pulse repetition rate results in a smoother surface. The possible reason maybe at low pulse repetition rates, the debris or recast material from laser ablation has sufficient time to cool down and accumulate into larger debris, resulting in a rougher surface. Conversely, at high pulse repetition rates, the debris can be bombarded by the subsequent laser pulses and scattered into much finer components, resulting in smoother surface topography [133].

These preliminary results suggest the etch depth depends on laser energy density and shots per area, and machining homogeneity can be improved by increasing the energy density, shots per area and laser pulse repetition rate. These conclusions help to maximise the use of the laser energy and minimize the machining time; thereby helping to machine surface structures more effectively.

3.4.4 Focus position

From the previous study, it was found that laser operating parameters such as energy density, shots per area and repetition rate determine the machining quality. As well as these parameters, the defocusing effects of the excimer laser can also create random surfaces on CMG glass. Defocusing means there is a deviation to the focusing plane which yields the best ablation effect [129]. Since the most uniform energy density is produced at the optimal focal plane, an inhomogeneous beam at a defocused position can be used for rougher surface machining. In addition, more laser energy is needed for ablation of substrates located at nonoptimal focal positions. A schematic of laser defocusing ablation position is shown in Figure 3.34.

Excimer laser systems can have the focal position adjusted with respect to the work stage in two ways; vertical translation of optical elements, and / or vertical translation of the sample work stage.

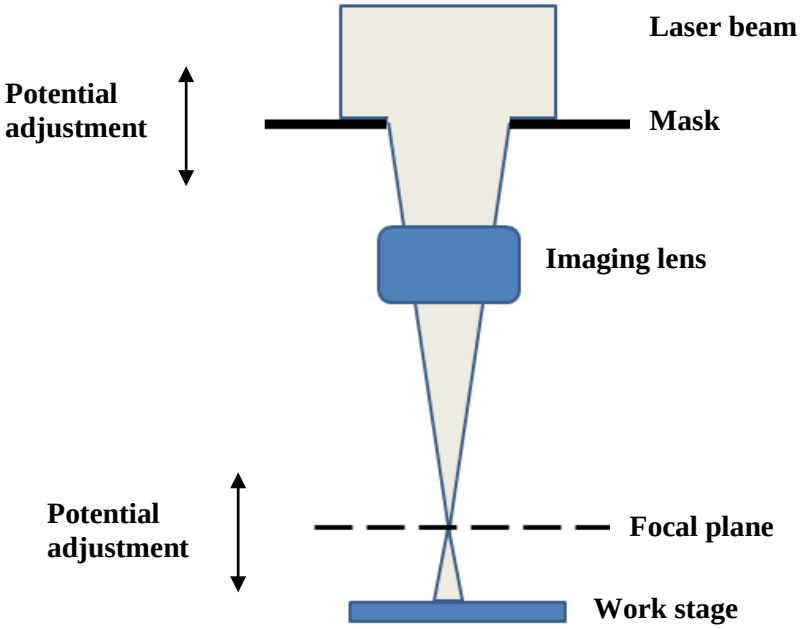

Figure 3.34 Schematic of laser defocusing ablation

Surface topography images of the examples machined by laser defocusing ablation are shown in Figure 3.35 and detailed laser operating parameters are shown in Table 3.1.

Table 3.1 Processing parameters details for structures shown in Figure 3.35

Sample number	**Focusing position**	**Energy density (J/cm^2)**	**Shots per area (n)**	**Repetition rate (Hz)**	***Sq* (μm)**
(a)	Δf = 0 mm	1.5	5	10	1.44
(b)	Δf = 2 mm	2.2	5	10	2.63
(c)	Δf = 2 mm	2.2	5	10	3.04
(d)	Δf = 2 mm	2.2	5	10	3.91

Table 3.1 shows that for excimer laser machining surface roughness is minimized when working at the focal plane (smallest *Sq* value as shown in (a)). However, the machined surface roughness increases when the laser works at a defocused plane. Even with the same excimer laser processing parameters as shown in (b), (c) and (d), the machined surface roughness (characterized by *Sq*) were different.

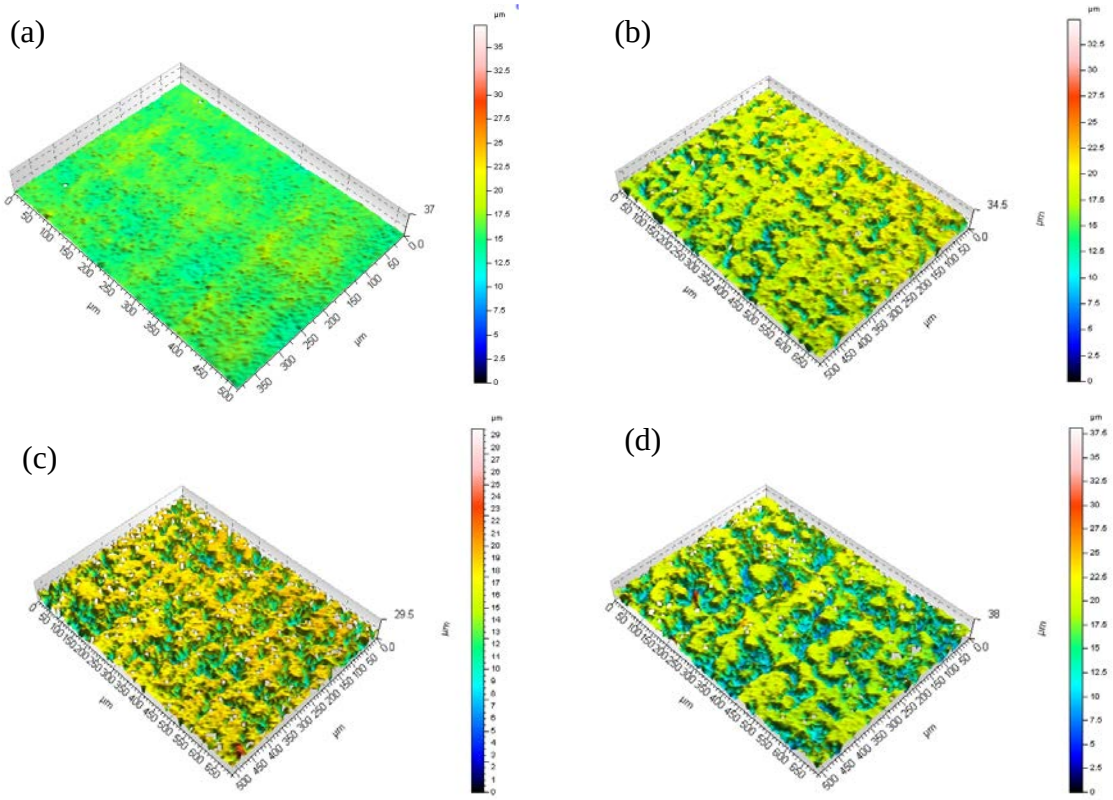

Figure 3.35 Random surfaces produced on CMG glass by defocusing effect

Figure 3.35 shows that random surfaces can be produced on CMG glass by the defocusing effect. Comparing with Figure 3.35 (a), it can be seen that there were more ablation pits on the ablated surfaces of Figure 3.35 (b), (c) and (d) when the focal plane deviated by 2 mm down from its optimal position. The areal parameter *Sq* also indicated that surface roughness increased from 1.44 µm (Figure 3.35 (a)) to 3.91 µm (Figure 3.35 (d)).

The results demonstrate that the excimer laser can also produce a random roughness surface on glass, however, it is a relatively high-cost and time-consuming technique. As a result, the excimer laser was not adopted in this study for generating solely random surfaces on CMG glass and the data was not used for plotting correlations in Chapter 6.

3.4.5 Machining direction study

In this element of the work, the excimer laser was used to generate micro pattern array structures on glass by using a mask projection and dragging process [137-139]. The challenge of this study was to produce and identify the optimal surface topography highly correlated

with adhesion plating on glass. Two direction machining and three direction machining were attempted to achieve structured surfaces on CMG glass.

3.4.5.1 Two direction machining

In two direction machining, the complex microstructure was produced in two steps. Firstly, the work piece was mounted on the work stage and moved at a constant velocity (determined by Equation 3-1) controlled by the computer to form a groove contour along one direction, then repeating the process to form another groove overlapping the previous groove partially in the same direction and so on. Secondly, grooves were machined across in the direction orthogonal to the initially machined grooves by running the same programme after rotating the sample by 90° to create a periodic structure as shown in Figure 3.36.

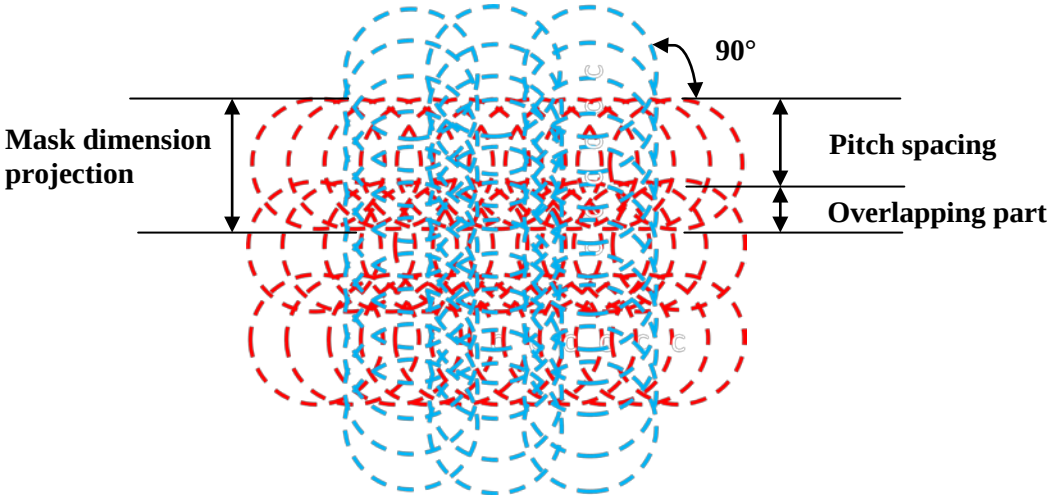

Figure 3.36 Direction of dragging process using a circular mask

A micro-pattern structure was generated on a glass surface using the dragging process as described above. The surface topography consists of both the large scale grid structure component and the micro-roughness component. The large scale structure is determined by the mask geometrical dimension projection and pitch spacing between the adjacent grooves. From the previous investigation in section 3.4.3, the micro-roughness component is affected by laser operation parameter setting such as energy density, shots per area and repetition rate.

Machining complex micro-pattern structures started with circular masks. Detailed processing parameters of machined examples are shown in Table 3.2 and surface topography images are shown accordingly in Figure 3.37.

Table 3.2 Processing parameters details for structures shown in Figure 3.37

Sample number	**Mask diameter (mm)**	**Energy density (J/cm^2)**	**Repetition rate (Hz)**	**Shots per area (n)**	**Feature pitch spacing (μm)**
(a)	7	2.4	20	15	350
(b)	5	2.4	10	5	200
(c)	5	2.4	10	5	200
(d)	2	2.2	10	5	100

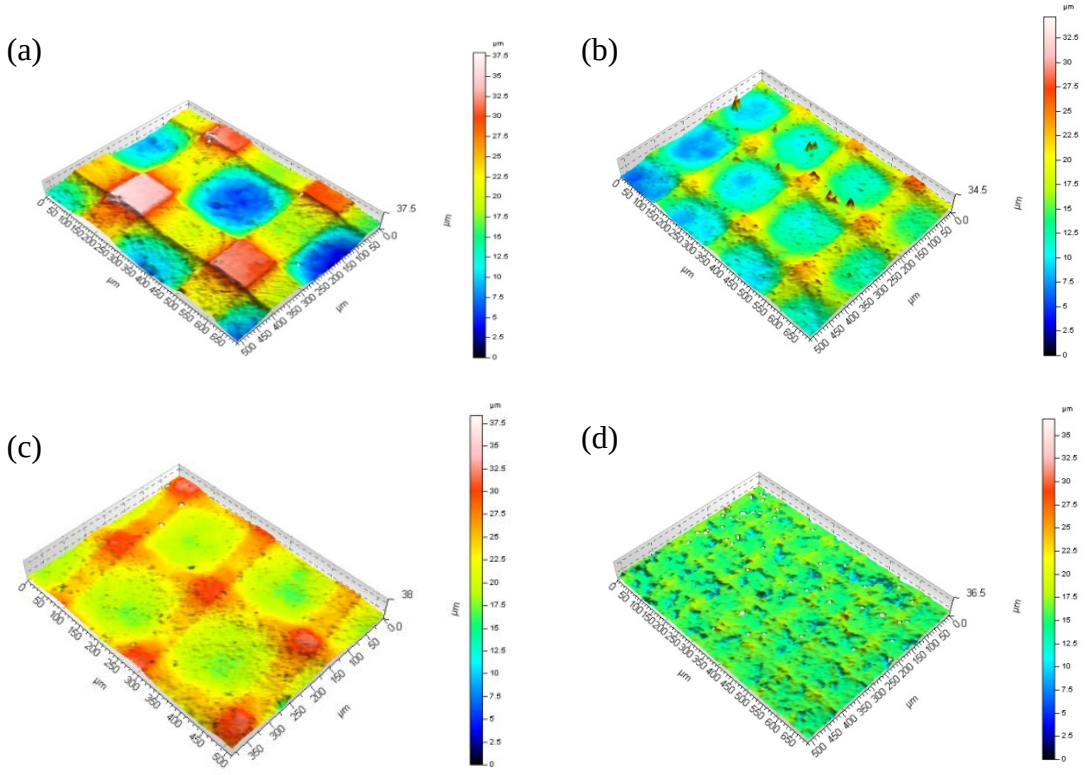

Figure 3.37 Micro pattern structures machined using circular masks

Figure 3.37 presents four typical grid-based microstructures generated on the CMG glass surfaces using circular masks. It can be seen that these four micro patterns exhibit different structures, different micro-roughness characteristics and different etched depths. Combining Figure 3.37 with Table 3.2, it can be seen that large scale structure spacing, as shown in Figure 3.37 (c), can be controlled by the laser input parameters. Deeper etched depth, as

shown in Figure 3.37 (a), is determined by larger energy density and more shots per area. Comparing with Figure 3.37 (a), (b) and (c), Figure 3.37 (d) exhibits more micro-roughness components. This is because less energy density, fewer shots per area and smaller repetition rate contributed to increase the surface micro-roughness.

In this process, features of the micro pattern structures are determined by mask geometrical dimensions and pitch spacing between adjacent grooves. As discussed earlier, the depth of the machined feature and micro-roughness component can be controlled wherever possible by changing the excimer laser operation parameters. Grid-based microstructures may potentially help to trap copper plating on the glass surface and therefore improve copper / glass adhesion performance.

Similar grid-based micro pattern structures can also be produced using square masks. Detailed processing parameters of machined examples are shown in Table 3.3 and surface topography images are shown accordingly in Figure 3.38.

Table 3.3 Processing parameters details for structures shown in Figure 3.38

Sample number	**Square dimension (mm)**	**Energy density (J/cm^2)**	**Repetition rate (Hz)**	**Shots per area (n)**	**Feature pitch spacing (µm)**
(a)	4	2.2	10	5	40
(b)	8	2.2	20	5	400
(c)	1	2.2	10	10	50
(d)	1	2.4	10	10	80

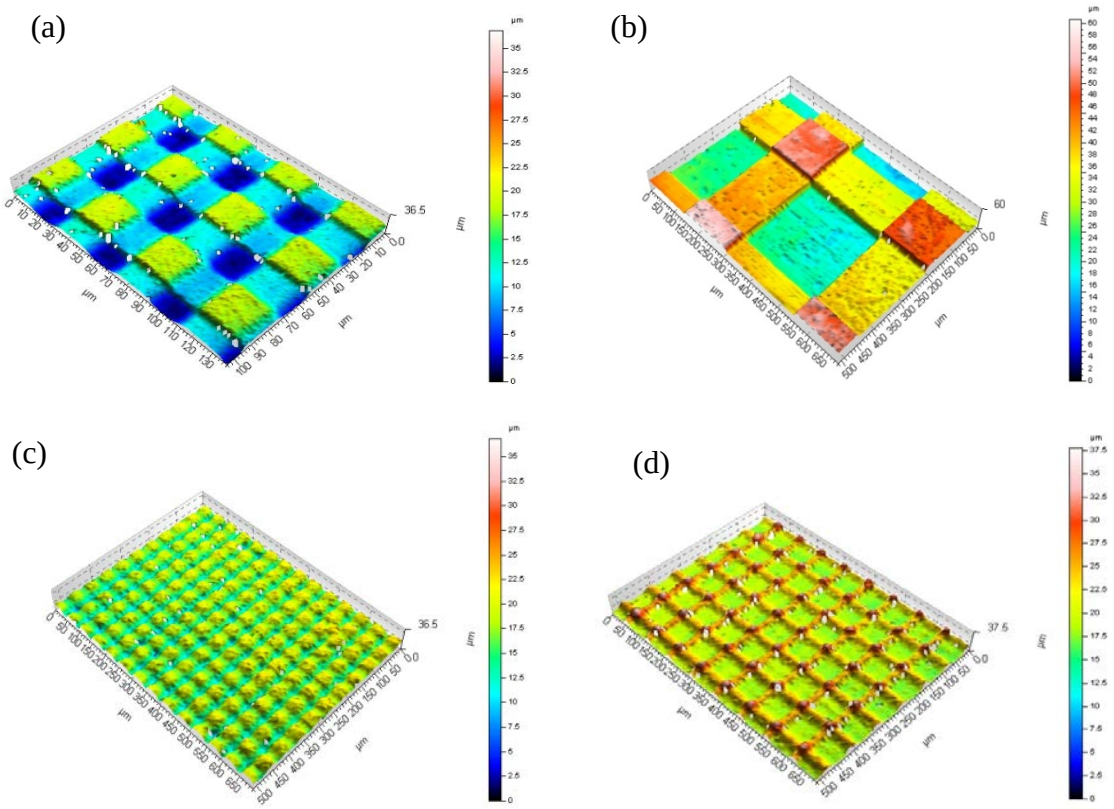

Figure 3.38 Micro pattern structures machined using square masks

Figure 3.38 shows that similar grid-based microstructues can be produced by applying square masks. Compared with circular mask processing, there are three distinct levels of depths on the surface, and sharp edges instead of pits amid the micro patterns. Such structure may potentially help to trap copper plating and therefore improve copper / glass adhesion performance.

Combining Figure 3.38 with Table 3.3, micro pattern features are also determined by either the mask geometrical dimensions or pitch spacing between grooves, and the depth of the machined feature. The micro-roughness component can be controlled by the laser operation parameter settings such as energy density, shots per area and repetition rate. It is noticed that the fine structure as shown in Figure 3.38 (c) can be produced by applying a small mask dimension and small pitch spacing. Fine substrate structures present higher critical loads in scratch testing results and perform better in adhesive strength, all of which will be discussed in Chapter 6.

From the groove study, micro ramp structures can be generated on CMG glass using triangular masks. In this study, three different shapes of triangular masks were attempted to produce pyramid micro structured surfaces. Mask dimensions are shown in Figure 3.39.

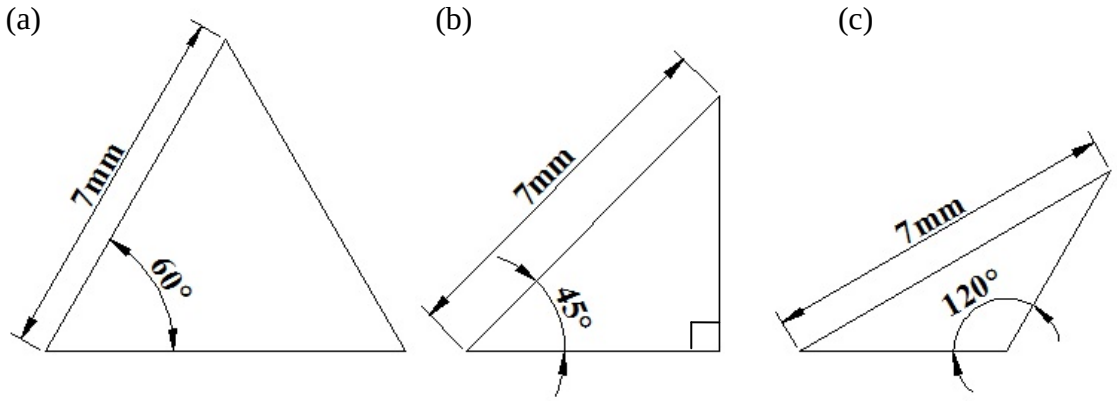

Figure 3.39 Schematic triangular masks

Firstly, equilateral triangular masks with different side lengths were used for machining. One equilateral triangular mask had side lengths of 7 mm (as shown in Figure 3.39 (a)) and the other was 2 mm. Detailed operating parameters are shown in Table 3.4 and surface topography images are shown accordingly in Figure 3.40.

Table 3.4 Processing parameters details for structures shown in Figure 3.40

Sample number	**Side length (mm)**	**Energy density (J/cm^2)**	**Repetition rate (Hz)**	**Shots per area (n)**	**Feature pitch spacing (µm)**
(a)	7	2.4	20	5	250
(b)	7	2.2	10	10	160
(c)	2	2.2	20	5	200
(d)	7	2.2	20	5	100

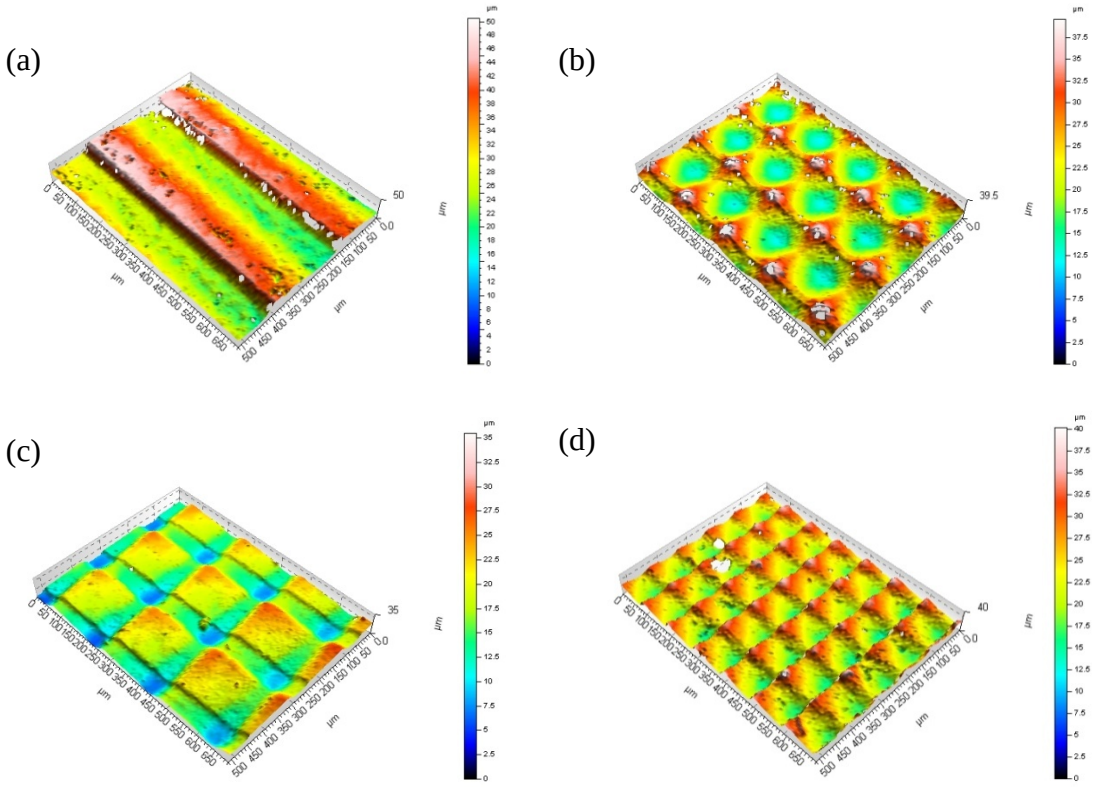

Figure 3.40 Micro pattern structures machined using equilateral triangular masks

Figure 3.40 presents typical micro-ramp and pyramid-based microstructures created on the CMG glass surfaces using equilateral triangular masks. Combining Figure 3.40 with Table 3.4, it can be noticed that: 1) The etched depth of machined features can be controlled by excimer laser processing parameters. 2) Micro-features can be affected by mask geometrical dimensions (i.e. triangle size). 3) Micro-feature dimensions are also related to pitch spacing between adjacent grooves. 4) Notwithstanding, Figure 3.40 (c) and Figure 3.40 (d) were machined with the same mask dimension and the same laser processing parameters, the surface structures are different. The reason is that the mask initial orientation on the mask holder were different, resulting in material ablation directions being different as shown in Figure 3.41. In conclusion, the features of the micro pattern structures are determined by mask geometrical dimension, pitch spacing between adjacent grooves and the mask initial place position.

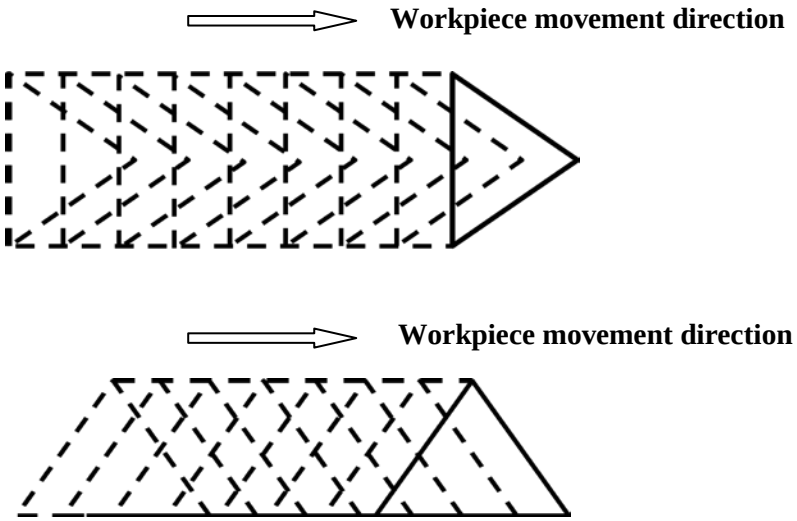

Figure 3.41 Microstructure characteristics determined by mask orientation

These micro ramp structures may be altered by using different triangular mask shapes, so other triangular masks were applied to generate structured surfaces on CMG glass to confirm this hypothesis. Micro ramp pattern structures were generated as shown in Figure 3.42. This micro structure was generated by using an isosceles right-angled triangular mask with a long length of 7 mm as shown in Figure 3.39 (b), energy density of 2.2 J/cm^2, shots per area 5, repetition rate 20 Hz and pitch spacing of 200 µm.

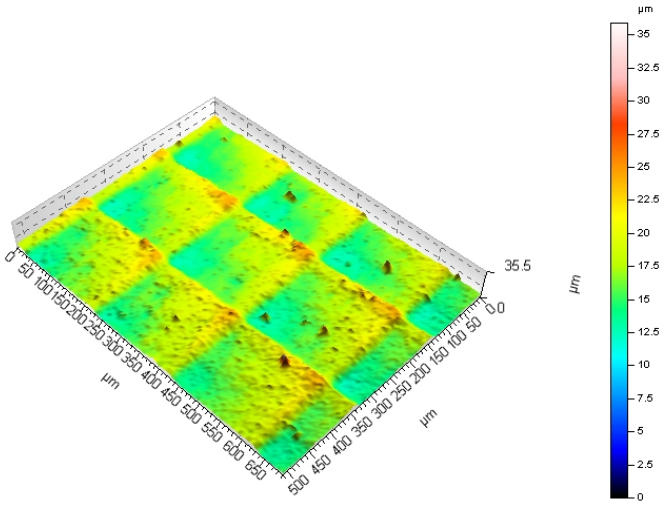

Figure 3.42 Micro pattern structure machined using an isosceles right-angled triangular mask

Another micro structured surface was created as shown in Figure 3.43. This micro structure was generated by using isosceles obtuse-angled triangular mask with a long length of 7 mm as shown in Figure 3.39 (c), energy density of 2.2 J/cm^2, shots per area 5, repetition rate 20 Hz and pitch spacing of 200 µm.

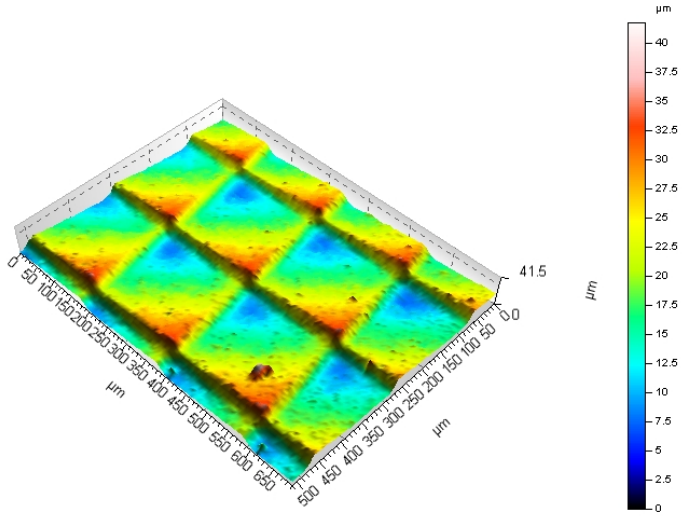

Figure 3.43 Micro pattern structure machined
using an isosceles obtuse-angled triangular mask

From the images shown in Figure 3.42 and Figure 3.43, it can be seen that both isosceles obtuse-angled triangular mask and isosceles right-angled triangular mask can produce micro ramp structures on the glass surface. It is noticed that micro feature dimensions are determined by pitch spacing during the machining process. In these examples, pitch spacings were both set to 200 µm. As a result, micro feature dimensions produced were 200 µm × 200 µm. However, the micro ramp produced by the isosceles obtuse-angled triangular mask is much deeper when using the same laser processing parameters setting.

Micro ramp structures can be produced by triangular masks on CMG glass. Unlike using circular and square masks, the dimensions of the micro pattern structures are not only determined by the mask geometrical dimensions and pitch spacing between adjacent grooves, but also determined by mask orientation. In addition, etched depth of micro features is controlled either by the laser processing parameters or by the shape of the triangular mask. Micro ramp structures may potentially help to increase contact area between the glass substrate and copper coating, and therefore improve copper / glass adhesion performance.

3.4.5.2 Three direction machining

Three direction machining dragging process was divided into three steps. Firstly, the workpiece was mounted on the work stage and moved at a constant velocity (determined by Equation 3-1) controlled by the computer to form the first group of grooves along one direction with a certain pitch spacing (between 30 µm and 700 µm). Secondly, the dragging operation was then repeated after rotating the sample by 60° to produce the second group of grooves by running the same programme. Thirdly, the same structure was machined after rotating the sample by 60° again, this process being shown in Figure 3.44.

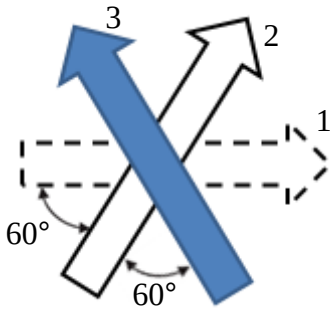

Figure 3.44 Direction of dragging process

An example of three direction 60º machining is shown in Figure 3.45. The equilateral triangular mask identified in Figure 3.39 (a) was chosen to tailor the laser beam, and laser parameter settings for machining were; energy density 2.2 J/cm^2, shots per area 5, repetition rate 5 Hz and pitch spacing of 200 µm.

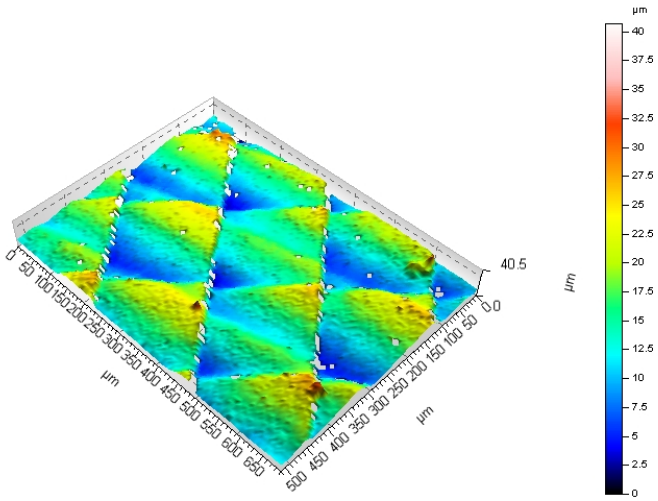

Figure 3.45 Micro pattern structure machined using three direction 60º machining

Figure 3.45 shows that complex micro ramp structures can be generated on the glass surface using three direction 60º machining. Micro feature dimensions are determined by pitch spacing as well. Compared with two direction machining, there are some channels on the micro ramps.

An additional three direction machining method was also attempted. Firstly, work table mounted CMG glass samples were moved at a constant velocity (determined by Equation 3-1) to form a grooved contour along one direction. Then the process was sequentially repeated to create a series of parallel grooves. Secondly, the stage mounted glass sample was rotated by 90º to allow further material ablation. Thirdly, the work table was rotated by 90º again repeating the same parallel groove structue. The samples were machined three times in the orthogonal direction. The dragging process is shown in Figure 3.46.

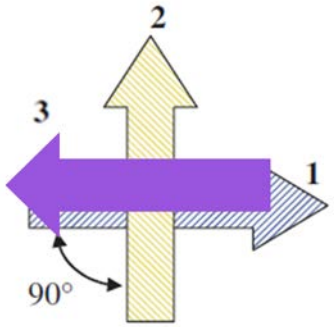

Figure 3.46 Direction of dragging process

The same equilateral triangular mask which was identified in Figure 3.39 (a) and the same laser parameter settings; energy density 2.2 J/cm^2, shots per area 5, repetition rate 5 Hz and pitch spacing of 200 µm, were used for the machining. An example of using three direction 90º machining is shown in Figure 3.47.

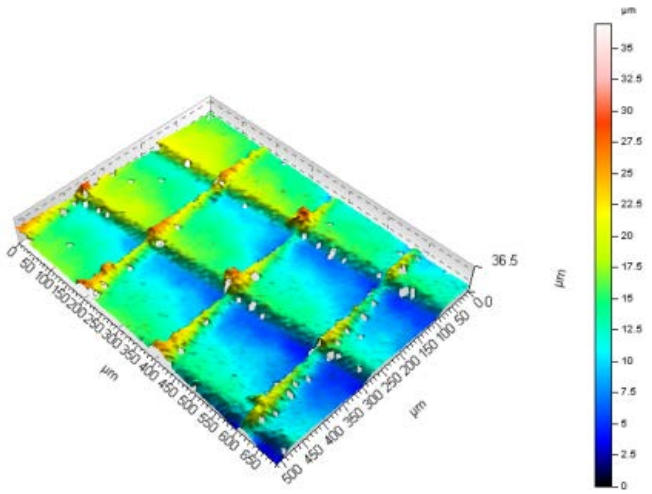

Figure 3.47 Micro pattern structure machined using three direction 90º machining

Figure 3.47 shows that micro blocks and surounding upward and downward ridges were produced on the surface. The dimensions of the micro blocks is approximately 200 µm square, which is the pitch spacing in the laser processing parameter setting. A triangular mask can not only produce micro ramp structures but can also produce micro block structures. This demonstrates that machining direction affects the final machined structure. The structured surfaces shown in Figure 3.46 and Figure 3.47 were machined at the same laser processing setting but with different machining directions.

In the experiment, the lines / spaces of the micro feature produced is affected by apertures on the mask and pitch spacing. Etched depth is determined by laser processing parameters. In order to keep high efficiency, increasing energy density instead of increasing number of shots per area to increase depth of space was adopted.

3.5 Summary

Plasma treatment, chemical etching and mechanical abrasion have been experimentally investigated for the surface modification of glass to generate random surfaces. All have limitations and advantages which are summarised in Table 3.5. It is also noticed that these surface treatment methods provide different surface roughness characteristics. The specific roughened method depends on the application and etched roughness characteristics demands. Bead blasting was eventually chosen to generate random surface texture on glass due to its low cost, simplicity and short manufacturing times.

Table 3.5 Comparison of random surface treatment methods (LU-Loughborough University)

Process	Advantages	Disadvantages
Plasma etching	Available at LU	High cost Time consuming Complexity
HF acid etching	Timesaving Low cost Simplicity Available at LU	Hazardous process Limited control
Grinding paper scratching	Low cost Simplicity Available at LU	Limited control
Micro Sand blasting	Simplicity	High cost Limited control Not available at LU
Bead blasting	Low cost Simplicity Timesaving Available at LU	Limited control

Excimer laser machining was employed to create different structured surfaces on glass because of its remarkable machining quality and accuracy. In this study, the excimer laser has been investigated systematically. Variables relating the effect of excimer laser machining to the laser settings during the machining process, were studied as listed in Table 3.6. A series of experimental results indicated that laser energy density, and shots per area significantly affect the etched depth of machined surfaces. However, repetition rate seems not to contribute much to this. Higher laser energy density, more shots per area and higher repetition rate can improve uniformity of the surface significantly. This chapter also demonstrates the feasibility of using the excimer laser to generate a variety of micro structured surface topography on CMG glass by changing mask dimensions, laser operating parameters (energy density, shots per area and repetition rate), and mask overlapping patterns.

Table 3.6 Excimer laser machining variables and effect

Variables		**Effect**
Mask	Mask dimension	Determine the size of machined features
	Triangular	Generate the grid-based structure
	Circular	Generate the grid-based structure
	Square	Generate the pyramid-based structure
Laser parameter setting	Pulse energy	Determine energy density
	Attenuator position	Determine energy density
	Shots per area	Determine the ectched depth and surface roughness of the machined features
	Repetition rate	Determine the speed of machining process
	Focusing position	Determine the micro-roughness characteristics of machined features
Laser operation process	Pitch spacing	Determine the characteristic of machined features
	Machined direction	

In summary, the following laser parameter settings were identified and used for the majority of glass samples reported in Chapter 6 of this thesis:

- Energy density – 2.2 J/cm^2 or 2.4 J/cm^2.
- Laser output pulse energy – 220 mJ or 250 mJ.
- Attenuator position – 0.8 or 0.9.
- Pulse duration – 20 ns.
- Pulse repetition rate – 10 Hz.
- Shots per area – 5 to 20.
- Pitch spacing – 30 μm to 200 μm.
- Focus position deviation – $\Delta f = 0$ mm.

Chapter 4 Electroless copper plating

4.1 Introduction

Copper with low electrical resistivity, high thermal conductivity, good mechanical properties and high electromigration resistance was chosen to be deposited on the glass to act as interconnect metallization. Electroless plating was chosen because the glass substrate is non-conductive and therefore not suitable for traditional electroplating techniques. Chapter 4 investigates the electroless plating, specifically considering key variables (temperature, time, chemical steps) in order to optimize the process.

4.2 Chemistry and mechanisms

There are two methods of electrodepositing metallic surfaces onto printed circuit boards (electroless plating and electroplating), and it is important to carry out the correct procedures for preparing the substrate surfaces for accepting metallic deposition. Compared with electroplating, electroless plating uses chemical reactions to reduce (deposit) metal ions. So it is not required that the substrate is electrically conductive. But the underlying chemistry and manufacturing operations are more complicated. Electroless plating has its own advantages over electroplating: 1) Uniform deposits are produced on plated components. 2) Electroless deposits are usually less porous than their electrolytic counterparts. 3) Coatings produced by electroless plating often have unique chemical or physical properties [140]. All of these are beneficial for adhesion.

Electroless metallization of glass for electronic packaging has already been studied at Loughborough University [7]. This previous work has investigated the feasibility of electroless copper plating on glass surfaces and explored the method of metallization of the smooth glass surface to improve adhesion, using Circuposit Electroless Cu 4750 [141]. In the study reported in this thesis, the improved electroless copper formula Circuposit™ 3350-1 (for low build applications using Cuposit Y-1 and Cuposit Z-1) was chosen due to its increased process speed and improved copper coating quality. The Circuposit™ 3350-1 electroless copper chemicals are provided by Rohm and Haas Electronic Materials Europe Ltd, developed for printed wiring board applications [142].

The basic electroless copper plating bath contains an oxidizing agent (also the copper source supply), reducing agent, a complexing agent and an alkaline medium. In the electroless copper plating process, the electrons required for the reduction of the metallic cations (Cu^{2+}) are supplied by the reducing agent and not by an external electrical source [143]. Complexing agents control the amount of free metal ions. In an electroless copper deposition process with formaldehyde (HCHO) as the reducing agent, only an alkaline electrolyte can be used [144]. An alkaline solution helps copper deposition and the value of the pH also affects the rate of deposition because the OH group is a reactant in the oxidation of HCHO. Ethylenediaminetetraacetic acid (EDTA) is the complexing agent and sodium hydroxide (NaOH) gives the pH control [145, 146]. The composition of the electroless copper bath is shown in Table 4.1.

Table 4.1 Composition of Circuposit™ 3350-1 electroless copper bath [142]

Component	**Concentration (g/L)**
Copper	2.0
EDTA	30
Sodium Hydroxide	7.5
HCHO	3.0

Electroless copper plating is a thermodynamically favorable and kinetically inhibited process. The two electrochemical reactions, anodic oxidation of a reducing agent and cathodic reduction of metal ions, occur simultaneously with a multistep catalytic redox mechanism [147, 148]. The redox potentials for the oxidation half reaction of formaldehyde at different pH condition and for the reduction half reaction of copper complex ions in solution are shown in Table 4.2.

Table 4.2 Redox potential for anodic and cathodic reactions [146]

Reaction	**Redox potential E (V)**	**pH**
$HCHO + 3OH^- \rightarrow HCOO^- + 2H_2O + 2e^-$	0.190	9
$HCHO + H_2O \rightarrow HCOOH + 2H^+ + 2e^-$	0.056	6
$2HCHO + 4OH^- \rightarrow 2HCOO^- + H_2 + 2H_2O + 2e^-$	0.320	12
$[CuEDTA]^{2-} + 2e^- \rightarrow Cu + EDTA^{4-}$	-0.216	-

The redox potential for the oxidation half reaction becomes larger when the pH of the electroless deposition solution is increased. A thermodynamically favourable reaction occurs when the sum of the standard redox potentials of anodic and cathodic reactions is positive and the change in the free energy is negative since

$$\Delta G^0 = -nFE^0 \qquad 4\text{-}1$$

Where ΔG^0 = change in Gibbs free energy at standard state conditions, *n* = number of electrons per mole product, F = Faraday constant and E^0 = electrode potential of the reaction at standard state conditions.

This is also the reason why in an electroless copper deposition process with formaldehyde as the reducing agent, only an alkaline electrolyte can be used. The electroless Cu deposition is a thermodynamically favourable reaction because the sum of the redox potentials $0.320 + (-0.216) > 0$ and Gibbs free energy $\Delta G^0 < 0$ [146, 148].

While electroless Cu deposition is a thermodynamically favorable process, spontaneous solution decomposition does not occur since the electroless Cu plating process is kinetically inhibited. The difference between redox potentials of the reducing agent and copper is not very large in order to obtain thin copper films without spontaneous copper deposition in the solution. The addition of ligands to the deposition solution can reduce the difference between redox potentials of the reducing agent and metal because of the decrease in the metal redox potential due to complex formation. The activation energy for this reaction is estimated to be about 0.63 eV and therefore it has a low probability of occurring near room temperature [149, 150].

In this study, a magnetic stirring hot plate (IKA RET Basic) with heat control accuracy of ± 1 K was utilized to provide good temperature control of the process. Exclusive beakers for each chemical solution and disposable pipettes were used to prevent contamination. Deionised water was chosen to mix chemical solutions and rinsing samples. Typically six CMG glass samples were bound together (shown in Figure 4.1) as a group to be immersed in the Cu bath at elevated temperature to ensure the concentration of the electroless copper solution was the same to each sample. After plating the samples and removing them from solution, the Cu bath was replaced by a fresh one for the next glass batch.

Figure 4.1 CMG glass samples in the Cu bath

Electroless deposition is a process in which metal ions are chemically reduced at catalytic surface substrates. Typical electroless copper plating procedures include substrate cleaning, catalyst dipping and copper bath dipping. The chemicals used for each step and their respective manufacturer are listed in Table 4.3.

Table 4.3 Chemicals and suppliers

Chemical	**Supplier**	**Application**
Decon 90	Fisher scientific	Substrate cleaning
Methanol (laboratory reagent grade)	Fisher scientific	Silanisation pretreatment
(3-aminopropyl) trimethoxysilane (APTS)	Sigma-Aldrich	Silanisation pretreatment
Circuposit™ 3344	Rohm and Haas Electronic Materials Europe Ltd company	Catalyzation
Circuposit™ 3350-1 (with Y-1 and Z-1)	Rohm and Haas Electronic Materials Europe Ltd company	Electroless copper plating

In this study, the catalyst and copper bath solutions were prepared according to manufacturer's recommendations [142].

4.3 Electroless copper plating procedures

It was desirable to optimize the chemistry of the electroless copper plating on the glass substrate. This was achieved by considering and investigating a number of variables:

- Substrate cleaning with Decon 90
- APTS pretreatment
- Catalyst temperature
- Copper bath temperature
- Copper bath dipping time

The following subsections detail these investigations.

4.3.1 Substrate cleaning

Cleaning is the first step of plating and Decon 90 solution was chosen as the detergent to remove contaminants on the glass surfaces. Previous research had developed a cleaning step that dipped samples into dilute Decon 90 solution (2.67 % concentration) at room temperature for 8 hours [7]. This was time-consuming, so an improved cleaning method was developed. The new cleaning method used non-dilute Decon 90 solution at 60 ºC for 5 minutes as supplied by the manufacturer. After the hot dip samples were rinsed with deionised water to remove any detergent residue. This improved cleaning method dramatically reduced the time for this step.

These two glass cleaning methods have been compared with quantified data generated via contact angle measurement. Contact angle measurement is a method for surface analysis related to surface energy and tension. This method is measured by a contact angle goniometer using an optical subsystem to capture the profile of a pure liquid on a solid substrate. The angle formed between the liquid / solid interface and the liquid / vapour interface is the contact angle. With this method, the relationship between the wettability (ability of a fluid to cover a surface) properties and chemistry of a surface could be demonstrated and the surface free energy determined by measuring contact angles as a function of surface tension of a series of liquids [151-153]. The theories of contact angle measurement are based on Young's

Equation [63], Fox and Zisman Plot [74], Fowkes Equation [76] and Owens-Wendt's Equation [78] as identified in Chapter 1. The contact angle measurement results are summarized in Table 4.4, which are the average values of five measurements for each substrate.

Table 4.4 Contact angle measurement results

Cleaning method	**Contact angle (°) Water**	**Standard deviation**
Uncleaned glass sample [7]	42.5	3.1
Previous cleaning method with diluted Decon 90 at room temperature for 8 hours	19.6	3.8
Improved cleaning method with non-dilute Decon 90 at 60 ºC for 5 minutes	10.8	3.6

The results show the contact angle of the improved cleaning method using non-dilute Decon 90 at 60 ºC for 5 minutes is much smaller than the previous cleaning method (diluted Decon 90 at room temperature for 8 hours). That means the wettability of improved cleaning method is much better than the previous cleaning method. Consequently, the surface is identified as being cleaner.

In order to confirm the effect wettability contributes to electroless copper plating, two bead blasting treated glass samples (Fisher Scientific glass slide) under different cleaning conditions were compared as shown in Figure 4.2. They were both processed with APTS pretreatment solution at room temperature for 1 hour, Circuposit™ 3344 catalyst solution for 5 minutes at 40 ºC, and electroless copper bath for 10 minutes at 46 ºC. Note that a description of APTS is provided in the next section.

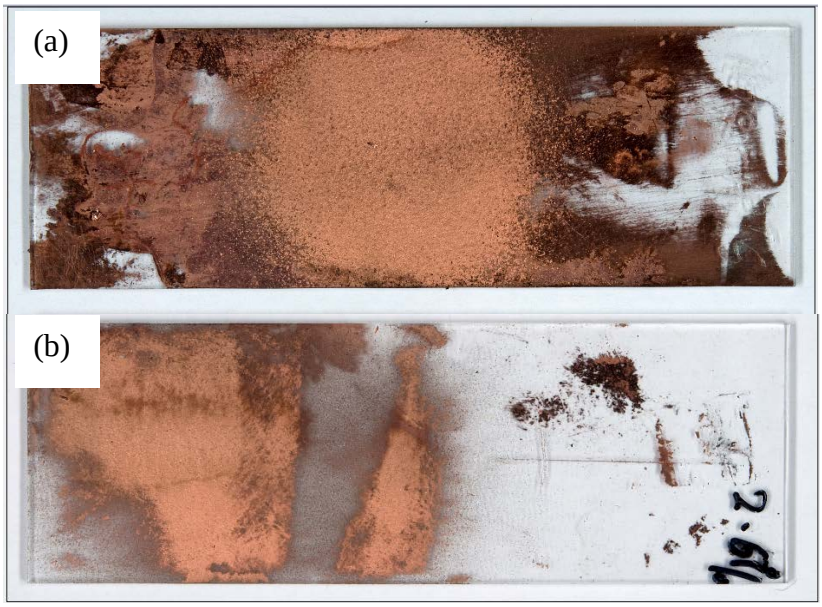

Figure 4.2 Electroless copper plating on glass with different cleaning methods (a) non-dilute Decon 90 at 60 ºC for 5 minutes, (b) 2.67 % Decon 90 at room temperature for 8 hours

It should be noted that the area of interest is only the bead blasted area on each glass slide when judging the efficiency and coverage of copper plating. From the Figure 4.2, it can be seen that the improved cleaning method not only shortens the time of the cleaning step but also enhances the wettability of the surface, hence resulting in more copper deposition. As a result, the improved cleaning methods (using non-dilute Decon 90 at 60 ºC for 5 minutes) were adopted for all samples instead of the previously referenced cleaning method.

4.3.2 Pretreatment study

It is difficult for glass metallization especially on smooth surfaces due to the incompatibility of physical, chemical and mechanical properties between the highly stiff, brittle glass substrate and the metallic coating [150]. Pretreatment is necessary before catalyst dipping for electroless copper deposition on glass due to the difficulty of metallization of the glass surface. Some pretreatment methods such as mechanical abrasion, plasma treatment, chemical etching and silanisation can be used for physical or chemical modification of the glass substrate surface to improve the attachment of palladium catalyst particles [150, 154].

In previous studies, (3-aminopropyl) trimethoxysilane (APTS) [NH_2 - $(CH_2)_3$ - $Si(OCH_3)_3$] was chosen to form a self-assembled monolayer (SAM) to change the chemical functionality

of the surface [155, 156]. The glass samples were immersed in a 5×10^{-3} mol/L solution of APTS with a mixture of methanol (95 %) and water (5 %), at room temperature for 1 hour. As shown in Figure 4.3, the SAM consists of a head group ($-Si(OCH_3)_3$) which couples to the glass surface to pack together thereby exposing the tail group (e.g. NH_2) at the surface so that it may couple well with the catalyst particles providing a base for deposited copper [154].

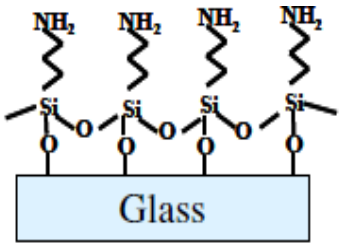

Figure 4.3 Self-assembled monolayer on a glass substrate

The influence of pretreatment methods comes from either physical morphology or chemical bonding state modification as shown in Figure 4.4. Previous researchers claimed the role of the APTS self-assembled monolayer was essential to enable electroless plating of the smooth glass because it could improve the adsorption of the palladium based catalyst on the glass surface [7]. In this study, textured surface production (by excimer laser machining or bead blasting) has been used as one of the pretreatment methods for physical surface modification that roughens the glass surface to improve catalyst attachment for copper coating deposition.

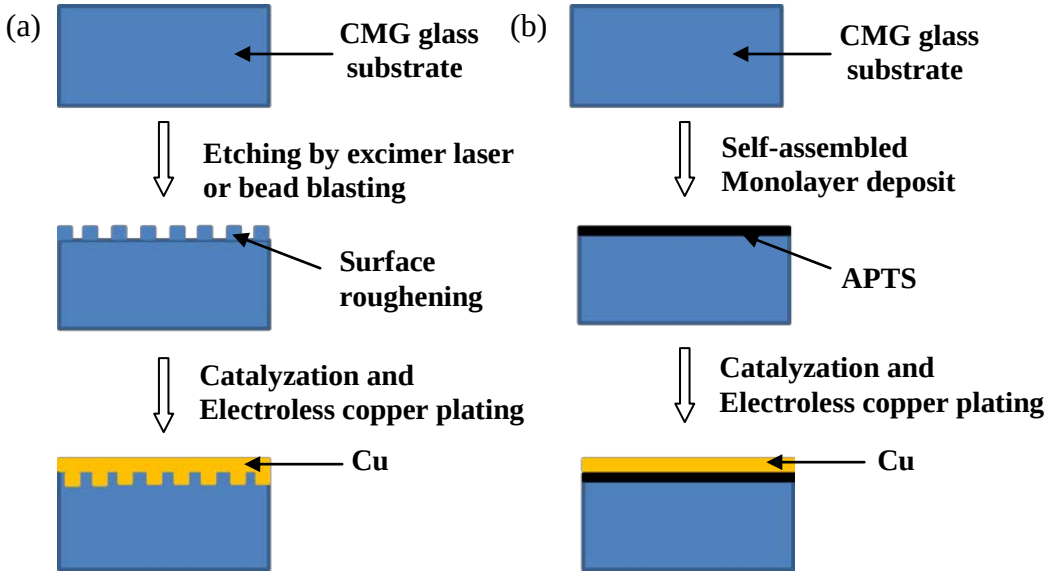

Figure 4.4 Electroless copper plating on glass using different pretreatments
(a) Surface roughening pretreatment, (b) APTS chemical pretreatment

In order to investigate the effect of surface roughening pretreatment on electroless copper plating, a bead blasted glass sample was plated without APTS pretreatment. This sample used the improved cleaning method, dipped in Circuposit 3344™ catalyst solution for 5 minutes at 40 ºC and electroless copper bath for 10 minutes at 46 ºC. The result is shown in Figure 4.5.

Figure 4.5 Electroless copper plating on roughened CMG glass without APTS pretreatment

Figure 4.5 suggests that the electroless copper chemical is strong enough to bond well to roughened glass surfaces without APTS pretreatment. In the context of this research APTS pretreatment was identified as not being an essential step for electroless copper plating on a roughened glass substrate. Hence APTS dipping was not used for excimer laser machining and bead blasting treatment samples in the later coating / scratch testing experimentation. Therefore, the results of all samples are comparable relative to each other.

4.3.3 Catalyst study

Catalyzation is essential to the electroless copper plating because copper deposition only occurs on an active surface. The Gibbs free energy diagram in Figure 4.6 shows that a catalyst can reduce the potential barrier for electroless copper deposition. The standard redox electrode potential relates to the Gibbs free energy (ΔG), and the potential barrier (Ea) which exists between the reactants and the products prevents spontaneous solution decomposition. The potential barrier can be reduced from Ea to a lower activation energy E* by the formation of reactive intermediate species on the catalytic surface [157].

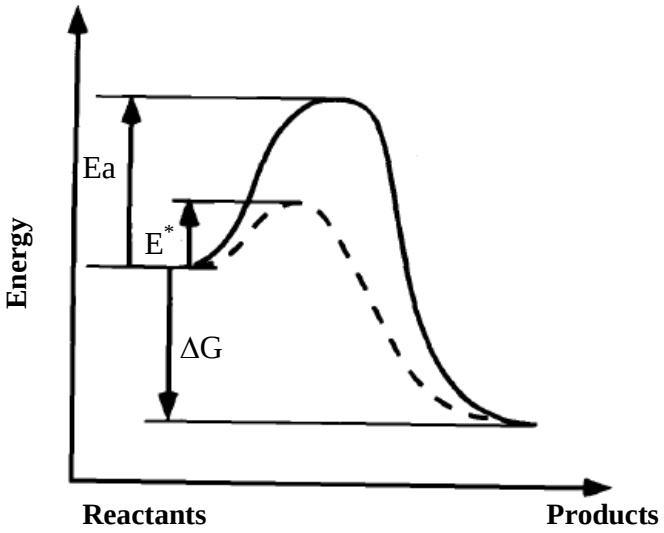

Figure 4.6 Gibbs free energy diagram [157]

The catalyst enables the reducing agent to react on the surface and perform as an electron carrier which transfers the electrons from the reducing agent to the metal ions. The different catalyzation methods have been compared and reviewed in the literature [143]. In this study, Circuposit™ catalyst 3344 was used. This is a colloidal palladium-tin catalyst which ensures reliable coverage and adhesion of electroless copper. The Pd^{2+} species is chemically reduced to the Pd^{0} state by the Sn^{2+} species, according to the following redox reaction [143, 158]

$$Sn^{2+} + Pd^{2+} \rightarrow Sn^{4+} + Pd^{0} \qquad 4\text{-}2$$

Under the catalytic action of palladium, metal cations are deposited into a metal layer by capturing electrons furnished by a reducing agent. Tin not only acts as the reducing agent for the Pd ions, it is also claimed to stabilize the small Pd nuclei (on the order of some nanometres in size) once they form, via strong specific Sn^{4+} adsorption [7].

In order to find out the effect of the catalyst operating temperature and moreover identify the optimal operating temperature, a series of experiments at different catalyst temperatures were carried out. The photograph images of copper metallization results are shown in Figure 4.7. All the microscope slide glass samples were bead blasting treated and used the improved cleaning method, dipping in Circuposit 3344™ catalyst solution for 5 minutes and electroless copper bath for 10 minutes at 46 ºC. However, catalyst operating temperatures varied; 30 ºC,

33 ºC, 36 ºC, 40 ºC, 43 ºC to 46 ºC. After immersion in the Pd activation solution, the samples were rinsed with deionised water.

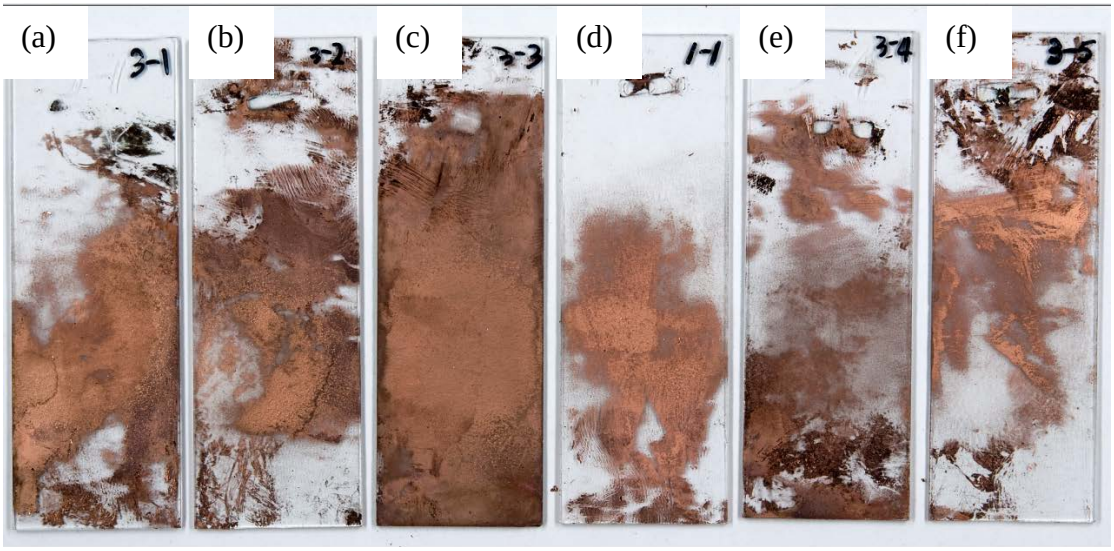

Figure 4.7 Electroless copper plating on glass at different catalyst temperatures
(a) 30 ºC, (b) 33 ºC, (c) 36 ºC, (d) 40 ºC, (e) 43 ºC, (f) 46 ºC

This study suggested that the catalyst operating temperature can affect plating quality. When the catalyst solution temperature is 36 ºC, the catalyst is more active and more copper is deposited on the surface of glass. This temperature is within the operating temperature range from 30 - 40 ºC on the chemical data sheet [142]. As a result, 36 ºC was the optimum operation temperature for catalyst chosen in this study.

It should also be identified that besides the solution temperature, the concentration of the catalyst is also a key parameter for copper deposition. The recommended concentration range of Circuposit™ catalyst 3344 is 1.5 % - 3 % by volume, and increasing catalyst concentration can dramatically improve the copper plating process. Firstly, a visible grey layer was formed on the surface of glass samples after removal from the catalyst solution. Secondly, plenty of bubbles were generated on the surface when the samples were dipped in the Cu bath. The bubbles formed in the chemical reaction were hydrogen which is discussed in the next section.

4.3.4 Copper bath study

Circuposit™ 3350-1 was chosen as the electroless copper solution in this study because of its increased process speed and improved copper coating quality. Electroless deposition is a

process in which metal ions are chemically reduced at catalytic surface substrates. The reducing agent supplies electrons to this surface and the metal ions receive these electrons to be reduced to a zero oxidation state. Circuposit 3350-1 electroless copper bath is based upon EDTA as the chelate. Copper deposition in a HCHO based plating bath with EDTA as the complexing agent is generally expressed as the chemical reaction shown below [159]:

Anodic oxidation reaction

$$2HCHO + 4OH^- \rightarrow 2HCOO^- + 2H_2O + H_2 + 2e^- \qquad 4\text{-}3$$

Cathodic reduction reaction

$$Cu(EDTA)^{2-} + 2e^- \rightarrow Cu + EDTA^{4-} \qquad 4\text{-}4$$

Overall chemical reaction

$$Cu(EDTA)^{2-} + 2HCHO + 4OH^- \rightarrow Cu + H_2 + 2H_2O + 2HCOO^- + EDTA^{4-} \qquad 4\text{-}5$$

Previous work has investigated electroless Cu deposition properties in relation to the chemical concentrations in the deposition solutions as well as on the deposition solution operating conditions including pH value and temperature [148]. The results of the study are summarized in Table 4.5. The electroless Cu deposition temperature has the strongest effect on deposition rate and resistivity of electroless Cu films. The high deposition rate of low resistivity electroless copper coating can only be achieved in a certain range of deposition temperatures.

Table 4.5 Electroless Cu deposition rate and resistivity versus deposition solution parameters [148]

Solution parameters	Effect on deposition rate	Effect on resistivity
$CuSO_4 \cdot 5H_2O$ concentration increases	Increases	Increases
HCHO concentration increases	Increases	Increases
EDTA concentration increases	Independent	Independent
pH (11.8-12.2)	Increases	Decreases
pH (12.2-12.8)	Independent	Independent
pH (>12.8)	Unstable solution	Unstable solution
Temperature	Increases	Decreases

In this study, chemical concentrations and pH value of the electroless copper solution were all fixed and used the recommended values as shown in Table 4.1. However, the copper bath operation temperature and dipping time needed to be optimized in the process.

4.3.4.1 Copper bath temperature effect study

In order to investigate the optimal operational temperature for the electroless copper bath, a series of samples at different copper bath temperatures were carried out. Images of copper metallization results are show in Figure 4.8. All the microscope slide glass samples were bead blasted and used the improved cleaning method, dipped in Circuposit™ 3344 catalyst solution at 40 ºC for 5 minutes and electroless Cu bath for 10 minutes. However, Cu bath operating temperatures of 40 ºC, 42 ºC, 44 ºC, 46 ºC, 48 ºC and 50 ºC were investigated.

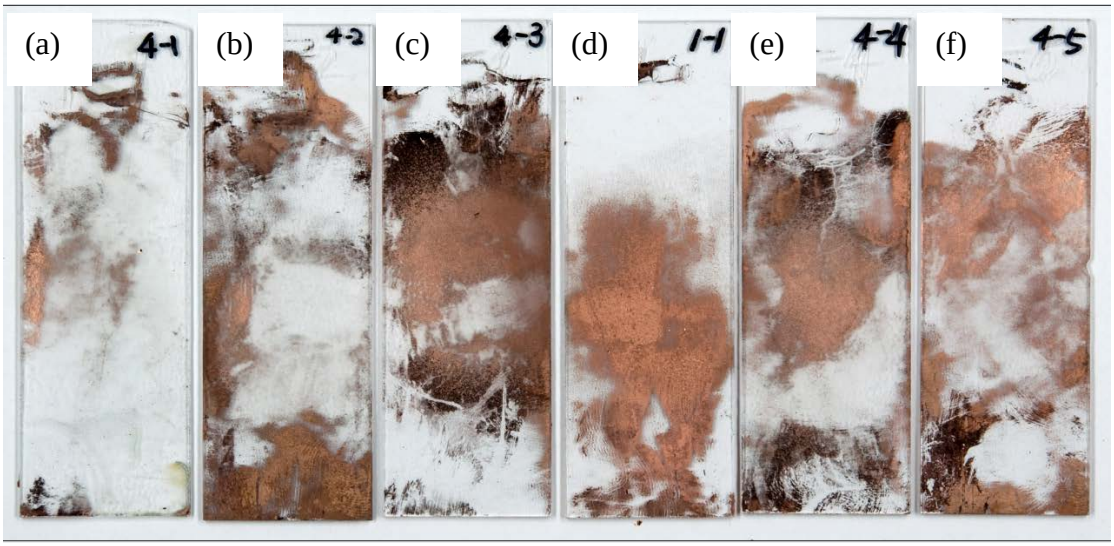

Figure 4.8 Electroless copper plating on glass at different Cu bath temperatures
(a) 40 ºC, (b) 42 ºC, (c) 44 ºC, (d) 46 ºC, (e) 48 ºC, (f) 50 ºC

Comparing the results in Figure 4.8, it can be seen that there is little copper deposit on glass when the temperature is 40 ºC. When the temperature of the bath solution is raised, more copper is deposited onto the blasted area on the glass surfaces. There is maximum deposition at 46 ºC but when the temperature is over 46 ºC, copper deposition reduces gradually. As a result, 46 ºC was the optimal copper bath solution temperature identified for this study and subsequent experimentation.

4.3.4.2 Dipping time effect study

In order to investigate the relationship between coating thickness and dipping time in electroless copper solution, a series of experiments for glass samples at different dipping times in the copper bath were carried out. Images of copper metallization results are shown in Figure 4.9. All the glass samples were bead blasted and used the improved cleaning method, dipped in Circuposit 3344 catalyst solution at 40 ºC for 5 minutes and electroless copper bath at 46 ºC. However, different dipping times of 5, 10, 15, 20 and 25 minutes were applied.

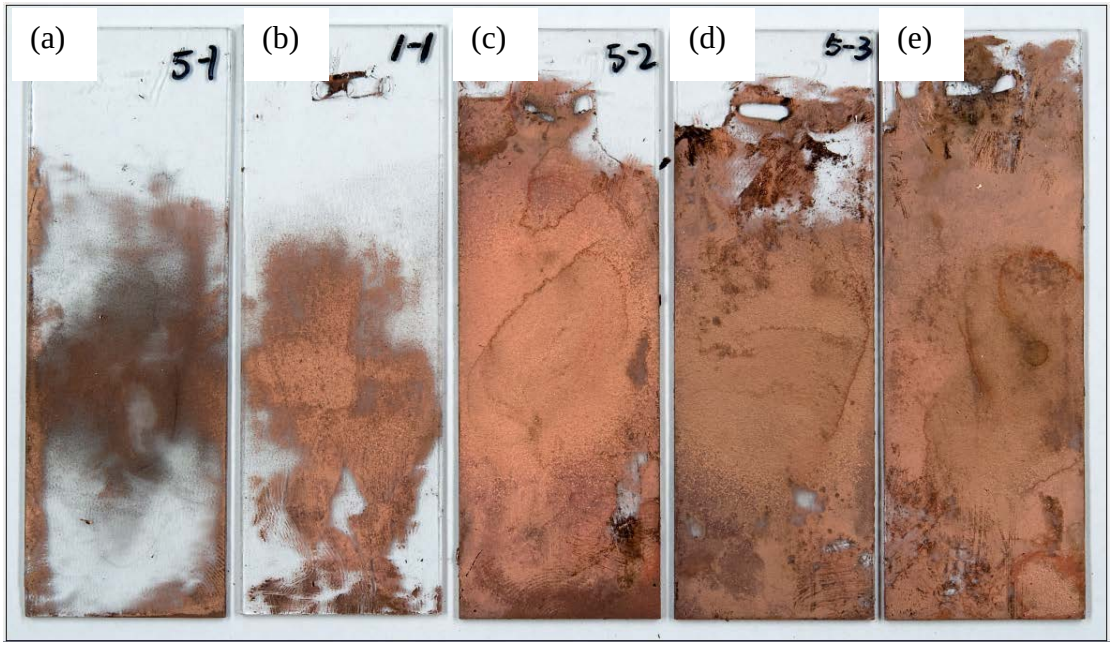

Figure 4.9 Electroless copper plating of CMG glass at different dipping time in Cu bath (a) 5 min, (b) 10min, (c) 15 min, (d) 20 min, (e) 25 min

These results in Figure 4.9 demonstrated that copper deposition on the surface of glass increased with dipping time in the electroless copper bath. Calibration graphs of the relationship between coating thickness and dipping time in electroless copper solution were made not only for glass but also for other substrate materials such as mild steel coins and FR4 circuit board samples, for comparative reasons.

This experimentation started with mild steel because it was straightforward to obtain a relatively flat surface (*Sq* = 15.4 nm). Mild steel coin samples were prepared through grinding and polishing to achieve a smooth surface. Each coin was half masked with tape before dipping into the electroless copper solution for metallization. After plating, a step was generated after peeling off the tape. This step height is the coating thickness after dipping for a designed time as shown in Figure 4.10.

Figure 4.10 Copper coating step on steel coin sample

A Taylor Hobson CLI 2000 with a contact stylus (tip angle 90° and tip radius 2 µm) was utilized to measure and analyse the surface step height. The data was generated by the average of five measurement results of the height of the step which was calculated automatically by the software, when the stylus tip drew a line across the step. The graph of coating thickness versus dip time for the mild steel coins is shown in Figure 4.11, with standard deviation error bars.

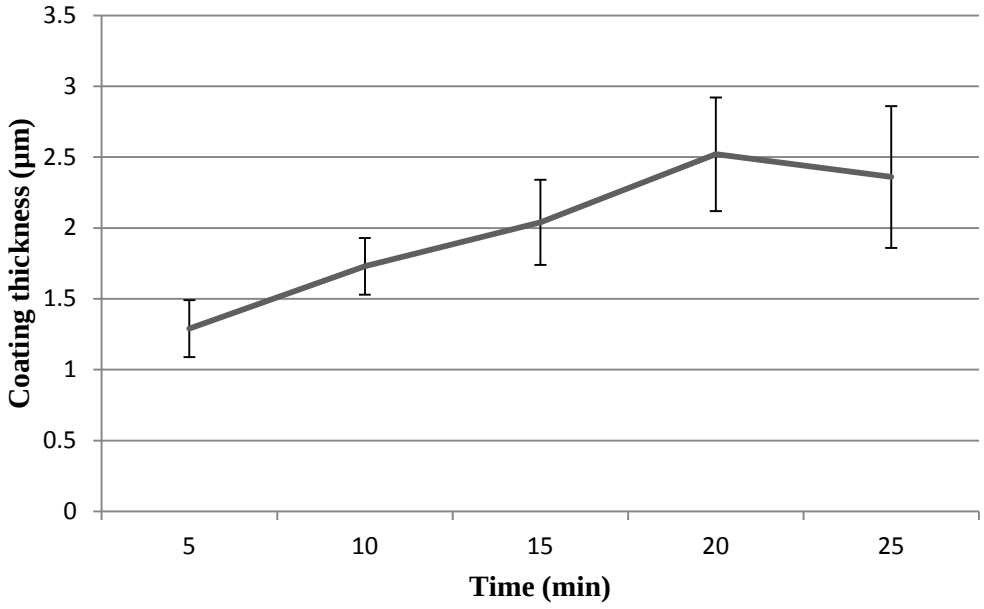

Figure 4.11 Coating thickness versus dipping time
in the Cu bath for mild steel coin substrates

From Figure 4.11, it can be seen that there was a linear relationship between coating thickness and dipping time when the plating time was less than 20 minutes. However, coating thickness appeared to decrease with longer dipping times.

In order to further confirm this hypothesis, another substrate material (circuit board FR4) was chosen to make calibration graphs because it is a common substrate material for electronic packaging manufacture. The samples were also half taped to create a step between the copper coated surface and original uncoated surface. Then the contact stylus was utilized to measure the step heights. The data was generated by the average of five measurement results of the height of the step which was calculated by the software automatically, when the stylus tip drew a line across the step. The relationship graph for the circuit board sample is shown in Figure 4.12, with standard deviation error bars.

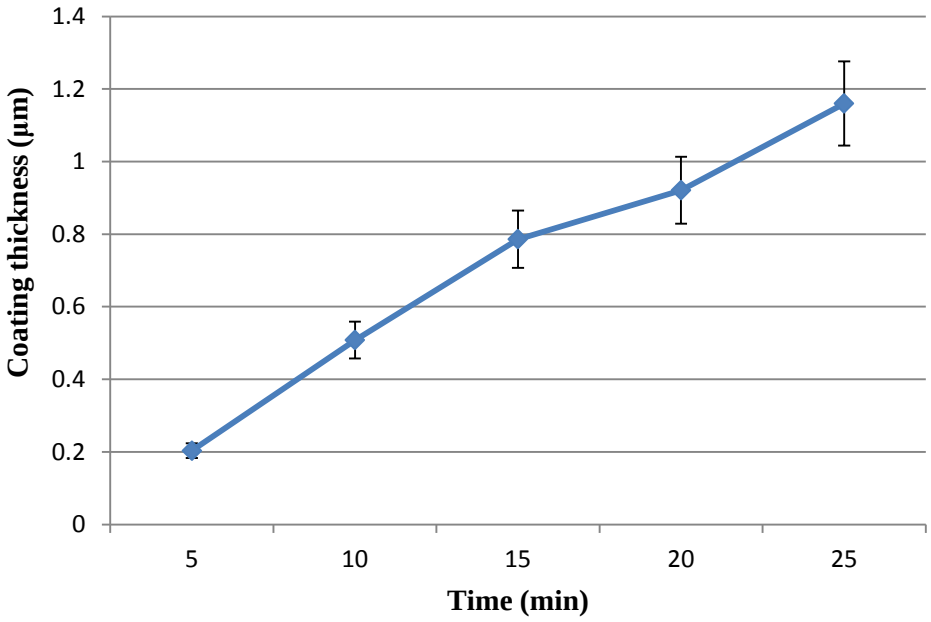

Figure 4.12 Coating thickness versus dipping time
in the Cu bath for circuit board substrate samples

From Figure 4.12, it can be seen there was an approximate linear relationship between coating thickness and dipping time for the circuit board samples. In this case, coating thickness increased up to and including 25 minutes because coating thickness had not reached the 2.5 µm limit. Comparing these two substrate materials (steel and FR4), aggradation rates were different and deposit rate on the metal surface was much greater than that of the

polymer. Copper thickness deposited onto mild steel coin surfaces could reach 2.5 µm in 20 minutes whereas for a circuit board sample, copper only deposited about 1.2 µm in 25 minutes.

The following work concentrated on making the calibration graph for glass. It is more challenging for two reasons. Firstly, it is difficult to deposit copper on smooth glass surfaces so the samples needed to be roughened before electroless copper plating. This work was carried out by bead blasting to produce random surfaces on glass. Secondly, how to measure coating thickness on roughened glass is the other issue, because the tape does not work well when the surface is not flat, because the Cu solution leaches under the tape. In this case, one section of Cu coated samples (about a half length) were dipped into 25 % nitric acid (HNO_3) solution for 2 minutes to remove the Cu sectional coating. As a result a step between the copper coated surface and original surface was formed. This step was then measured using the stylus technique. The data was generated by the average of five measurement results of the height of the step which was calculated by the software automatically, when the stylus tip drew a line across the step. Deposition efficacy and thickness of coating are illustrated as shown in Figure 4.13, showing increasing plating coverage and thickness as a function of time, with standard deviation error bars.

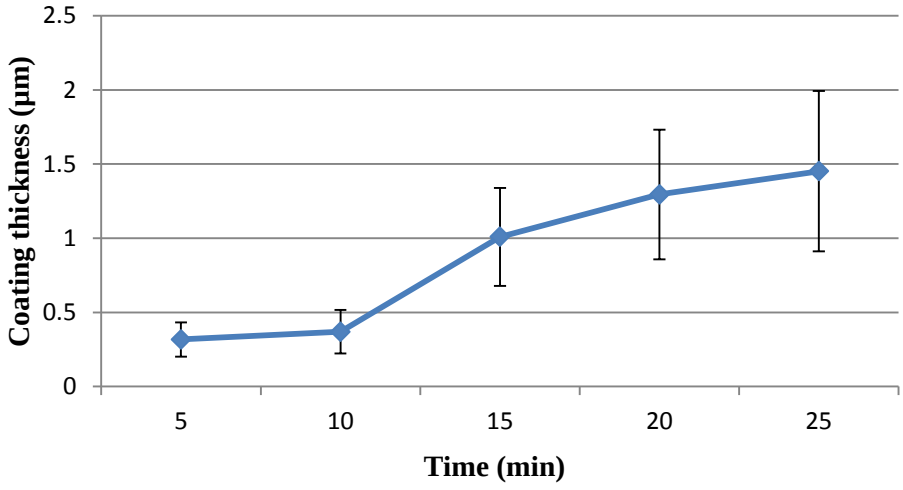

Figure 4.13 Coating thickness versus dipping time in Cu bath for glass substrate samples

From Figure 4.13, it can be seen that copper thickness increased with dipping time. However, copper thickness increased slowly when the dipping time was less than 10 minutes. Then the

aggradation process was much quicker after 10 minutes. There is an approximate linear relationship between coating thickness and dipping time from 15 minutes to 25 minutes. From the result, 15 minutes dipping time is identified as the optimal dipping time for the future plating on CMG glass. The coating thickness is approximately 1 µm which can cover the underneath roughened surfaces on glass for later scratch testing.

4.3.5 Process optimization

The basic procedure for electroless copper plating on roughened CMG glass in this research is illustrated in Figure 4.14 and can be summarized as:

- Glass roughened by either excimer laser or bead blasting pretreatment
- Substrate cleaning with non-dilute Decon 90 and followed by deionised water rinse.
- Catalyst solution to activate the glass surface and followed by deionised water rinse.
- Final dip of the treated glass substrates in electroless copper bath followed by final deionised water wash and dry.

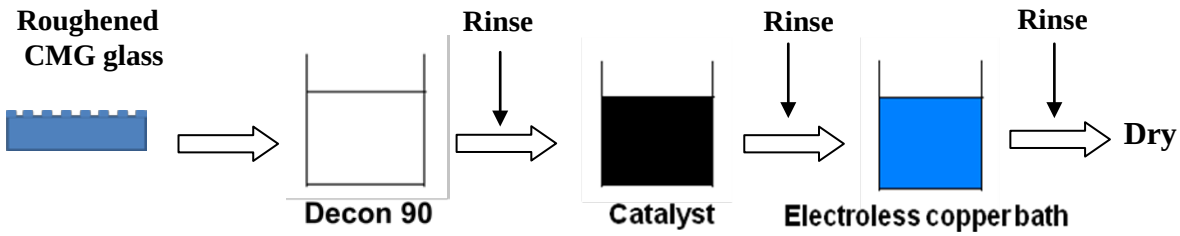

Figure 4.14 Schematic procedure of electroless copper plating for smooth CMG glass

It was noticed that final rinse and dry were essential to the electroless copper plating process to remove any residual chemicals and prevent coating oxidation. An example of a coated sample without thorough rinsing and drying is shown in Figure 4.15. Oxidation changes the color of the copper coating.

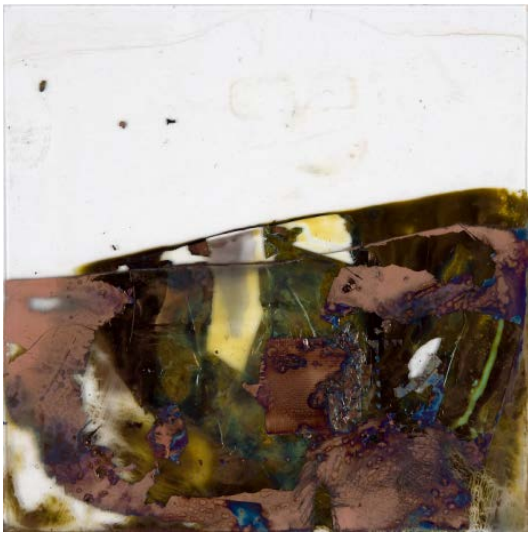

Figure 4.15 Oxidation of the copper coating on CMG glass

4.3.6 Plating on machined CMG glass

Figure 4.16 shows the images of CMG glass samples removed from the Cu bath. It can be seen that the large pieces of copper film which were originally attached to the smooth glass surface came off easily, especially after washing with deionised water, but with copper firmly adhered on the machined substrate regions. The reason was discussed in Section 4.3.2.

Figure 4.16 CMG glass samples being removal from the Cu bath

Examples of copper plating on roughened glass patches are shown in Figure 4.17. Based on the knowledge and experimental scheme identified, CMG glass with micropattern structured surfaces and random surfaces were plated with copper after the surface topography measurement.

Figure 4.17 shows that copper preferentially deposits on the roughened areas rather than the smooth surfaces. The copper coating which is deposited on the surface of samples is uniform in colour. Detailed processing parameters of the machined examples shown in Figure 4.17 are listed in Table 4.6.

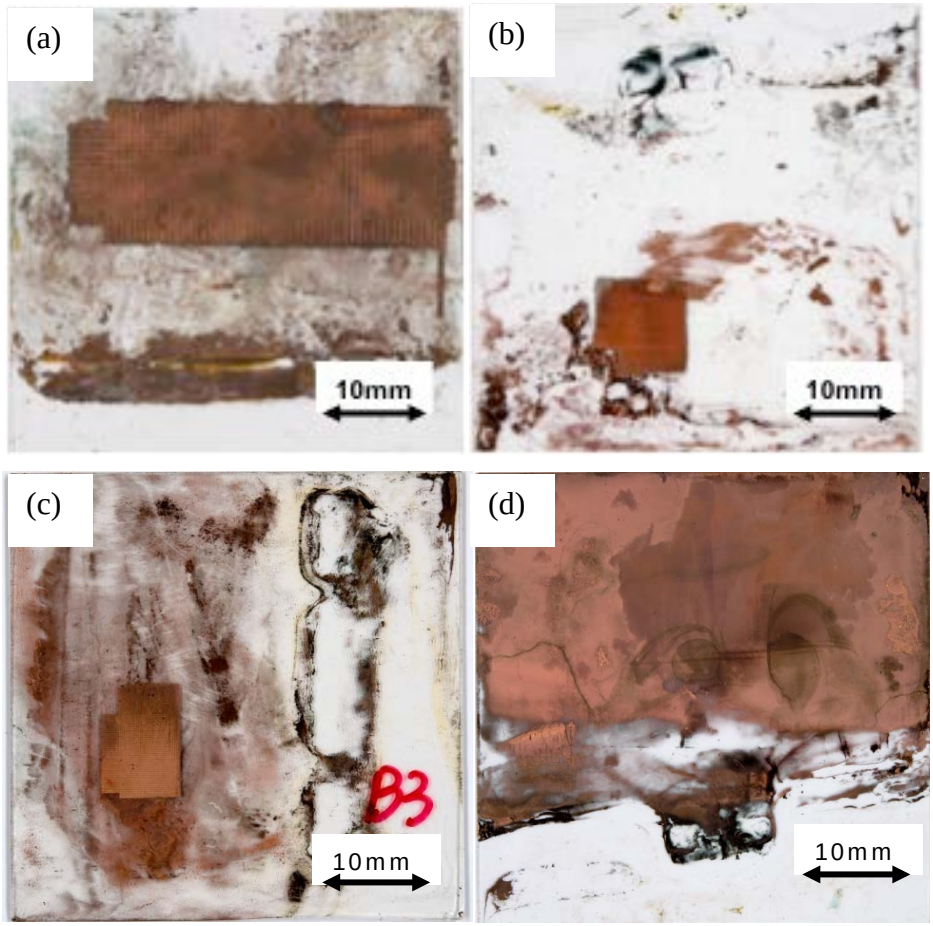

Figure 4.17 Electroless copper plating on CMG glass

Table 4.6 Processing parameter details for plated CMG glass samples shown in Figure 4.17

Sample number	**Surface pretreatment method**	**Processing parameters**				
Structured surfaces	Excimer laser	**Mask diameter (mm)**	**Energy density (J/cm^2)**	**Repetition rate (Hz)**	**Shots per area (n)**	
(a)		7	2.4	20	15	
(b)		5	2.4	10	5	
(c)		2	2.4	10	10	
Random surfaces	Bead blasting	**Exposure time (s)**		**Nominal size range of glass bead (µm)**		
(d)		2		75-150		

4.4 Summary

The whole electroless copper plating process was studied systematically. All the major steps including cleaning, pretreatment, catalyst and electroless bath were investigated individually. From the results, the optimal experimental conditions were identified and all the variables were attempted. Final plating experimental procedure was established and is identified in Table 4.7.

Table 4.7 Experimental procedure for electroless copper plating on CMG glass

Step	Process	Solution	Time	Temperature
1	Cleaning	Decon 90 (non-dilute)	5 minutes	60 ºC
2	rinse	Deionised water	3-5 minutes	room temperature
5	catalyst	Circuposit 3344	5 minutes	36 ºC
6	rinse	Deionised water	3-5 minutes	room temperature
7	Electroless copper	Circuposit 3350-1	15 minutes	46 ºC
8	Rinse and dry	Deionised water	10 minutes	room temperature

Chapter 5 Scratch testing on plated glass

5.1 Introduction

The quality of copper plating on glass requires quantitative testing to measure bond strength. This data can then be used to correlate against areal parameters. Chapter 5 examines the various methods for testing plating bond strength and concentrates specifically on scratch testing. Issues concerning testing set-up and variables are discussed, as well as the relationship between the interaction of the instrument and the surfaces.

5.2 Adhesion test method

5.2.1 Test methods review for coating adhesion

Testing for adhesive bonding is useful in checking the adhesion performance and in determining the adequacy of copper coating strength. The most commonly used measurement methods for coating adhesion are listed in Table 5.1 [160, 161]:

Table 5.1 Summary of the most commonly used test methods for coating adhesion

Test methods	Advantages	Disadvantages
Peel test	1) Simple and reliable test 2) Ease of sample preparation	1) For coatings on substantially flat surfaces 2) Does not provide quantitative values of adhesion 3) Applicable only to tough flexible coating
Pressure-sensitive Tape test	1) Simple and cheap test 2) Ease of sample preparation	1) Results tend to be qualitative only 2) The adhesive strength of the tape must be greater than that of the coating.

Table 5.1 Continued

Test methods	Advantages	Disadvantages
Pull test	1) Applicable to a wide variety of coating and substrates 2) Simple and cheap test	1) Difficult data analysis, especially for quantitative measurements 2) Rapid uncontrollable failure mode 3) Wide scatter in data
Indentation debonding test	1) Applicable to a wide variety of coating /substrate systems 2) Provide a quantitative rate 3) Quick and simple test 4) Ease of sample preparation	1) Rate the sample adhesion by fracture and delamination pattern around the indent 2) Difficult quantitative analysis
Scratch testing	1) Provide quantitative values 2) Quick and simple test 3) Ease of sample preparation	1) Care is needed when defining the damage type 2) Mechanically complex

Based on Table 5.1, scratch testing is the most effective quantitative assessment of adhesion strength between the copper coating and CMG glass substrates. This method can provide quantitative values for evaluating adhesion performance, furthermore, the simplicity of the test and ease of sample preparation also make scratch testing the most effective method for adhesion evaluation.

5.2.2 Failure mechanisms related to adhesion

Scratch testing was introduced in the 1950's as a qualitative test of adhesion [162]. Existing researchers have demonstrated correlation of coating adhesion measurement by scratch testing with adhesive bond strength, through a number of proposed failure models [163].

Some progress has been made for the scratch adhesion test regarding the relationship between work of adhesion and the critical load for coating detachment. Benjamin and Weaver [164] performed the first analysis of the mechanics of the scratch testing in 1960 using the theories developed for fully plastic indentation, giving a simple relationship between the shearing force at the coating / substrate interface and the Vickers hardness of the substrate. This model was later modified by Weaver, but was insufficient to describe the behaviour of most practical coatings [165]. Later Laugier [166, 167] suggested that the adhesion behaviour could be modelled in terms of the strain energy released during removal of the coating using

a Griffith energy balance approach. The coating ahead of the indenter can reduce its stored elastic energy by detachment from the substrate at the critical load. However, this model was insufficient to describe the stresses for materials where some plasticity occurred. Burnett and Rickerby identified three contributions (an indentation term, an internal stress term and a frictional term) to the stresses responsible for coating detachment [168], whilst Bull *et al*. more recently suggested that scratch adhesion testing, could be represented as the sum of these three contributions [169-171]. This illustrates the importance of some plastic deformation at the crack tip during the coating removal process. Chen *et al*. have proposed a further model for assessing the adhesion of very thin (<100 nm) coatings on glass [172].

Although a range of possible failure modes were proposed, none of them could reflect the reality of failure occurring when a stylus tip crosses a coated surface, due to the complexity of the scratch testing. In some cases more than one failure model can occur and not all of them are dependent on adhesion. Other failure modes may occur which depend on plastic deformation and fracture within the coating, rather than any adhesive failure at the coating / substrate interface. As a result, failure models were not explored and employed in this study and only critical load was regarded as representative of coating adhesion.

5.2.3 Scratch testing

In scratch testing, a diamond stylus is drawn across the coated surface by a constant or increasing load against the sample until failure occurs. The increasing load applied to the stylus is either stepwise or linearly increased. Scratches can be single or multi pass. Coating failure is defined at the point where surface defects are visually identified, at a load which is often termed the critical load, *Lc*, however the failure point identification can be very subjective [161]. Figure 5.1 shows a representation of the scratch testing method.

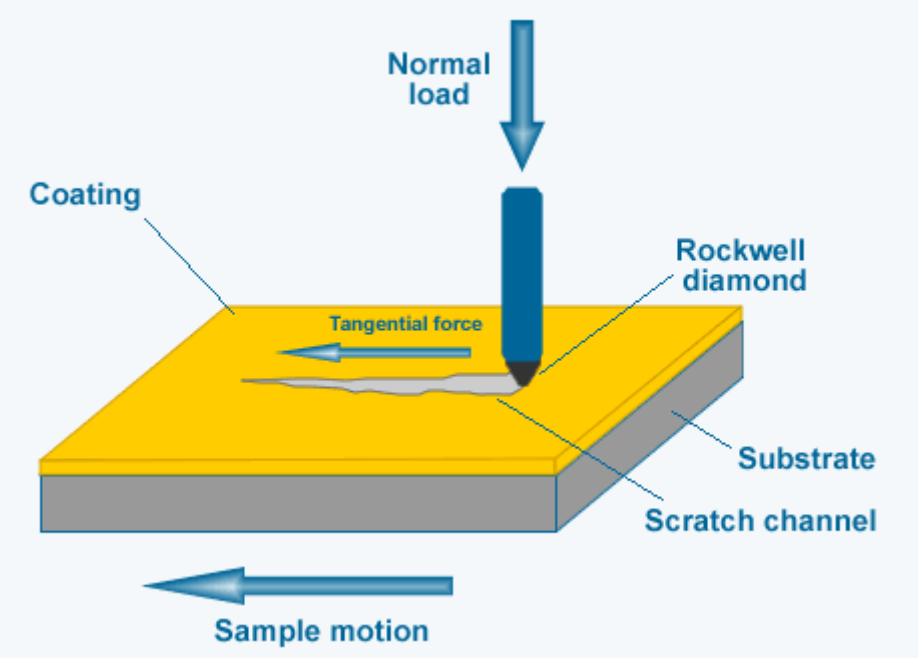

Figure 5.1 Schematic showing the scratch testing

The scratch testing is relatively quick (typically a few minutes for a single scratch) and simple to undertake, however considerable care is needed when defining the failure type that is used to determine the critical load values. There is a well-defined delamination mode present under the scratch as shown in Figure 5.2. Damage patterns on the surface can be correlated with acoustic emission and friction forces to derive the critical loads at which various failure mechanisms occur [161].

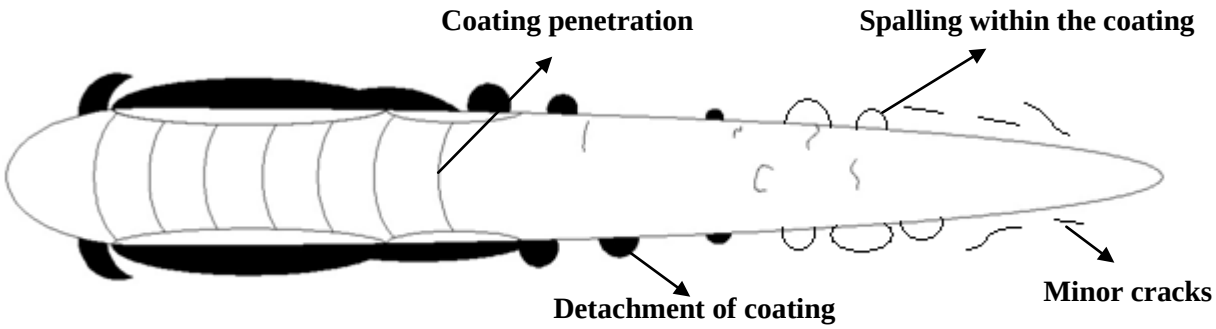

Figure 5.2 Diagram illustrating the different types of damage that may be observed in a scratch test [161]

Scratch testing is usually only regarded as a semiquantitative method because there are a number of intrinsic and extrinsic factors which are known to influence the derived value of

critical load, and this makes comparison between laboratories with various types of machine quite difficult. Table 5.2 lists the intrinsic and extrinsic factors in scratch testing.

Table 5.2 Intrinsic and extrinsic factors in scratch testing [173]

Intrinsic factors	Loading rate
	Scratching speed
	Indenter tip radius
	Indenter wear
	Machine stiffness/design
Extrinsic factors	Substrate properties (hardness, elastic modulus)
	Coating properties (thickness, hardness, modulus, residual stress)
	Friction coefficient
	Surface roughness

The intrinsic parameters associated with the scratch testing are directly related to the instrumentation and can therefore be chosen by the operator. The critical load has also been found to be a sensitive function of coating and substrate property. Table 5.3 illustrates general observations concerning scratch testing as a function of coating / substrate hardness.

Table 5.3 Qualitative summary of failure modes in the scratch testing as a function of coating / substrate hardness [160]

Substrate hardness / Coating hardness	Soft	Medium	Hard
Soft	Plastic deformation extrusion	Coating thinning scrape off	Coating thinning scrape off
Medium	Plastic deformation extrusion	Delamination	Delamination fracture
Hard	Plastic deformation extrusion	Delamination fracture	Delamination fracture

In this study, the hardness of copper coating falls into the medium category and the hardness of CMG glass substrate falls into the hard category, so the failure modes are delamination and fracture.

5.3 Experimental setup

This research has used the ST 3001 scratch testing system at the UK NPL with increasing ramp loading (calibrated by a certified reference load cell). A Rockwell C diamond stylus was used with a 200 µm tip radius and a cone apex angle of 120° as shown in Figure 5.3. The high hardness and superior durability of the diamond ensures uniform tip geometry during the entire experiment. In addition, the diamond tip could readily penetrate the film surface and create a clear track from which the adhesion properties of the film could be assessed.

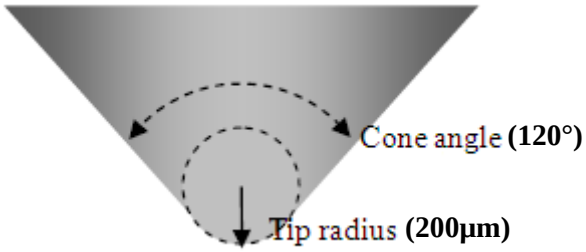

Figure 5.3 Geometry of the ST3001 diamond stylus tip

The critical load data is used to quantify the adhesive properties of the copper coating and glass substrate combination by the ramp loading scratch test. Ramp loading was increased from a minimum load of 1 N to a maximum load, incrementing in a number of steps. A series of preliminary experiments were completed prior to operation parameter setting. When the loading force was in the range of 16 N to 25 N, cracks running from the scratch edges in the CMG glass substrate were observed as shown in Figure 5.4, causing substrate failure.

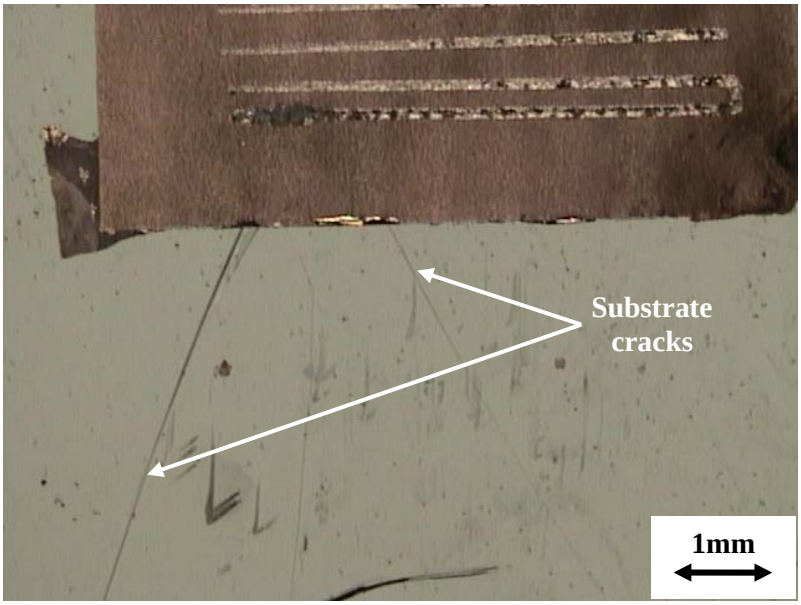

Figure 5.4 Image of substrate failure due to large loading force

It should be noticed that the glass samples were not annealed after laser machining which is known to cause sporadic microcracking [6]. The maximum loading which caused the glass substrate failure varied because the residual stresses developed within the glass sample during the machining process were different. As a result, the maximum loading was set to 15 N in this study because it would be high enough to cause coating failure but also not damage the samples. Thirty 0.5 load steps (1 N → 15 N) were chosen for the ramp loading profile.

The scratch length is another parameter for the user to select for scratch testing. Figure 5.5 shows the comparison of different scratch lengths of 5 mm and 8 mm for scratching the specimen surface (ramp loading from 1 N to 15 N with 30 steps). The deviation of critical load measured from 5 mm scratch length and 8 mm scratch length was typically less than 10 %. However, short scratch lengths meant the coated surface area being tested could be smaller; therefore the time of preparation for glass samples using laser machining processes could be shorter (and cheaper). As a result, 5 mm scratch lengths were used throughout this study. The final parameter settings for scratch testing in this study are shown in Table 5.4.

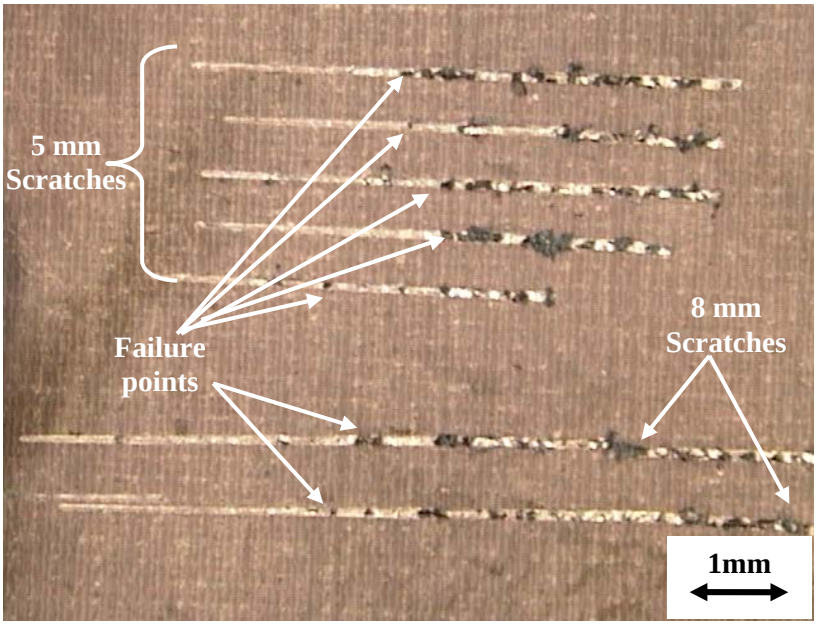

Figure 5.5 Comparison of different scratch lengths

Table 5.4 Scratch testing parameters

Load type	Ramp loading
Initial load	1.0 N
Final load	15.0 N
Loading rate	15.0 N / minute
Load steps	0.5 N
Scratch speed	5 mm / minute
Scratch length	5 mm

A common feature of existing scratch testing analysis is the description of the coating removal process in terms of an interfacial shear force, and coating failure is considered to occur when a critical load is reached.

Scratch tracks created by the ramp loading scratch testing were measured either by an optical microscope or SEM. Via the scratch testing result, knowledge of the sample stress state leading to delamination failure is available through direct measurement of the distance from the loading start point to coating penetration and by theoretical calculation.

In this case, the value of the critical load *Lc* (N) can be calculated by the following mathematical equation:

$$Lc = F_{\text{Start load}} + (F_{\text{End load}} - F_{\text{Start load}}) \times L_{\text{Delamination length}} / L_{\text{Scratch length}} \quad 5\text{-}1$$

In this study, $F_{\text{Start load}} = 1.0$ N,

$F_{\text{End load}} = 15.0$ N,

$L_{\text{Scratch length}} = 5.0$ mm,

So $Lc = 1.0 + (15.0 - 1.0) \times L_{\text{Delamination length}} / 5.0 = 1 + 2.8 \times L_{\text{Delamination length}}$

As an alternative to observational measurement and calculation, the critcal load of failure could also be aquired by reading from the loading graph. Frictional force and applied load can be generated by computer automatically during the process. Graphs were drawn based on experimental data, giving a direct route to reading the critical load of coating delamination.

5.4 Coating characterization

The normal force was gradually increased during the scratch testing to generate a ramp loading condition. Moreover, the frictional force and normal force during the scratch testing were also obtained. Eight scratches were drawn on each of the manufactured and tested glass specimens (samples listed in Chapter 6 Table 6.2 and Table 6.5). Scratches were visualized after testing using an optical coordinate measuring machine (OGP FLASH 200 CMM), and a scanning electron microscope (CAO147 SEM), providing pictures for subsequent image processing.

5.4.1 Optical CMM observation

The optical coordinate measuring machine (OGP FLASH 200) is a reliable method for the detection of surface damage. This technique allows the user to visually differentiate between cohesive failure within the coating and adhesive failure at the interface of the coating / substrate system. Failure points along the scratch are typically distinguished by backlighting penetrating through the copper layer and are easier to recognize using white light techniques compared to SEM images. Recognition of different failure modes may change depending on eventual copper / glass use and manufacturer. Failure was initially identified as the point of first observable failure (any mode as defined in Figure 5.2).

Although the copper film deposited on smooth glass surfaces was very prone to peel off during the electroless copper plating process, there were still a few coatings attached to the smooth area in some cases. The stylus tip was drawn across these films to test the adhesive strength using the test parameters identified in Table 5.4. Figure 5.6 illustrates scratch testing results on the copper coating deposited on the smooth CMG glass surface.

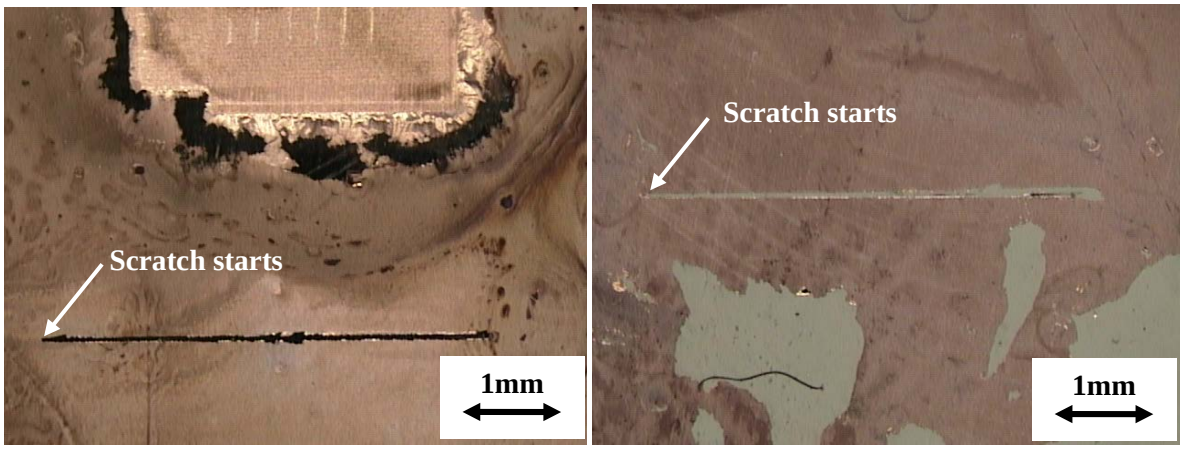

Figure 5.6 Optical CMM images for scratch testing on smooth CMG glass surfaces

The results suggested the coating penetration and delamination failure occurred almost at the beginning of the scratch track, indicating that the critical load for copper coating on a smooth glass substrate was less than 1.0 N and the adhesive bond could be disrupted with a small mechanical external force.

Scratch testing was carried out for assessing roughened CMG glass surfaces under the same experimental operation parameters. Figure 5.7 and 5.8 illustrate the optical CMM images for scratches of copper coating on roughened CMG glass surfaces treated by bead blasting and excimer laser respectively. Table 5.5 and Table 5.6 listed specific machining operation parameters.

Table 5.5 Machining operation parameter details for each sample in Figure 5.7

Sample number	**Exposure time (s)**	**Nominal size range of glass bead (μm)**
(a)	1	75-150
(b)	2	
(c)	3	
(d)	3	

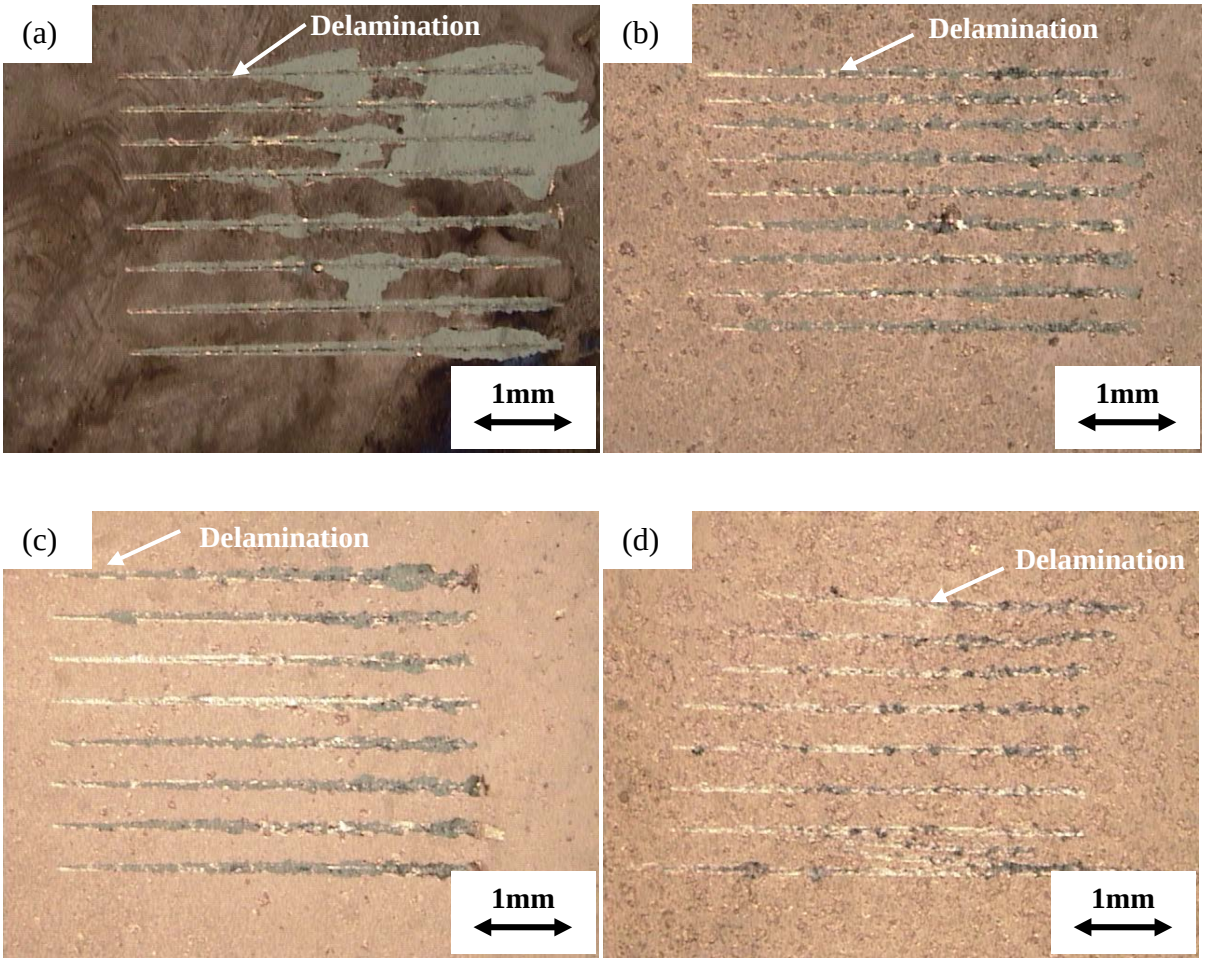

Figure 5.7 Optical CMM images for scratch testing on bead blasted treated CMG glass

Figure 5.7 suggests that coating adhesion did not fail at the beginning of scratch testing and the critical load of coating adhesion could be improved to a few Newtons. From the images, it can also be seen that coating delamination failure occurred on every sample. There were even large pieces of copper film flaking off the glass substrate in Figure 5.7 (a). The possible reason is that this sample was exposed to the bead blasting fluid for only 1 second and there were still virgin glass surface areas which could reduce the adhesive bonding between coating and substrate. The samples illustrated in Figure 5.7 (b), (c) and (d) show randomly rough glass substrate surface topography with inconsistent adhesion strength (illustrated for one track on each sample with a white arrow). The delamination onset position differs from scratch to scratch. Even along one scratch, sometimes the failure started early, and then the delamination halted even with the increasing loading force.

Table 5.6 Machining operation parameter details for each sample in Figure 5.8

(S- square mask)

Sample number	Energy density (J/cm^2)	Shots per area (n)	Mask size / shape (µm)
(a)	2.2	10	S1
(b)		10	S4
(c)		5	S1
(d)		5	S1

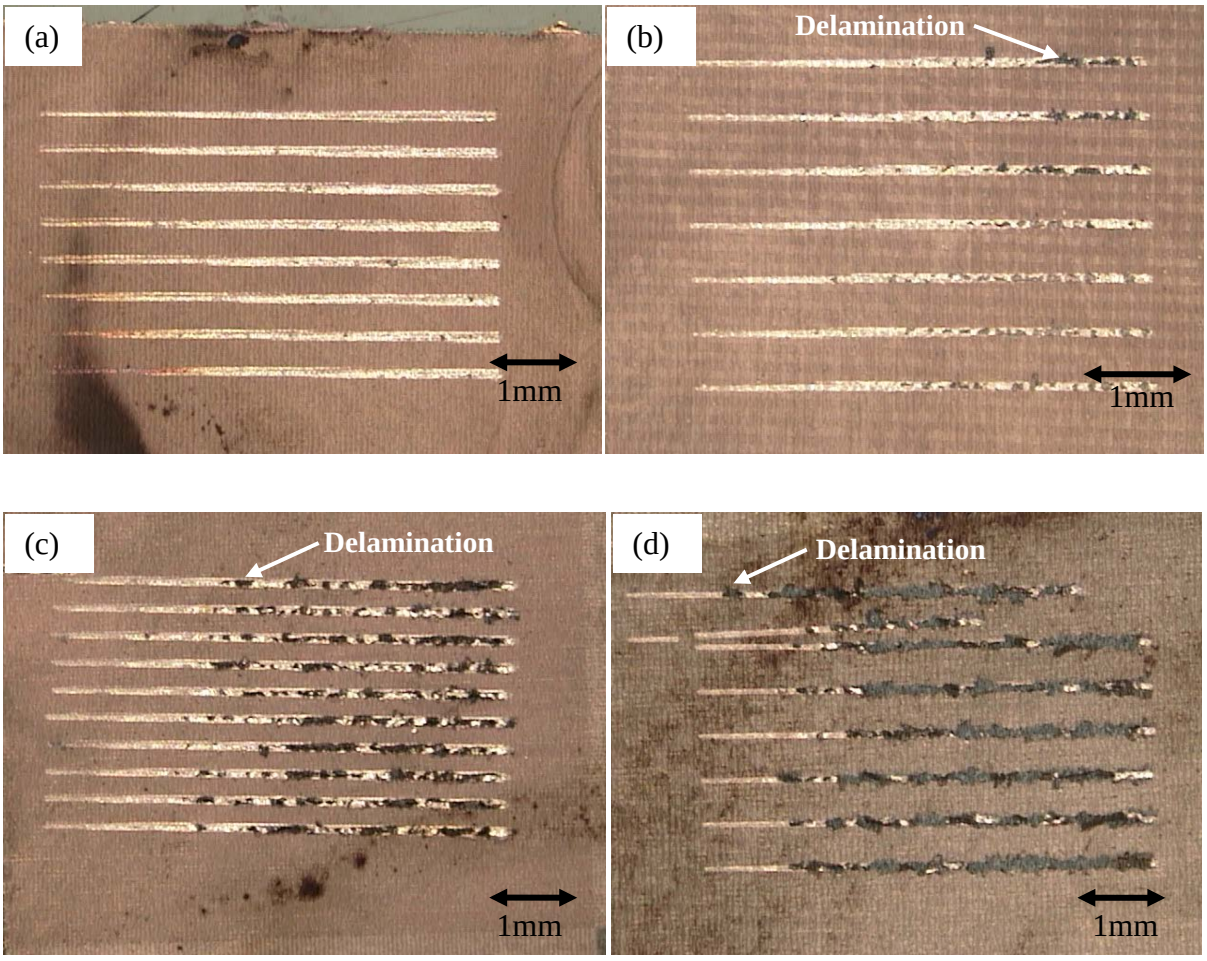

Figure 5.8 Optical CMM images for scratch testing on excimer laser machined CMG glass

The results in Figure 5.8 indicated that excimer laser roughened CMG glass surface could improve the adhesion between the copper coating and the glass substrate. The scratches show failure consistency due to the structured substrate surfaces. In Figure 5.8 (a), there are not any

obvious coating delamination failures shown during the loading range. That means the copper adhesion is better than the maximum load applied during scratch testing. The critical loads were different since the underneath substrate structured surfaces were different. The samples illustrated in Figure 5.8 (b), (c) and (d) present different delamination onset positions.

5.4.2 Scanning Electron Microscope analysis

A scanning electron microscope (SEM) with large magnification and deep depth of field could provide detailed observation of copper coating failure on CMG glass, such as spalling which is difficult to identify with an optical instrument. Figure 5.9 illustrates typical failure elements found during coating delamination; cracking, spalling, coating detachment and coating penetration / delamination. This sample was generated by excimer laser machining using a triangular mask with a long length of 7 mm, energy density of 2.2 J/cm^2, 5 shots per area and repetition rate of 20 Hz.

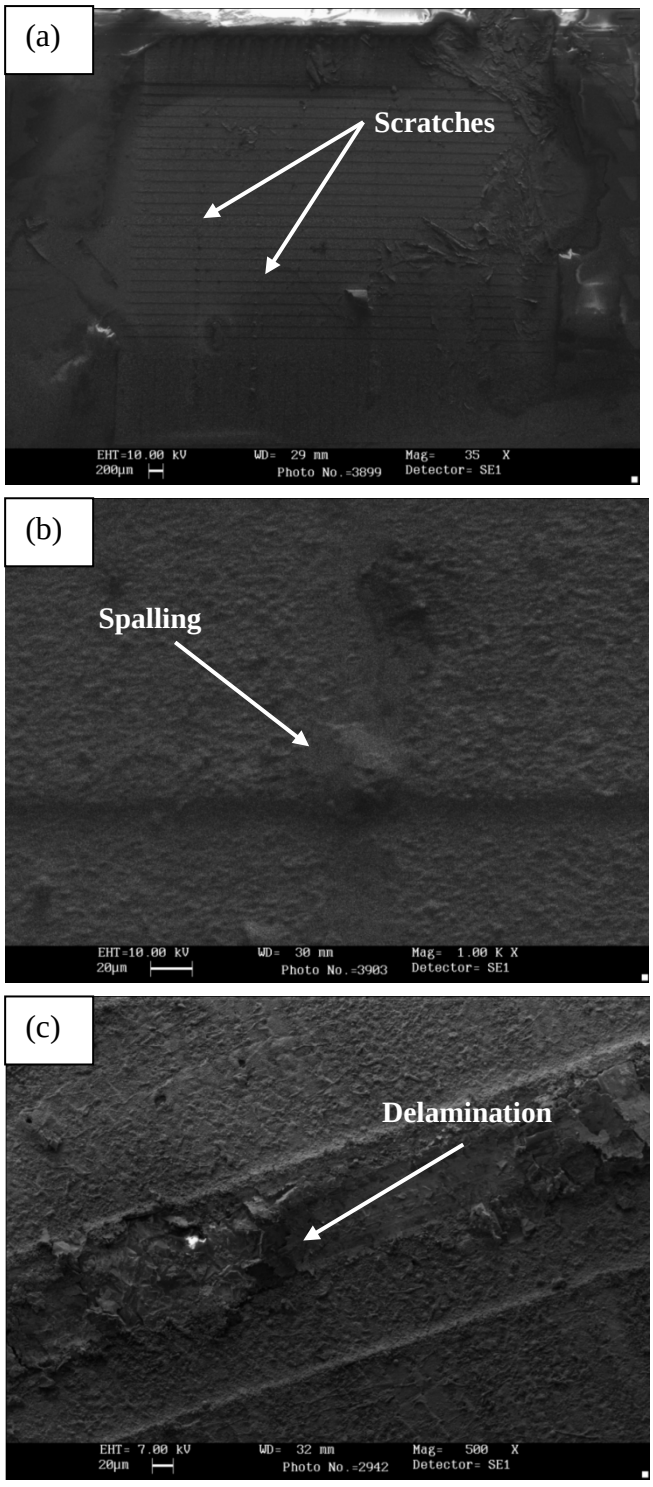

Figure 5.9 SEM images for scratches of copper coating on CMG glass (a) Overall scratches (b) Spalling position (c) Delamination position

5.4.3 Graphical representation

Frictional force recording enables the force fluctuations along the scratch to be studied and correlated to the failures observed under the microscope. Acoustic emission and frictional force measurements provide traceable signals which can be used to compare results from different samples and may avoid some of the subjectivity of measurements made by eye.

Frictional responses to failures are very specific to the coating-substrate system. Typically, a failure in the coating results in a change (a step, or a change in slope) in the Frictional Force – Load graph. Damage patterns on the surface are correlated with acoustic emission and friction forces from the ST 3001 test system, to derive the critical loads at which various failure mechanisms occur. Figure 5.10 shows the graph of a typical normal load variation with respect to frictional force. Graphical representation of the experimental data provides an alternative direct method of identifying the critical load of coating delamination. The failure point on the graph as shown in Figure 5.10 identifies the probable point of copper coating failure.

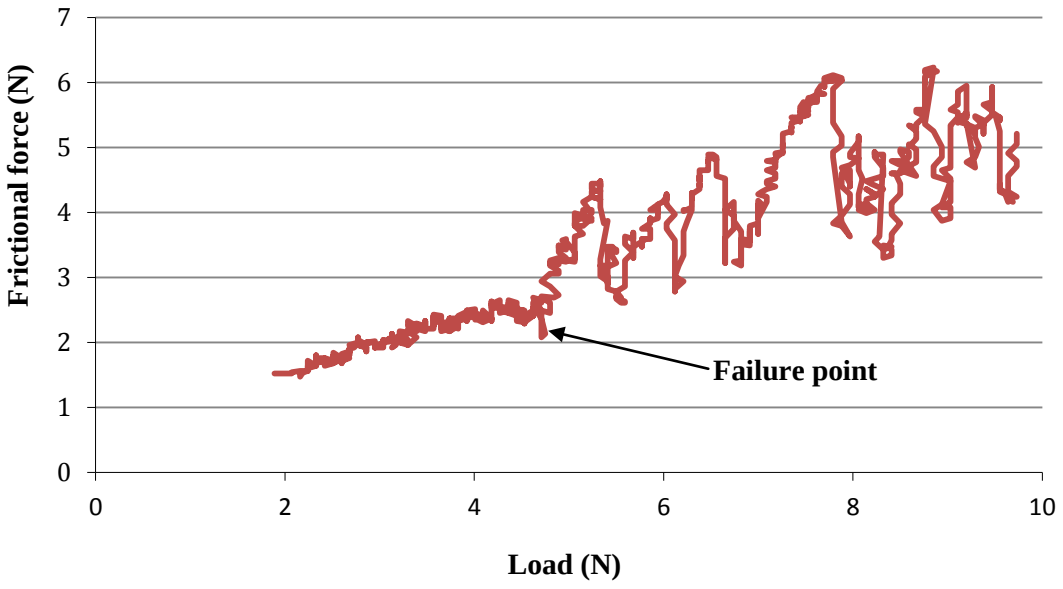

Figure 5.10 Graph of a typical normal load variation with respect to frictional force

Figure 5.10 demonstrates that the critical load can be estimated when an abrupt change is observed in the form of the Frictional Force – Load graph, in the example the load value being 4.62 N.

However, not every graphical scratch testing result provides definitive changes and requires subjective visual analysis to identify the points of failure as shown in Figure 5.11, although graphical data may lead to an indeterminate result with respect to critical load. Furthermore, the graphical analysis does not necessarily allow for the identification of the different failure models.

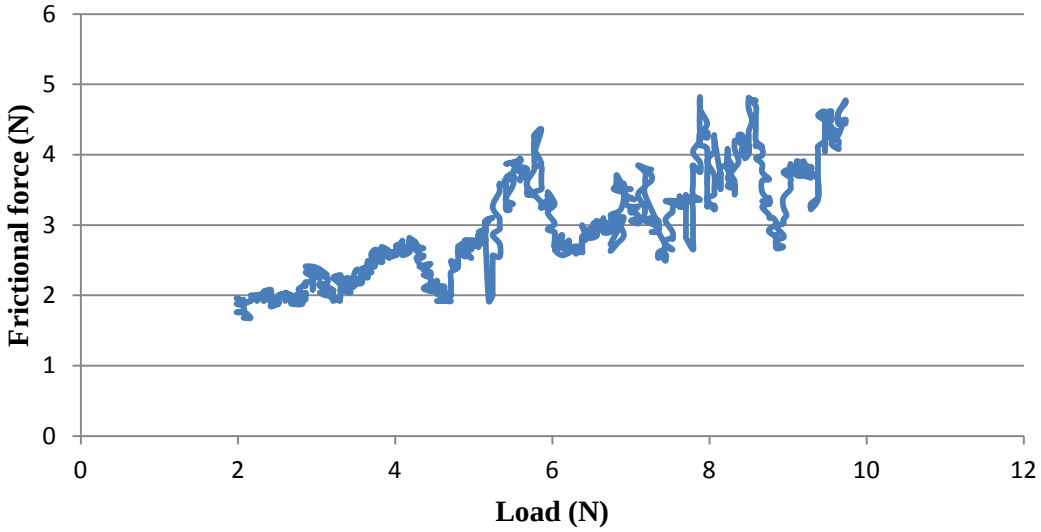

Figure 5.11 Graph is indeterminate for the identification of the failure point

5.5 Results discussion

5.5.1 Repeatability analysis

In order to analyze the repeatability of the experiments in this study, four groups of excimer laser machined glass samples were made with the same laser energy density, shots per area and pitch for each group. The glass samples were electroless copper coated using the procedure identified in Table 4.7. Table 5.7 shows the comparison results of the critical load of delamination positions for each group of samples.

Table 5.7 Repeatability of excimer laser machined samples (S-square mask)

Sample number	Mask side length (mm)	Energy density (J/cm^2)	Shots per area (n)	Pitch spacing (μm)	Critical load of delamination(N)
1-1	S1	2.2	5	40	13.9
1-2					13.0
2-1	S1	2.2	5	50	13.3
2-2					13.4
3-1	S1	2.2	5	60	12.6
3-2					14.8
4-1	S1	2.2	15	50	15
4-2					15

From the table, it can be seen that the repeatability of excimer laser machined samples is approximately 10 % variation or less. The possible reason is due to the high machining precision and high quality of excimer laser machining which makes the process repeatable.

To investigate the repeatability of bead blasted samples, four CMG glass samples were exposed to the bead blasting fluid for one second, and then the critical loads of the delamination positions were tested as shown in Table 5.8.

Table 5.8 Repeatability of bead blasting treated samples

Sample number	Exposure time (second)	Critical load of delamination(N)
5-1	1	2.8
5-2		7.6
5-3		4.6
5-4		3.5

Table 5.8 suggests that the variation of critical load for the bead blasting treated samples is significant. Possible reasons are as follows. Firstly, the repeatability of the bead blasting technique is not very good. There are a number of variables for this technique, such as the fluctuation of the size of the bead, the difficulties of controlling the fluid pressure and the human error of controlling exposure time. Secondly, the surface topography is randomly distributed, and therefore the scratch testing experiment is stochastic and less traceable. Consequently, the repeatability of bead blasting treated glass samples is not as good as

excimer laser machining samples, or in other words the repeatability of the samples with random surfaces is not as good as structured surfaces.

5.5.2 Effect of depth

From the excimer laser study in Chapter 3, shots per area is regarded as being representative of the machining depth when the laser energy density is fixed. In order to study the effect of machining depth to adhesive strength of copper plating, five groups of the glass samples were machined using 1 mm × 1 mm square mask with the same laser energy density and pitch, but with different shots per area. Critical load was measured as the load at the onset position of copper coating failure. Table 5.9 presents the machining operation parameter details for each sample and the graph of relationship of critical load variation with respect to shots per area is shown in Figure 5.12, with standard deviation error bars.

Table 5.9 Machining operation parameter details for each sample

Group number	**Energy density (J/cm^2)**	**Shots per area (n)**	**Laser machining variable (pitch) (μm)**
1	2.2	5	30
		10	
		15	
2		5	40
		10	
		15	
3		5	50
		10	
		15	
4		5	60
		10	
		15	
5		5	70
		10	
		15	

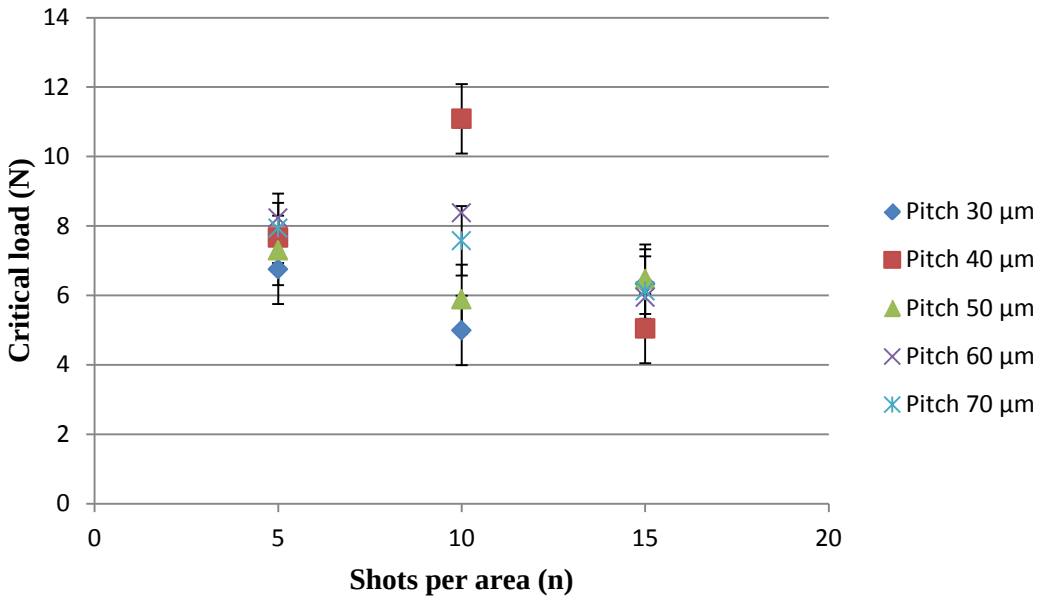

Figure 5.12 Graph of critical load variation with respect to shots per area

The graph does not show a strong relationship between critical load and shots per area, suggesting that there is not a strong relationship between copper plating adhesion and machining depth. However, in general the adhesive strength of shallow machining depth tends to be stronger than the deeper features. The possible reason may be related with stylus / discontinuity impact which will be discussed later in Section 6.4.2, and the deeper machining depth structures have relatively sharper edges which are more prone to random copper bond failure.

5.5.3 Effect of pitch

In order to study the influence of machining pitch to adhesive strength of copper plating, three groups of glass samples were machined using a 1 mm × 1 mm square mask with the same laser energy density and shots per area, however, with different overlapping pitch under the dragging process. Critical load was measured as the load at the onset position of copper coating failure. Table 5.10 lists the machining operation parameter details for each sample and the graph of relationship of critical load variation with respect to pitch is shown in Figure 5.13, with standard deviation error bars.

Table 5.10 Machining operation parameter details for each sample

Group number	Energy density (J/cm^2)	Shots per area (n)	Laser machining variable (pitch) (µm)
1	2.2	5	30
			40
			50
			60
			70
2		10	30
			40
			50
			60
			70
3		15	30
			40
			50
			60
			70

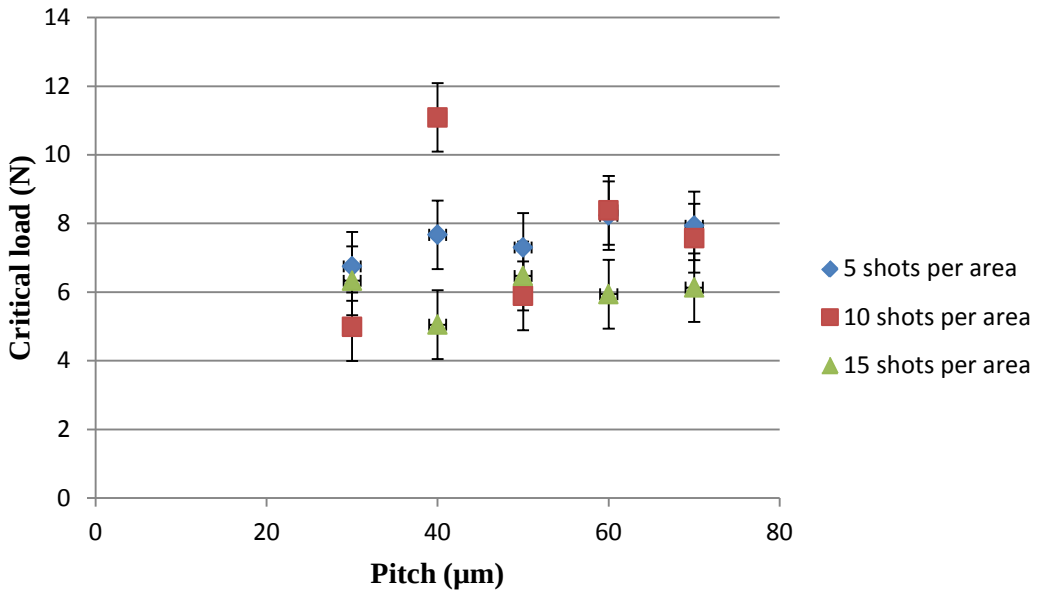

Figure 5.13 Graph of critical load variation with respect to pitches

Again, the graph does not show an obvious relationship between critical load and overlapping pitches and there is no strong effect of pitch to adhesive bonding strength. Taking the first group of samples for example, the pitch of 60 µm was the strongest compared to other pitches.

However, some trends can be seen when relating the critical load with surface topography as shown in Figure 5.14, which show group 1 glass surfaces (Table 5.10).

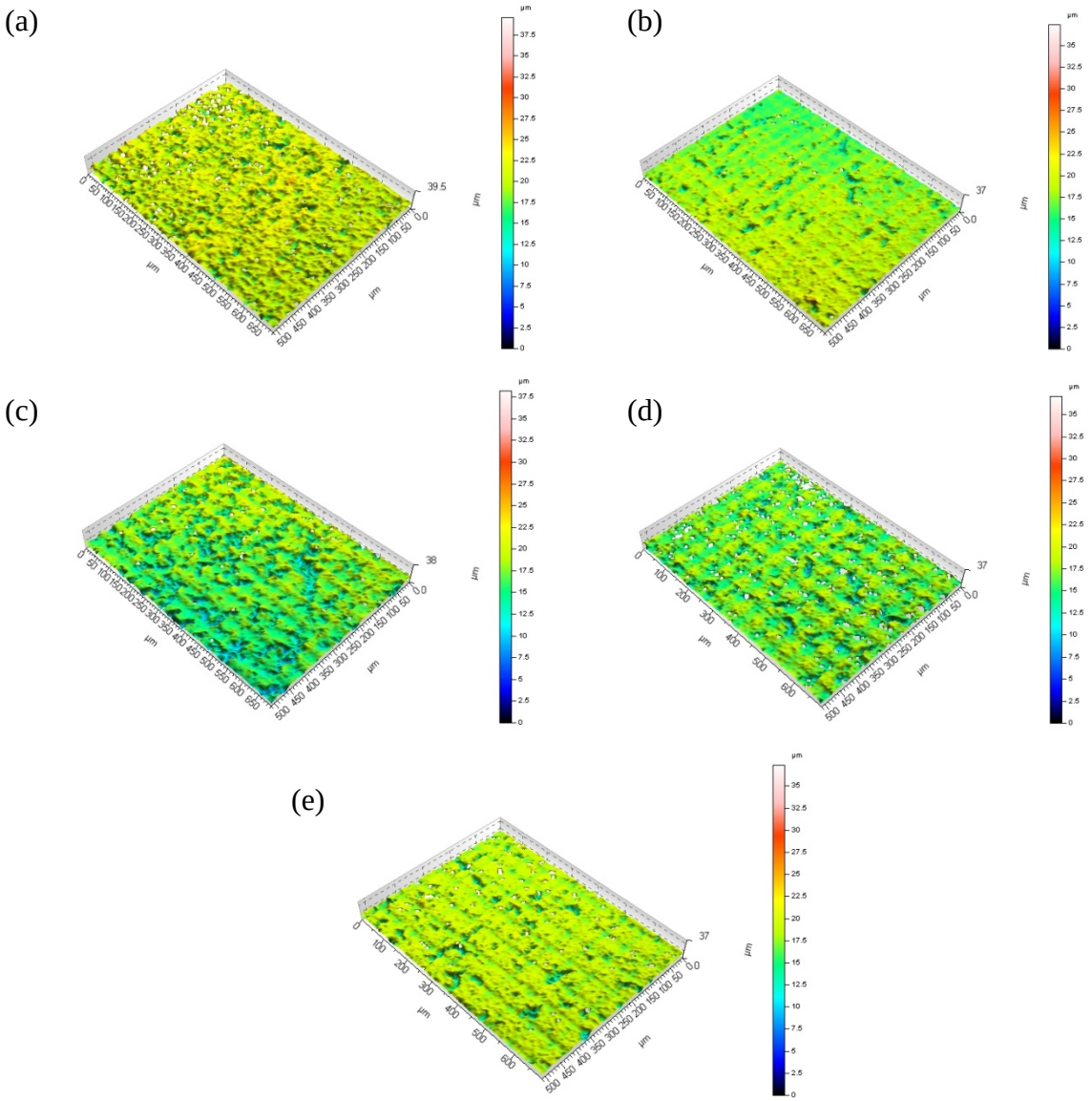

Figure 5.14 Excimer laser machined samples with different laser machining variable (pitch) (a) 30 µm (b) 40 µm (c) 50 µm (d) 60 µm (e) 70 µm

Figure 5.14 shows samples (b) and (d) have the most well defined structures compared with samples (a), (c) and (e). Moreover, sample (a) with pitch spacing of 30 µm was rougher than other samples, and it is also noticed from Figure 5.12 that the critical load of sample (a) was the lowest. The results are consistent with the expectation that the adhesion characteristics of substrates with structured surfaces are better than the samples with random surfaces. This

assumption can also be further confirmed by Figure 5.15 which presents a well defined micro pattern arrayed structure that had the largest critical load shown in Figure 5.13.

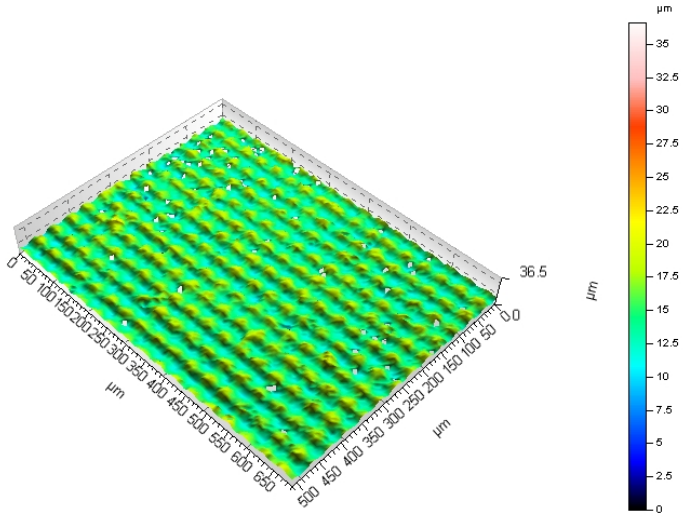

Figure 5.15 Excimer laser machined sample with 10 shots per area and 40 µm pitch

5.5.3 Effect of exposure time

In order to study the relationship between exposure time to the bead fluid and the adhesive strength of copper plating, glass samples were treated with different exposure times. Critical load was measured as the load at the onset position of copper coating delamination and the result was the average values of each group. Table 5.11 shows the machining operation parameter details for each sample and the graph of relationship of critical load variation with respect to exposure time is shown in Figure 5.16.

Table 5.11 Machining operation parameter details for each sample

Sample group	**Exposure time (s)**	**Nominal size range of glass bead (µm)**
1	1	75-150
2	2	
3	3	

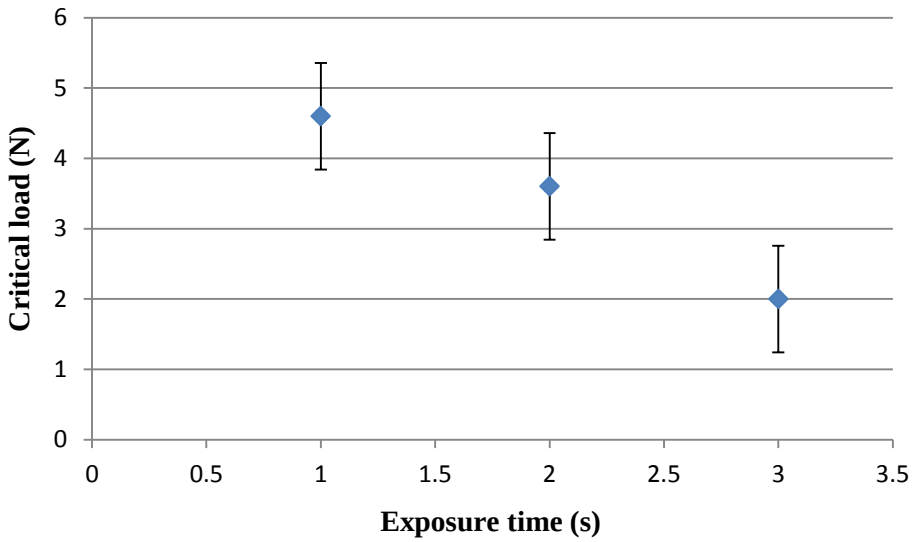

Figure 5.16 Graph of critical load variation with exposure time

The graph illustrates that the critical load of bead blasting treated samples decreases with extended exposure time. The possible reason maybe that increasing exposure time makes the surfaces rougher and sharper which are prone to random copper bond failure at sharp discontinuities. This issue is discussed later in Section 6.4.2.

5.6 Summary

Scratch testing was chosen as a quantified technique to evaluate the adhesive properties of the copper / glass system, and the critical load was used to quantify the adhesive properties of the copper coating on the glass substrate. The instrument parameters used for all testing in Chapter 6 are identified in Table 5.4. The testing of copper plating bond strength is however susceptible to a number of interfering factors that should be controlled as much as possible:

Firstly, the scratch testing is actually regarded as a semiquantitative method because there are a number of intrinsic and extrinsic factors which are known to influence the derived value of critical load (as shown in Table 5.1), and this makes the results difficult to compare with other scratch testing machines. It is therefore important to only use one machine, with consistent processing parameters.

Secondly, copper coating quality (such as variation of thickness) affects the scratch testing result because the coating failure usually occurs easily on weak and thin coated area. For

example, preferential failure occurs at sharp discontinuities of the glass surface, which may not be representative of the bulk adhesion (as shown in Figure 5.9).

Thirdly, identification of spalling and delamination is subjective and prone to human error, so extra care must be taken for recognition of coating failure.

Scratch testing results showed that structured surfaces may be more ideal for adhesive bonding. There are some possible reasons for this. Firstly, micro pattern array structures increase surface contact area between the adherend and adhesive copper. Secondly, micro pattern array structures enhance mechanical locking of adhesive (copper) between microcolumns. The influence of surface topography on plating adhesion will be discussed in Chapter 6.

Chapter 6 Correlation of areal parameters with critical load

6.1 Introduction

Chapter 6 brings all the elements of the research together; glass machining, metrology, areal parameterization, electroless copper plating, scratch testing, and critical load analysis. This allows a systematic investigation of the effectiveness of different CMG glass substrates, and the strength of correlation between the areal parameters and the bond strength – expressed as the critical load. This chapter concludes by identifying the key areal parameters.

Over 100 CMG glass samples were produced in four batches, and the samples for plotting correlation graphs come from Batch 3 and Batch 4;

- Batch 1 – Basic understanding and demonstrating of the experimental methodology (including laser machining, electroless copper plating, and scratch testing on glass); no intention to correlate with areal parameters.

- Batch 2 – Exploring the relationships between adhesion strength and glass structures with different machining variables (mask shapes, ablation depths and feature dimensions) no intention to correlate with areal parameters; Batch 3 and Batch 4 will focus on square mask and small feature dimension structure machining due to the high critical loads based on the scratch testing results.

- Batch 3 – Samples prepared and tested with consistent electroless copper plating and scratch testing process; acquiring the initial correlations between areal parameters and adhesive strength.

- Batch 4 – Concentrating on the samples with shallow depth and ultra fine structures for exploring optimal surface topography for strong copper / glass plating adhesion and reinforcing the correlations between areal parameters and adhesive strength initially acquired from batch 3.

6.2 Filter selection and three failure criteria proposal

6.2.1 Filter selection

As identified in Chapter 2, a Zygo NewView 5000 CSI system was used to measure the surface topography of each machined glass sample, with consistent lens (10 x) and magnification settings (1 x) and field of view (700 µm x 500 µm). Surface topography and areal parameters were generated and analysed using Talymap (DigitalSurf Mountains v5.1) surface texture processing software that is compliant to ISO / FDIS 25178:2. The sampling area (700 µm x 500 µm) was selected to guarantee that there were a number of dominant micro topographical features presented on the evaluation area which conforms with ISO / DIS 25178.

Evaluation of the laser machined surfaces identified three scenarios that exist which required clarification and quantification:

- The potential correlation between the micro-roughness component of the glass surface and the critical load.

- The potential correlation between the structural component of the glass surface and the critical load.

- The potential correlation between the micro-roughness and structural components of the glass surface, and the critical load.

Micro-roughness on the glass surface is an inherent function of the inhomogeneous nature of the excimer laser wavefront spatial characteristics (Chapter 2), and has been evaluated in its own right with glass samples featuring micro-roughness, but no structure. Relatively large scale structure without micro-roughness is the skeleton of the laser machined structured surface which is initially designed to be machined.

The areal filter techniques and the effect of filtration were introduced in Chapter 2. Section 2.4.3 elaborated how to realize the separation of micro-roughness and structure through the

filter selection. In order to individually study the contributions of micro-roughness and large scale structures to the plating adhesion, a 25 μm L-filter was employed to extract the micro-roughness component and acquire an S-L surface. Filtering of the data initially considered a consistent and fixed nesting index value (typically 80 μm) to evaluate the total contribution of the micro-roughness and structural components. However, the feature spacing for each sample is different, and therefore the use of standard filter parameters for all glass samples was found not to allow appropriate differentiation of structural components for large pitch micro feature samples, leading to subsequently limited correlation with critical load.

Based on the investigation of the effect of filter selection to areal parameters value (Section 2.4.3), a compromise selection of the nesting indices for S-filter was determined based on the specific pitches of samples to remove all the unwanted large scale noisy components and keep both micro-roughness components and structural components. In this study, the micro features of interest had scales ranging from 30 μm to 200 μm, and Table 6.1 illustrates the details of filter values in this study. By keeping the same filtering conditions for the same micro-feature scale glass samples, it enabled consistent surface topography comparison, avoiding the issues and complexities associated with filtering.

Figure 6.1 shows a machined structured surface separated into micro-roughness component and structural component by filtration technique application to focus on specific component prior to analysis.

Table 6.1 Filter selections in this study

Pitch (μm)	Filter selections (μm)					
	L-Filter	S-Filter				
	25	80	100	120	150	250
30	√	√				
40	√	√				
50	√	√				
60	√	√				
70	√		√			
80	√			√		
100	√				√	
160	√					√
200	√					√
Random roughness	√					√

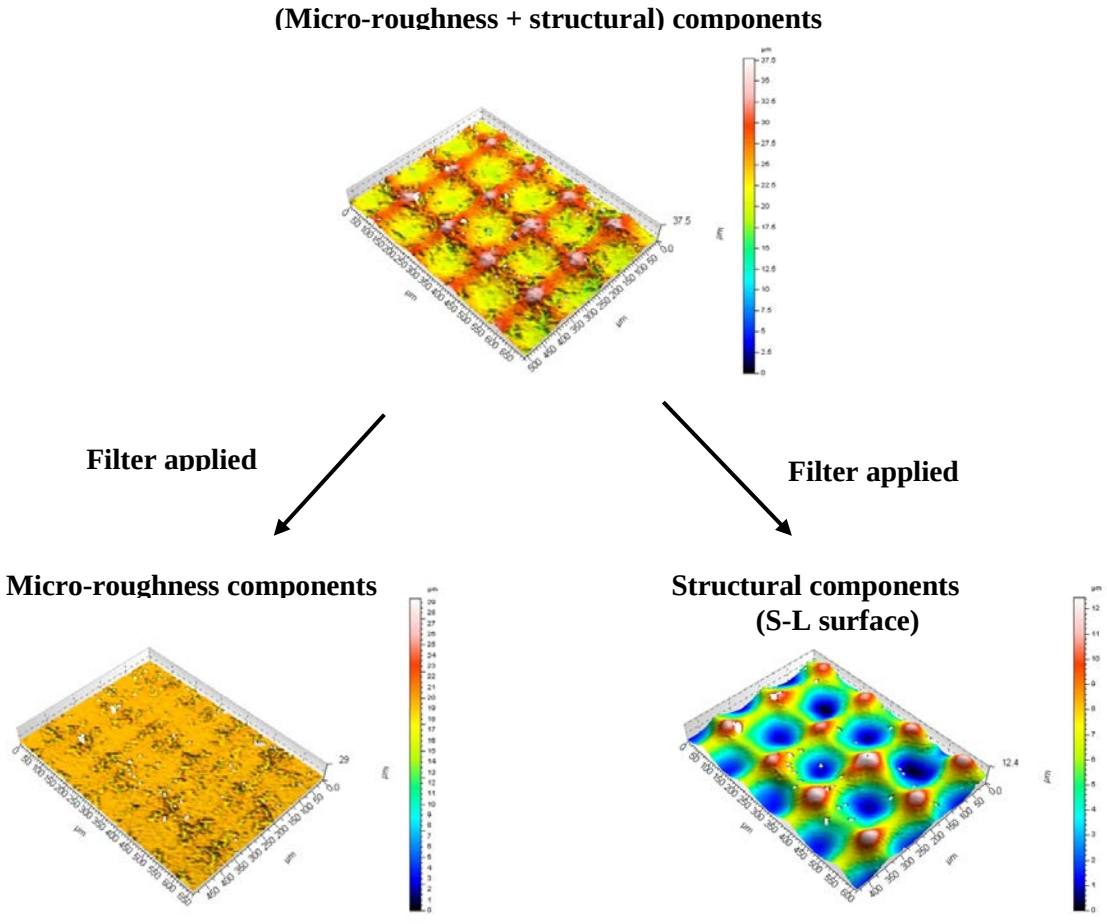

Figure 6.1 Filter applied to help focus on specific component prior to analysis

6.2.2 Three failure criteria proposal

Sometimes coating failure (as a function of scratch testing) commenced at micro pattern edges because of stress concentrations and edge effects caused by stylus tip penetration. Alignment of the scratch testing stylus with the sample was a manual process and therefore difficult to guarantee alignment with the preferential direction of the structured surface. Figure 6.2 shows slight misalignment of the scratch track causing a prolonged impact on a structure edge along each track (half way along each track – seen as a black line across the scratch). Once the stylus leaves the feature edge and continues along the structure surface, plating failure is no longer observed, until the stylus load reaches the critical value at the end of each scratch. Failure at this point is again indicated by much wider long dark elements on the scratch. Figure 6.3 shows a surface topography image of the edge structure.

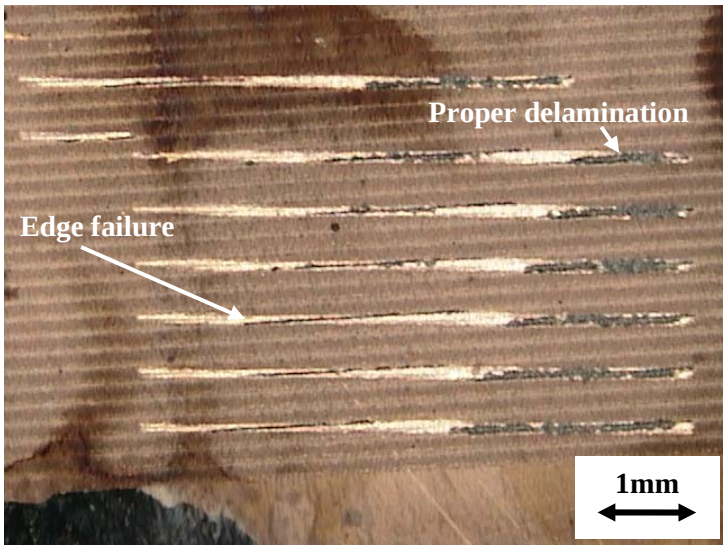

Figure 6.2 Premature plating failure as a function of stylus / discontinuity impact

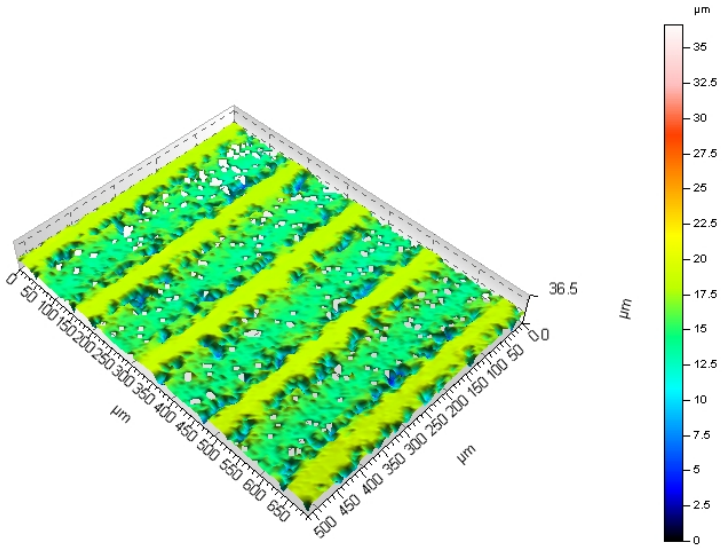

Figure 6.3 View of edge structure on glass substrate

There is no typical delamination model for this sample with the angle between the scratch track and micro groove edges, as shown in Figure 6.2. It can be seen that when the stylus tip hits the profile edges, the top surface edge is prone to penetration. When the stylus tip leaves the profile edge, the coating shows strong adhesion because the copper is firmly adhered. However, the delamination occurs again when the stylus tip goes over the next edge. Figure 6.4 helps to illustrate this issue.

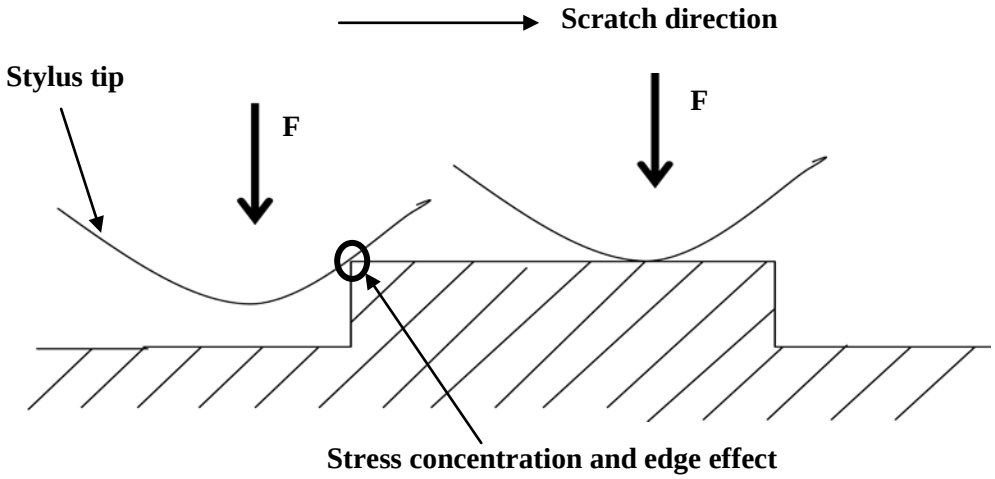

Figure 6.4 Schematic showing micro pattern edge effect failures

Furthermore, process consideration of data sets confirmed the requirement to investigate a number of potential failure modes for data processing investigation. Figure 6.5 presents the preliminary graph of correlation of areal parameter *Sq* values (S-L surface) and critical load. In this graph, critical loads were identified as the load applied to the position of the very first failure spot observed. Some data processing processes were attempted to seek the correlation such as classifying data by machining mask dimensions as shown in Figure 6.5, but still results in a random distribution. No clear trends were observed from other areal parameters either. This is because the failure mode analysis is prone to premature and / or random copper bond failure. This is typified by a scratch testing stylus impacting on a structural discontinuity, causing a localized stress concentration resulting in localized failure that is not indicative of bulk bond strength as illustrated in Figure 6.2.

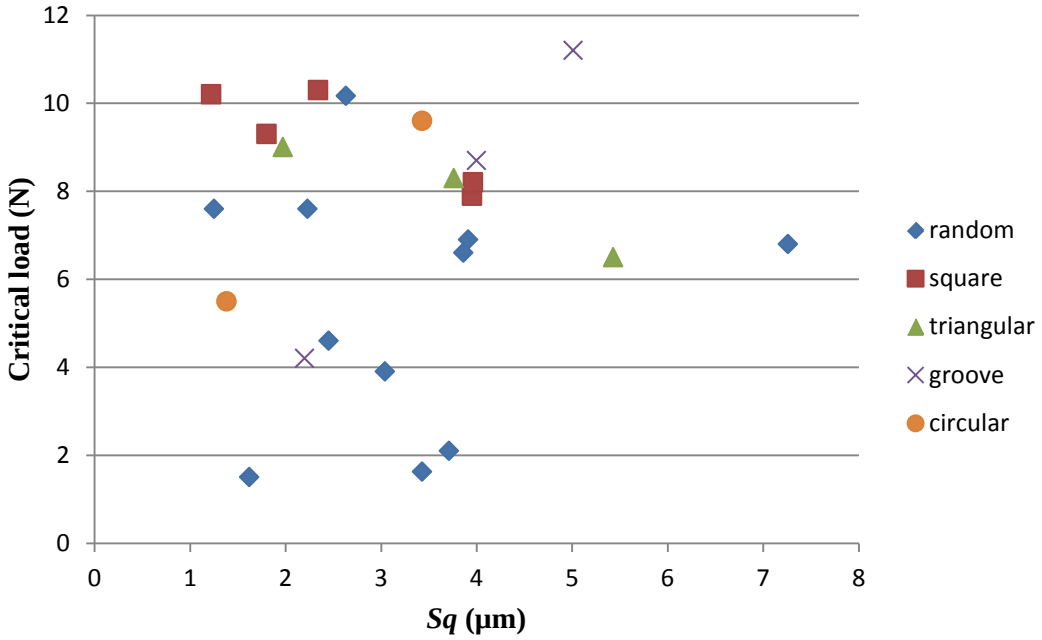

Figure 6.5 *Sq* as a function of initial failure critical load

Consequently, data analysis has considered three failure criteria as being more representative of bulk copper adhesion and potential user application scenarios. In this study, three failure criteria can be assessed as follows and are illustrated in Figure 6.6.

- Criterion 1 - Simple - The point where the very first failure occurs on the plated glass surface. This position is quite unpredictable due to the variables identified in this experiment (as illustrated in Figure 6.2 and Figure 6.6).

- Criterion 2 - Consecutive - The point where more than three consecutive observable individual failures are identified, by counting the number of failure points that occur within a predefined length of 0.5 mm (typically a higher critical load obtained compared to the first definition).

- Criterion 3 - Continuous - The point where continuous delamination occurs for a minimum length of 0.2 mm (typically the highest critical load compared to the first two definitions).

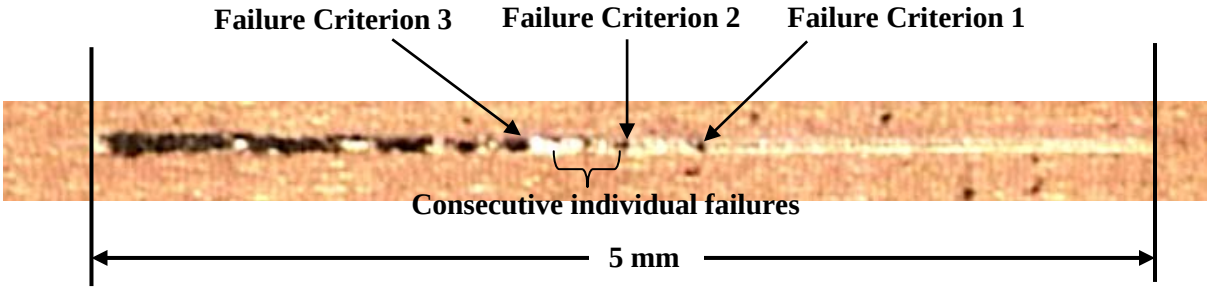

Figure 6.6 Schematic of three failure criteria

Comparisons between different samples are only valid if the mechanism of failure (failure criterion) is the same. The correlations of areal parameter (including field and feature parameters) according to ISO 25178:2 and critical load under three different failure criteria for samples (from Batch 3) were generated.

In this study, Failure criterion 3 was used because it represented catastrophic failure of the copper, when assessing the adhesive bond strength from scratch testing of electroless coated glass substrates. Failure Criteria 1 and 2 were susceptible to spurious, non-representative plating failure as a function of edge effect stress concentrations in the case of Criterion 1, and localized random defects in the case of Criterion 2. Failure Criterion 3 was regarded as the most rigorous and consistent test for copper plating failure.

6.3 Statistical correlation analysis

Correlation coefficients give a numerical summary of the degree of association between two variables. Two correlation coefficients, the Pearson product-moment correlation coefficient

and Spearman's rank correlation coefficient, have been employed to quantify the strength of relationship between the areal parameter values and the associated critical loads [174, 175].

6.3.1 Pearson product-moment correlation coefficient

For n data pairs (X_i, Y_i), Pearson's correlation coefficient is given by

$$r = \frac{\sum_{i=1}^{n}(X_i - \overline{X})(Y_i - \overline{Y})}{\sqrt{\sum_{i=1}^{n}(X_i - \overline{X})^2 \sum_{i=1}^{n}(Y_i - \overline{Y})^2}} \qquad 6\text{-}1$$

Where $\overline{X}$ and $\overline{Y}$ are the means of the X and Y values.

The Pearson product moment correlation coefficient provides a measure of the strength of linear dependence between two variables, giving a value between +1.0 and -1.0 inclusive. If r = 1.0, there is a perfect positive correlation and the data lie on a straight line with a positive slope. If r = -1.0, there is a perfect negative correlation and the line has a negative slope. If r is close to zero, a plot will show scattered data points. Because Pearson's r is based on the idea of linearity, it can be quite misleading in the presence of curvature.

6.3.2 Spearman's rank correlation coefficient

The Spearman correlation coefficient is defined as the Pearson correlation coefficient between the ranked variables, and tied values are assigned a rank equal to the average of their positions in the ascending order of the values. In applications where ties are known to be absent, a simpler formula is given by

$$\rho = 1 - \frac{6\sum d_i^{\,2}}{n(n^2 - 1)} \qquad 6\text{-}2$$

Where d_i is the difference in the ranks given to the two variable values for each item of data and n is the number of characteristics ranked.

Spearman's rank correlation coefficient provides a non-parametric measure of statistical dependence between two variables, varying from +1.0 to -1.0. If there are no repeated data values, a perfect Spearman correlation of +1 or -1 occurs when each of the variables is a perfect monotone function of the other [176].

6.4 Areal surface texture parameter analysis

The critical load determined by the scratch testing is widely regarded as being representative of coating adhesion, and this value strongly depends on the direction in which the scratch is taken. For the CMG glass samples with micro grid pattern structures or random surfaces, the directions of scratches were parallel (as shown in Figure 6.7 (a) and (b)), whereas for the samples with micro ramp pattern structures (as shown in Figure 6.7 (c)), the directions of scratches were vertical, perpendicular and diagonal. The critical load values were the average values of the results generated from all the scratches.

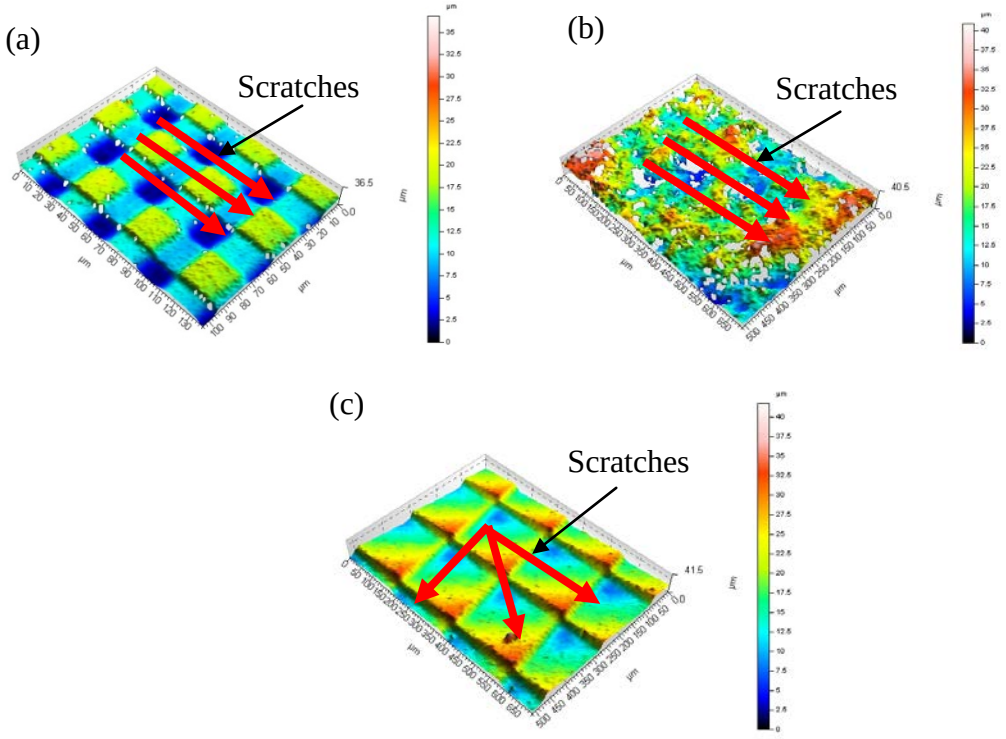

Figure 6.7 Scratch direction relative to the substrate structure
(a) micro grid pattern structure (b) random surface (c) micro ramp pattern structure

Reference surfaces without any bespoke patterns were machined by excimer laser and an example is shown in Figure 6.8. Scratch testing results indicate that the critical load of the reference surfaces falls into the range of 1.0 N – 2.0 N depending on the machining processing parameters, which are much smaller than those of the micro pattern surfaces. This result further confirms that structured surfaces on substrates can increase adhesive bonding strength of copper / glass system.

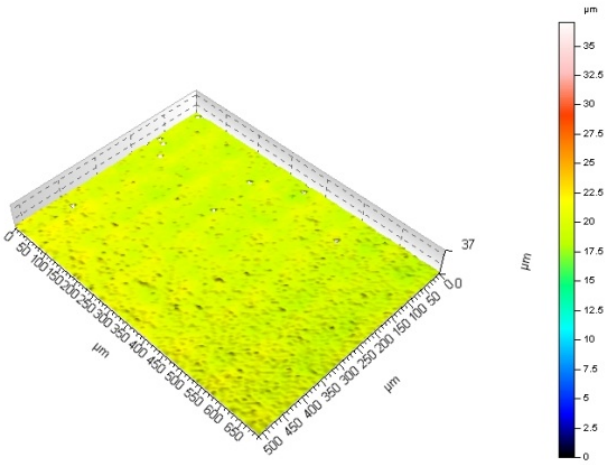

Figure 6.8 Topographic image of reference surface machined by excimer laser (energy density 2.2 J/cm^2, repetition rate 10Hz, 10 shots per area)

In this study, CMG glass samples with various structured surfaces and random surfaces were produced for identifying the optimal surface topography which presents strong copper plating adhesion performance. Detailed processing parameters for each sample by excimer laser are listed in Table 6.2.

Table 6.2 Processing parameters details of structured surface samples for plotting (S-square mask, T-triangular mask, C-circular mask)

Sample number	Side length (mm)	Energy density (J/cm^2)	Repetition rate (Hz)	Shots per area (n)	Pitch spacing (µm)
1	S1	2.2	10	5	40
2	S1	2.2	10	5	50
3	S1	2.2	10	5	60
4	S1	2.2	10	5	70
5	S4	2.2	10	5	200
6	S4	2.2	10	5	200
7	T2	2.2	10	10	100
8	T7	2.2	10	5	200
9	S4	2.2	10	5	80
10	C9	2.2	10	5	100
11	S1	2.2	10	20	50
12	S1	2.2	10	20	50
13	T2	2.2	10	10	160
14	S1	2.4	10	10	80
15	S1	2.2	10	5	30
16	S1	2.2	10	5	40
17	S1	2.2	10	5	50
18	S1	2.2	10	5	50
19	S1	2.2	10	5	60
20	S1	2.2	10	5	70
21	S1	2.2	10	10	30
22	S1	2.2	10	10	40
23	S1	2.2	10	10	70
24	S1	2.2	10	15	30
25	S1	2.2	10	15	40
26	S1	2.2	10	15	70

It has been possible to categorize each areal parameter in terms of the strength of correlation with the critical load values under three failure criteria, being mindful of the definition and relevance of each parameter. Table 6.3 shows correlation values for the main areal parameters with the copper / glass critical load values from scratch testing and the values that demonstrate the strongest behavioural relationships with the copper / glass critical load values have been highlighted (*). These correlation coefficients have been calculated from the graphs presented in Figure 6.9 to Figure 6.65.

From the table it can be seen that in most analysis cases, the quality of correlation has increased as the failure criterion has been changed from simple (Failure Criterion 1 (C1)), to consecutive (Failure Criterion 2 (C2)), to continuous (Failure Criterion 3 (C3)). Most

strongest behavioural relationships show in Failure Criterion 3 and in the total work of (micro-roughness + structure) components. These results also confirm the conclusion that Failure Criterion 3 is the most rigorous and consistent test for copper plating failure and therefore adhesive bond strength, and the hypothesis of both micro-roughness and large scale structure contribute to plating adhesion performance.

From the experimental results, individual graphs for the specific areal parameters that have demonstrated the strongest behavioural relationships with the copper / glass critical load values from the scratch testing results (Table 6.3) have been plotted and discussed. In the graphs, data points are labelled by sample number, as shown in Table 6.2 for tracing and comparison purpose. All data reflects a Failure Criterion 3 analysis.

Graphs are plotted showing:

- Areal parameters versus critical load for the micro-roughness component of structured glass surfaces
- Areal parameters versus critical load for the micro-roughness and structural components of structured glass surfaces
- Areal parameters versus critical load for the micro-roughness and structural components of structured glass surfaces and random glass surfaces

Table 6.3 Areal parameters and associated correlation coefficient values

(C1 - Failure Criterion 1, C2 - Failure Criterion 2, C3 - Failure Criterion 3)

Areal parameters	Figure No.	Failure Criterion	Spearman Coefficient Value (r)			Pearson Coefficient value (ρ)		
			Micro-roughness	Structure	Micro-roughness+ Structure	Micro-roughness	Structure	Micro-roughness+ Structure
Sq	6.9, 6.10	C 1	-0.38	-0.25	-0.32	-4.0	-0.26	-0.34
		C 2	-0.45	-0.30	-0.38	-0.47	-0.31	-0.39
		C 3	-0.72*	-0.58	-0.71*	-0.75*	-0.60	-0.74*
Ssk	6.13	C 1	-0.11	-0.31	-0.19	-0.12	-0.32	-0.20
		C 2	-0.11	-0.27	-0.18	-0.11	-0.28	-0.18
		C 3	-0.21	-0.19	-0.15	-0.22	-0.10	-0.15
Sku	6.15	C 1	0.23	0.13	0.18	0.24	0.14	0.18
		C 2	0.28	0.16	0.21	0.29	0.16	0.22
		C 3	0.50	0.38	0.41	0.53	0.40	0.43
Sa	6.17, 6.18	C 1	-0.40	-0.26	-0.33	-0.42	-0.27	-0.34
		C 2	-0.44	-0.30	-0.36	-0.46	-0.31	-0.37
		C 3	-0.74*	-0.60	-0.71*	-0.77*	-0.62	-0.74*
Sal	6.20	C 1	0.27	-0.24	-0.03	0.28	-0.25	-0.04
		C 2	0.34	-0.36	-0.11	0.35	-0.38	-0.11
		C 3	0.20	-0.69*	-0.02	0.21	-0.72*	-0.02
Str	6.23	C 1	-0.22	-0.36	-0.28	-0.23	-0.38	-0.29
		C 2	-0.32	-0.48	-0.38	-0.33	-0.50	-0.39
		C 3	-0.20	-0.40	-0.27	-0.20	-0.41	-0.28
Sdq	6.25 6.26 6.27	C 1	-0.31	-0.13	-0.31	-0.32	-0.13	-0.32
		C 2	-0.38	-0.16	-0.37	-0.40	-0.17	-0.38
		C 3	-0.65*	-0.59	-0.66*	-0.68*	-0.62	-0.69*
Sdr	6.29 6.30 6.31	C 1	-0.29	-0.14	-0.29	-0.30	-0.14	-0.30
		C 2	-0.35	-0.17	-0.33	-0.36	-0.17	-0.35
		C 3	-0.62*	-0.59	-0.61*	-0.65*	-0.61	-0.64*
Sxp		C 1	-0.32	-0.15	-0.23	-0.34	-0.15	-0.24
		C 2	-0.44	-0.23	-0.34	-0.46	-0.24	-0.36

Table 6.3 continued

Sxp	6.33	M 3	-0.63*	-0.54	-0.59	-0.66*	-0.57	-0.61
Vm	6.35	C 1	-0.36	-0.22	-0.34	-0.37	-0.23	-0.36
		C 2	-0.47	-0.27	-0.46	-0.49	-0.28	-0.48
		C 3	-0.61*	-0.10	-0.27	-0.63*	-0.11	-0.28
Vmp	6.37	C 1	-0.36	-0.22	-0.31	-0.37	-0.22	-0.33
		C 2	-0.47	-0.27	-0.44	-0.49	-0.28	-0.46
		C 3	-0.60*	-0.12	-0.26	-0.62*	-0.13	-0.27
Vmc	6.39	C 1	-0.45	-0.25	-0.36	-0.47	-0.26	-0.38
		C 2	-0.44	-0.28	-0.36	-0.46	-0.30	-0.38
		C 3	-0.74*	-0.62	-0.70*	-0.77*	-0.65	-0.73*
Vv	6.42	C 1	-0.39	-0.25	-0.32	-0.40	-0.26	-0.34
		C 2	-0.43	-0.28	-0.34	-0.44	-0.30	-0.36
		C 3	-0.72*	-0.51	-0.66*	-0.74*	-0.53	-0.68*
Vvc	6.44 6.45	C 1	-0.40	-0.26	-0.33	-0.42	-0.27	-0.34
		C 2	-0.42	-0.29	-0.33	-0.44	-0.30	-0.34
		C 3	-0.70*	-0.50	-0.61*	-0.73*	-0.52	-0.63*
Vvv	6.47	C 1	-0.16	-0.004	-0.007	-0.17	-0.004	-0.007
		C 2	-0.29	-0.13	-0.16	-0.31	-0.13	-0.16
		C 3	-0.51	-0.44	-0.38	-0.53	-0.46	-0.40
Spd	6.49 6.50	C 1	-0.49	-0.32	-0.48	-0.51	-0.33	-0.50
		C 2	-0.50	-0.25	-0.48	-0.52	-0.26	-0.49
		C 3	-0.63*	-0.38	-0.66*	-0.66*	-0.40	-0.69*
Spc	6.52	C 1	-0.22	-0.38	-0.23	-0.22	-0.39	-0.24
		C 2	-0.29	-0.38	-0.29	-0.30	-0.39	-0.30
		C 3	-0.55	-0.60*	-0.50	-0.57	-0.62*	-0.52
Sda	6.54	C 1	0.35	0.10	0.15	0.36	0.10	0.16
		C 2	0.38	-0.03	0.11	0.39	-0.03	0.12
		C 3	0.37	-0.05	0.27	0.39	-0.05	0.28
Sha	6.56	C 1	0.41	0.14	0.25	0.42	0.15	0.26
		C 2	0.39	0.07	0.22	0.41	0.08	0.23
		C 3	0.45	0.24	0.40	0.47	0.25	0.42

6.4.1 Height parameters (*Sq*, *Ssk*, *Sku*, *Sa*)

Height parameters give information regarding the areal height deviation of the surface topography (see Section 2.3.1). Table 6.3 shows that micro-roughness components for height parameters present high associated correlation with critical load, and for the areal height dispersion (*Sq* and *Sa*), both micro-roughness and (micro-roughness + structural) components show a strong correlation.

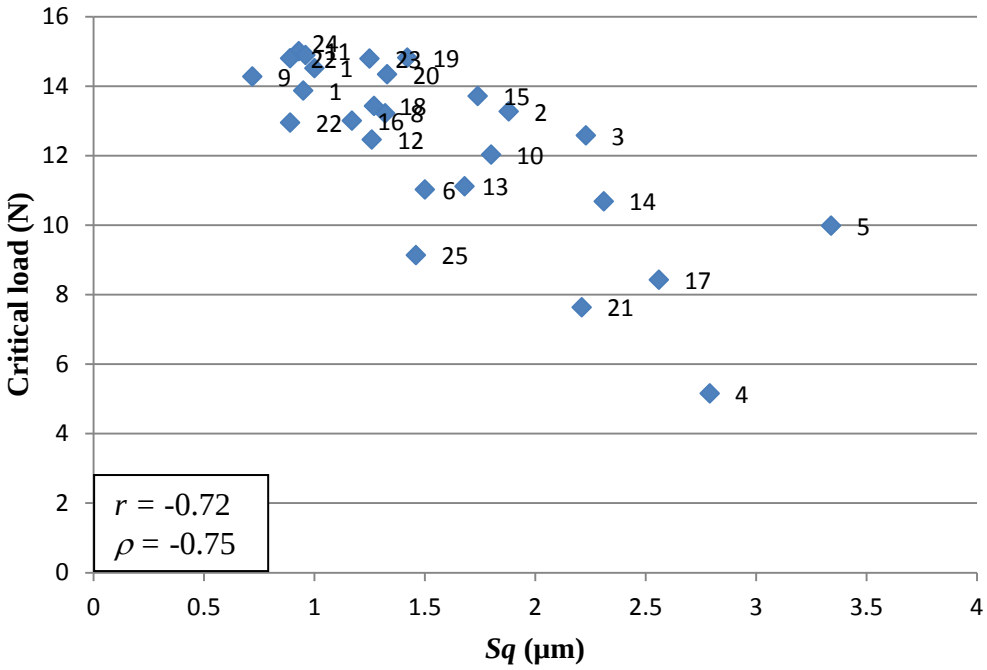

Figure 6.9 *Sq* versus critical load (micro-roughness component) for structured glass

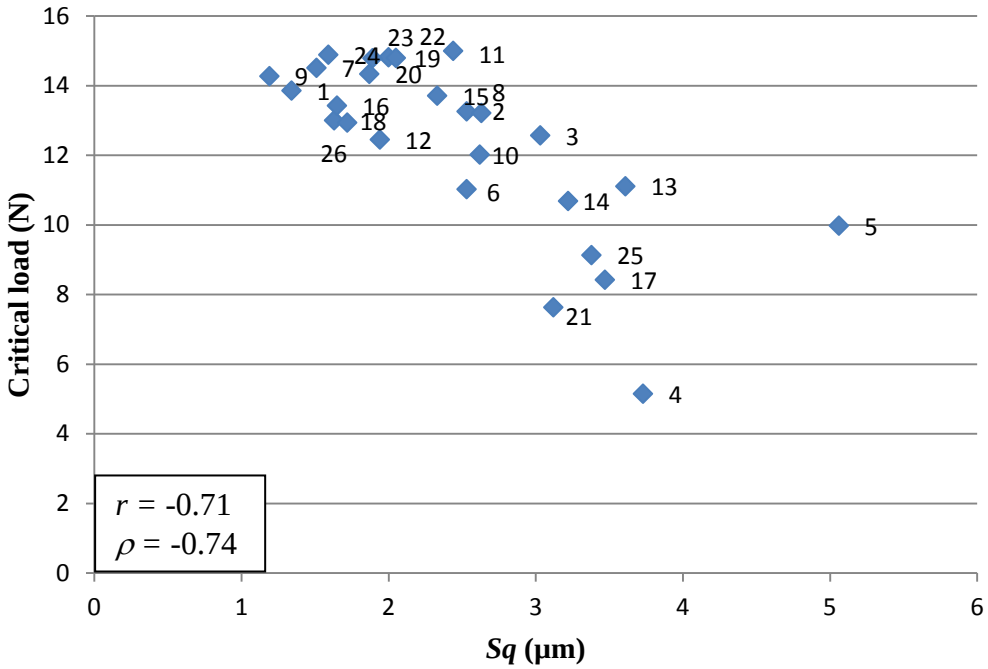

Figure 6.10 *Sq* versus critical load (micro-roughness + structural components) for structured glass

Figure 6.9 and Figure 6.10 indicate there are general marked decreasing trends with critical load increase, for both micro-roughness component and micro-roughness together with structural components. *Sq* is the root mean square height of the scale limited surface, and has direct analogies to the non-areal *R* and *W* two dimensional line profile derived parameters. As one of the height parameters, the *Sq* value depends on height deviation of the surface and is one of the most widely used parameters which indicates surface roughness in a well-known statistical form.

The reason that surface micro-roughness aids in adhesive bonding, is the mechanical interlocking effects. In Figure 6.11, arrows indicate micro-roughness on a segment of the structured surface. In this segment, the copper has completely filled pores on the surface. At this position, the exit of the copper is partially blocked by part of the glass substrate from scratch testing. This place in the interface will exhibit the so-called mechanical interlocking effect. The copper in a pore cannot move past the “overhang” of the pore without plastically deforming such as spalling because of the physical impediment. Plastic deformation acts as an energy absorbing mechanism and the strength of the adhesive bond appears to increase, therefore the critical load from scratch testing is higher. However, if the micro-roughness is

too large, as shown as the failure start point in Figure 6.11, it will also cause the random failure.

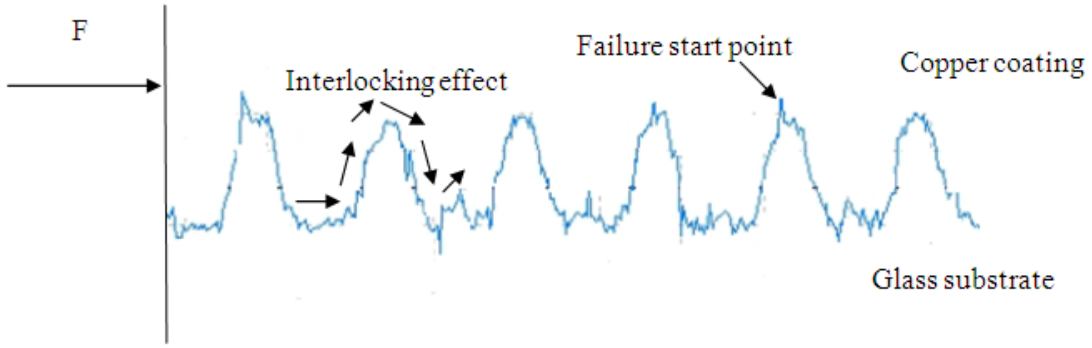

Figure 6.11 Schematic showing roughness affects copper plating adhesion by mechanical interlocking effect

Generally speaking, micro-roughness together with structural components can also be regarded as the surface roughness, and the correlation can also be explained by mechanical interlocking of the copper adhesive with glass substrate surface roughness. Roughness provides copper plating and glass substrate with intimate contact along a tortuous path. If a force is driven into the edge of this bond, there is no abrupt plane of stress transfer. Rather, for the crack to propagate across the bond, the lines of force have to take detours. Some of the detours go into the copper coating. If the copper coating plastically deforms during the debonding, energy is consumed and the strength of the adhesive bond appears to be higher.

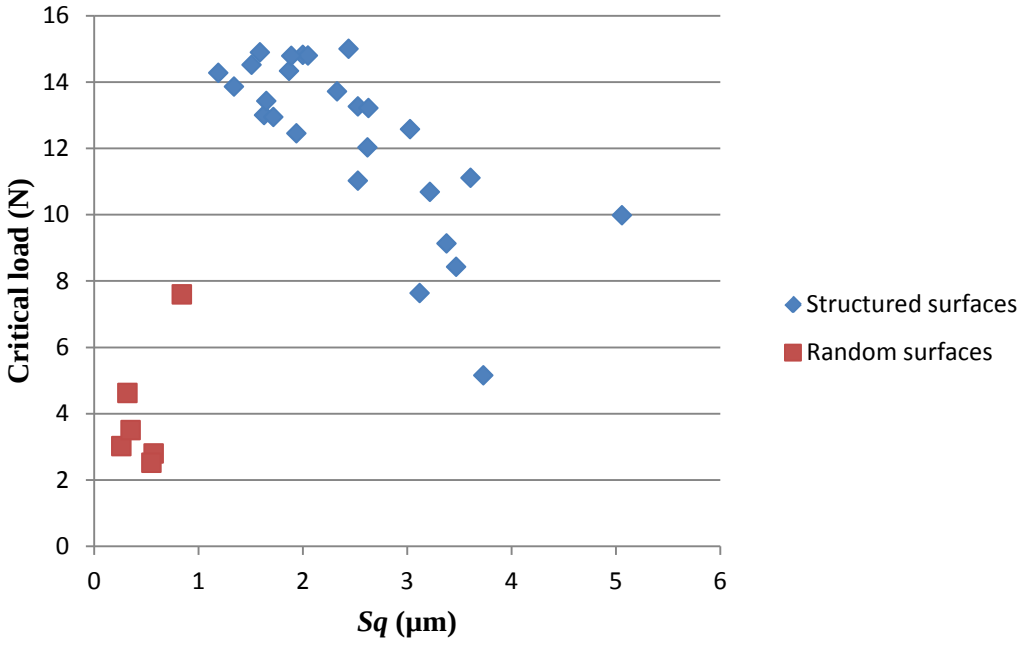

Figure 6.12 *Sq* versus critical load (micro-roughness + structural components) for structured surfaces and random surfaces

Figure 6.12 shows two distinct clusters for the correlation between *Sq* and critical load for structured surfaces and random surfaces. There is no obvious trend for random surfaces. The possible reason is that the failure criteria for structured surfaces and random surfaces are different. For structured surfaces, mechanical interlocking effect and sharp edges effect interact, and mechanical interlocking effect aids in adhesive bonding. However, for random surfaces, there are more random sharp edges distributed across the surface and therefore stochastic failure dominates the failure modes. Compared with structured surfaces, random surfaces show much lower critical load which confirms that structured surfaces can improve plating adhesion.

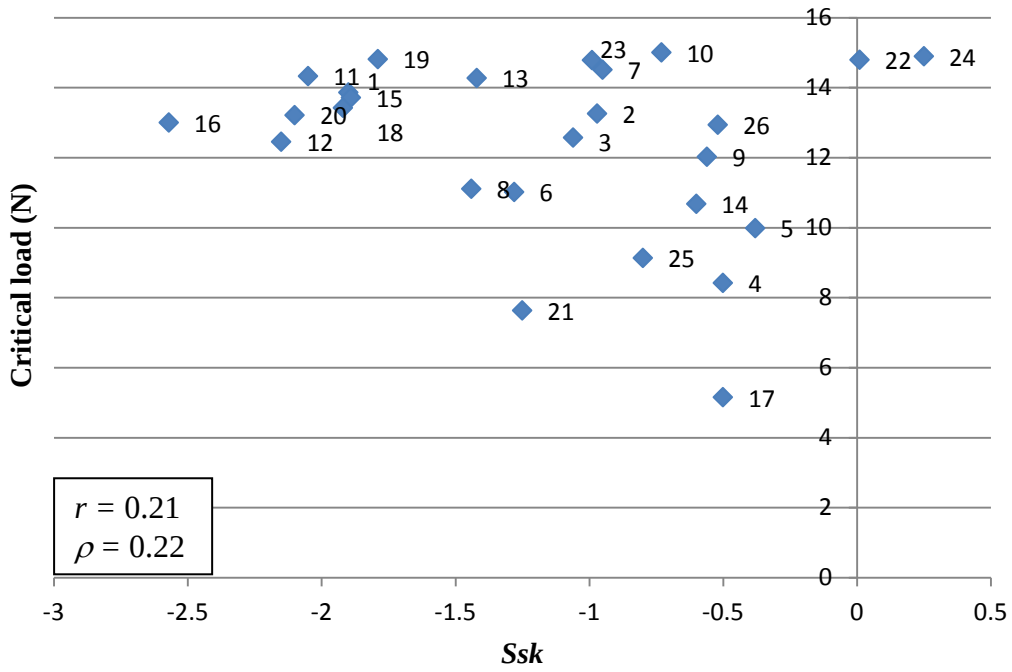

Figure 6.13 *Ssk* versus critical load (micro-roughness component) for structured glass

In Figure 6.13, most *Ssk* values are negative, which shows laser machined structured surfaces have an asymmetric distribution of topography heights, and the height of the surface is mainly above the mean plane with the surface tending towards having a flatter top and some deep valleys below the mean surface plane. This result shows an agreement with the excimer laser machining process which is based on groove generation.

Ssk is the measurement of asymmetry of surface deviations about the mean reference plane. Although there is no significant correlation for *Ssk* with critical load, this parameter can effectively be used to describe certain aspects of the shape of a topographic height distribution. From a surface function point of view, this parameter can give some indication of the existence of valley dominated surfaces.

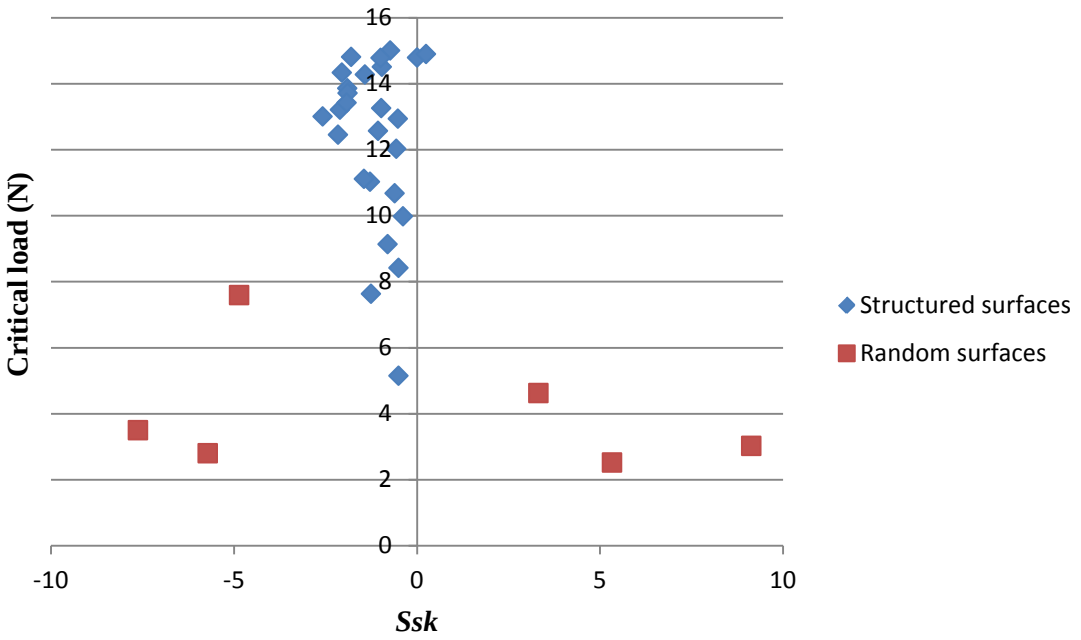

Figure 6.14 *Ssk* versus critical load (micro-roughness + structural components) for structured surfaces and random surfaces

Figure 6.14 shows that the absolute values of *Ssk* for random surfaces have a larger spread than the structured surfaces equivalents, which indicates the distribution has a longer tail in both the upward and downward direction of the mean plane. The depth and the peaks of the surface are quite random and unpredictable due to the nature of random surfaces.

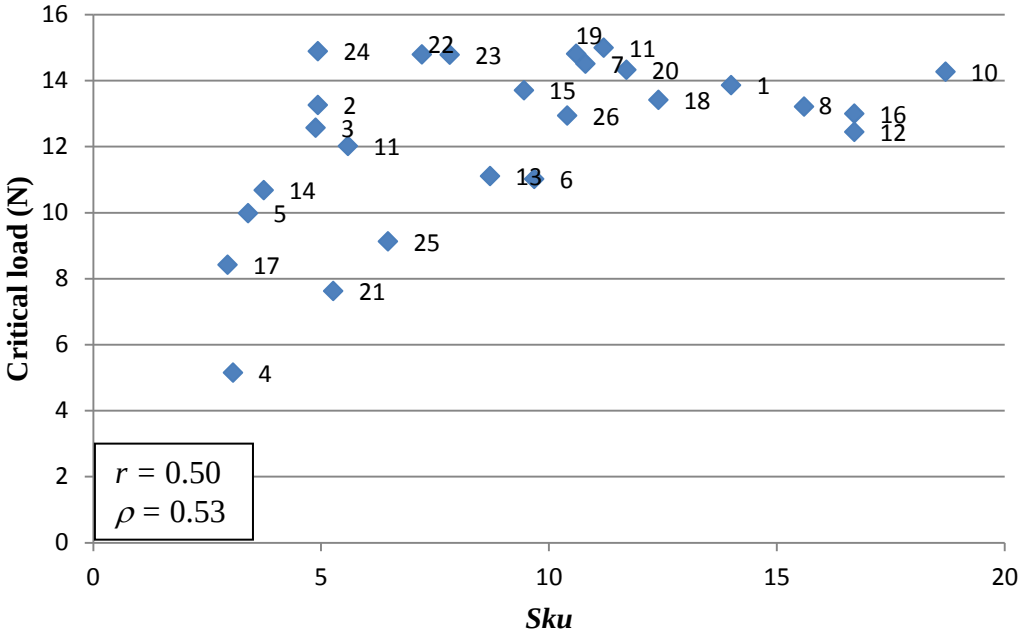

Figure 6.15 *Sku* versus critical load (micro-roughness component) for structured glass

Figure 6.15 suggests that there is no significant correlation for *Sku* with respect to critical load. *Sku* characterizes the spread of the height distribution and provides a measure of the sharpness of the area. A spiky surface will have a high kurtosis value while a bumpy surface will have a low kurtosis value. A kurtosis of a Gaussian surface characterized by normally distributed heights about the mean plane has a typical value of 3. A centrally distributed topography height distribution has a kurtosis value of larger than 3, whereas the kurtosis of a well spread height distribution is less than 3.

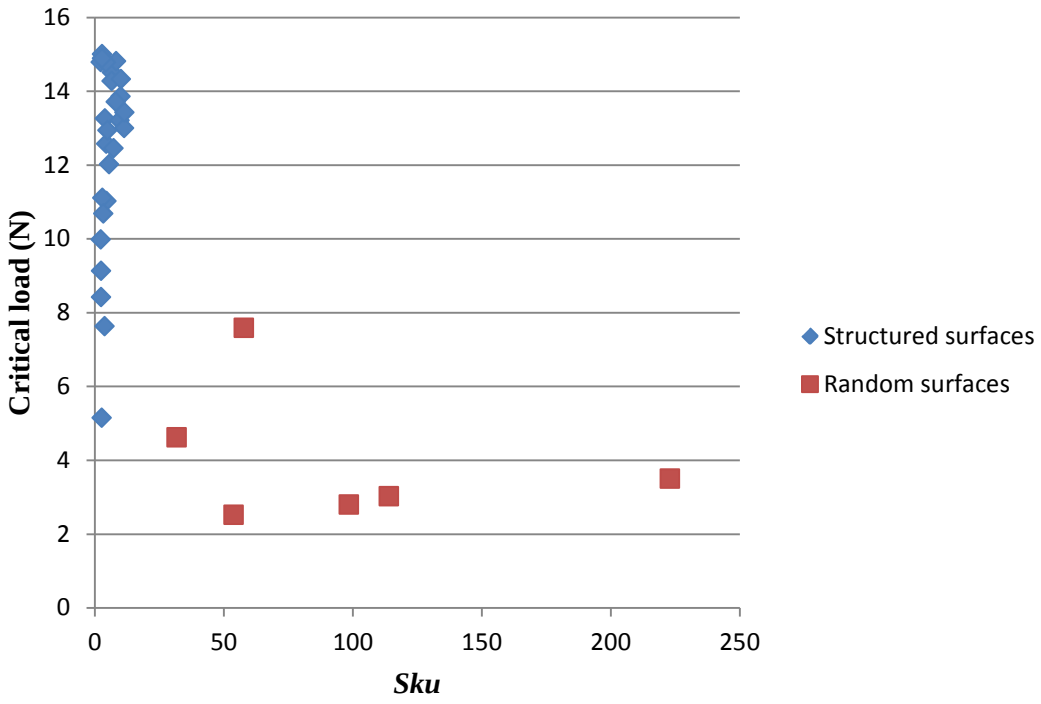

Figure 6.16 *Sku* versus critical load (micro-roughness + structural components) for structured surfaces and random surfaces

Figure 6.16 shows the values of *Sku* for random surfaces are much larger than the structured surfaces, which indicates a centrally distributed topography height distribution of the mean plane. This is because of the nature of random surfaces.

Although *Ssk* and *Sku* do not show strong correlation between critical load for copper plating adhesion, with the combination of these two parameters it may be possible to identify deep valleys and flat tops in surfaces.

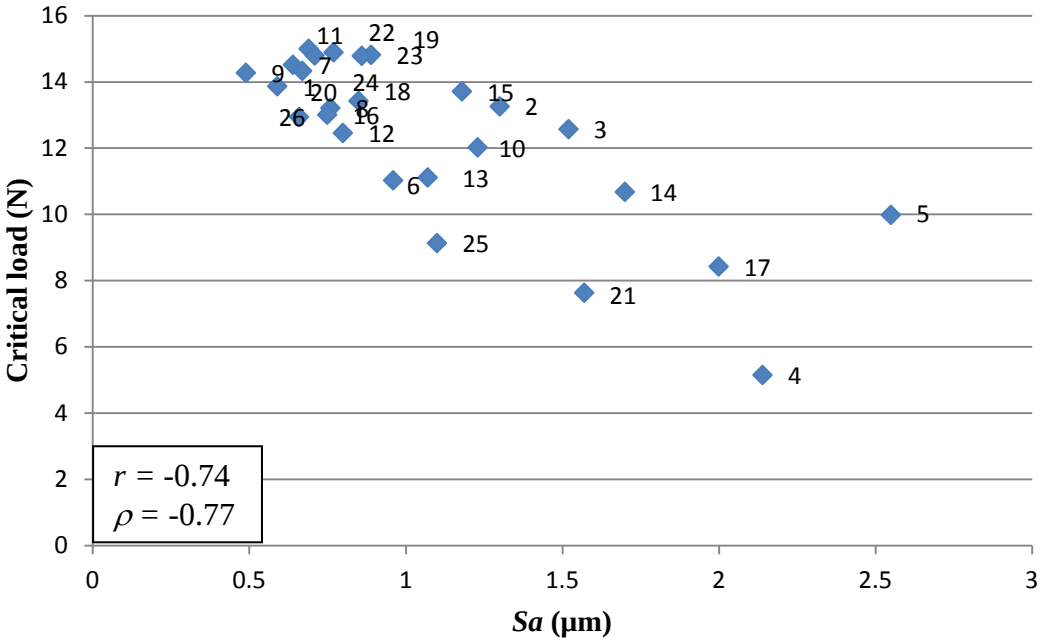

Figure 6.17 *Sa* versus critical load (micro-roughness component) for structured glass

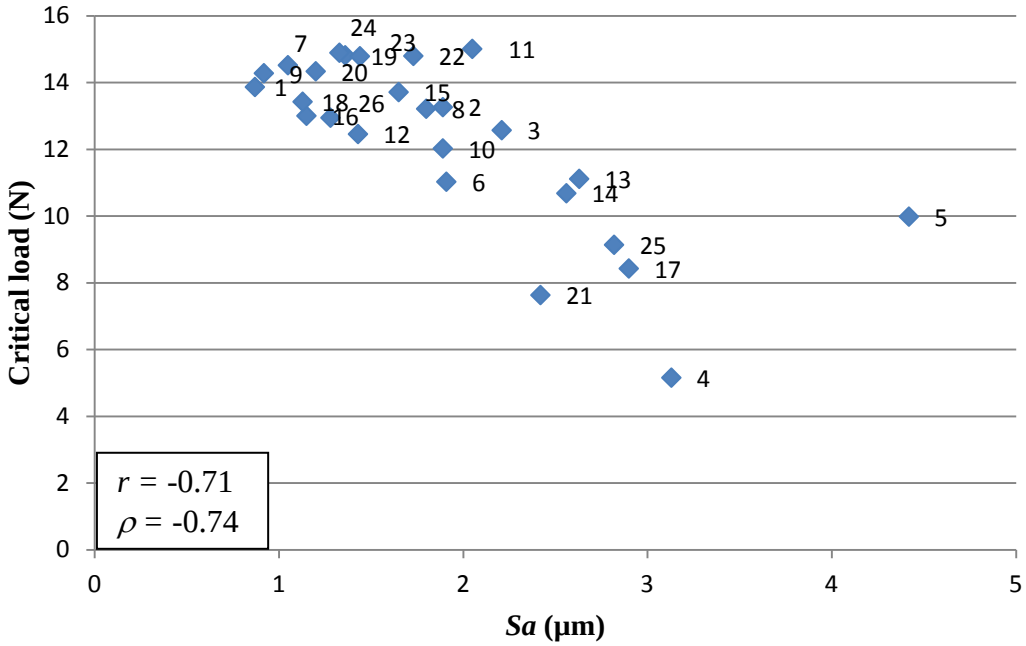

Figure 6.18 *Sa* versus critical load (micro-roughness + structural components) for structured glass

Sa, mean roughness, is the arithmetic mean of the departure of the surface from the mean line in the roughness profile. Therefore, the larger the value of *Sa*, the greater the roughness profile of the surface roughness. The parameters *Sa* and *Sq* are highly correlated and show the

same trends as illustrated in Figure 6.17 and Figure 6.18 (compared to Figure 6.9 and Figure 6.10). The idea that plating adhesion depends on the mechanical interlocking of the copper adhesive with glass substrate surface roughness is shown in Figure 6.11.

Figure 6.19 also suggests the same trend as *Sq* shown in Figure 6.12. This is because these two parameters *Sa* and *Sq* are highly correlated. Possible reasons and explanations are given earlier.

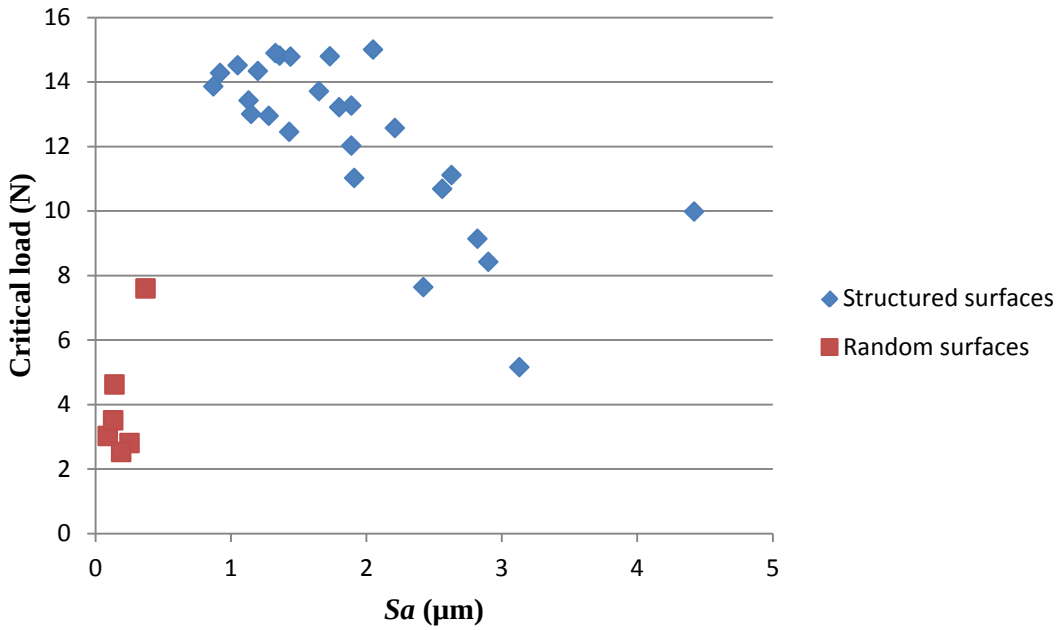

Figure 6.19 *Sa* versus critical load (micro-roughness + structural components) for structured surfaces and random surfaces

Sa and *Sq* both measure the dispersion of the heights from a reference surface, so it is appropriate to adopt only one of these parameters, *Sq*, for the future plating adhesion prediction and discussion.

6.4.2 Spatial parameters (*Sal*, *Str*)

From Table 6.3, it can be seen that the spatial parameters (*Sal* and *Str*) present the strongest correlation with critical load for the structural component of the glass surfaces. The reason is that these two parameters are used to characterize the spacing of topographic features and identify the texture patterns.

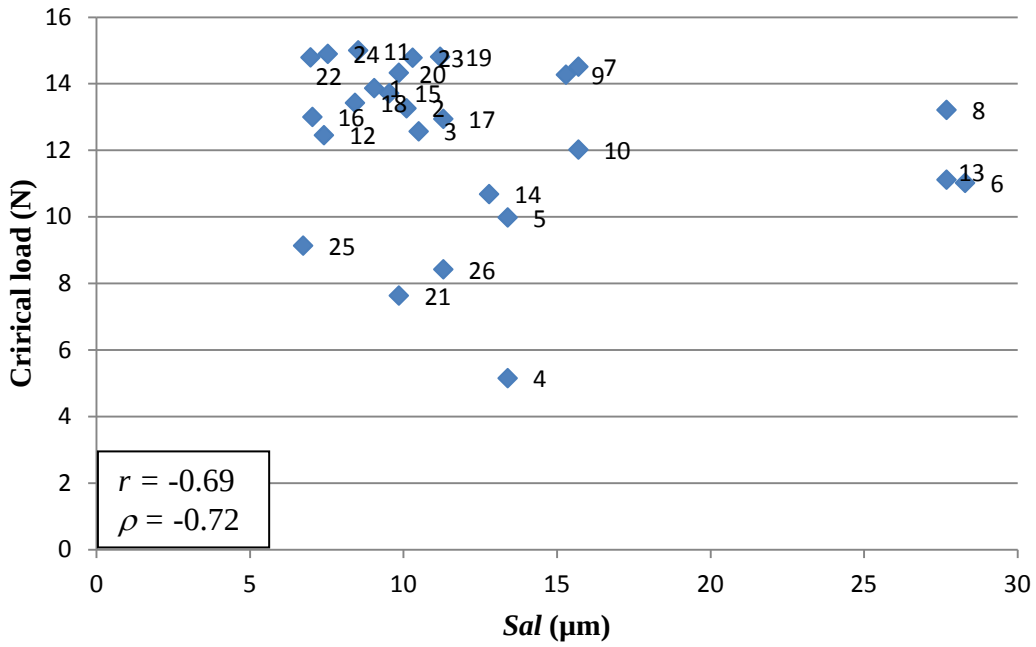

Figure 6.20 *Sal* versus critical load (structural component) for structured surfaces

The fastest decay autocorrelation length *Sal* is a parameter in length dimension used to describe the autocorrelation character of the areal autocorrelation function (see Section 2.3.2). A large value of *Sal* denotes that the surface is dominated by low spatial frequency (or long wavelength) components, while a small value of the *Sal* denotes the opposite situation. In the experiments, the frequency component refers to the feature size of the structure including pitch spacing and overlapping part which are determined by the excimer laser processing parameter settings.

Figure 6.20 indicates the presence of higher critical loads go with smaller *Sal* value which is dominated by higher frequency components in the structural component. This trend also confirms the previous conclusion: substrate glass with fine structured surfaces which is machined by smaller mask dimensions can improve copper plating adhesion. The possible

reason is that large scale micro features are susceptible to spurious, non-representative plating failure as a function of sharp edge effect stress concentrations and thin coating thickness in scratch testing as shown in Figure 6.21.

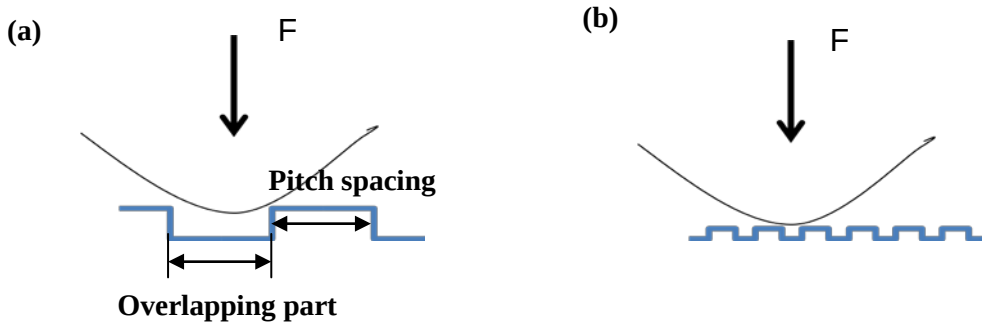

Figure 6.21 Schematic showing the stylus tip crossing the surface of different sizes of substrate structure feature (a) Large features (b) Small features

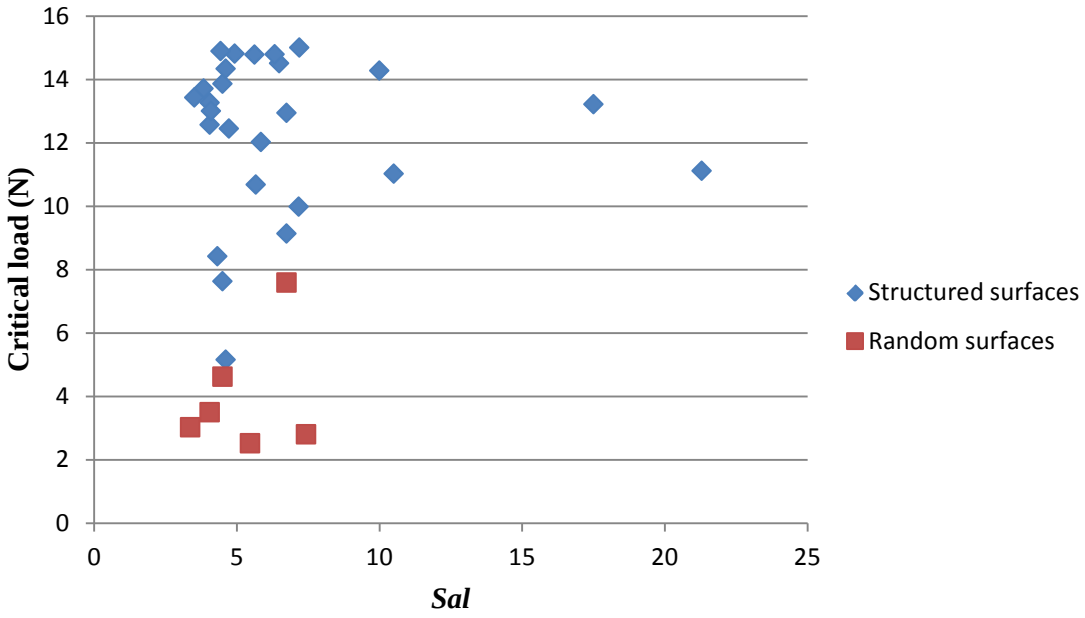

Figure 6.22 *Sal* versus critical load (micro-roughness + structural components) for structured surfaces and random surfaces

Figure 6.22 also illustrates two distinct clusters for the correlation between *Sal* and critical load. Comparing with structured surfaces, there is no extreme large *Sal* value shown for random surfaces. This could be explained by the nature of random surfaces. Unlike the large

scale structures designed by excimer laser processing, random surfaces are dominated by short wavelength structural components.

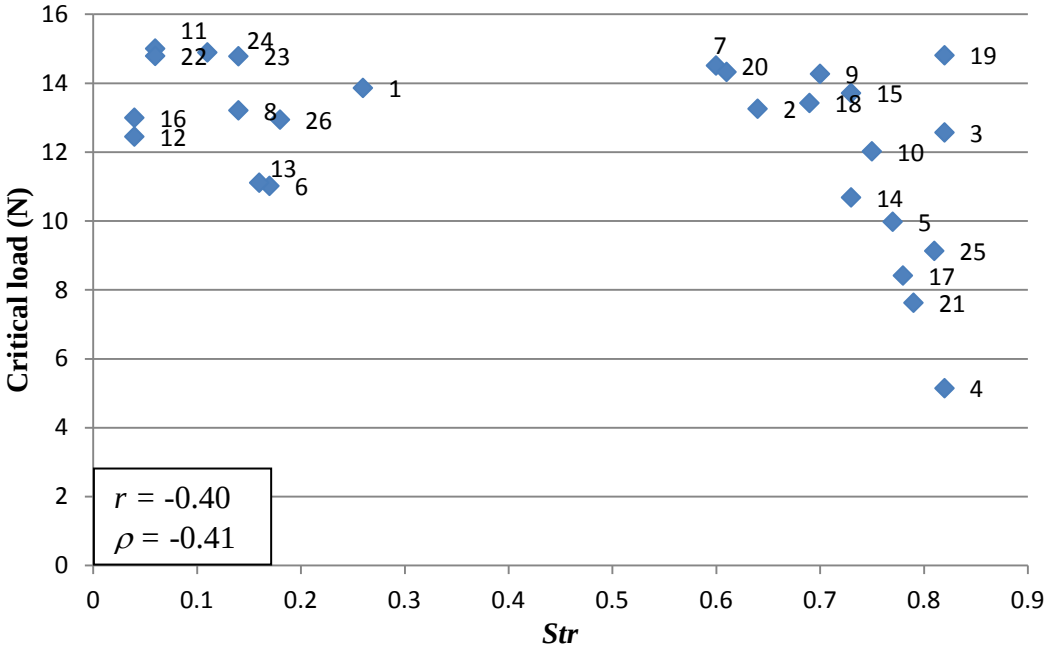

Figure 6.23 *Str* versus critical load (structural component) for structured surfaces

When plotting the *Str* value against the critical load, it is found that the *Str* does not yield a significant trend as shown in Figure 6.23. The mathematical definition of *Str* determines the gap of data distribution between 0.3 and 0.5 (see Chapter 2, Table 2.3). The texture aspect ratio of surface *Str* is a parameter used to identify the topographic texture pattern, uniformity of the texture aspect in all directions. Larger values, *Str* > 0.5, indicate isotropy in different directions, whereas smaller values, *Str* < 0.3, indicate stronger anisotropy (see Section 2.3.2).

Micro-grid based structured surfaces are highly micro-isotropic which have *Str* values of larger than 0.5. The micro-isotropy is a natural outcome of structured surfaces through the excimer laser machining process. However, some micro ramp structured surfaces or pyramid-based structured surfaces are anisotropic, so some *Str* values fall into the range smaller than 0.3.

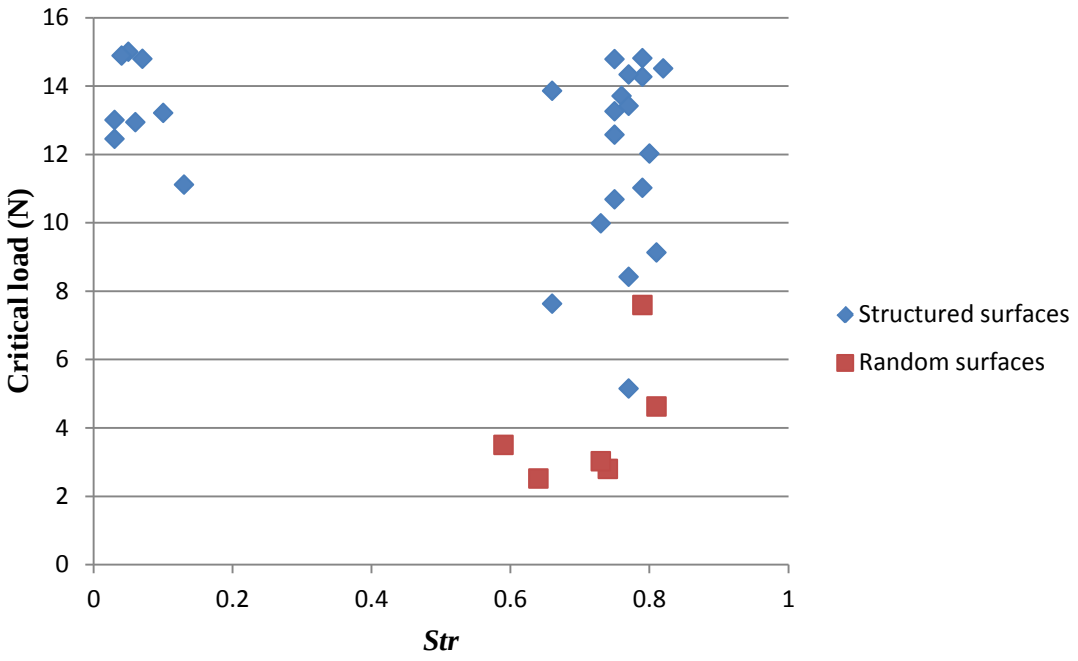

Figure 6.24 *Str* versus critical load (micro-roughness + structural components) for structured surfaces and random surfaces

Figure 6.24 shows all *Str* values for random surfaces are larger than 0.5 which indicates isotropy in different directions. This observation demonstrates and reveals the nature of random surfaces.

Spatial parameters refer to the spacing of certain topographic features. It is noticed that spatial parameters, both *Sal* and *Str*, show the highest associated correlation coefficient values for structural component, which suggests spatial parameters are useful to identify the large scale structure.

6.4.3 Hybrid parameters (*Sdq*, *Sdr*)

The hybrid parameters are parameters based on both amplitude and spatial information (see Section 2.3.3). Any changes that occur in either amplitude or spacing may have an effect on the hybrid property of the surface. So from Table 6.3, it can be seen that all the components for hybrid parameters present high associated correlation with critical load.

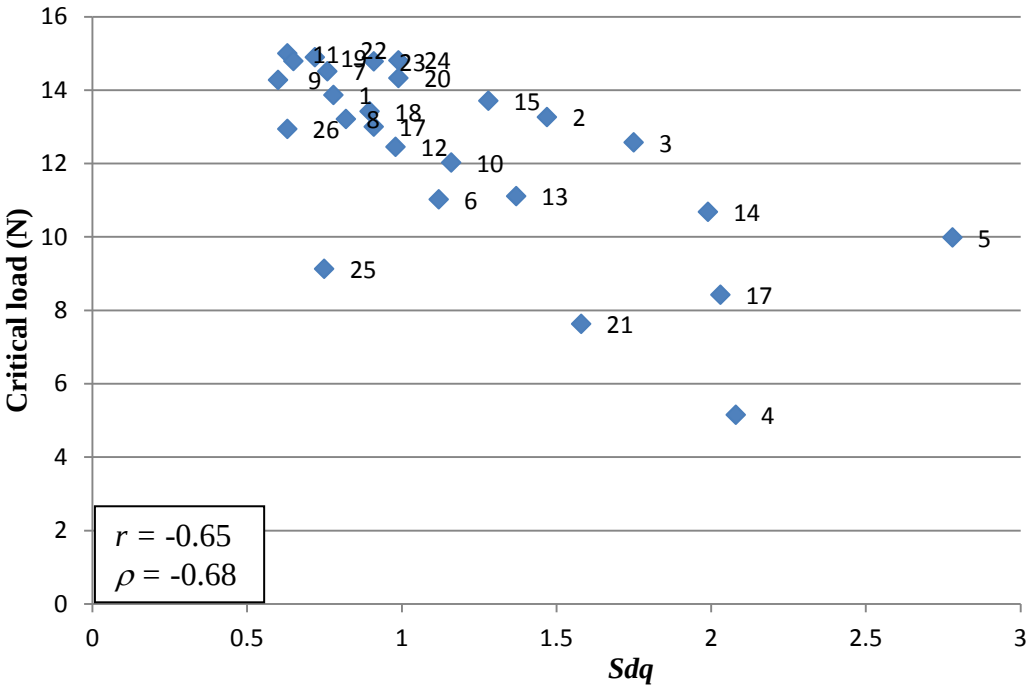

Figure 6.25 *Sdq* versus critical load (micro-roughness component) for structured surfaces

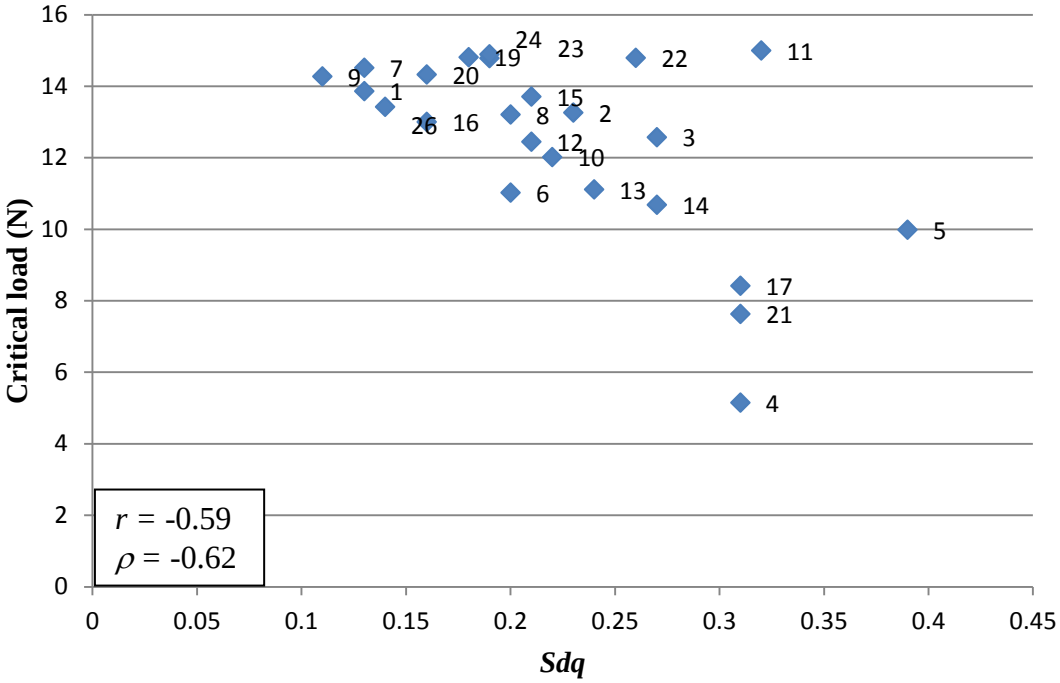

Figure 6.26 *Sdq* versus critical load (structural component) for structured surfaces

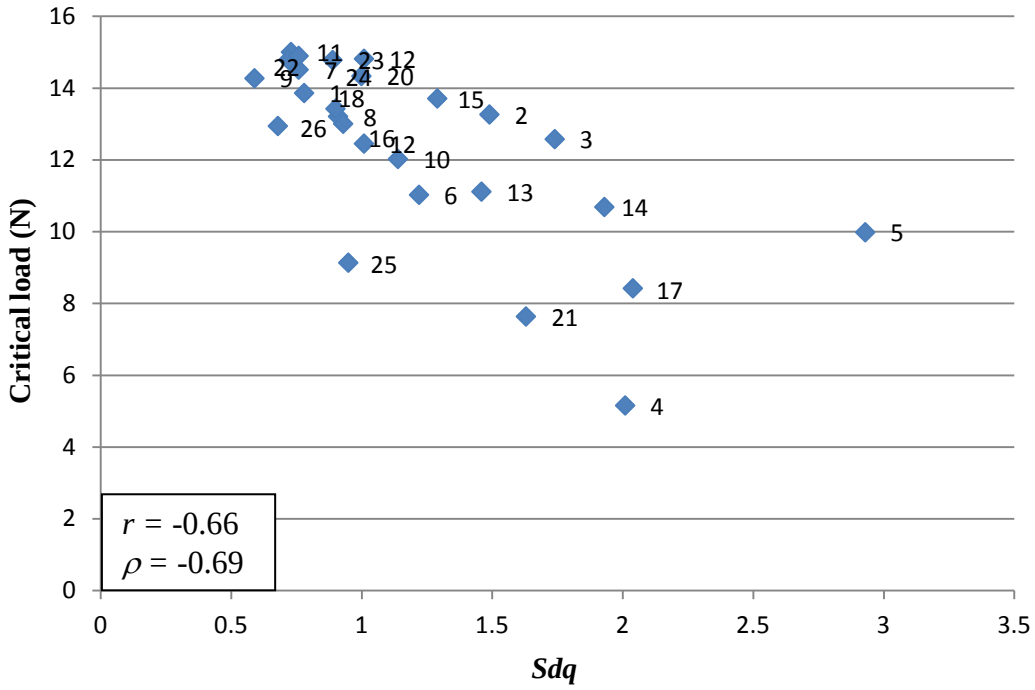

Figure 6.27 *Sdq* versus critical load (micro-roughness + structural components) for structured surfaces

Figure 6.25 to Figure 6.27 illustrate there are decreasing trends with critical loads increasing for micro-roughness component, structural component, and micro-roughness together with structural components. *Sdq* is the root mean square value of the surface slope with the sampling area, and generated on the basis of amplitude and spatial information about the surface. The difference of *Sdq* means that not only the size of peaks and valleys is higher in case of a rough surface, but they are steeper as well.

In addition, Figure 6.25 to Figure 6.27 all indicate that scratch testing failures occur earlier with relatively large *Sdq*. A higher *Sdq* value may signify a peaky surface with many sharp edges and this trend shows the same expectation in this study, i.e. sharp edges are susceptible to premature and / or random copper bond failure. This is typified by a scratch testing stylus impacting on a structural discontinuity, resulting in localized failure as illustrated in Figure 6.2.

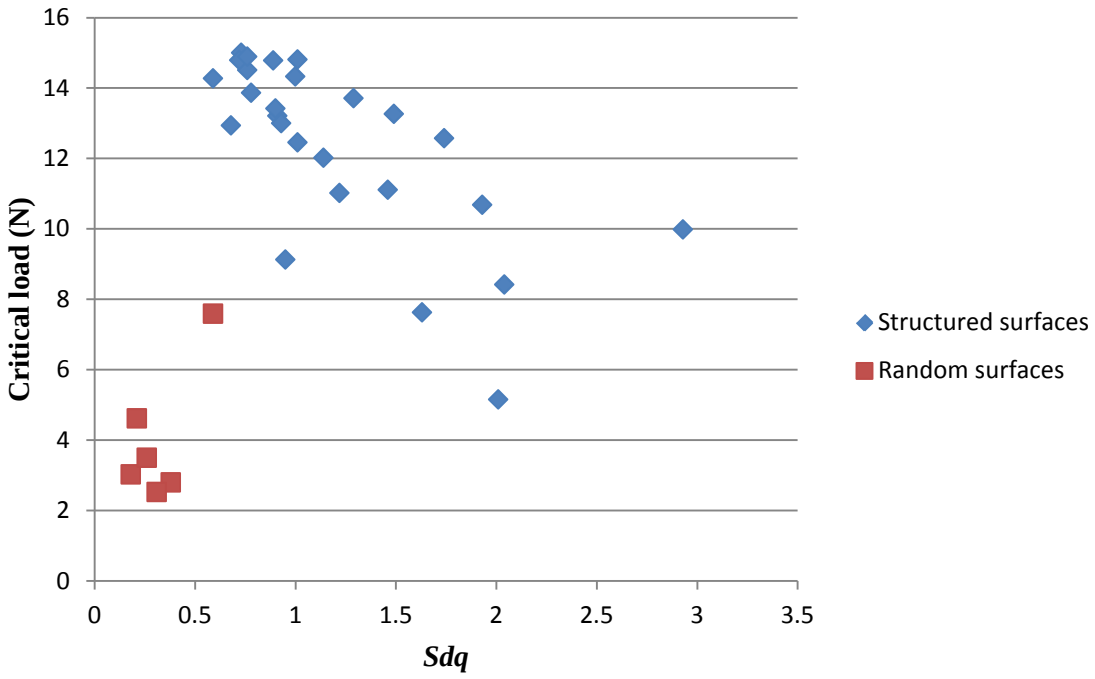

Figure 6.28 *Sdq* versus critical load (micro-roughness + structural components) for structured surfaces and random surfaces

Figure 6.28 shows two distinct clusters for the correlation between *Sdq* and critical load. This parameter can be affected by changes that occur in either amplitude or spacing of the surface. This could also be explained by the fact that the failure modes for structured surfaces and random surfaces are different. For structured surfaces, the mechanical interlocking effect and sharp edges affect interaction, and the mechanical interlocking effect aids in adhesive bonding. However, for random surfaces, there are more randomly sharp edges distributed across the surface and therefore stochastic failure dominates the failure modes.

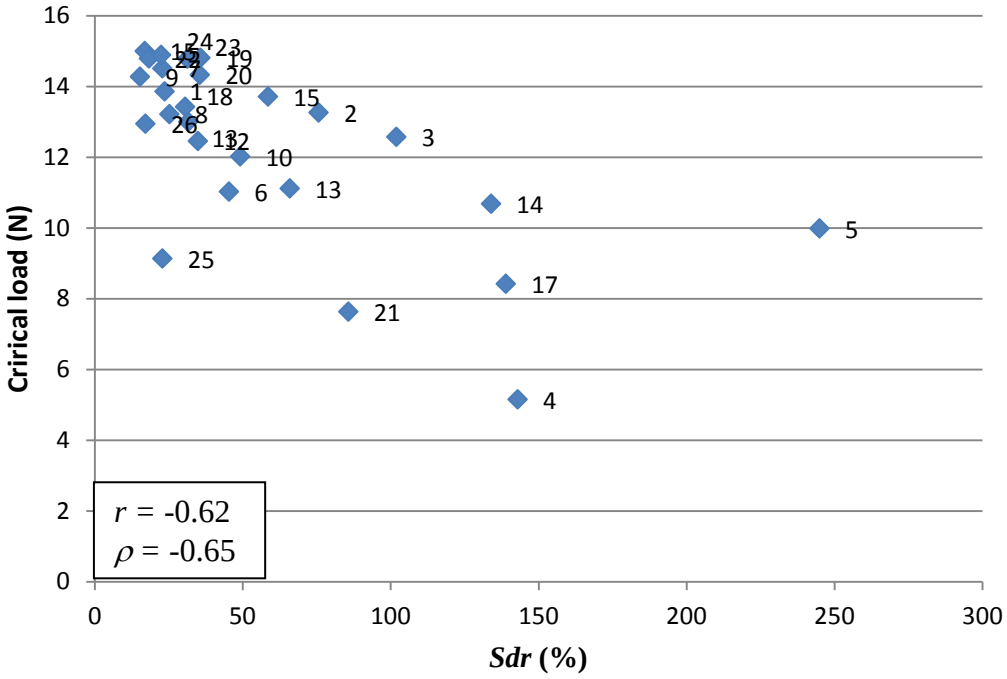

Figure 6.29 *Sdr* versus critical load (micro-roughness component) for structured surfaces

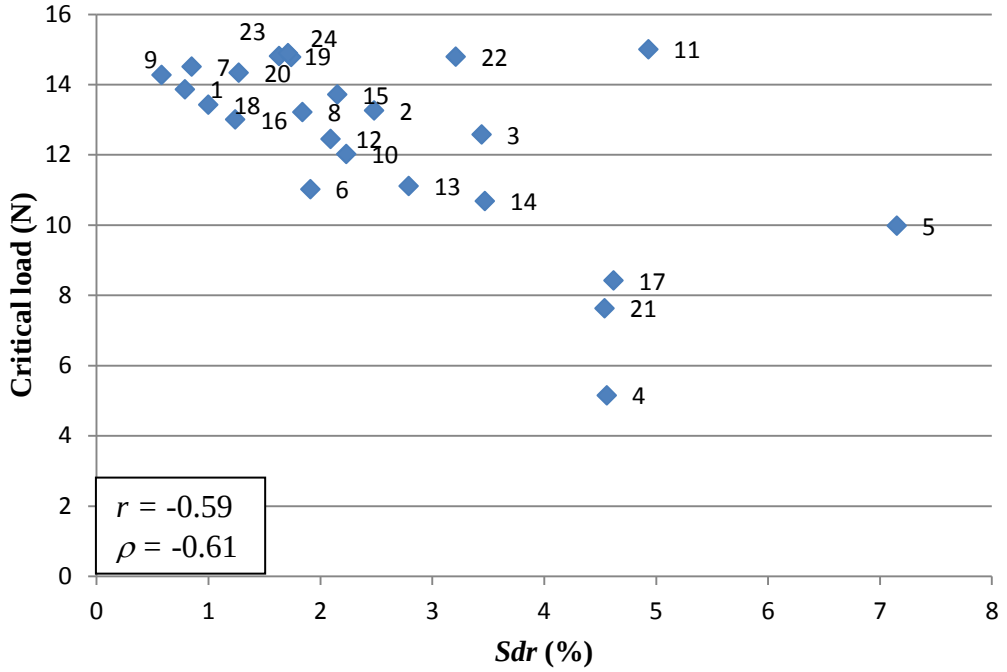

Figure 6.30 *Sdr* versus critical load (structural component) for structured surfaces

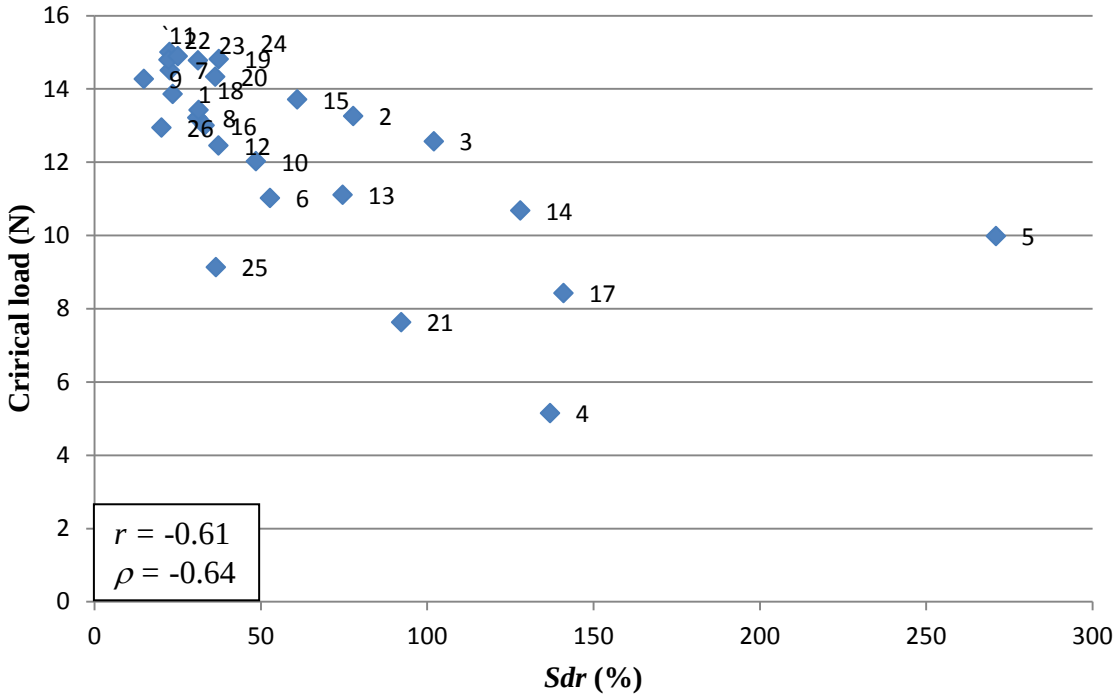

Figure 6.31 *Sdr* versus critical load (micro-roughness + structural components) for structured surfaces

Clear trends can be observed in *Sdr* with respect to critical loads from scratch testing for micro-roughness component, structural component, and micro-roughness plus structural components as shown in Figure 6.29 to 6.31. *Sdr* is the ratio of the increment of the interfacial area of a surface over the sampling area. A large value of *Sdr* indicates the significance of either the amplitude, or the spacing, or both.

Functionally in adhesion applications, *Sdr* characterizes the real contact area between adherend and adhesive. If interfacial interactions are the basis for adhesion, the sum of those interactions will scale as the area of contact. If the actual area of contact is increased by a large amount, the total energy of surface interaction increases by an amount proportional to the surface area. However, for rough surfaces such as very steep surfaces, the values of the developed interfacial area ratio are usually larger and the critical loads are smaller which means failure occurs earlier. Once again, this trend could be explained by the situation that sharp edges are susceptible to premature and / or random copper bond failure.

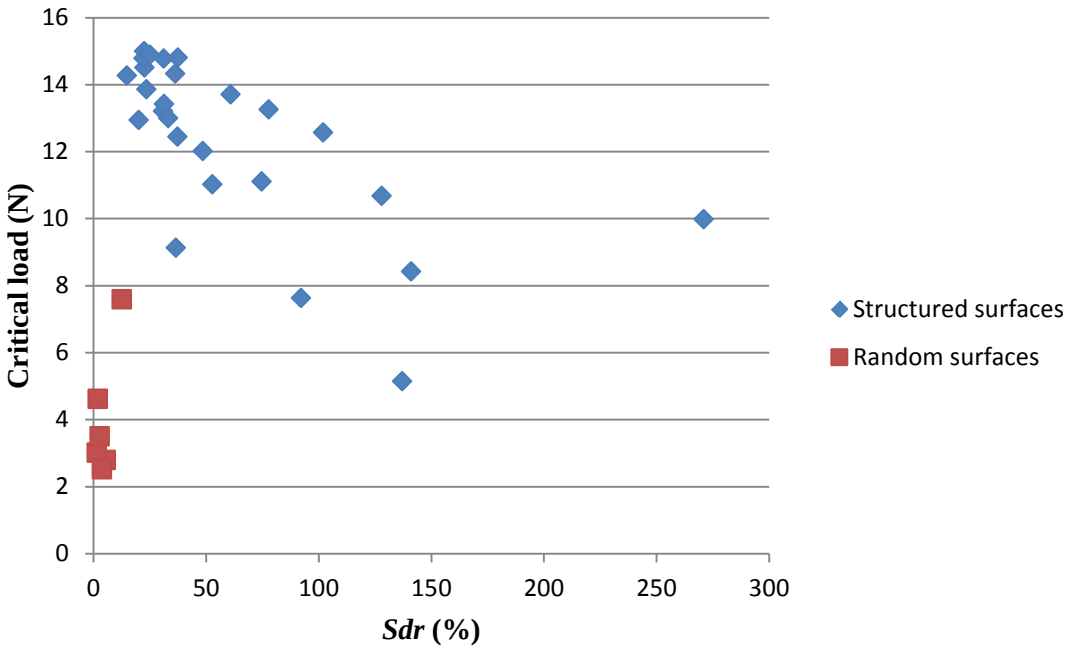

Figure 6.32 *Sdr* versus critical load (micro-roughness + structural components) for structured surfaces and random surfaces

From Figure 6.32 it can be seen that the *Sdr* values for random surfaces are much smaller. This is because in copper plating adhesion, *Sdr* characterizes the real contact area between copper coating and glass substrate. Structured surfaces should enlarge the interfacial area of the surface and therefore enhance plating adhesion strength which is signified by critical load from scratch testing.

6.4.4 Functional parameters (*Sxp*, *Vm*, *Vmp*, *Vmc*, *Vv*, *Vvc*, *Vvv*)

Areal parameters presented in this section are associated with the material ratio of the scale limited surface, which refers to the ratio of the area of the material at a specified height to the evaluation area. The height of the material ratio curve is termed the total roughness, and the width is the percent of material at different profile amplitudes. The slope of this curve can be useful in determining how fast a surface will wear (see Section 2.3.4).

From Table 6.3, it can be seen that high associated correlation coefficient values for functional parameters are present in the relationship between micro-roughness component and the critical load. The reason is that material ratio curve and the functional parameters

derived from it are correlated with some functional properties of surfaces, such as bearing, wear, running in and fluid retention. Surface micro-roughness dominates in these fields.

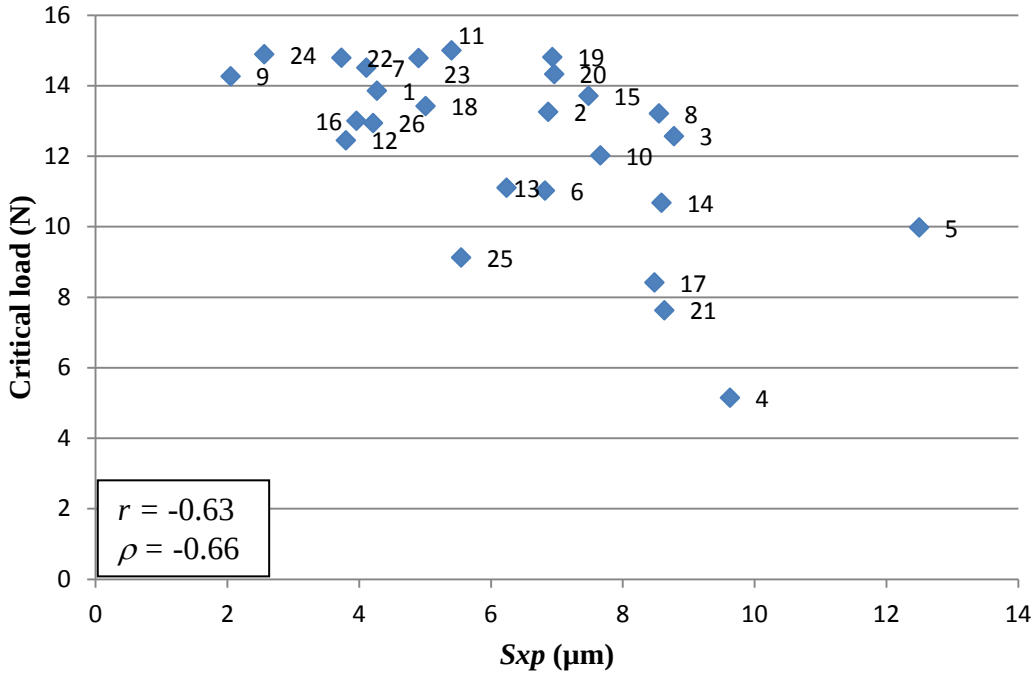

Figure 6.33 *Sxp* versus critical load (micro-roughness component) for structured surfaces

Peak extreme height parameter *Sxp* refers to the difference in height between 2.5 % and 50 % of the material ratio. *Sxp* is important in bearing applications and this parameter indicates the depth from the surface material (2.5 %) to the remaining material area (50 %) by wear or modification. Figure 6.33 presents a generally decreasing distribution trend and failure occurred earlier with larger *Sxp* values. Large scale structures such as deep valleys may result in large *Sxp* value and show weaker plating adhesion. Reasons for this are similar to those discussed earlier.

From Figure 6.34 it can be seen that there are two distinct clusters for the correlation between *Sxp* and critical load, and the *Sxp* value for random surfaces are significantly smaller. This could also be explained by the nature of random surfaces. It is easier for random surfaces to be worn because there are more sharp peaks on the surface.

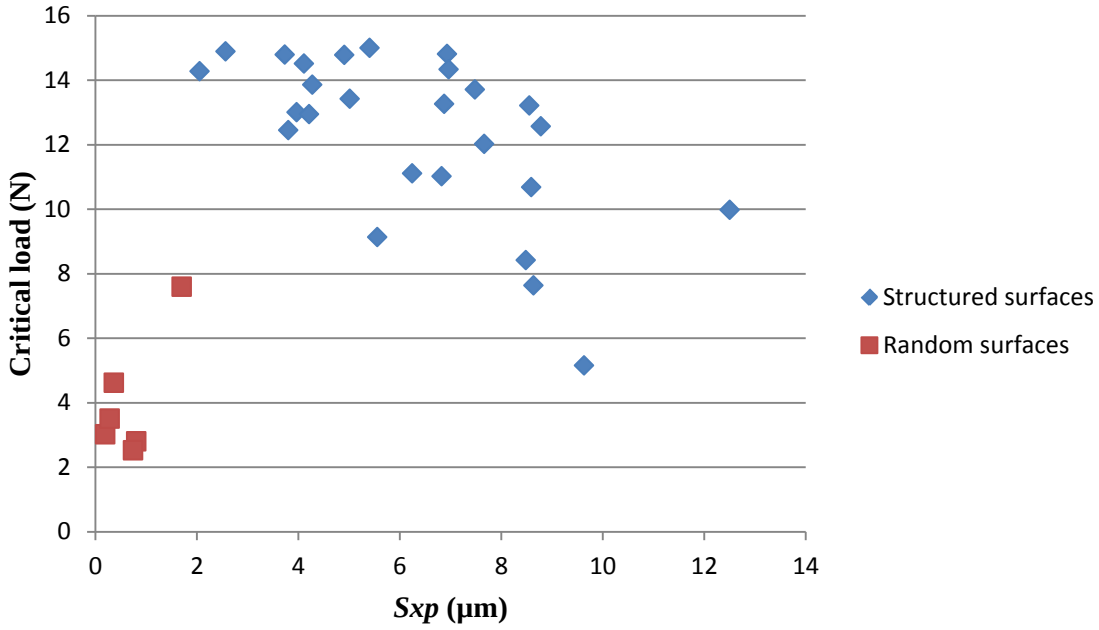

Figure 6.34 *Sxp* versus critical load (micro-roughness + structural components) for structured surfaces and random surfaces

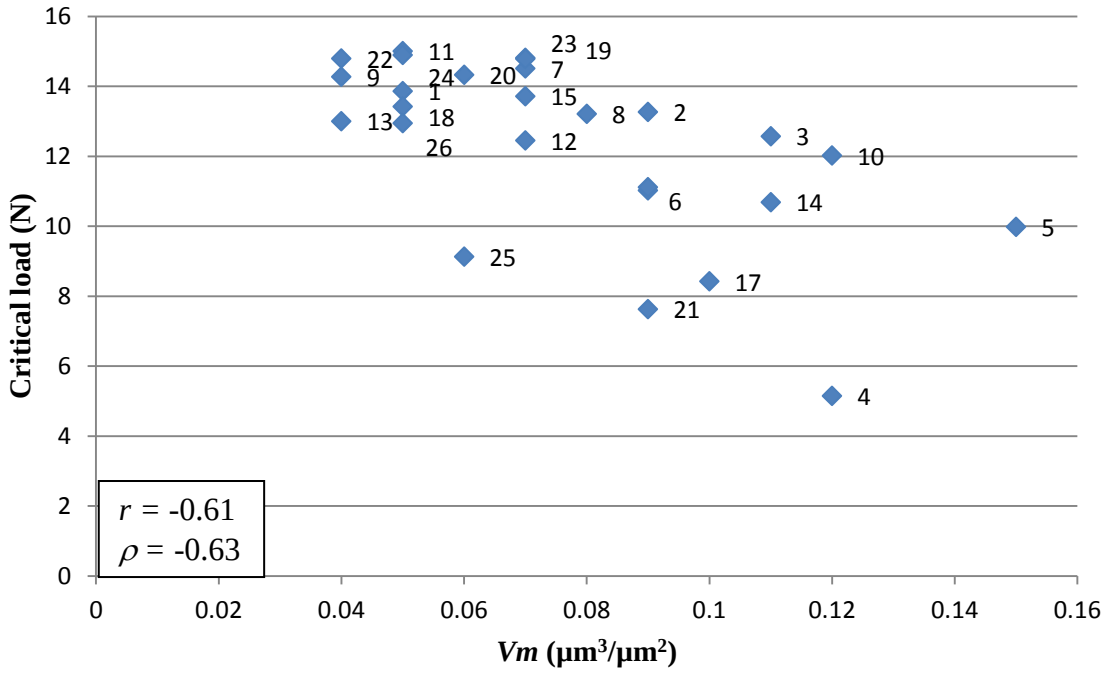

Figure 6.35 *Vm* versus critical load (micro-roughness component) for structured surfaces

Vm (*mr*), the material volume, is the volume of material per unit area at a given material ratio calculated from the areal material ratio curve. For example, *Vm* (*mr*) = A $\mu m^3/\mu m^2$ would

indicate that a layer A µm thick of material over the measured cross section would account for all the material from the highest peak to the *mr* % point on the material ratio curve [112]. Figure 6.35 indicates that critical load slowly increases when the *Vm* parameter decreases. That is because extreme peaks may contribute to the *Vm* value and surfaces with extreme peaks are also prone to localized random failure caused by the sharp edge effect as mentioned before. For excimer laser machined samples, the peaks can be formed as a function of deep depth machining.

However, there is no significant difference for *Vm* between structured surfaces and random surfaces as shown in Figure 6.36.

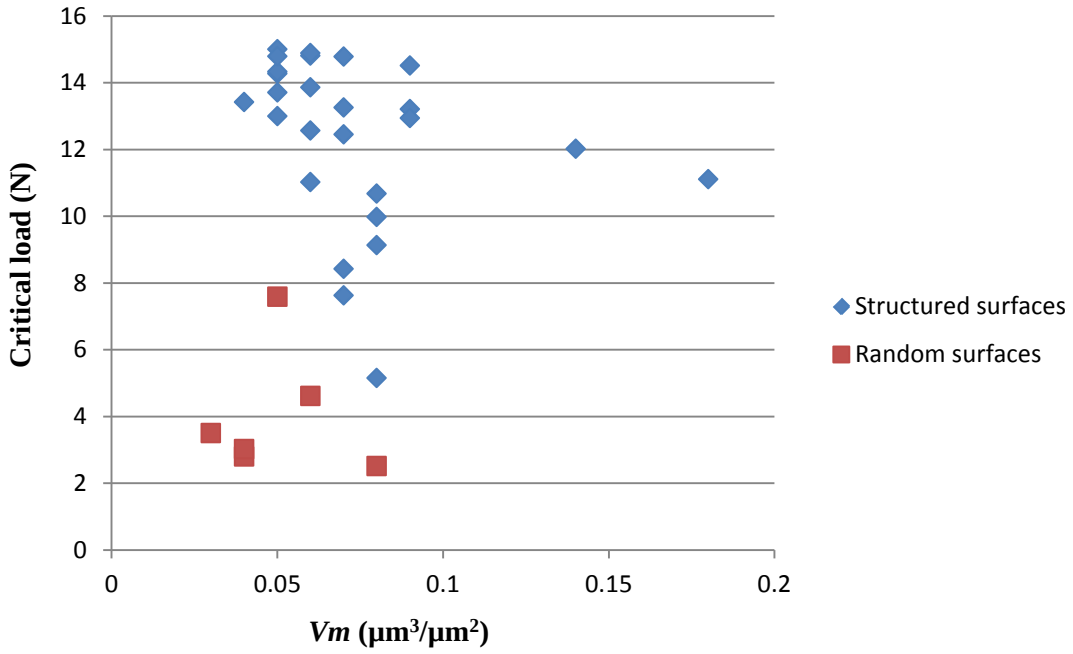

Figure 6.36 *Vm* versus critical load (micro-roughness + structural components) for structured surfaces and random surfaces

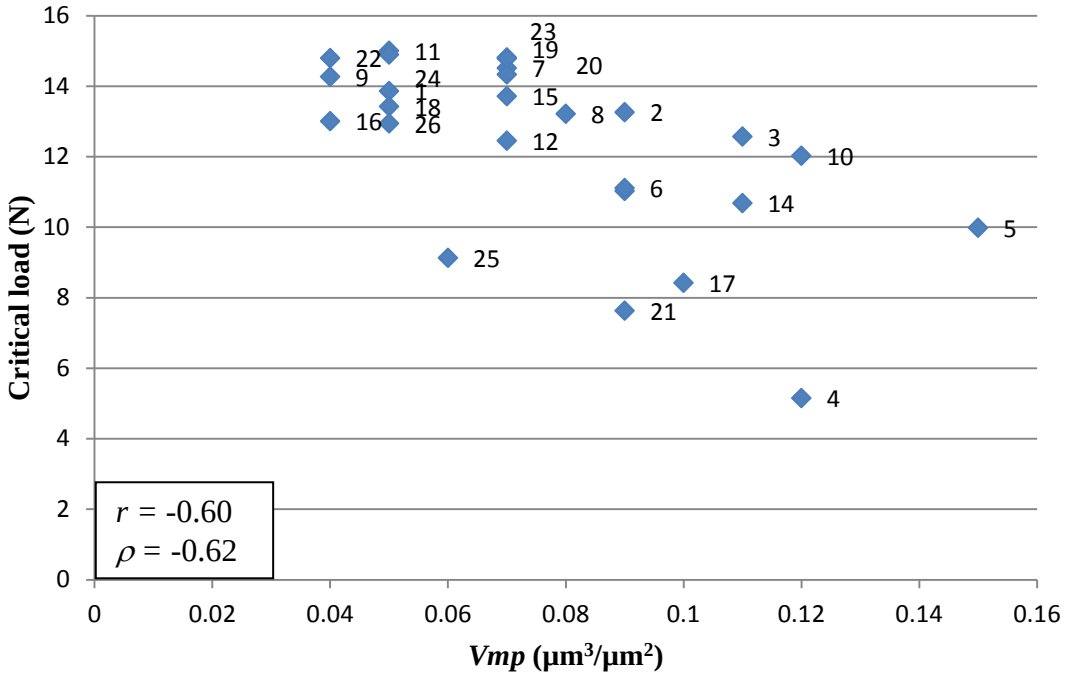

Figure 6.37 *Vmp* versus critical load (micro-roughness component) for structured surfaces

Vmp, the peak material volume, is the volume of material comprising the surface from the height corresponding to a material ratio level, "*p*", to the highest peak. The default value of *p* is 10 % but may be changed as needed. A larger peak material volume *Vmp* indicates a good bearing property. This parameter is useful to understand how much material may be worn away for a given depth of the bearing curve.

Figure 6.37 suggests higher critical load occurs with smaller *Vmp* value. This is because a larger *Vmp* value is usually due to large peaks on the surface. For plating adhesion evaluated by scratch testing, surfaces with large peaks are prone to local random failure modes and show poor plating adhesion, and vice versa.

However, there is no significant difference for *Vmp* between structured surfaces and random surfaces as shown in Figure 6.38.

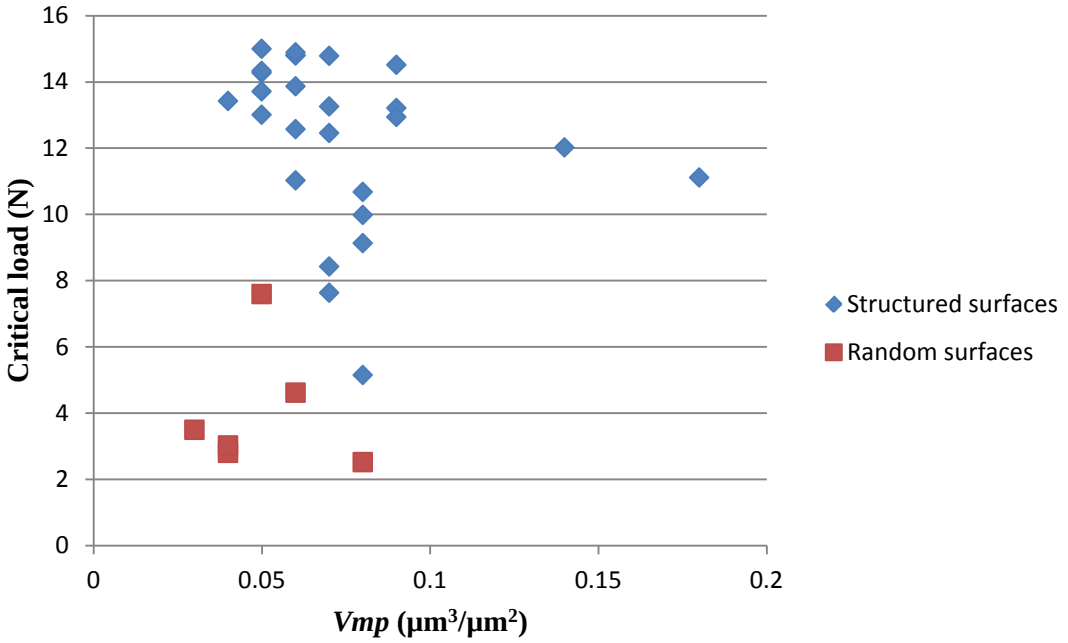

Figure 6.38 *Vmp* versus critical load (micro-roughness + structural components) for structured surfaces and random surfaces

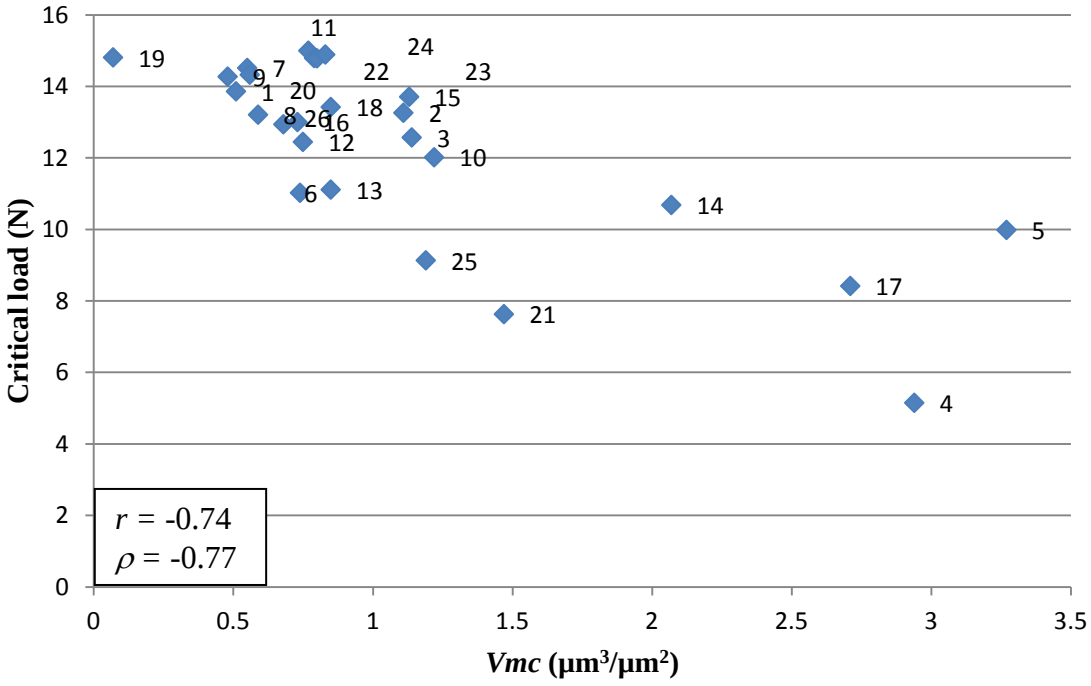

Figure 6.39 *Vmc* versus critical load (micro-roughness component) for structured surfaces

Vmc (*p*, *q*), the core material volume, is the volume of material comprising the texture between heights corresponding to the material ratio values of *p* and *q*. The default value for *p*

is 10 % and the default value for *q* is 80 % but may be changed as needed. This parameter shows how much material is available for load support once the top levels of surfaces are worn away [112].

Figure 6.39 suggests higher critical load occurs with smaller *Vmc* value. This parameter is generated based on the material ratio curve which is termed the total roughness, and *Vmc* indicates a measure of the material forming the surface between various heights which strongly depends on the amplitude of surface roughness. Hence *Vmc* shows a similar trend compared to the micro-roughness characterization *Sq*. Another explanation is the schematic shown in Figure 6.40. Surfaces with extreme valleys result in large *Vmc* values. These extreme valleys from local micro-roughness could be regarded as being equivalent to the large scale structured surface edge. From the previous discussion, it is suggested that this could result in failure due to the sharp edge effect.

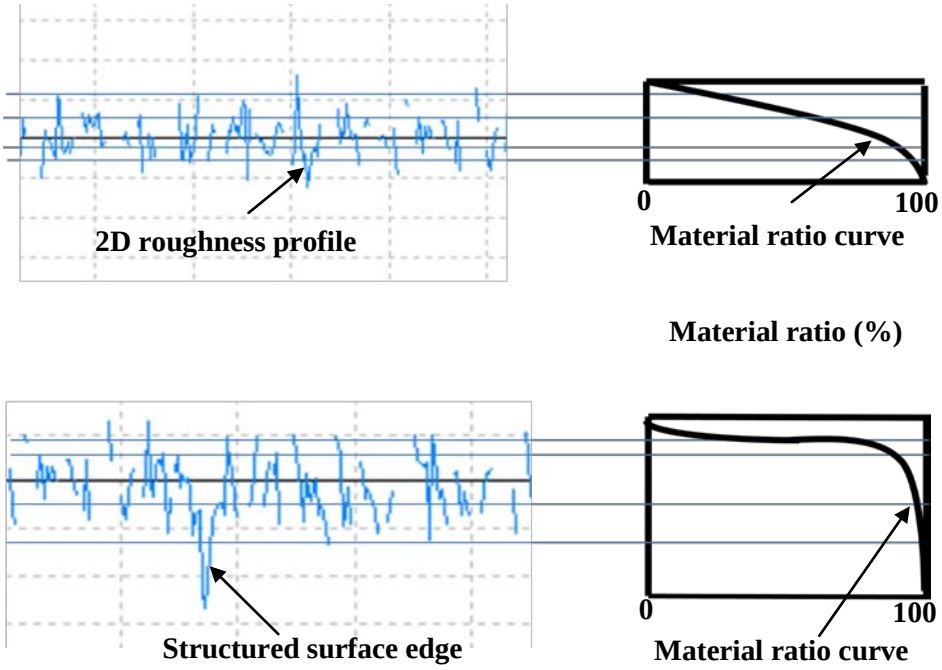

Figure 6.40 Relationship between surface roughness and material ratio curve

Figure 6.41 shows there are two distinct clusters for the correlation between the *Vmc* parameter and critical load for structured surfaces and random surfaces, with *Vmc* values of the random surfaces tending to be smaller.

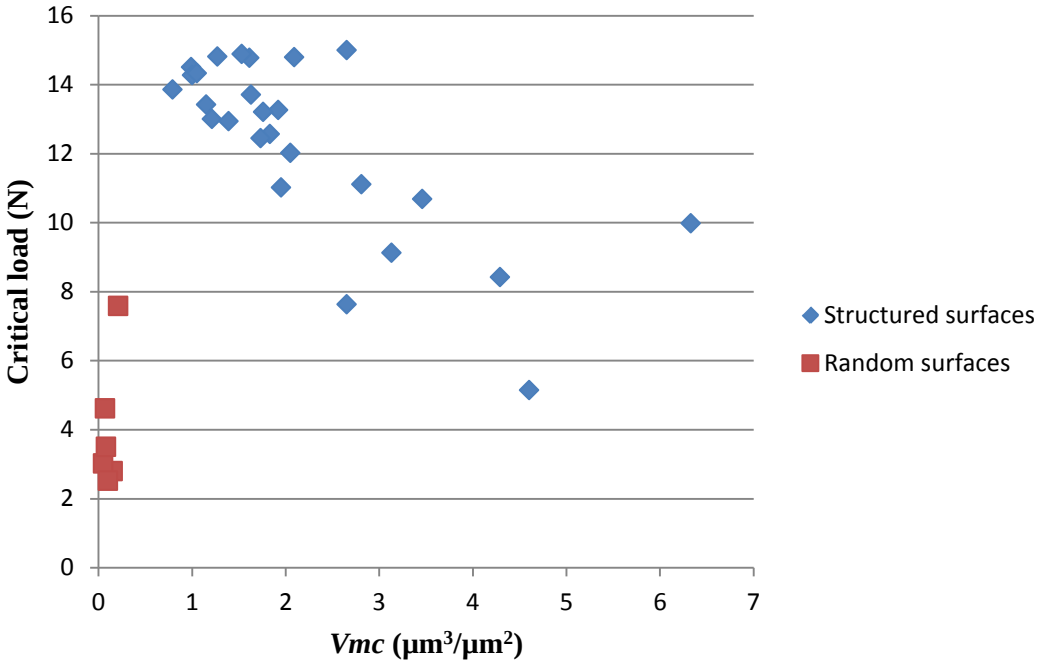

Figure 6.41 *Vmc* versus critical load (micro-roughness + structural components) for structured surfaces and random surfaces

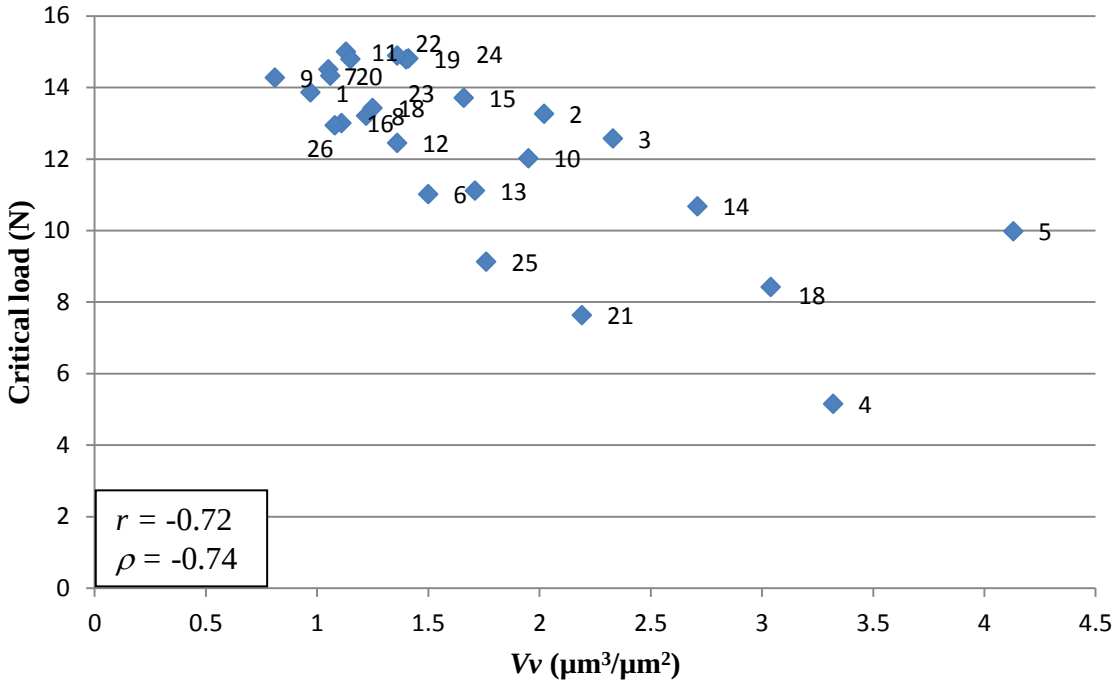

Figure 6.42 *Vv* versus critical load (micro-roughness component) for structured surfaces

Vv (*mr*), the void volume, is the volume of the voids per unit area at a given material ratio calculated from the areal material ratio curve. This parameter refers to the volume of space

bounded by the surface texture from a plane at a height corresponding, to a chosen "*mr*" value to the lowest valley. For example, a *Vv* (*mr*) = A $\mu m^3/\mu m^2$ in that a A µm thick film over the measurement area would provide the same volume of fluid as needed to fill the measured surface from a height corresponding to *mr* % to the lowest valley. A new surface may be specified by *Vv* (0 %) which would indicate the total initial void volume provided by the texture [112].

Figure 6.42 shows a clear trend between *Vv* (*mr*) parameter and critical load. Good plating adhesion occurs with smaller *Vv* (*mr*) value. It should be noticed that this trend is present for this particular case, i.e. copper plating adhesion strength which is characterized by critical load from delamination failure mode. Surfaces with sharp edges and fluctuated roughness amplitude may cause local random failure which would lower plating adhesion strength.

Figure 6.43 shows there are two distinct clusters for the correlation between *Vmc* parameter and critical load for structured surfaces and random surfaces with *Vv* (*mr*) values of the random surfaces being much smaller.

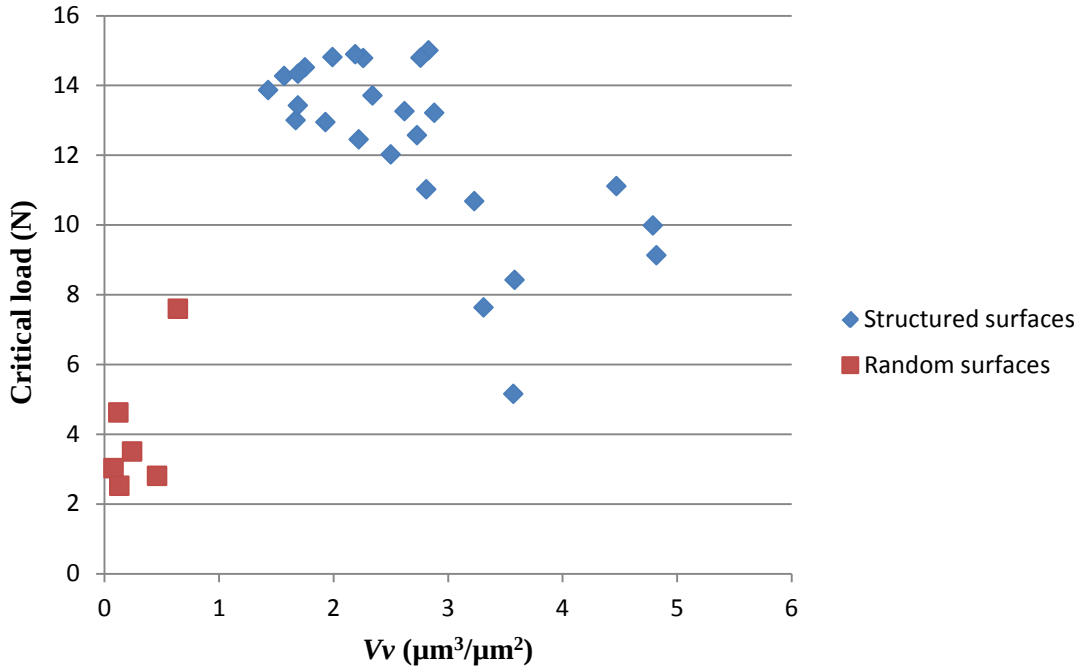

Figure 6.43 *Vv* versus critical load (micro-roughness + structural components) for structured surfaces and random surfaces

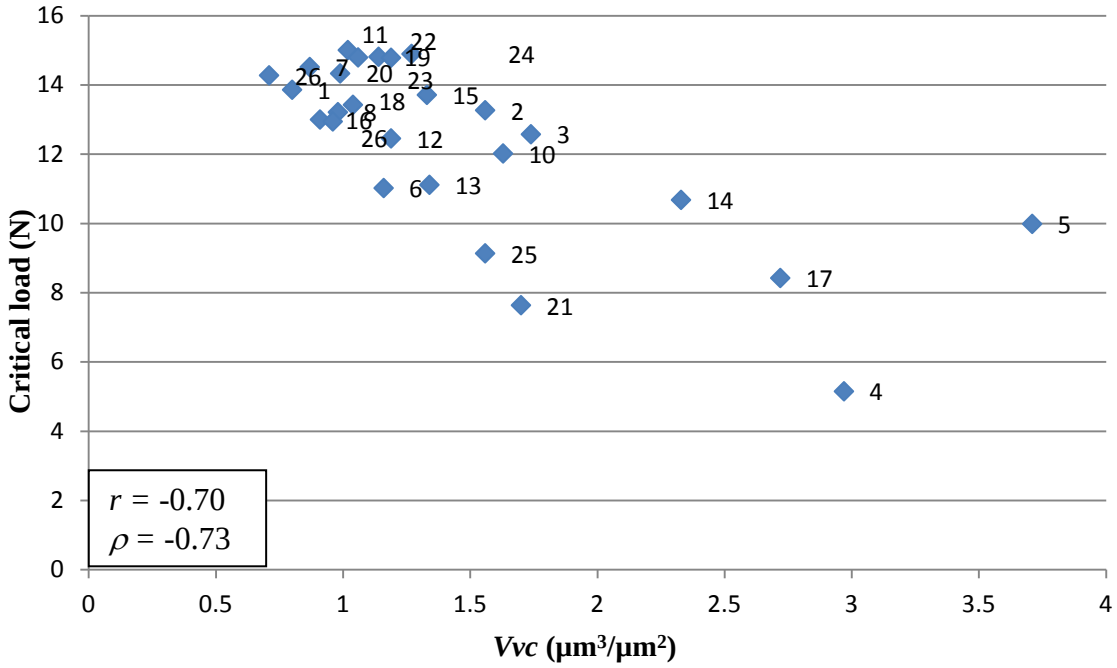

Figure 6.44 *Vvc* versus critical load (micro-roughness component) for structured surfaces

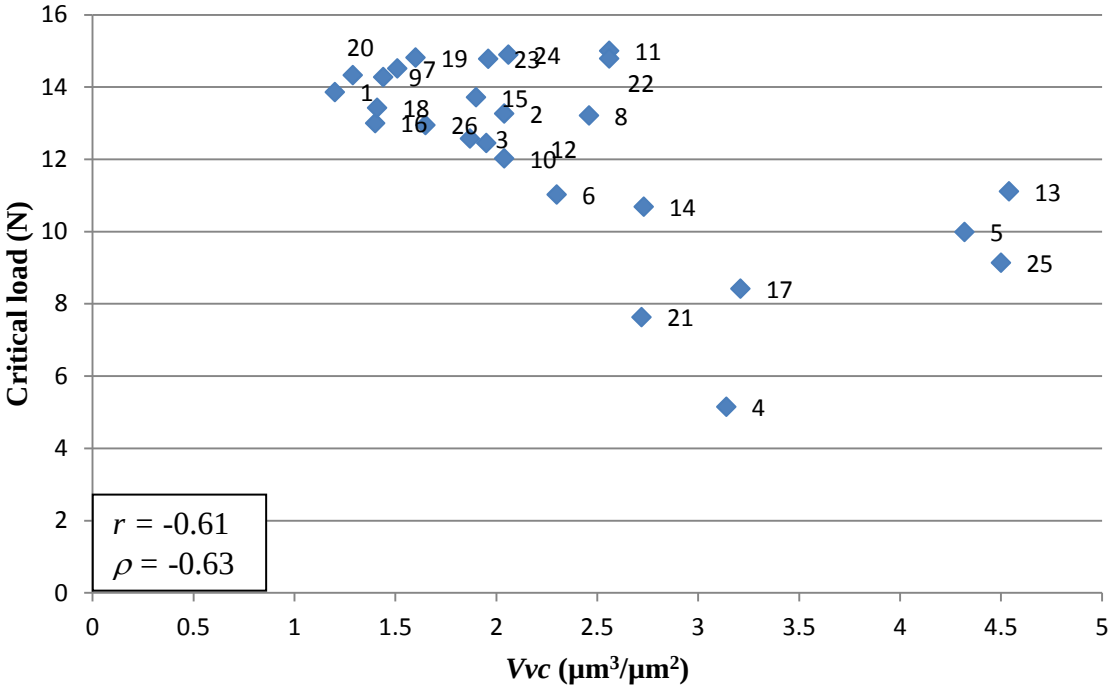

Figure 6.45 *Vvc* versus critical load (micro-roughness component + structural component) for structured surfaces

Vvc (*p*, *q*), the core void volume, is the difference in void volume between *p* and *q* material ratio. This parameter is also derived from the material ratio curve, and refers to the volume of

space bounded by the texture at heights related to the 10 % to 80 % range of the material ratio. The default value for *p* is 10 % and the default value for *q* is 80 %. *Vvc* (*p*, *q*) may provide information about the resulting void volume for fluid entrapment or leakage. A larger *Vvc* value indicates good fluid retention.

Vvc may be useful to establish how much core space is available once a surface has been run-in, resulting in decreased peak heights. From Figure 6.44 and Figure 6.45, it can be seen that there is a clear trend between the *Vvc* parameter and the critical load. Good plating adhesion occurs with smaller *Vvc* value. Reasons for this are similar to those discussed.

Figure 6.46 indicates there are two distinct clusters for the correlation between *Vvc* parameter and critical load for structured and random surfaces. Compared with structured surfaces, *Vvc* values for the random surfaces are much smaller, with no clear trends or correlation.

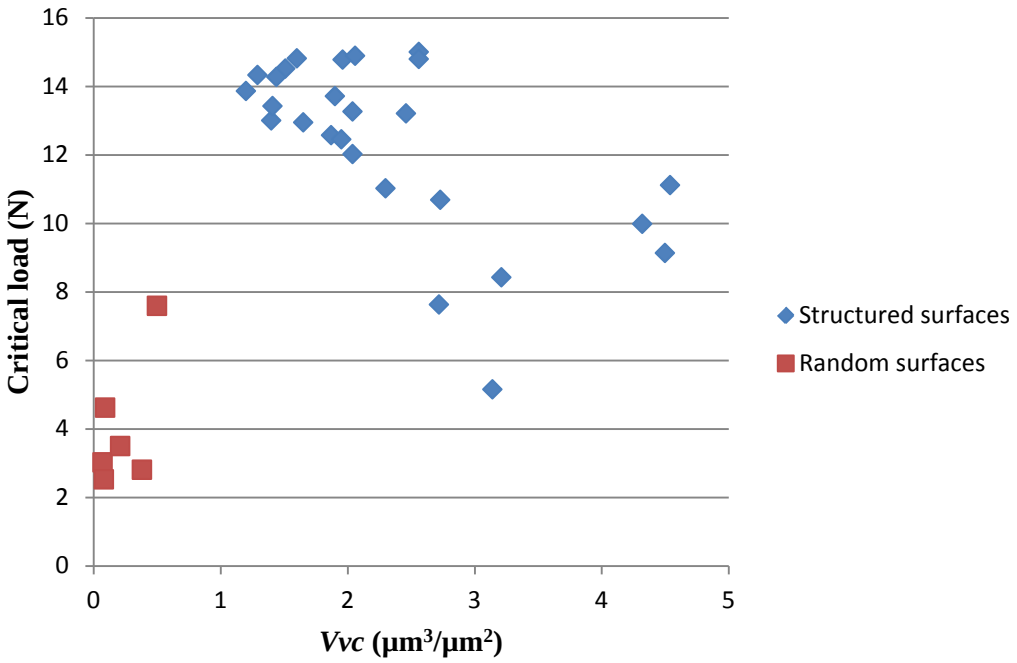

Figure 6.46 *Vvc* versus critical load (micro-roughness + structural components) for structured surfaces and random surfaces

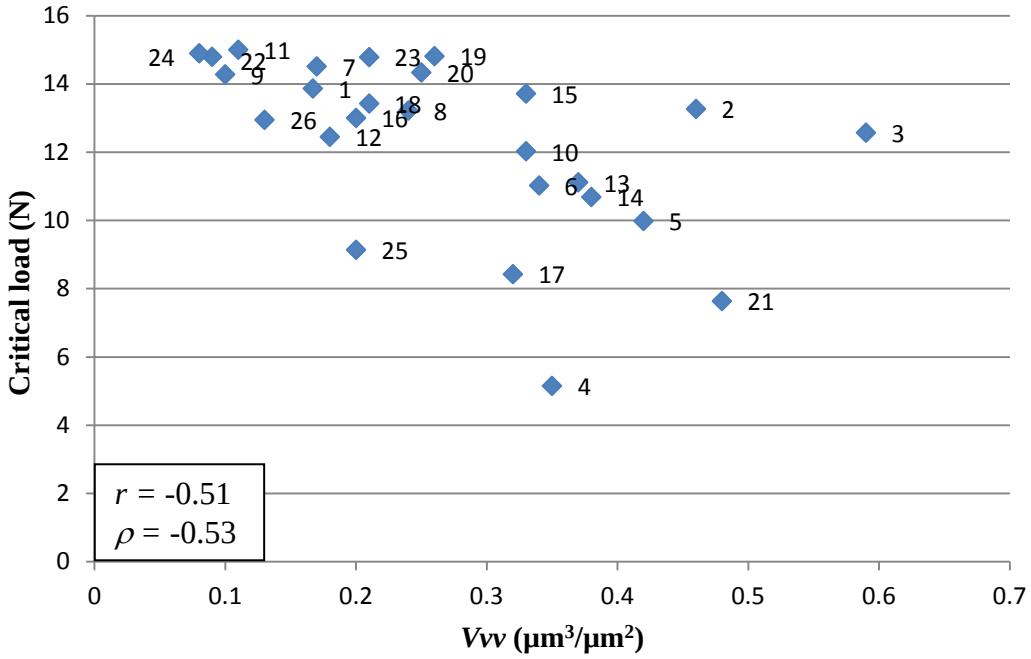

Figure 6.47 *Vvv* versus critical load (micro-roughness component) for structured surfaces

Vvv (*p*), the dale void volume, is the volume of space bounded by the surface texture from a plane at a height corresponding to a material ratio level *p* to the lowest valley. The default value for *p* is 80 % but may be changed as needed. A larger *Vvv* indicates a good fluid retention capability in the valley zone [112]. This parameter may be useful in indicating the potential remaining volume after significant wear of a surface has resulted.

Figure 6.47 indicates there is a clear trend between *Vvv* parameter and critical load. Good plating adhesion occurs with smaller *Vvv* values. The possible reason is discussed earlier.

Figure 6.48 shows there are two distinct clusters for the correlation between *Vvv* parameter and critical load for structured surfaces and random surfaces, with *Vvv* values for the random surfaces being much smaller. Again there are no clear trends or correlation with the random surface data.

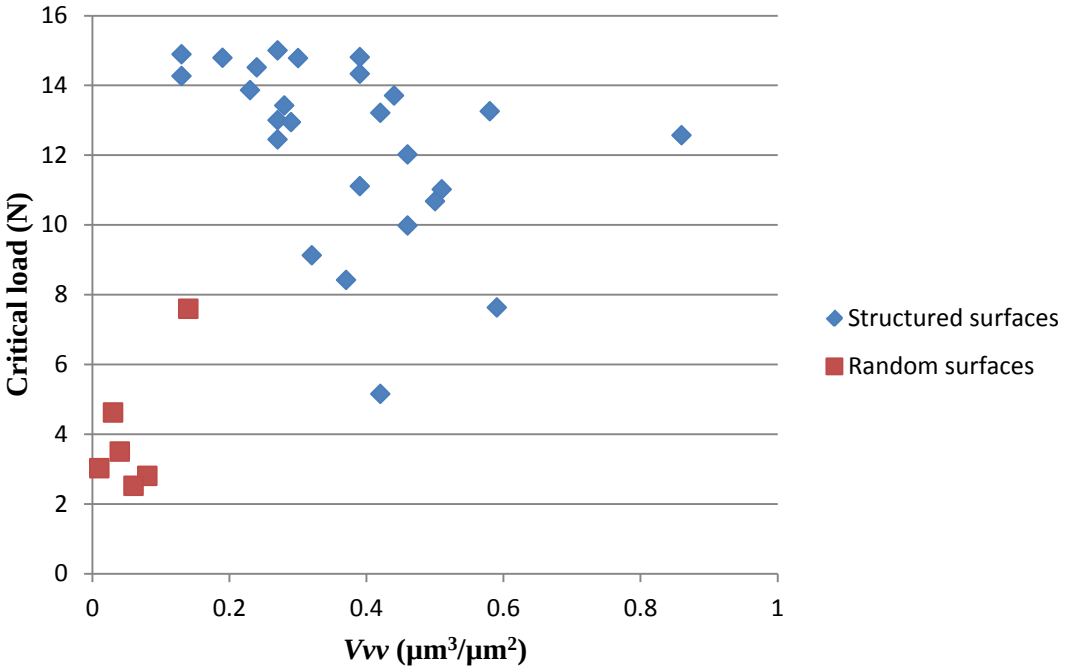

Figure 6.48 *Vvv* versus critical load (micro-roughness + structural components) for structured surfaces and random surfaces

Vm (*mr*), *Vmp* (*p*) and *Vmc* (*p*, *q*) all indicate a measure of the material forming the surface at the various heights down from the highest peak of surface, or between various heights as defined for *Vmc* (*p*, *q*). *Vv* (*mr*), *Vvv* (*p*) and *Vvc* (*p*, *q*) all indicate a measure of the void volume provided by the surface between various heights as established by the chosen material ratio values. Thus these void volume parameters indicate how much fluid would fill the surface (normalized to the measurement area) between the chosen material ratio values.

It should be noted that these functional parameters were originally designed for bearing applications. In this study, all the trends observed are present for this particular case, i.e. copper plating adhesion strength is characterized by critical load from scratch testing. Critical load is derived from the delamination failure mode caused by a stylus tip tracing across the surface. Surfaces with sharp edges and fluctuating roughness amplitude may cause local random failure, and therefore would lower the measured plating adhesion strength. Because the height of the material ratio curve is termed the total roughness, it is not surprising these functional parameters show the same trend as the microroughness amplitude characterization *Sq*.

6.4.5 Feature parameters (*Spd*, *Spc*, *Sda*, *Sha*)

Feature parameters directly consider and quantify the influence of surface features (hills, dales saddle points, ridge lines and course lines), as a function of surface segmentation and filtration (see Section 2.3.5). In this study, feature parameters were directly generated by the TalyMap Platinum v5.1 (DigitalSurf Mountains) surface processing software. Four selected feature parameters *Spd*, *Spc*, *Sda* and *Sha* were used for examing the quality of the correlation with respect to critical load.

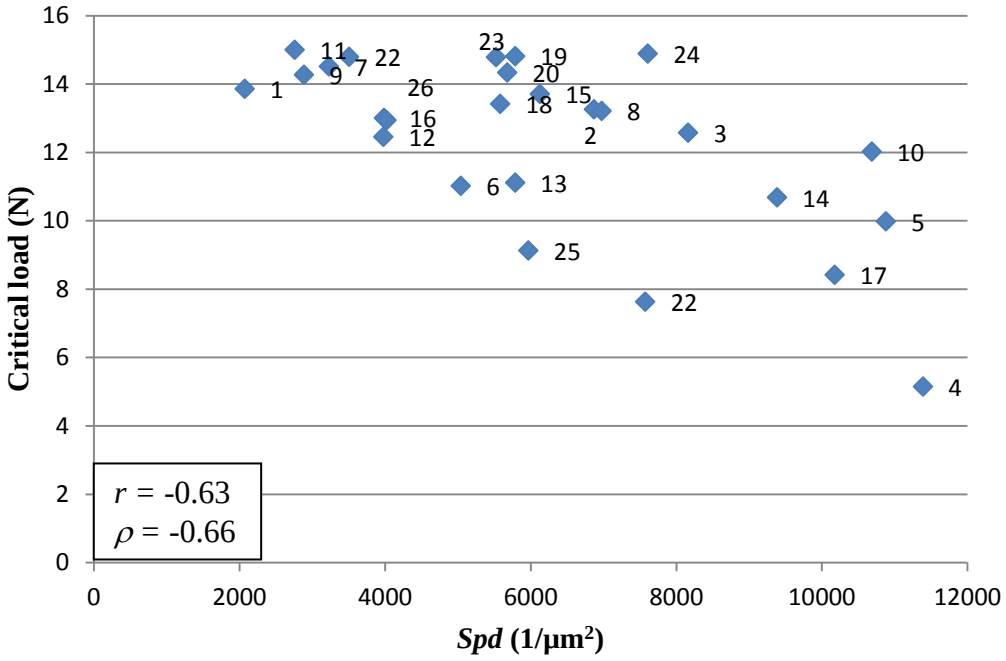

Figure 6.49 *Spd* versus critical load (micro-roughness component) for structured surfaces

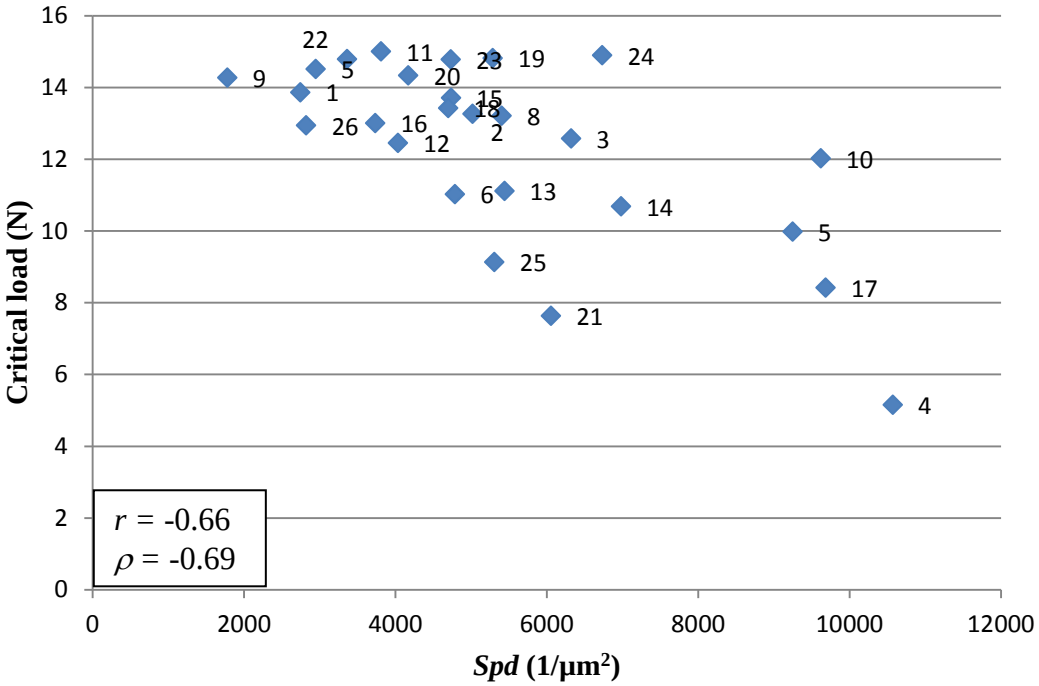

Figure 6.50 *Spd* versus critical load (micro-roughness + structural components) for structured surfaces

Spd, density of peaks, is the number of peaks in a unit sampling area. Physically, the *Spd* parameter is assumed to provide a good estimate of the average number of asperities per unit area. A higher value of *Spd* signifies that there are more summits on the same area.

Figure 6.49 and Figure 6.50 illustrate both micro-roughness component, and micro-roughness plus structural components, show approximately the same trend. Critical load increases slightly when the *Spd* value increases. This may be because the higher the number of asperities, the larger the real area of contact, therefore resulting in stronger adhesion. A larger summit density may cause increased interference of asperities or increased area of contact and, therefore, increase of the mechanical interlocking effect. However, when the peak density further increases, the critical load decreases. The possible reason is that a large density of peaks value indicates spiky surfaces that will lower the critical load due to the local random failure caused by the sharp edge effect.

Figure 6.51 shows there are two distinct clusters for the correlation between *Spd* parameter and critical load for structured surfaces, and random surfaces. Comparing with the structured

surfaces, *Spd* values of random surfaces are much smaller, and show no clear trends or correlation.

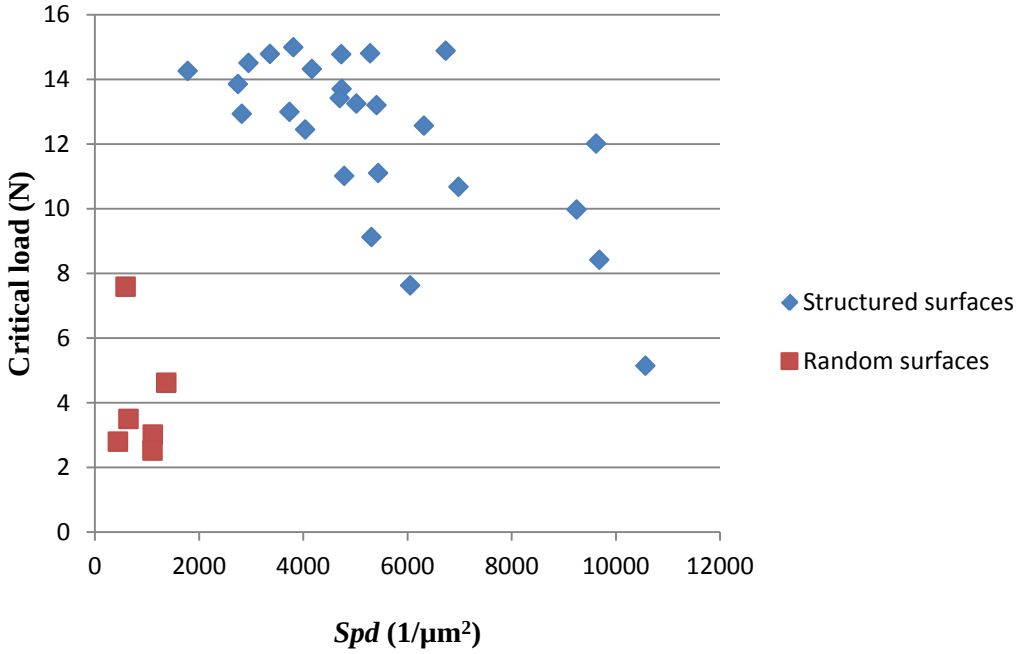

Figure 6.51 *Spd* versus critical load (micro-roughness + structural components) for structured surfaces and random surfaces

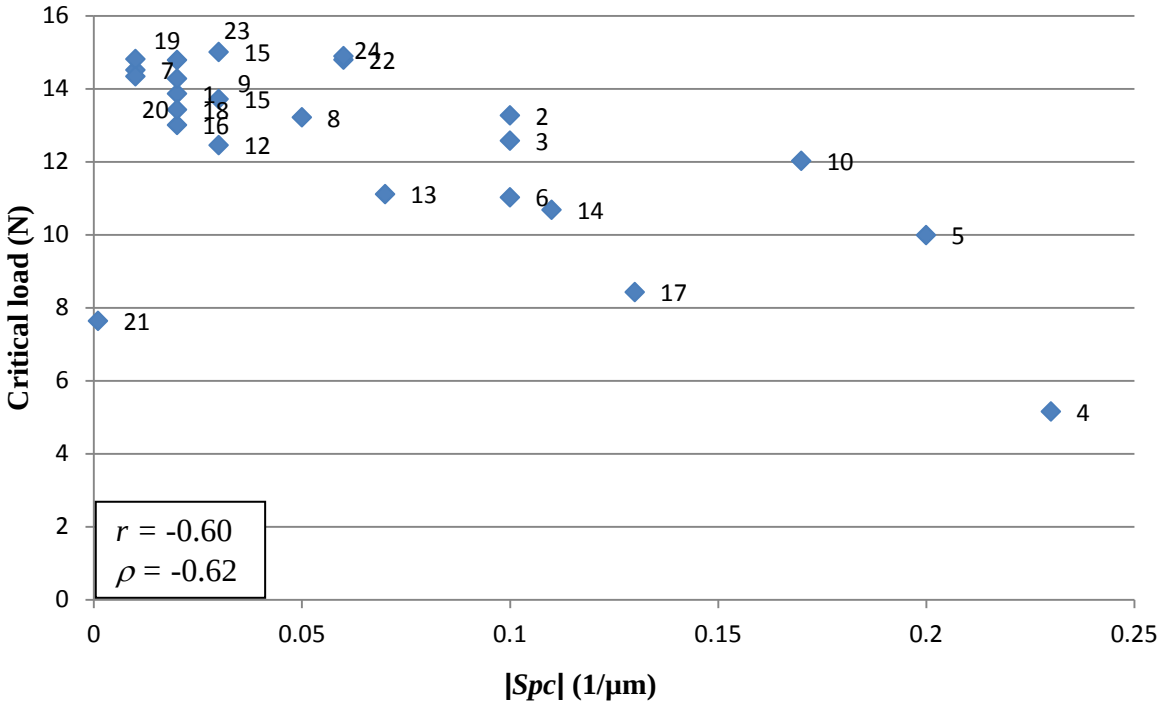

Figure 6.52 *Spc* versus critical load (structural component) for structured surfaces

Spc is defined as an average of the principal curvatures of the peaks within the sampling area. The curvatures of the peaks can be positive or negative which depend on the slope direction, so absolute values may be more useful to compare among different samples. The absolute values of *Spc* plotted against critical load is shown in Figure 6.52. A particularly strong relationship is shown for the structural component. It can be seen that there is a clear decreasing trend for *Spc* value with respect to critical load. Good plating adhesion occurs with smaller *Spc* value. This can be explained because *Spc* also characterizes the roughness of the surface. Large *Spc* values caused by spiky surfaces may be particularly prone to random failure as discussed before.

Figure 6.53 shows two distinct clusters for the correlation between *Spc* and critical load for structured surfaces and random surfaces. Random surfaces have much lower critical loads, but very similar *Spc* values.

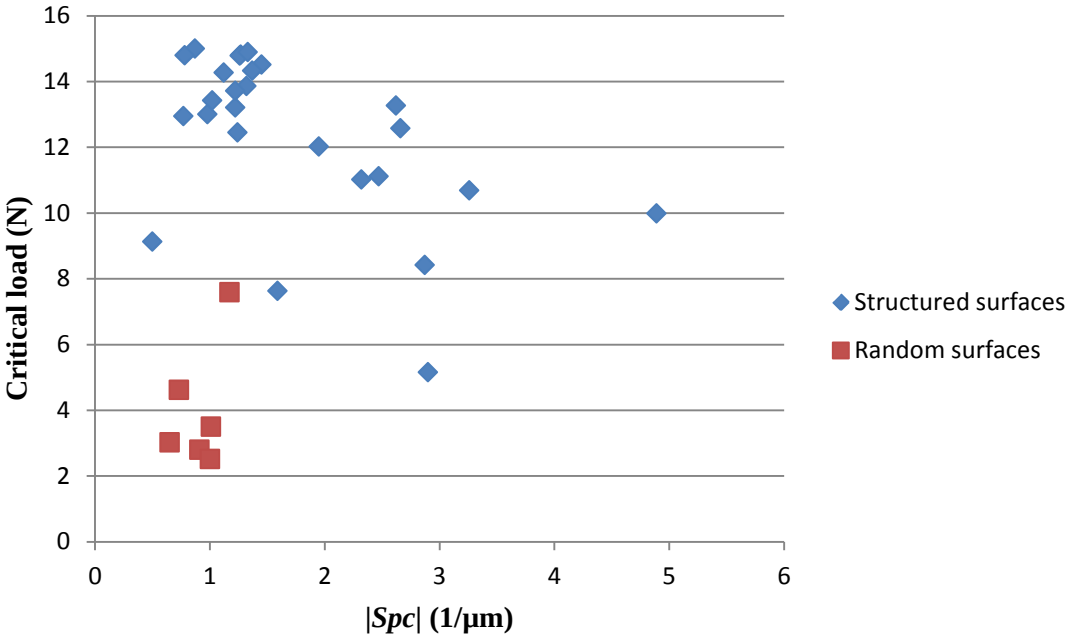

Figure 6.53 *Spc* versus critical load (micro-roughness + structural components) for structured surfaces and random surfaces

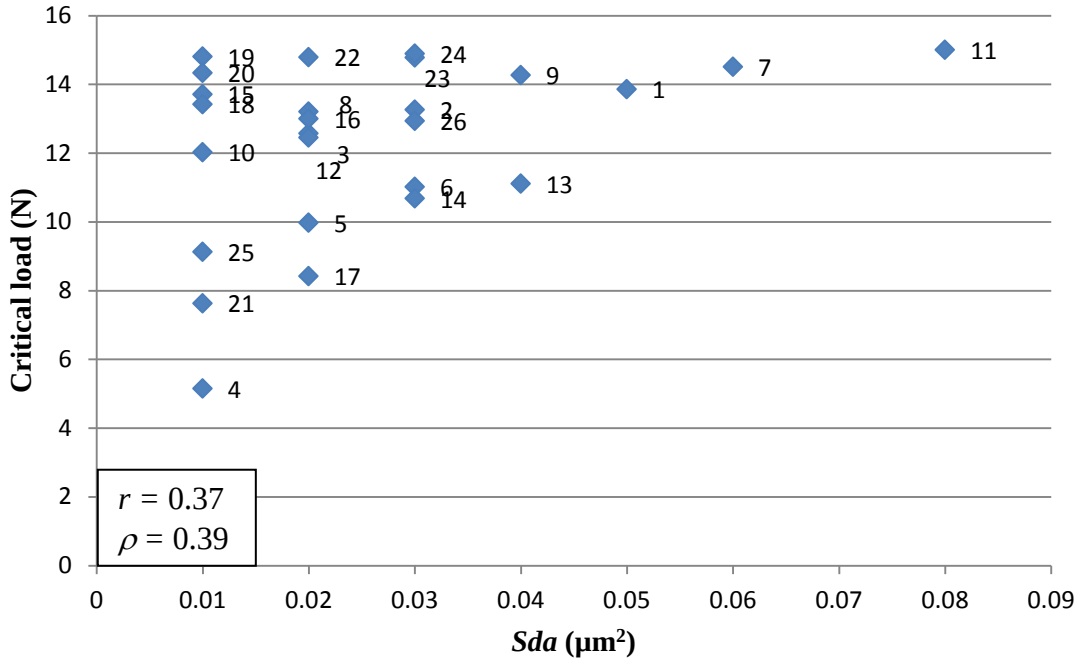

Figure 6.54 *Sda* versus critical load (micro-roughness component) for structured surfaces

Sda (*c*), closed dale area, is the average area of dales connected to the edge at height *c*. When plotting the *Sda* value against the critical load, there is no significant trend as shown in Figure 6.54. From Figure 6.55, it is can be seen that *Sda* values are much higher for random surfaces compared with the structured surface.

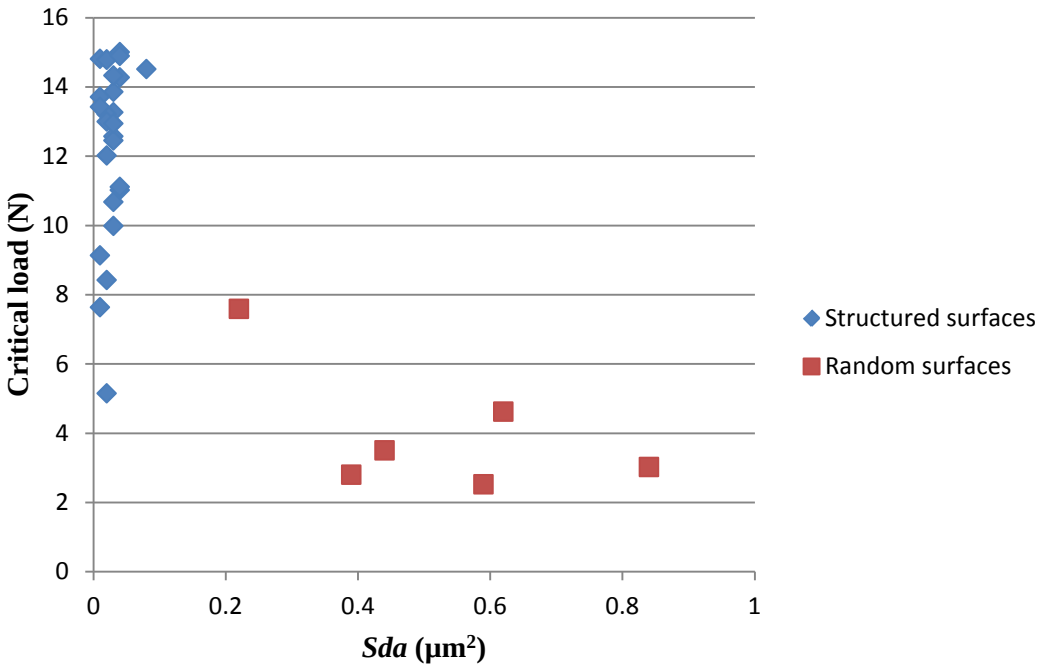

Figure 6.55 *Sda* versus critical load (micro-roughness + structural components) for structured surfaces and random surfaces

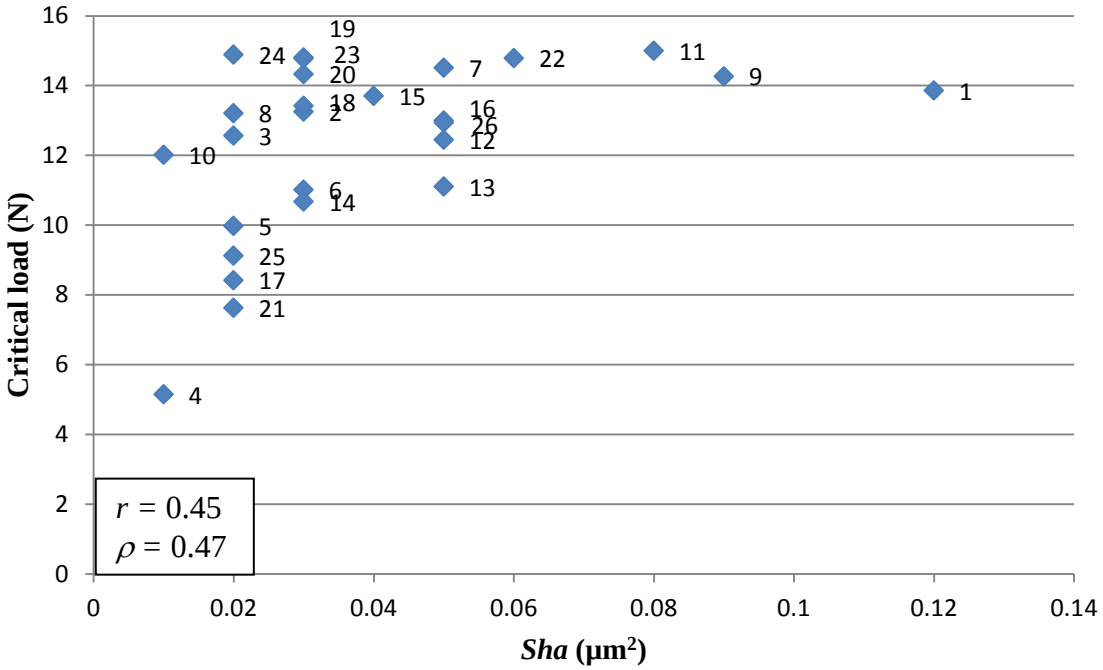

Figure 6.56 *Sha* versus critical load (micro-roughness component) for structured surfaces

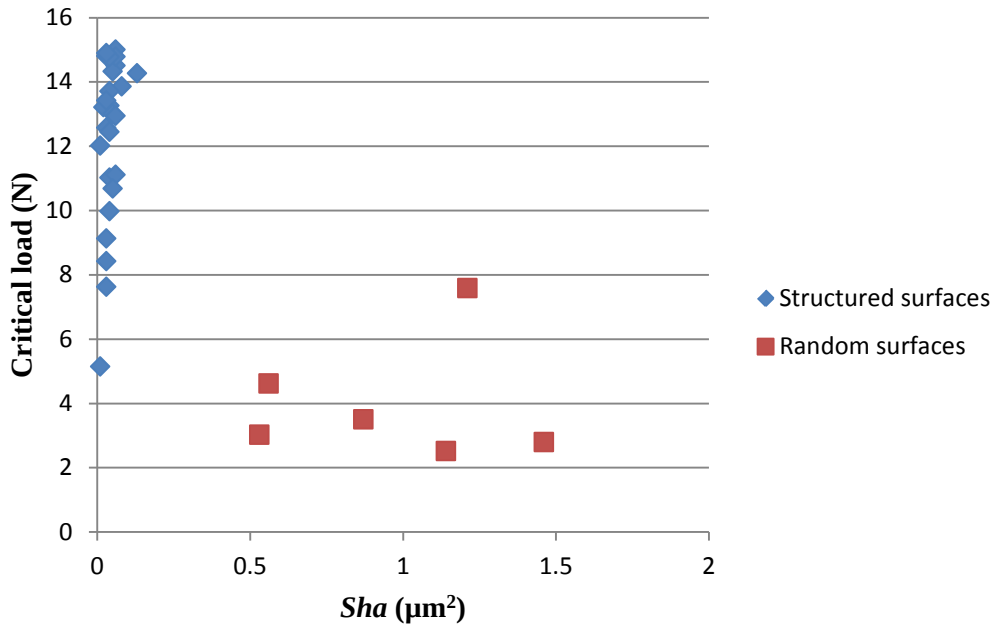

Figure 6.57 *Sha* versus critical load (micro-roughness + structural components) for structured surfaces and random surfaces

Sha(*c*), closed hill area, is the average area of hills connected to the edge at height *c*. When plotting the *Sha* value against the critical load, there is no clear trend as shown in Figure 6.56. Figure 6.57 suggests that *Sha* values are much higher for random surfaces compared with structured surfaces. The reason is also due to the nature of random surfaces.

6.5 Plating adhesion prediction

This study has systematically investigated the characterization of adhesion between copper coating and glass substrate via areal surface texture parameters. A number of parameters have been identified as showing a strong correlation with critical load, and are regarded as having the potential for appropriately describing the glass surfaces in the context of bonding, on the basis of the correlations results within the data sets, but also with reference to their descriptions and mathematical functions as identified in ISO / FDIS 25178:2.

However, the areal surface topography of engineered surfaces is complex and cannot be described completely by a single or a few parameters. However some parameters have similar or overlapping meanings. For example: *Sa* and *Sq* both measure the dispersion of the heights from a reference surface and are highly correlated with each other, so it is appropriate to adopt one of these parameters, *Sq*, for the present study. The second issue is that some

parameters are correlated. For example: many parameters and indices are associated with the material ratio curve.

The key parameters identified which show the strongest correlations and may functionally be most relevant with respect to their formal descriptions cover; height, hybrid, functional and feature aspects of the surface, and are shown in Table 6.4. It should be noticed that:

- The recommended parameter range values are only valid for structured surfaces. The failure criteria for structured surfaces and random surfaces are different. Only structured surface samples show strong correlation with plating adhesion in this study.

- Appropriate filter techniques should be applied for the data processing, the nesting indices of the S filter and L filter need to be selected based on the micro-pattern features.

- When using the recommended values, for height and hybrid parameters, an L filter is applied whereas for functional parameters an S filter is selected.

This set of selected areal parameters is considered to be most likely to allow a comprehensive characterization of the relationship between areal surface topography and adhesion. The reasons are identified as follows:

- These parameters describe some important topographic features.

- These parameters measure different aspects of the topography.

- These parameters are based on sound mathematical and / or statistical principles.

Table 6.4 Areal parameters and recommended values for predicting copper plating adhesion

	Parameters	**Spearman Coefficient Value (*r*)**	**Pearson Coefficient value (ρ)**	**Recommended value of parameters**	**Confirmed by graph**
Height parameter	*Sq*	-0.71	-0.74	1 µm – 2.5 µm	Figure 6.58
Hybrid parameters	*Sdq*	-0.66	-0.69	0.5 – 1	Figure 6.59
	Sdr	-0.61	-0.64	10 % – 50 %	Figure 6.60
Functional parameters (for micro-roughness)	*Sxp*	-0.63	-0.61	0.5 µm – 5 µm	Figure 6.61
	Vv	-0.72	-0.74	0.5 $\mu m^3/\mu m^2$ – 2 $\mu m^3/\mu m^2$	Figure 6.62
	Vmc	-0.74	-0.77	0.4 $\mu m^3/\mu m^2$ – 1.5 $\mu m^3/\mu m^2$	Figure 6.63
	Vvc	-0.70	-0.73	0.5 $\mu m^3/\mu m^2$ – 1.5 $\mu m^3/\mu m^2$	Figure 6.64

For the parameters identified in Table 6.4, there are strong trends being shown between critical load and the respective areal parameter. Furthermore, it is recognized that these conclusions can be reinforced by the graphical and numerical comparisons with data points from glass samples, without any delamination during the scratch testing within the load between 1.0 N and 15.0 N. It should be noted that the maximum load applied by the scratch testing equipment was 15.0 N, this being determined by failure of the glass substrate at greater loads. If no copper plating failure was observed during a scratch test, then the default critical load value was regarded as 15.0 N, however, this unfailed data was excluded from the data processing shown in the previous graphs. Consequently, it is possible that some of the copper / glass samples may have higher bond strengths than 15.0 N, but it has not been possible to quantify this unless thicker CMG glass substrates are subsequently used to investigate this issue.

Data points on glass samples that showed no failure (default 15.0 N critical load – without delamination) have been added to and are highlighted in Figures 6.58 to 6.64. These graphs also have estimated ideal parameter value zones (dashed vertical lines). It is suggested that parameter values within these zones represent surface values appropriate for good quality

copper bonding on laser machined CMG glass. These parameters form the basis for predictive design of ideal surfaces for electroless copper plating.

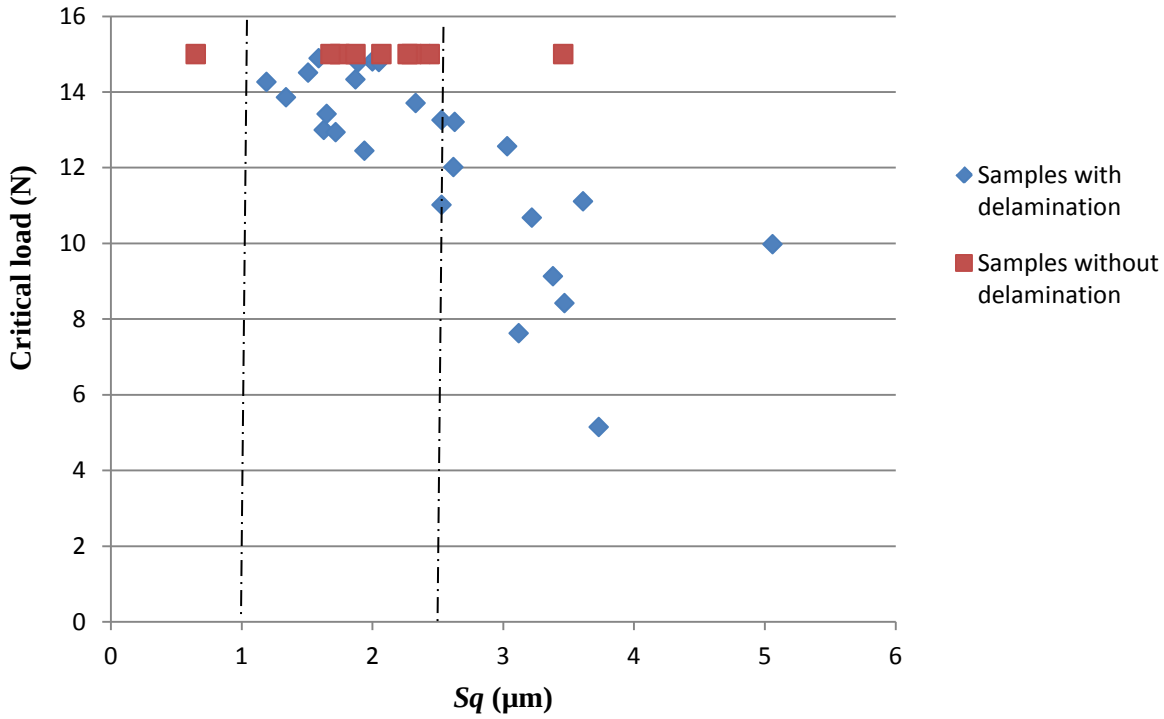

Figure 6.58 Correlation of *Sq* with critical load further reinforced by samples without any delamination during the scratch testing

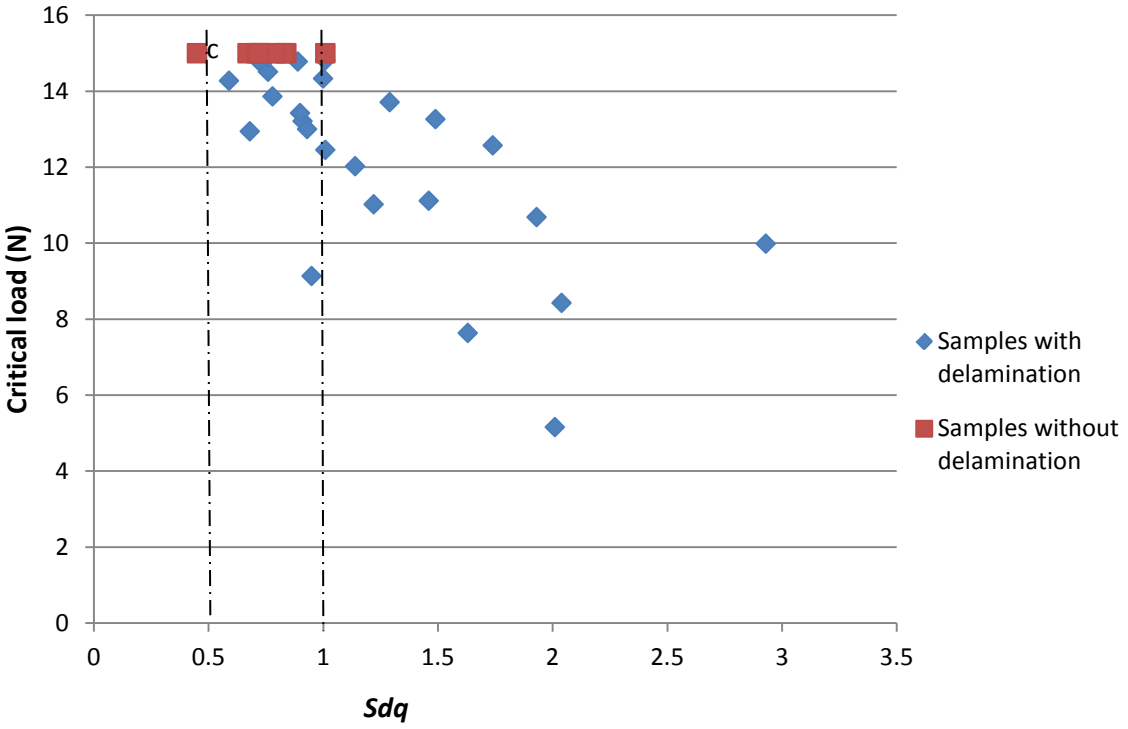

Figure 6.59 Correlation of *Sdq* with critical load further reinforced by samples without any delamination during the scratch testing

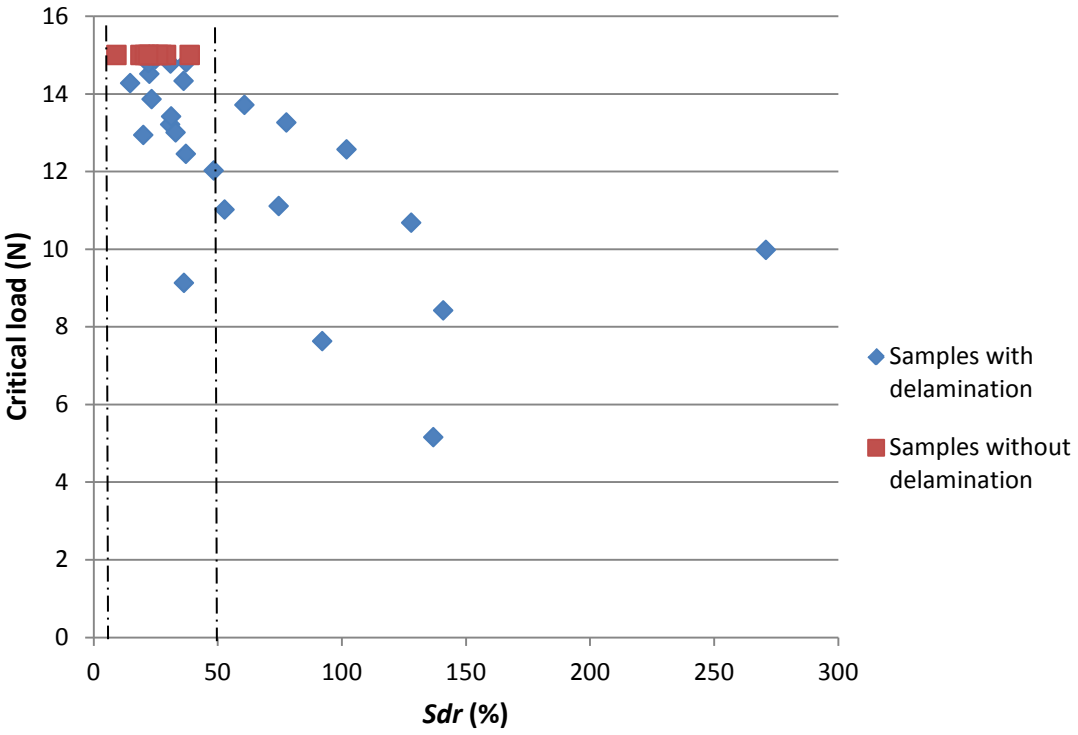

Figure 6.60 Correlation of *Sdr* with critical load further reinforced by samples without any delamination during the scratch testing

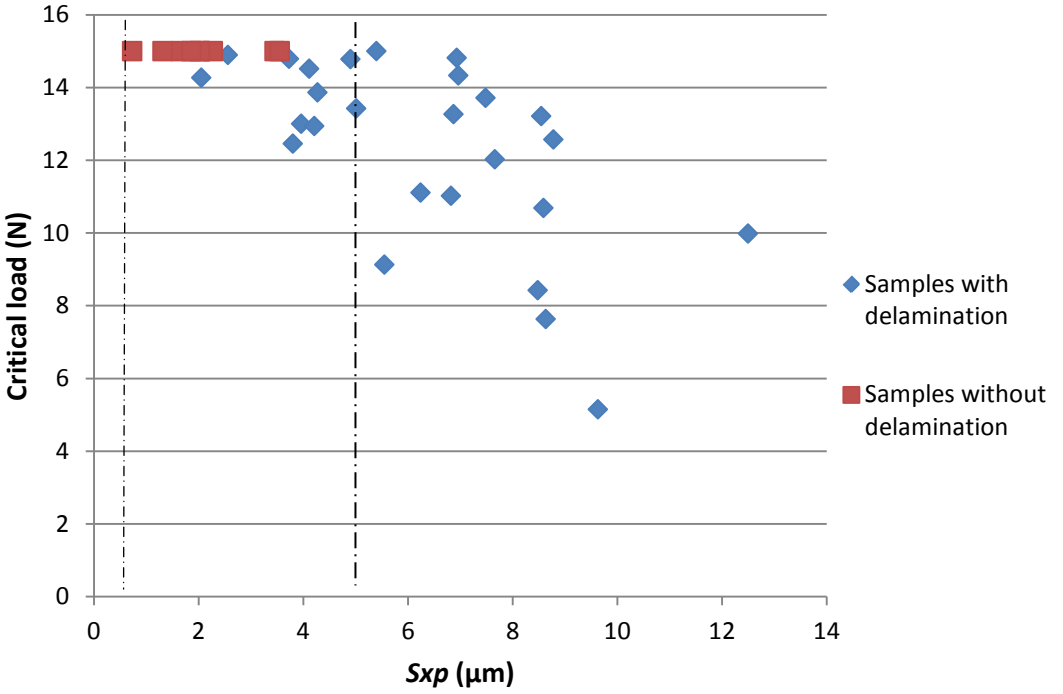

Figure 6.61 Correlation of *Sxp* with critical load further reinforced by samples without any delamination during the scratch testing

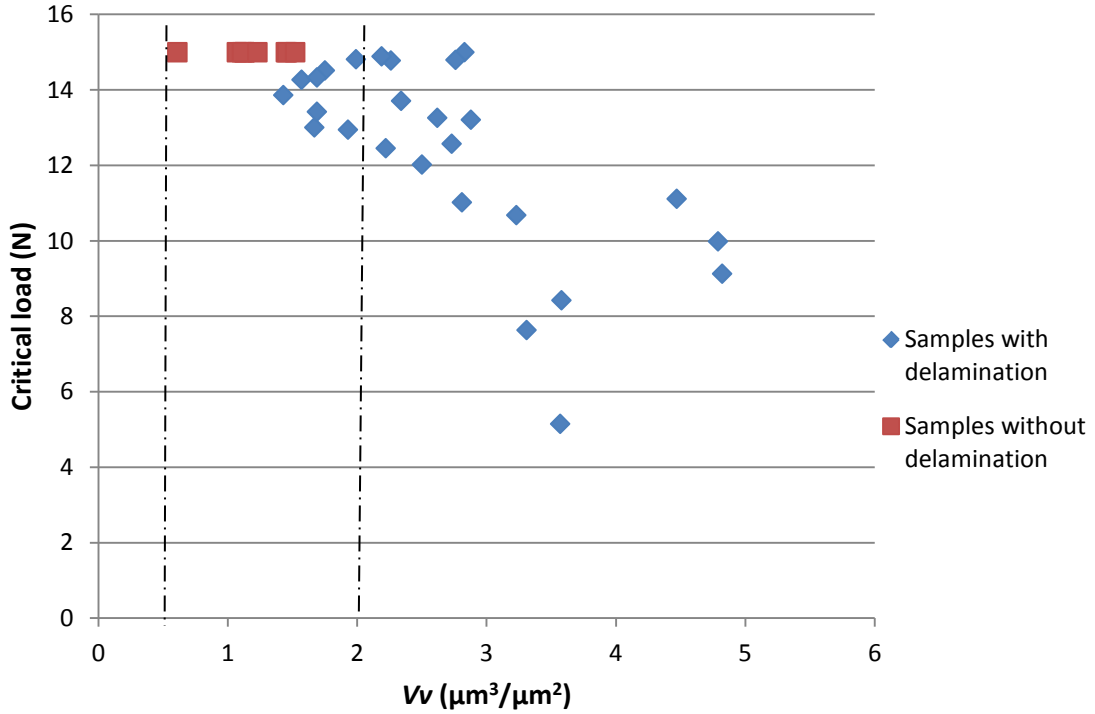

Figure 6.62 Correlation of *Vv* with critical load further reinforced by samples without any delamination during the scratch testing

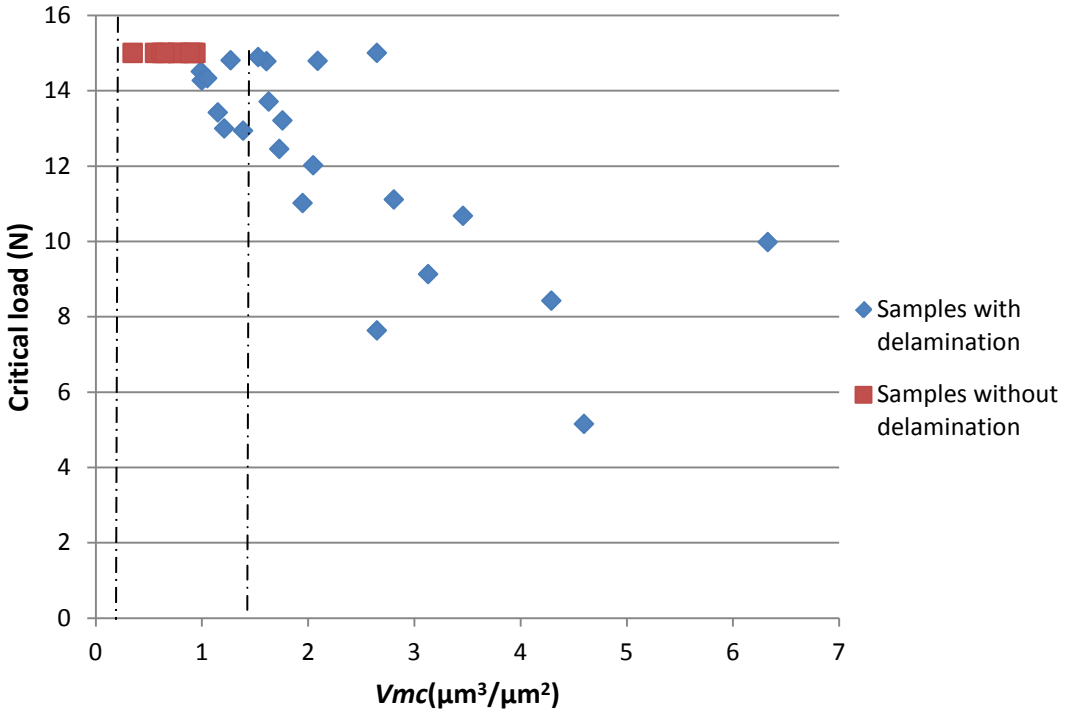

Figure 6.63 Correlation of *Vmc* with critical load further reinforced by samples without any delamination during the scratch testing

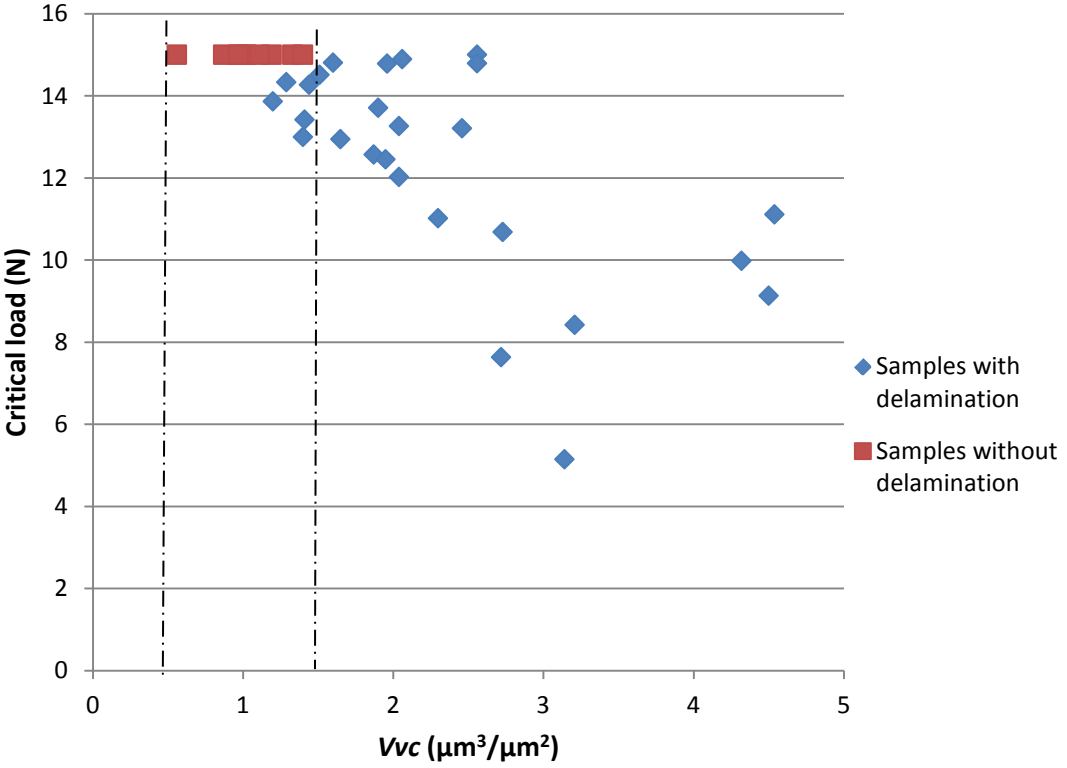

Figure 6.64 Correlation of *Vvc* with critical load further reinforced by samples without any delamination during the scratch testing

Detailed processing parameters for CMG glass samples without any delamination during the scratch testing are listed in Table 6.5. Examples of the topographic images of optimal structured surfaces for adhesion are shown in Figure 6.66.

Table 6.5 Processing parameters details of structured surface samples without delamination (S- square mask, C-circular mask)

Sample number	Side length (mm)	Energy density (J/cm^2)	Repetition rate (Hz)	Shots per area (n)	Laser variable (pitch) (µm)
27	S4	2.2	10	5	100
28	C2	2.2	10	20	100
29	S1	2.2	10	20	50
30	S1	2.2	10	10	80
31	S1	2.2	10	10	50
32	S1	2.2	10	10	60
33	S1	2.2	10	15	40
34	S1	2.2	10	15	50
35	S1	2.2	10	15	60

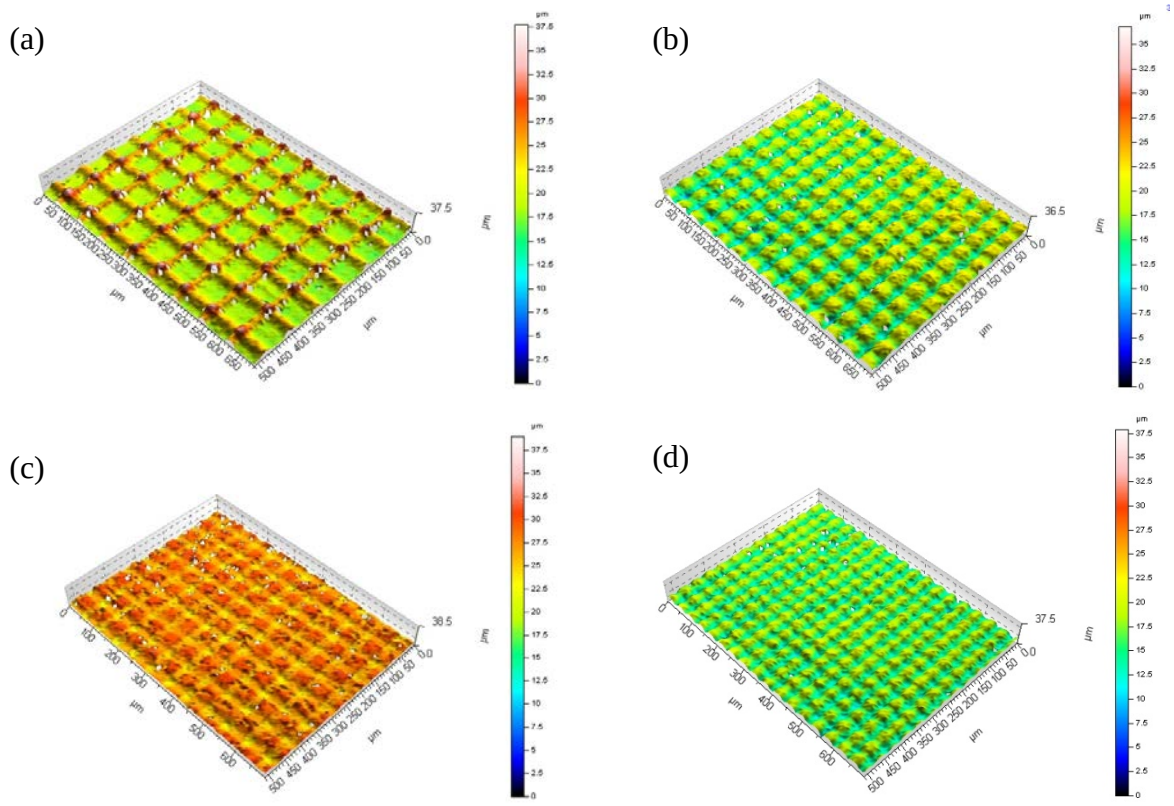

Figure 6.66 Structured surfaces without delamination

(a) Sample Number 28 (b) Sample Number 29 (c) Sample Number 32 (d) Sample Number 33

Table 6.5 and Figure 6.66 suggest the optimal laser processing parameters setting for CMG glass substrate machining and the topographic images of structured surfaces for achieving strong copper / glass plating adhesion. It can be concluded that:

- Fine micro-grid based structured surfaces are ideal for strong copper / glass plating adhesion on CMG glass substrates.
- Square masks and circular masks are suitable for generating micro-grid based structures on CMG glass substrates.
- Small geometric dimension masks used in laser processing are preferred (<100 μm).

It should be noted that there is no data for areal parameters between zero and the dashed vertical lines as shown in Figures 6.58 to 6.64. This is due to the limitation of the experimental capability for laser machining and surface roughness generation, as defined by the laser mask sizes. However, section 5.4.1 showed the critical load of copper coating on smooth glass substrate was below 1 N. It is therefore anticipated that there should be an increasing trend between zero parameter value and the dashed vertical lines, with the highest critical load values expected to fall in the range as predicted. This will require the development of finer scale masks for the laser and additional research effort.

6.6 Summary

In this chapter, three coating failure criteria were proposed to meet different requirements for industry. Based on three coating failure criteria, graphs concerning the relationships between areal surface texture parameters and critical load for different failure criteria were drawn and some clear trends could be identified.

In order to distinguish between the contribution of plating adhesion from large scale surface structure, and from surface micro-roughness of the glass samples, different and specific filters were chosen for each sample. As a result, graphs of the relationships between surface micro-roughness and critical load, structure and critical load, (micro-roughness +structure) and critical load were investigated respectively.

Two statistical methods (Pearson product-moment correlation coefficient and Spearman's rank correlation coefficient) were employed to analyze the linear and statistical dependence

between the two variables (surface areal parameters and critical load). These coefficients allow clear definition of the strength of correlation between the areal parameters and the critical load values and allow the user to rank order the parameters as shown in Table 6.6.

Table 6.6 Rank ordered areal parameters

Areal parameters	**Spearman Coefficient Value (r)**	**Pearson Coefficient value (ρ)**	**Recommended value**
Vmc	-0.74	-0.77	0.4 $\mu m^3/\mu m^2$ – 1.5 $\mu m^3/\mu m^2$
Vv	-0.72	-0.74	0.5 $\mu m^3/\mu m^2$ – 2 $\mu m^3/\mu m^2$
Sq	-0.71	-0.74	1 µm – 2.5 µm
Vvc	-0.70	-0.73	0.5 $\mu m^3/\mu m^2$ – 1.5 $\mu m^3/\mu m^2$
Sdq	-0.66	-0.69	0.5 – 1
Sxp	-0.63	-0.61	0.5 µm – 5 µm
Sdr	-0.61	-0.64	10 % – 50 %

Examples of optimal surface topography for strong copper / glass plating adhesion have been presented and a key list of areal parameters which are highly correlated with adhesion performance identified and used for adhesion prediction of copper / glass system.

Chapter 7 Conclusions and future work

7.1 Introduction

The research presented in this thesis has been very challenging, because in order to achieve the primary aims, expertise and motivation has had to be gained in two key underpinning technologies:

- Excimer laser based machining
- Electroless copper plating

Both of these disciplines could form research projects in their own right, and the Future Work identified in Section 7.3 offers further laser and chemistry issues that require more effort.

7.2 Conclusions

The primary stated aims of this research (Chapter 1) have been to;

- Improve the adhesive bond quality of electroless copper plating on glass substrates
- Evaluate ISO / FDIS 25178:2 areal parameters to assess suitability for describing the potential of surfaces for good quality copper bonding.

Objectives and perceived novelty of this work were also identified in Chapter 1 (Section 1.3). Table 7.1 identifies how well these objectives have been met and the resultant novelty value of each element of the work.

Table 7.1 Objectives completion and resultant novelty

Objectives	Outcome	Chapter	Novelty
1,2,3	A range of surface modification methods have been identified and evaluated. Bead blasting was selected for generating random surfaces. Excimer laser processing was selected for structured surface generation and key operational variables investigated.	3	Laser machining of glass has high novelty in this context.
4	Metrology techniques were investigated. A Zygo NewView 5000 CSI instrument was chosen as the most appropriate metrology tool and used routinely. TalyMap Platinum (DigitalSurf Mountains) was used to generate areal parameters.	2	No novelty in this context.
5	Electroless copper plating techniques were investigated and optimized for the CMG glass.	4	Medium level of novelty with respect to application on CMG glass.
6	Investigated methods for quantifying copper / glass bond strength. Identified scratch testing as the most appropriate method. Evaluated scratch testing parameters and critical load identification.	5	Medium / high level of novelty with respect to application on copper coated structured glass
7	A large range of glass samples have been produced, measured, plated and evaluated for bond strength. Detailed analysis has been completed identifying correlation trends between ISO / FDIS 25178:2 parameters and critical load values. Key failure criteria have been identified.	6	Very high level of novelty in terms of the use of the areal parameters.

Table 7.1 continued

8	Key areal parameters have been identified through the use of Pearson / Spearman correlation statistics and graphical techniques. Key surface structures have been identified that significantly improve copper plating adhesion on CMG glass substrates.	6	Very high novelty in terms of ideal glass surfaces for improved copper plating adhesion.

As a function of the literature survey, it can be identified that very few existing formalized studies on excimer laser machining for glass surface texture generation have been reported. No investigation has been found on linking areal surface texture parameters with plating adhesion. This further reinforces the unique and novel findings of this research.

The research has identified the role that surface topography has on influencing the mechanical bond strength of electroless copper plating on glass substrates. This is achieved via controlled excimer laser machining of glass, areal parameterization of the surfaces, electroless copper plating, critical failure criterion identification using scratch testing, and finally correlation / statistical analysis of critical load to areal parameter. The process can be visualized as shown in Figure 7.1.

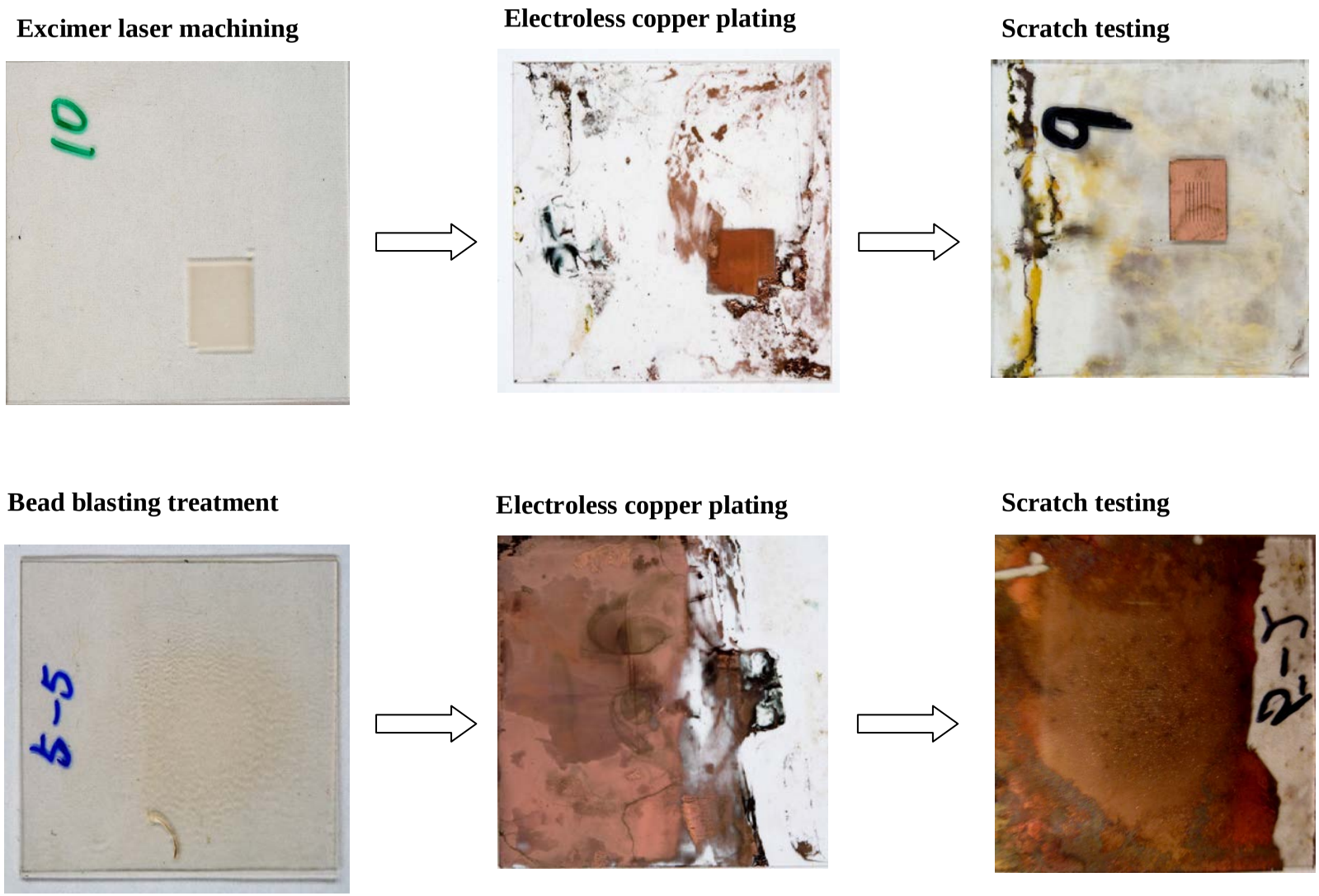

Figure 7.1 Visualized experimental process

Key conclusions based on this research are presented as follows:

- This work has clearly demonstrated the feasibility of using an excimer laser to generate a variety of controlled micro structured surface topography on CMG glass, by changing mask dimensions, laser operating parameters (fluence, shots per area and repetition rate), and mask overlapping patterns.

- Grid pattern microstructures can be generated on the CMG surfaces using circular and square masks. Micro ramp and pyramid pattern structures can be produced using triangular masks. However, even under the same mask and laser parameter settings, micro pattern structure may still be different, as determined by the machining process such as overlapping pitch between parallel grooves.

- Excimer laser investigation suggests that the ablation or etch depth depends on laser fluence and shots per area, and machining homogeneity can be improved by increasing the energy density, shots per area and laser pulse repetition rate. These conclusions help to use this technique to maximise the use of the laser energy and minimize the machining time, and the controllability of the laser surface treatment can be optimized via the processing parameters. It is also recognized that the excimer laser is an ideal research tool, but not necessarily an ideal production tool.

- Various techniques (plasma treatment, excimer laser machining, chemical etching and mechanical methods) have been used in the surface treatment of glass to generate random surfaces. Bead blasting has been identified as a relatively feasible technique for producing random surfaces due to its competitive low cost and experimental capability. Various surface roughness levels can be approximately controlled by different exposure times.

- Excimer laser machining and bead blasting treatment are both regarded as pretreatment methods to roughen the glass surface. This is a physical surface modification to improve catalyst attachment for copper coating deposition, compared to a smooth surface. Over 100 glass samples were machined and prepared.

- Copper has been deposited onto machined CMG glass surfaces to form the basis of interconnection tracks by electroless copper plating. Optimal copper plating parameters such as substrate cleaning, pretreatment, catalyst and electroless bath variables were identified and the variables were minimized to acquire consistent and uniform copper metallization prior to scratch testing.

- Scratch testing techniques have been implemented to quantify adhesive bond strength of the copper plating, leading to the identification of critical loads.

- Areal data sets have been produced using Zygo NewView 5000 CSI technique, with ISO / FDIS 25178:2 areal parameters being identified and produced for different glass structures.

- Three failure criteria have been identified as being more representative of bulk copper adhesion and potential user application scenarios and have been assessed. Each areal parameter has been categorized in terms of the strength of correlation with the critical load values under the three failure criteria. Failure Criterion 3 analysis (the point where continuous delamination occurs over a minimum length of 0.2 mm), provided clear trends with the data sets.

- Two correlation coefficients (Spearman and Pearson correlation ranking coefficients) have been employed to quantify the strength of relationship between the areal parameter values and the associated critical loads. The strongest behavioural relationships show in Failure Criterion 3 which indicate Failure Criterion 3 is the most rigorous and consistent test for copper plating failure and therefore adhesive bond strength.

- Experimental relationships between critical load and areal surface parameters, as well as the discussions of a theoretical approach, have been analyzed in detail. A rank ordered list of key areal parameters has been identified (with recommended parameter ranges). *Vmc*, *Vv*, *Sq*, *Vvc*, *Sdq*, *Sxp* and *Sdr* that clearly demonstrate potential for predicting surface capability for improved plating characteristics.

- Key surface structures have been identified from the work that have been shown to significantly improve copper plating adhesion. It has been shown that structures produced using square mask excimer techniques tend to perform best.

- All results are relevant to the use of CMG glass, as a substrate, and may not be relevant to other substrates unless verification work is completed.

7.3 Future work

This research has already successfully demonstrated the correlation between areal parameters and copper / glass plating adhesion, however further study still needs to be invested in various aspects of the work. The future priorities can be summarized as follows:

- Modelling techniques need to be developed to simulate the excimer laser processing of glass with different mask designs. This will allow faster development of mask shape, to further refine bespoke texture features on the glass surface.

- The mechanism of the interaction of excimer laser radiation with glass needs to be further investigated in order to optimize material removal and surface finish.

- Copper coating thickness measurements and scratch adhesion models need to be further investigated and implemented (where relevant).

- There is a significant recognition that the current excimer laser is an ideal research tool, but may not be appropriate for production values. Further work needs to consider how to improve the speed of manufacture using laser based techniques, or, other techniques.

- The extent of micro-cracking (as a function of laser ablation) needs to be investigated, and annealing process introduced to reduce stress concentration sites. This may allow higher scratch testing loads to be applied.

- Alternative scratch testing stylus and load profiles need to be investigated to assess the difference of the testing system on the derived critical load values. It is anticipated that changing the size of the indenter tip will modify the critical load values.

- Design modelling capability needs to be generated, to allow predictive design of surfaces using areal parameters. If areal parameters can be used in a virtual environment, then design cycle times for surfaces may be reduced.

- Electroless plated glass needs to have thicker plating. This can partly be achieved using electroless techniques. However, electroplating on top of electroless plating needs to be investigated, in order to produce copper thickness suitable for viable circuits.

- For electronics manufacture, the application of the structured surfaces at the size of features required (e.g. the length and the width of tracks) will need to be controlled and adjusted according to the specific industrial requirement. Electronic circuits need to be designed and machined using the techniques described in this thesis. This will allow the investigation of the suitability of the manufacturing methods.

- Electroless copper plated samples need to be subjected to environmental conditioning and thermal cycling to assess quality of bond strength as a function of in-service conditions.

- The ideas and concepts developed in this work need to be exploited for alternative substrate materials (ceramics for instance) and other electroless plated materials (nickel for instance).

REFERENCE

1. Lau, J.H. and Lee, R.S.W., Microvias: low cost, high density interconnects. *London: McGraw-Hill*, 2000.
2. Electronic Materials Handbook, vol. 1: Packaging. *ASM International Handbook Committee*, Materials Park, OH, 1998.
3. Schroder, H., Amdt-Staufenbiel, N., Cygon, M. and Scheel, W., Planar glass waveguides for high performance Electrical-Optical-Circuit Boards (EOCB) The glass layer concept. *Proceedings of 53rd Electronic Components and Technology Conference*, New Orleans, May 2003, pp. 1053-1059.
4. Hutt, D.A., Williams, K., Conway, P.P., Khoshnaw, F.M., Cui, X. and Bhatt, D., Challenges in the manufacture of glass substrates for electrical and optical interconnect. *Circuit World*, 2007, Vol. 33 (1), pp. 22-30.
5. Bhatt, D., Williams, K., Hutt, D.A., and Conway, P.P., Process optimisation and characterization of excimer laser drilling of microvias in glass. *9th Electronics Packaging Technology Conference*, 2007, pp. 196-201.
6. Bhatt, D., Excimer laser machining of glass for high density substrate manufacture. PhD thesis, Loughborough University, June 2009.
7. Cui, X.Y., Electroless metallization of glass for electrical interconnect applications. PhD thesis, Loughborough University, 2009.
8. ISO / FDIS 25178-2, Geometrical product specifications (GPS) - Surface texture: Areal - Part 2: Terms, definitions and surface texture parameters, 2010.
9. Whitehouse, D., Surface and their measurement. *Hermes Penton Ltd*, *London*, 2002.
10. ISO 4287, Geometrical product specifications (GPS) - Surface texture: Profile method - Terms, definitions and surface texture parameters, 1998.
11. ISO 4288, Geometrical product specifications (GPS) - Surface texture: Profile method - Terms, Rules and procedures for the assessment of surface texture, 1998.
12. Grieve, D.J., Kaliszer, H. and Rowe, G.W., A “Normal Wear” Process Examined by Measurements of Surface Topography. *CIRP Annals*, 1970, vol. 16 (4), pp. 585-592.
13. Blunt, L, Jiang X, Advanced techniques for assessment surface topography - Development of a basis for the 3D Surface Texture Standards. *SURFSTAND Kogan Page Science*, www.kogenpagescience.com, ISBN 1903996112, 2003.

14. Stout, K.J. and Sullivan P.J., The use of 3D topographic analysis to determine the micro-geometric transfer characteristics of textured sheet surfaces through rolling. *CIRP Annals (Switzerland)*, 1992, vol. 41 (1), pp. 621-624.
15. Wennerberg, A., Ohlssont, R., Rosknt, B.G. and Andersson, B., Characterizing three-dimensional topography of engineering and biomaterial surfaces by confocal laser scanning and stylus techniques. *Medical Engineering Physics*, 1996, vol. 18 (70), pp. 548-556.
16. Dong, W.P. and Stout, K., An integrated approach to the characterisation of surface wear I: Qualitative characterisation. *Wear,* 1995, vol. 181-183, pp. 700-716.
17. Blunt, L. and Ebdon, S., The application of three-dimensional surface measurement technique to characterising grinding wheel topography. *International Journal of Machine Tools and Manufacture,*, 1996, vol. 36 (11), pp. 1207-1226.
18. Xie, H.C., Chen, D.R. and Kong, X.M., An analysis of the three-dimensional surface topography of textured cold-rolled steel sheets. *Tribology International*, 1999, vol. 32, pp. 83-87.
19. Jiang, X.Q. Blunt, L. and Stout, K.J., Three-dimensional surface characterisation for orthopaedic joint prostheses. *Journal of Engineering in Medicine*, 1999, vol. 213 (H1), pp. 49-68.
20. Ramasawmy, H. and Blunt, L., 3D surface topography assessment of the effect of different electrolytes during electrochemical polishing of EDM surfaces. *International Journal of Machine Tools and Manufacture,* 2002, vol. 42, pp. 567-574.
21. Ramasawmy, H., Blunt, L. and Rajurkar, K.P. Investigation of the relationship between the white layer thickness and 3D surface texture parameters in the die sinking EDM process. *Precision Engineering*, 2005, vol. 29, pp. 479-490.
22. Butler, D.L., Blunt, L.A., See, B.K., Webster J.A. and Stout, K.J. The characterisation of grinding wheels using 3D surface measurement techniques. *Journal of Materials Processing Technology,* 2002, vol. 127, pp. 234-237.
23. Al-Nawas, B. and Götz, H., Three-dimensional topographic and metrologic evaluation of dental implants by Confocal Laser Scanning Microscopy. *Clinical Implant Dentistry and Related Research*, 2003, vol. 5 (3), pp. 176-183.
24. Suh, A.Y., Polycarpou, A.A. and Conry, T.F., Detailed surface roughness characterisation of engineering surfaces undergoing tribological testing leading to scuffing. *Wear*, 2003, vol. 255, pp. 556-568.

25. Bénard, Q., Fois, M. and Grisel, M. Influence of fibre reinforcement and peel ply surface treatment towards adhesion of composite surface. *International Journal of Adhesion and Adhesives*, 2005, vol. 24, pp. 404-409.
26. Kundrak, J., Osanna, P.H., Afjehi-Sada, A. and Bana, V., Surface quality of hard turned bore holes, *Metrology for a Sustainable Development*, XVIII IMEKO WORLD CONGRESS, Rio de Janeiro, Brazil, September 2006.
27. Krzyzak, Z. and Pawlus, P., 'Zero-wear' of piston skirt surface topography. *Wear*, 2006, vol. 260, pp. 554-561.
28. Senin, N., Ziliotti, M. and Groppetti, R., Three-dimensional surface topography segmentation through clustering. *Wear*, 2007, vol. 262, pp. 395-410.
29. Sul, Y.T., Kang, B.S., Johansson, C., Um, H.S., Park C.J. and Albrektsson, T., The roles of surface chemistry and topography in the strength and rate of oseointegration of titanium implants in bone. *Journal of Biomedical Materials Research*, 2009, Part A, vol. 89 (4), pp. 942-950.
30. Le Guéhennec, L., Soueidan, A., Layrolle, P. and Amouriq, Y., Surface treatments of titanium dental implants for rapid osseointegration. *Dental materials*. 2007, vol. 23, pp. 844-854.
31. Ávila, R.F., Godoy, C., Abrão A.M. and Lima, M.M. Topographic analysis of the crater wear on TiN, Ti(C, N) and (Ti, Al)N coated carbide tools. *Wear*, 2008, vol. 265, pp. 49-56.
32. Michalski, J., Surface topography of the cylindrical gear tooth flanks after machining. *International Journal of Advanced Manufacturing Technology*, 2009, vol. 43, pp. 513-516.
33. Waikar, R.A. and Guo, Y.B., A comprehensive characterisation of 3D surface topography induced by hard turning versus grinding. *Journal of Materials Processing Technology*, 2008, vol. 197, pp. 189-199.
34. Nguyen, A.T. and Butler, D., Correlation of grinding wheel topography and grinding performance: A study from a viewpoint of three-dimensional surface characterisation. *Journal of Materials Processing Technology*, 2008, vol. 208 (1-3), pp. 14-23.
35. Aris, N.F.M. and Cheng, K., Characterisation of the surface functionality on precision machined engineering surfaces. *International Journal of Advanced Manufacturing Technology*, 2008, vol. 38, pp. 402-409.

36. Scardino, A.J., Hudleston, D., Peng, Z., Paul, N.A. and De Nys, R., Biomimetic characterisation of key surface parameters for the development of fouling resistant materials. *Biofouling*, 2009, vol. 25 (1), pp. 83-93.
37. Czifra. Á and Horváth, S., Complex microtopography analysis in sliding friction of steel-ferodo material pair. *Meccanica*, 2011, vol.46, pp. 609-616.
38. Wang, J., Jiang, X.J. Gurdak, E., Scott, P, Leach, R, Tomlins, P. and Blunt, L, Numerical characterisation of biomedical titanium surface texture using novel feature parameters, *Wear*, 2011, vol. 271, pp. 1059-1065.
39. Tian, Y., Wang, J., Peng, Z. and Jiang, X., Numerical analysis of cartilage surfaces for osteoarthritis diagnosis using field and feature parameters. *Wear*, 2011, vol. 271, pp. 2370-2378.
40. Comyn, J. Adhesion science. *Cambridge: Royal Society of Chemistry*, 1997.
41. Lee, L.H., Fundamentals of adhesion. *New York; London: Plenum Press*, 1991.
42. Ebnesaijad, S, Adhesive technology handbook, 2nd edition. *William Andrew Inc, New York*, 2008.
43. Alphonsus, P., Adhesion and adhesive technology: an introduction. *Hanser Gardner*, 2002.
44. Petrie, E.M., Handbook of adhesives and sealants. *McGraw-Hill*, 2007.
45. Packham, D.E., Handbook of adhesion. *Longman Scientific & Technical*, 1992.
46. Hiderbrand, J. and Scott, R., The solubility of non-electrolytes, 3rd edition, *Reinhold, New York*, 1950.
47. Iyengar, Y. and Erickson, D.E., Role of adhesiv-substrate compatibility in adhesion. *Journal of Applied Polymer Science*, 1967, vol. 11, pp. 2311.
48. Takadoum, J. and Bennani, H., Influence of substrate roughness and coating thickness on adhesion, friction and wear of TiN films. *Surface and Coatings Technology*, 1997, vol. 96, pp. 272-282.
49. Hallab, N.J., Bundy, K.J., Connor, K.O, Moses, R.L. and Jacobs, J.J., Evaluation of metallic and polymeric biomaterial surface energy and surface roughness characteristics for directed cell adhesion. *Tissue Engineering*, 2001, vol. 7 (1), pp. 55-71.
50. Shahid, M. and Hashim, S.A., Effect of surface roughness on the strength of cleavage joints. *International Journal of Adhesion and Adhesives*, 2002, vol. 22, pp. 235-244.
51. Chong, E.K., Stevens, M.G. and Nissen, K.E., Effect of surface roughness on the adhesion of electrolessly plated platinum to poly (ethylene terephthalate) films. *The Journal of Adhesion*, 2003, vol. 79, pp. 667-681.

52. Garbacz, A. Courard L. and Kostana. K. Characterisation of concrete surface roughness and its relation to adhesion in repair systems. *Materials Characterisation*, 2006, vol. 56, pp. 281-289.
53. Bénard, Q., Fois, M., and Grisel, M., Surface treatment of carbon/epoxy and glass/ epoxy composites with an excimer laser beam. *International Journal of Adhesion and Adhesives*, 2006, vol. 26, pp. 543-549.
54. Minaki, K., Kitajima, K., Minaki, K., Izawa. M., and Tosha, K., Improvement of surface texture of stainless steel by utilizing dry blasting – 2nd report: Effect of blasting conditions on wettability. *Key Engineering Materials*, 2005, vol. 291-292, pp. 265-270.
55. Minaki, K., Kitajima, K., Minaki, K., Izawa. M., and Tosha, K., Improvement of surface texture of stainless steel by utilizing dry blasting – 3rd report: Effect of blasting surface texture on adhesion of plating. *Key Engineering Materials*, 2007, vol. 329, pp. 353-358.
56. Menezes, P.L. Kishore and Kailas, S.V., Studies on friction and transfer layer: role of surface texture. *Tribology Letters*, 2006, vol. 24 (3), pp. 265-273.
57. Jiang, Z.X., Huang, Y.D., Liu, L. and Long, J., Effects of roughness on interfacial performances of silica glass and non-polar polyarylacetylene resin composites. *Applied Surface Science*, 2007, vol. 253, pp. 9357-9364.
58. Zappone, B., Rosenberg, K.J. and Israelachvili, J., Role of nanometre roughness on the adhesion and friction of a rough polymer surface and a molecularly smooth mica surface. *Tribology Letters*, 2007, vol. 26 (3), pp. 191-201.
59. Novák, I., Sysel, P., Zemek, J., Špírková, M., Velić, D., Aranyosiová, M., Florián, Š., Pollák, V., Kleinová, A., Lednickỳ, F. and Janigová, I., Surface and adhesion properties of poly (imide-siloxane) block copolymers. *European Polymer Journal*, 2009, vol. 45, pp. 57-69.
60. Indolfi, L., Causa F. and Netti, P.A., Coating process and early stage adhesion evaluation of poly (2-hydroxy-ethyl-methacrylate) hydrogel coating of 316L steel surface for stent applications. *Journal of Material Science: Materials in Medicine*, 2009, vol.20, pp. 1541-1551.
61. Ayrilmis, N. and Winandy, J.E. Effects of post heat-treatment on surface characteristics and adhesive bonding performance of medium density fibreboard. *Materials and Manufacturing Processes*, 2009, vol. 24, pp. 594-599.

62. Audry, M.C., Ramos, S and Charlaix, E., Adhesion between highly rough alumina surfaces: An atomic force microscope study. *Journal of Colloid and Interface Science*, 2009, Vol. 331, pp. 371-378.
63. Young, T., An essay on the cohesion of fluids, *Philosophical Transactions of the Royal Society of London*, 1805, vol. 95, pp. 65.
64. Wenzel, R.N., Resistence of solid surfaces to wetting by water. *Industrial and Engineering Chemistry*, 1936, vol. 28, pp. 988-994.
65. Cassie, A.B.D. and Baxter, S., Wettability of porous surfaces. *Transactions of the Faraday Society*, 1944, vol. 40, pp. 546.
66. Johnson Jr. R.E. and Dettre, R.H., Contact Angle, Wettability, and Adhesion. *American Chemical Society, Washington, DC, Advances in Chemistry Series*, 1964, vol. 43. pp. 112-135.
67. De Coninck, J., Dunlop, F. and Rivasseau, V. On the microscopic validity of the Wulff construction and of the generalized Young equation. *Communications in Mathematical Physics*, 1989, vol. 121, pp. 401.
68. Zhou, X.B. and Hosson, J.Th.M.De, Influence of surface roughness on the wetting angle. *Journal of Materials Research*, 1995, vol. 10 (8), pp. 1984-1992.
69. Chen, Y., He., B., Lee, J., and Patankar, N.A., Anisotropy in the wetting of rough surfaces. *Journal of Colloid and Interface Science*, 2005, vol. 281, pp. 458-464.
70. Swain, P. and Lipowsky, R., Contact angles on heterogeneous surfaces: a new look at Cassie's and Wenzel's Laws. *Langmuir*, 1998, vol. 14, pp. 6772-6780.
71. Palasantzas, G. and De Hosson, J.Th.M., Wetting on rough surfaces. *Acta Materialia*, 2001, vol. 49, pp. 3533-3538.
72. Zhang, X.P., Yu, S.R., He, Z.M. and Miao, Y.X., Wetting of rough surfaces. *Surface review and letters*, 2004, vol. 11(1), pp. 7-13.
73. Nosonovsky, M., On the range of applicability of the Wenzel and Cassie equations. *Langmuir*, 2007, vol. 23, pp. 9919-9920.
74. Fox, H.W. and Zisman, W.A., The spreading of liquids on low-energy surfaces. *Journal of Colloid and Interface Science*, 1950, vol. 5, pp. 514.
75. Good, R.J. and Girifalco, L.A., A theory for the estimation of surface and interfacial energies. III. Estimation of surface and interfacial energies of solids from contact angle data. *The Journal of Physical Chem*istry, 1960, vol. 64, pp. 561.
76. Fowkes, F.M., Contact angle, wettability and adhesion. *Advances in Chemistry Series*, No. 43, American Chemical Society, Washington DC, 1964.

77. Kaelble, D.H. and Uy, K.C., A reinterpretation of organic liquid-polytetrafluorethylene surface interactions, *Journal of Adhesion*, 1970, vol. 2, pp. 50.
78. Owens, D.K. and Wendt, R.C., Estimation of surface free energy of polymers. *Journal of Applied Polymer Science*, 1969, vol. 13, pp. 1741-1747.
79. Tamai, Y. and Aratani, K., Experimental study of the relation between contact angle and surface roughness. *The Journal of Physical Chemistry*, 1972, vol. 76, pp. 3267.
80. Oliver J.F., Huh, C and Mason, S.G., Resistance to Spreading of Liquids by Sharp Edges. *Journal of Colloid and Interface Science*, 1977, vol. 59, pp. 568.
81. Garoff, S., Sirota, E.B., Sinha, S.K. and Stanley, H.B., The effects of substrate roughness on ultrathin water films. *The Journal of Chemical Physics*, 1989, vol. 90, pp. 7505-7515.
82. Wolansky, G. and Marmur, A., The actual contact angle on a heterogeneous rough surface in three dimensions. *Langmuir*, 1998, vol. 14, pp. 5292-5297.
83. Miller, J.D., Veeramasuneni.S., Drelich. J., Yalamanchili, M.R. and Yamauchi, G., Effect of roughness as determined by Atomic Force Microscopy on the wetting properties of PTFE thin film. *Polymer Engineering and Science*, 1996, vol. 36 (14), pp. 1849-1855.
84. Shibuichi, S., Onda, T., Satoh, N. and Tsujii, K., Super water-repellent surfaces resulting from fractal structure. *The Journal of Physical Chemistry*, 1996, vol. 100, pp. 19512-19517.
85. Onda, T., Shibuichi, S., Satoh, N. and Tsujii, K., Super-Water-Repellent fractal surfaces. *American Chemical Society*, 1996, vol. 12 (9), pp. 2125-2127.
86. Bico, J., Thiele, U. and Quéré, D., Wetting of textured surfaces. *Colloids and Surfaces A: Physicochemical and Engineering Aspects*, 2002, vol. 206, pp. 41-46.
87. Lau, K.K.S, Bico, J., Teo, K.B.K, Chhowalla, M., Amaratunga, G.A.J., Milne, W.I., McKinley, G.H, Gleason, K.K, Superhydrophobic carbon nanotube forests. *Nano Letters*, 2003, vol. 3 (12), pp. 1701-1705.
88. Jopp, J., Grüll, H. and Yerushalmi-Rozen, R., Wetting behavior of water droplets on hydrophobic microtextures of comparable size. *Langmuir*, 2004, vol. 20, pp. 10015-10019.
89. Fan, J.G., Tang, X.J. and Zhao, Y.P. Water contact angles of vertically aligned Si nanorod arrays. *Nanotechnology*, 2004, vol.15, pp. 501-504.
90. Meiron, T.S., Marmur A and Saguy, S.I., Contact angle measurement on rough surfaces.

Journal of Colloid and Interface Science, 2004, vol. 274, pp. 637-644.

91. Abdelsalam, M.E., Bartlett, P.N., Keif, T. and Baumberg, J., Wetting of regularly structured gold surfaces, *Langmuir*, 2005, vol. 21, pp. 1753-1757.
92. Extrand, C.W., Contact Angle hysteresis on surfaces with chemically heterogeneous islands. *Langmuir*, 2003, vol. 19, pp. 3793-3796.
93. Gao, L. and McCarthy, T.J., How Wenzel and Cassie Were Wrong. *Langmuir*, 2007, vol. 23, pp. 3762-3765.
94. Bhushan, B., Nosonovsky, M. and Jung, Y.C., Towards optimization of patterned superhydrophobic surfaces. *Journal of the Royal Society Interface.* 2007, vol, 4, pp. 643.
95. Marmur, A., Soft contact: Measurement and interpretation of contact angles. *Soft Matter*, 2006, vol. 2, pp. 12-17.
96. Butt, H., Capillary forces: influence of roughness and heterogeneity. *Langmuir*, 2008, vol.24, pp. 4715-4721.
97. Stout, K.J. and Blunt, L., A contribution to the debate on surface classifications-random, systematic, unstructured, structured and engineered. *International Journal of Machine Tools and Manufacture*, 2001, vol. 41, pp. 2039-2044.
98. Product specification for manufacture and quality assurance of uncoated CMG solar cell coverglasses, Thales Space Technology, PS 602 (issue 2), 1995.
99. Leach, R.K., Optical measurement of surface topography. *Springer-Verlag, Berlin*, 2011.
100. Whitehouse, D.J., Review article: surface metrology, *Measurement Science and Technology*, 1997, vol. 8, pp. 955-972.
101. Whitehouse, D.J., Comparison between stylus and optical methods for measuring surfaces, *Annals of the CIRP*, 1988, vol. 37 (2), pp. 649-653.
102. Leach, R., Brown, L., Jiang, X. and Blunt, R., Guide to the Measurement of Smooth Surface Topography using Coherence Scanning Interferometry, Measurement Good Practice Guide No. 108, National Physical Laboratory, 2008.
103. Petzing, J., Coupland, J. and Leach, R., Guide for the measurement of rough surface topography using Coherence Scanning Interferometry, Measurement Good Practice Guide No.116, National Physical Laboratory, 2010.
104. NewView 5000 Operating Manual OMP-0423H, Zygo Corporation.
105. Dong, W.P., Sullivan, P.J. and Stout, K.J., Comprehensive study of parameters for characterizing three-dimensional surface topography I: some inherent properties of parameter variation, *Wear*, 1992, vol. 159, pp. 161-171.

106. Dong, W.P., Sullivan, P.J. and Stout, K.J., Comprehensive study of parameters for characterizing three-dimensional surface topography II: Statistical properties of parameter variation, *Wear*, 1993, vol. 167, pp. 9-21.
107. Dong, W.P., Sullivan, P.J. and Stout, K.J., Comprehensive study of parameters for characterising three-dimensional surface topography III: Parameters for characterising amplitude and some functional properties, *Wear*, 1994, vol. 178, pp. 29-43.
108. Dong, W.P., Sullivan, P.J. and Stout, K.J., Comprehensive study of parameters for characterising three-dimensional surface topography IV: Parameters for characterising spatial and hybrid properties, *Wear*, 1994, vol. 178, pp. 45-60.
109. Jiang, X., Scott, P.J., Whitehouse, D.J. and Blunt, L., Paradigm shifts in surface metrology. Part I. Historical philosophy, *Proceedings of the Royal Society*, 2007, vol. 463, pp. 2049-2070.
110. Jiang, X., Scott, P.J., Whitehouse, D.J. and Blunt, L., Paradigm shifts in surface metrology. Part II. Historical philosophy, *Proceedings of the Royal Society*, 2007, vol. 463, pp. 2071-2099.
111. ISO / FDIS 25178-3, Geometrical product specifications (GPS) - Surface texture: Areal - Part 3: Specification operators, 2010.
112. http://www.michmet.com/index.html. Access date: January 2012.
113. Smith, G.T., Industrial metrology surfaces and roundness. *Springer, London*, 2002, pp. 13-15.
114. Stout, K.J. and Blunt, L., Three-dimensional surface topography. *Penton Press, London*, 2000, pp. 97-142.
115. ISO/FDIS 16610:21, Geometrical product specifications (GPS) - Filtration - Part 21: Linear profile filters: Gaussian filters, 2008.
116. Balden A., Review: adhesively bonded joints and repairs in metallic alloy, polymers and composite materials: adhesives, adhesion theories and surface pretreatment. *The Journal of Materials Science*, 2004, vol. 39 (1). pp. 1-49.
117. Packham, D.E., Surface energy, surface topography and adhesion. *International Journal of Adhesion and Adhesives*, 2003, vol. 23, pp. 437-448.
118. Starikov, D., Boney, C., Pillai, R., Bensaoula, A., Shafeev, G.A. and Simakin, A.V., Spectral and surface analysis of heated micro-column arrays fabricated by laser-assisted surface modification, *Infrared Physics and Technology*, 2004, vol. 45, pp. 159-167.

119. Baburaj, E.G., Starikov, D., Evans, J., Shafeev, G.A. and Bensaoula, A., Enhancement of adhesive joint strength by laser surface modification, *International Journal of Adhesion and Adhesives*, 2007, vol. 27, pp. 268-276.
120. Zhang X.M., Yue T.M. and Man H.C., Enhancement of ceramic-to-metal adhesive bonding by excimer laser surface treatment, *Materials Letters*, 1997, vol. 30, pp. 327-332.
121. http://www.oxford-instruments.com/products/etching-deposition-growth/processes-techniques/plasma-etch/Pages/plasma-etch.aspx. Access date: January 2012.
122. Manos, D.M. and Flamm, D.L., Plasma etching, an introduction. *Academic Press Inc, Boston*, 1989.
123. Choi, S.W., Choi, W.B., Lee, Y.H. Ju, B.K., Sung, M.Y. and Kim, B.H., The analysis of oxygen plasma pretreatment for improving anodic bonding, *Journal of The Electrochemical Society*, 2002, vol. 149 (1), pp. G8-G11.
124. Williams, K.R. and Muller, R.S., Etch rates for micromachining processing, *Journal of Microelectromechanical System*, December 1996, vol. 5 (4), pp.256-268.
125. Williams, K.R., Gupta, K. and Wasilik, M., Etch rates for micromachining processing-Part II, *Journal of Microelectromechanical System*, December 2003, vol. 12 (6), pp.761-777.
126. http://en.wikipedia.org/wiki/Hydrofluoric_acid. Access date: January 2012.
127. http://www.metallographic.com/. Access date: January 2012.
128. Blast media data sheet, GUYSON HONITE, Guyson International Limited, United Kingdom.
129. Zhang, B. and Yung, K.C., Feasibility of the 248 nm Excimer laser in the laser structuring of fine circuit lines on printed circuit board, *The International Journal of Advanced Manufacturing Technology*, 2007, vol. 33, pp. 1149-1158.
130. Chen, Y.T., Ma, K.J., Zhou J.G. and Tseng, A.A., Excimer laser ablation of glass-based arrayed microstructures for biomedical, mechanical, and optical applications, *Journal of Laser Applications*, February 2005, vol. 17 (1), pp. 38-46.
131. Tönshoff, H.K., Overmeyer, L. and Ostendorf, A., General machining concept for producing micro-optics with high-power UV lasers. *Proceedings of SPIE*, 1997, vol. 2992, pp. 86-95.
132. Crafer, R.C. and Oakley, P.J., Laser Processing in Manufacturing. *Chapman and Hall, London*, 1993.

133. Chen, Y.T., Ma, K.J., Tseng, A.A., Chen, P.H., Projection ablation of glass-based single and arrayed microstructures using excimer laser, *Optics and Laser Technology*, 2005, vol. 37, pp. 271-280.
134. Harvey, E.C., Rumsby, P.T., Gower, M.C. and Remnant, J.L., Microstructuring by Excimer Laser. *Micromachining and Microfabrication Technology*, 1995, vol 2639, pp. 266-277.
135. Tseng, A.A., Recent developments in micromachining of fused silica and quartz using excimer lasers. *Physica Status Solidi*, 2007, vol. 204 (3), pp. 709-729.
136. KrF Excimer laser (mode EMG 203) Operating Manual, Lambda Physik.
137. Wang, S.Y., A computer simulation for mask-shape effect in the fabrication of an aspheric micro lens array by using a dragging process with excimer laser. *Journal of Micromechanics and Microengineering*, 2005, vol. 15, pp. 1310-1316.
138. Harvey, E.C. and Rumsby, P.T., Fabrication techniques and their application to produce novel micromachined structures and devices using excimer laser mask projection. *Micromachining and microfabrication process technology III*. 1997, vol. 3223, pp. 26.
139. Rizvi, N.H. Production of novel 3D microstructures using excimer laser mask projection techniques SPIE Conference on Design. *Test and Microfabrication of MEMS and MOEMS*, 1999, vol. 3680, pp. 546-552.
140. Durney, L.J. Electroplating engineering handbook. *Wokingham*: *New York*, 1984.
141. Circuposit Electroless Copper 4750 data sheet, Shipley Europe Limited, United Kingdom.
142. CIRCUPOSIT™ 3344 and 3350-1 data sheets, Rohm and Haas Electronic Materials.
143. Charbonnier, M., Goepfert, Y., Romand, M. and Leonard, D., Electroless plating of glass and silicon substrates through surface pretreatments involving plasma-polymerization and grafting process. *The Journal of Adhesion*, 2004, vol. 80, pp. 1103-1130.
144. Van Den Meerakker, J.E.A.M., On the mechanism of electroless plating. 1I. One mechanism for different reductants. *Journal of Applied Electrochemistry*, 1981, vol. 11, pp. 395-400.
145. Tseng, W.T., Lo, C.H. and Lee, S.C., Electroless deposition of Cu thin films with $CuCl_2$-HNO_3 based chemistry I. Chemical formulation and reaction mechanisms. *Journal of the Electrochemical Society*, 2001, vol. 148 (5), pp. C327-C332.
146. Yosi, S.D., Dubin, V. and Angyal, M., Electroless copper deposition for ULSI, *Thin Solid Films*, 1995, vol. 262, pp. 93-103.

147. Feldman, B.J. and Melroy, O.R., The mechanism of electroless Cu deposition: extraction of the oxidative and reductive electrochemical half-cell currents from a complete bath. *The Journal of The Electrochemical Society*, 1989, vol. 136 (3), pp. 640-643.
148. Shacham-Diamand,Y. and Dubin, V., Copper electroless deposition technology for ultra-large-scaleintegration (ULSI) metallization. *Microelectronic Engineering*, 1997, vol. 33, pp. 47-58.
149. Mishra, K.G. and Paramguru, R.K., Kinetics and mechanism of electroless deposition of copper, *The Journal of The Electrochemical Society*, 1996, vol. 143 (2), pp. 510-516.
150. Charbonnier, M. and Romand, M., Tin-free electroless metallization of glass substrates using different PACVD surface treatment processes. *Surface and Coatings Technology*, 2002, vol. 162, pp. 19-30.
151. Meiron, T.S., Marmur, A. and Saguy, I.S., Contact angle measurement on rough surfaces, *Journal of Colloid and Interface Science*, 2004, vol. 274, pp. 637-644.
152. Chau, T.T., A review of techniques for measurement of contact angles and their applicability on mineral surfaces. *Minerals Engineering*, 2009, vol. 22, pp. 213-219.
153. Kim, W.S., Yun, H., Lee, J.J. and Jung, H.T., Evaluation of mechanical interlock effect on adhesion strength of polymer-metal interfaces using micro-patterned surface topography. *International Journal of Adhesion and Adhesives*, 2010, vol. 30, pp. 408-417.
154. Zhu, P., Masuda, Y. and Koumoto, K. Seedless micropatterning of copper by electroless deposition on self-assembled monolayers. *Journal of Materials Chemistry*, 2004, vol. 1 4, pp. 976-981.
155. Cui, X., Hutt, D.A. and Conway, P.P., An Investigation of Electroless Copper Films Deposited on Glass. *Proceedings of 2nd IEEE Electronics System-Integration Technology Conference, London*, September 2008, pp. 105-110.
156. Cui, X., Bhatt, D, Khoshnaw, F.M, Hutt, D.A. and Conway, P.P., Glass as a Substrate for High Density Electrical Interconnect. *Proceedings of the 10th International IEEE Electronics Packaging Technology Conference*, Singapore, December 2008, pp. 12-17.
157. Dubin, V.M. and Shacham-Diamand,Y., Selective and Blanket Electroless Copper Deposition for Ultralarge Scale Integration, *The Journal of The Electrochemical Society*, 1997, vol. 144 (3), pp. 898-908.

158. Shukla, S., Seal. S., Akesson, J., Oder, R., Carter, R. and Rahman, Z., Study of mechanism of electroless copper coating of fly-ash cenosphere particles. *Applied Surface Science*, 2001, vol. 181, pp. 35-50.
159. Matsuoka, M., Murai, J. and Iwakura, C., Kinetics of Electroless Copper Plating and Mechanical Properties of Deposits. *The Journal of The Electrochemical Society*, 1992, vol. 139 (9), pp. 2466-2470.
160. Lacombe, R., Adhesion measurement methods. *CRC Press, Taylor & Francis Group*, 2006.
161. Maxwell, A.S., Review of test methods for coating adhesion, NPL REPORT MATC (A) 49, September 2001.
162. Heavens, O.S., Some features influencing the adhesion of films produced by vacuum evaporation. *Journal of Physical Radium*, 1950, vol. 11, pp. 355.
163. Bull, S.J. and Berasetegui, E.G. An overview of the potential of quantitative coating adhesion measurement by scratch testing. *Tribology International* 2006, vol. 39, pp. 99-114.
164. Benjamin, P. and Weaver, C., Measurement of Adhesion of Thin Films. *Proceedings of the Royal Society of London. Series A, Mathematical and Physical Sciences*. 1960, vol. 254, pp. 163-176.
165. Weaver, C. and Parkinson, D.T. Diffusion in Cold-Aluminum. *The Philosophical Magazine*, 1970, vol. 22, pp. 377.
166. Laugier, M.T., An energy approach to the adhesion of coatings using the scratch test. *Thin Solid Films*, 1984, vol. 117, pp. 243-249.
167. Laugier, M.T., Adhesion of TiC and TiN coatings prepared by chemical vapour deposition on WC-Co-based cemented carbides. *Journal of Materials Science*, 1986, vol. 21, pp. 2269-2272.
168. Burnett, P.J. and Rickerby, D.S., The relationship between hardness and scratch adhesion. *Thin Solid Films*, 1987, vol. 154, pp. 403.
169. Bull, S.J., Rickerby, D.S., Matthews, A., Lcyland, D.S., Pace A.R. and Valli, J., The use of scratch adhesion testing for the determination of interfacial adhesion-The importance of frictional drag. *Surface and Coatings Technology*, 1988, vol. 36, pp. 503.
170. Bull, S.J. and Rickerby, D.S., Evaluation of coatings, *British Ceramic Transactions and Journal*, 1989, vol. 88, pp. 177.
171. Bull, S.J., and Rickerby, D.S., The sliding wear of titanium nitride coatings. *Surface and Coatings Technology*, 1990, vol.42, pp. 149.

172. Chen, J.J., Lin, Z.H. Bull, S.J., Phillips, C.L. and Bristowe, P.D., Experimental and modelling techniques for assessing the adhesion of very thin coatings on glass, *Journal of Physics D: Applied Physics*, 2009, vol. 42, pp. 11.
173. Chalker, P.R., Bull, S.J. and Rickerby, D.S., A review of the methods for the evaluation of coating-substrate adhesion, *Materials Science and Engineering*, 1991, vol. 140, pp. 583-592.
174. Hand, D.J., A hand book of small data sets. *Chapman and Hall, London*, 1994.
175. Moore, D. S., The basic practice of statistics. *W.H. Freeman, New York*, 2004.
176. Hollander, M. and Wolfe, D. A. Nonparametric statistical methods. *Wiley, New York*, 1999.

APPENDIX

1. GUYSON Formula F1400 equipment for bead blasting

2. Focussing programme

```
V1=75.2940; Mask z position
V2=66.4230; Mask u position
V3=103.3360; Start Workpiece X Position
V4=160.7510; Start Workpiece Y Positio
V5=5; Laser repetition rate
V6=0.1; Elevator height step
V7=3.5; Stage start height (goes up)
V8=6; No. of different focus position
V9=20; No. of shots at each mask
V10=1; Amount to move Y between marks

BO1; Select board 1
EN x y z u; Enable x y z and u
Home z f 100; Home mask x axis
Dwell 5000; Dwell 5 s
Home x y u f200; Home stage x and y axis and mask y axis
BO 2; Select board 2
EN x y z; Enable attenuator rotation and elevator axis
Home u f10; Home attenuator
Home y z f200; Home attenuator and elevator
Enable y
U=0.8 f10

BO1; Select board 1
G90 X=V3 Y=V4 Z=V1 U=V2 F1000 Move to start position
BO2; Select board 2
G91 z=V7 F10; Move to focus start position
BO1; reselect Board 1
Mo; Wait for F9 key to be pressed
WA ON; Wait for stage motion to finish
BO1
PSOP.1.0. 50.(10000/V5)-50; Defines Repetition rate
Loop V8; Loop through each mark
BO1
PSOF.2.V9; Fire shots
PW 3000
G91 G1 X=V10 F100; Move to next mark position
WA ON
PW 3000
BO2; Select board 2
G91 G1 z=V6 F50; Move to next elevator position
PW3000
NEXT
PSOF, O; Disable laser output
BO1; Select board 1
G91 X-80 Y-80 F3000; Move to front
EXIT; Exit programme
```

3. Groove generating programme

```
BO1; Select board 1
EN x y z u; Enable x y z and u
Home z f 100; Home mask x axis
Dwell 5000; Dwell 5 s
Home x y u f200; Home stage x and y axis and mask y axis
BO 2; Select board 2
EN x y z; Enable attenuator rotation and elevator axis
Home u f10; Home attenuator
Home y z f200; Home attenuator and elevator
Enable y

V1=75.2940; Mask z position
V2=66.4230; Mask u position
V3=103.3360; Start Workpiece X Position
V4=160.7510; Start Workpiece Y Positio
V5=5; Laser repetition rate
V7=4.0; Focus position
V8=0.1; Beam length along groove length
V9=10; Shots per are
V10=10; Groove length
V11=1; No. of passes of groove
V12=100; No. of grooves
V13=0.08; Periods of grooves

V6=60*V5*V8/V9; Feedrate calculation

Bo2; Select board 2
G91 G1 Z=V7 F40; Move beam focus position
G91 G1 u=0.9 F10; Set attenuator

Bo1; Select board 1
G91 G1 X=V3 Y=V4 F1500; Move WP to beam
G90 G1 Z=V1 U=V2 F1500; Move to mask position

Loop V12; No of grooves loop
Loop V11; Passes loop
BO1
PSOP,1.0.50.(10000/V5)-50; Define trigger pulse
PSOP,1; Define fire on Y motion
G91 G1 Y=V10 F=V6; Move WP along groove
PSOF,0; Disable laser
G90 G1 Y=V4 F500; Return to start of groove
Next
G91 G1 X=V13 F100; Move to next groove
Next
G90 G1 Y=10 F1500; Move sample away from optics
EXIT
```

4. Matrix programme

```
V1= 99.4400; Start workpiece X position
V2=139.2580; Start workpiece Y position
V3=4; Focus position
V4=71.5170; Mask position in Z axis
V5=62.8640; Mask position in U axis
V6=0.2; Initial attenuator position
V7=7; Number of different attenuator positions
V8=0.1; Value to increase attenuator opening by
V9=25; Starting number of shots
V10=200; End number of shots
V11=25; Shot number step
V12=[(V10-V9)/V11]+1; Number of different shot
V13=0.5; Amount to move in X and Y between sites
V14=5; Laser rep rate

BO1; Select board 1
EN x y z u; Enable x y z and u
Home z f 100; Home mask x axis
Dwell 5000; Dwell 5 s
Home x y u f200; Home stage x and y axis and mask y axis
BO 2; Select board 2
EN x y z; Enable attenuator rotation and elevator axis
Home u f10; Home attenuator
Home y z f200; Home attenuator and elevator
WA ON; Wait for motion to complete

BO 1
G91 X=V1 Y=V2 Z=V4 U=V5 F1500; Move stage to initial position
BO2
G91 U=V6 Z=V3F30; Move attenuator and stage elevation to initial position
WA ON

BO1
PSOP.1.0.50. (10000/V14)-50; Defines rep rate
Dwell 11000
V15=V9; Reset counter for laser shots
Loop V7; Loop through attenuator  position
   Loop V12; Loop through number of pulses
   BO1
   PSOF.2.V9; Fire shots
   DW 11000
   G91 G1 Y=V13 F1000; Move to near Y position
   WA ON
   DW 11000
   V15=V15+V11
   NEXT

BO1
```

```
G90 G1 Y=V2 F1000; Return to first Y position
G91 G1 X=V13 F1000; Move to next X position
WA ON

BO2
G91 G1 U=V8 F30; Increase attenuator opening
WA ON; Wait for motion to complete
Next
PSOF.O; Disable laser output
EXIT
```

5. Excimer laser equipment – Model EMG 203, Lambda Physik